Winding loss optimisation for high power density permanent magnet machines for aerospace propulsion

By:

Yangyu Sun

A thesis submitted in partial fulfilment of the requirements for the degree of

Doctor of Philosophy

The University of Sheffield

Faculty of Engineering

Department of Electronic and Electrical Engineering

08/01/2024

Abstract

This thesis reports on an investigation into the winding losses of high power density brushless permanent magnet machines. The research is performed in the context of a design study for a 350kW, 6000rpm machine for aerospace propulsion with an emphasis on methods for increasing the electric loading that can be sustained in the stator. A particular focus of the research is the use of solid bar conductors although this type of conductor tends to give high level of AC losses if not properly designed.

A design study is undertaken to establish a machine design capable of meeting the 350kW specification which includes initial sizing and sensitivity studies on various design features and dimensions. This yields a design based on a large cross-section solid bar winding, which on the basis of quasi-static considerations, was capable of meeting the specification. However, consideration of AC losses in the stator winding caused by induced eddy currents result in almost an order of magnitude increase in conductor loss which would be unsustainable in practice.

A series of strategies to reduce AC loss were investigated specifically the re-positioning of conductors, magnetic slot-wedges, paralleling and transposition, consideration of aluminium and hybrid copper / aluminium windings and the optimisation of core geometry to alleviate flux in the stator slot. The optimum combination of these strategies result in a near 7-fold reduction in the conductor loss, making a solid bar winding competitive with a traditional wound machine in terms of loss while retaining the heat-transfer advantages.

The role of Litz wire as an alternative conductor is investigated in detail, including a comparison in both two- and three-dimensions of various methods for calculating eddy current losses in Litz. Machine level simulations of the reference design equipped with Litz wire are reported and comparison drawn with bar conductors.

The thesis culminates with a series of experimental measurements on a motorette for both strip wound bar conductor and Litz wire, which provide a level of validation for the simulations and highlight the challenges of measuring AC loss in Litz winding in representative stator cores.

Acknowledgements

During my 4-year PhD study, my supervisor, professor Geraint Jewell, has been always supportive and has helped me a lot through many difficulties. I would like to express my sincere thanks to him for his continuous support and guidance throughout this journey. His expertise, broad insights and constructive feedback have great influence on me.

I am indebted to my colleagues Wenjun Zhu, Dr Xiao Chen, Professor Jiabin Wang, Han Wu and colleagues from my office for their help and support during my PhD study. Their support has been invaluable during the PhD study. I would also like to thank my friends for their encouragement, company, discussions and assistance during various stages of my PhD.

Finally, I would like to thank my family for their unconditional support and encouragement through the years of my PhD study.

Table of Contents

List of symbols

Symbol	Explanation	Unit
	Chapter 2	
P	Rated power	W
T	Torque	Nm
ω	Angular speed	Rad/s
D_{ro}	Rotor outer diameter	mm
L	Axial length	mm
B	Magnetic loading (averaged flux density)	T
Q	Electrical loading	kA/m
N_s	Number of slots	-
k_p	Packing factor	-
A_s	Area of slot	mm^2
J	Current density	A/mm^2
D_{out}	stator outer diameter	mm
D_{si}	Stator inner bore diameter (rotor diameter):	mm
l_m	Magnet thickness:	mm
l_g	Airgap length:	mm
W_s	Slot width	mm
h_s	Slot depth	mm
h_{bi}	Back-iron	mm
B_{tt}	Flux density at tooth tip	T
B_{tb}	Flux density at tooth body	T
h_{tt}	Tooth tip height	mm
H_{iron}	Magnetic field strength of soft magnetic material	A/m
l_{iron}	Length of average flux path in iron core	m
H_g	Magnetic field strength of air gap	A/m
l_g	Length of average flux path of air gap	m
H_m	Magnetic field strength of magnet	A/m
l_m	Length of average flux path of magnet	m
N	Number of turns	-
I	Current	A
B_m	Magnetic flux density of magnet region	T
A_m	Area of magnet in the magnetic circuit	mm^2
B_g	Magnetic flux density of air gap region	T
A_g	Area of airgap in the magnetic circuit	mm^2
μ_0	Vacuum permeability	H/m

μ_r	Relative permeability	-
B_r	Remanence of permanent magnet	T
λ	Tooth pitch to slot pitch ratio	-
D_{si}	Stator bore diameter (stator inner diameter)	mm
W_{tb}	Width of tooth body	mm
W_{to}	Tooth width at the back of slot	mm
D_{out}	Stator outer diameter	mm
σ_{max}	Maximum hoop stress	MPa
δ_c	Density of carbon fibre	kg/m^3
v_c	Poisson's ratio	-
d_{co}	Outer diameter of rotor sleeve	mm
d_{ci}/d_{mo}	Inner diameter of rotor sleeve	mm
m_{eq}	Equivalent magnet mass	kg
r_{meq}	Equivalent radius of gyration	m
d_{mi}	Rotor hub outer diameter	mm
δ_m	Density of magnet	kg/m^3
δ_{ip}	Density of interpole material between adjacent magnet poles	kg/m^3
α	Pole arc	° (electrical)
I_a, I_b, I_c	Three phase sinusoidal current waveform	-
I_{max}	Amplitude of sinusoidal current waveform	A
γ	Angular offset which aligns the current waveform and back-emf waveform	° (electrical)

Chapter 3

P_{cu}	Quasi-static losses	W
I_{rms}	RMS current	A
R	Resistance of winding	Ω
J_{rms}^2	RMS current density	A/mm^2
ρ	Resistivity of copper	kg/m^3
V_{cu}	Volume of copper	m^3
L	Axial length	mm
P_{skin}	Eddy current loss caused by skin effect	W
k_s	Skin effect eddy current loss coefficient	-
J_{mz}	Amplitude of exciting current density	A/mm^2
f	Frequency	Hz
a	Radius of round wire (or half thickness of bar conductor)	mm
σ	Conductivity	S/m
k_b	Wire width to wire thickness ratio	-

δ	Skin depth	mm
P_c	Eddy current loss caused by proximity effect	W
k_c	Proximity effect eddy current loss coefficient	-
B_{my0}	Flux density amplitude in y axis direction of specified cartesian coordinate system	T
$k_{\xi 0}$	Coefficient used for proximity loss calculation	-
ξ	Ratio of rectangular wire thickness over skin depth	-
h_{total}	Total conductor height in slot	mm
h_{Al_turn}	Turn height of aluminium	mm
h_{Al_strip}	Strip height of aluminium	mm
s	Scaling ratio	-
h_{Cu_turn}	Turn height of copper	mm
h_{Cu_strip}	Strip height of copper	mm
N_{Al}	Number of turns for aluminium	-
S_{Al}	Number of strips for aluminium	-
N_{Cu}	Number of turns for copper	-
S_{Cu}	Number of strips for copper	-
h_i	Insulation thickness	mm
h_t	Polyester tape thickness	mm

Chapter 4

W	Bundle width of Litz wire	mm
H	Bundle height of Litz wire	mm
r	Strand diameter of Litz wire bundle	mm
k (in rectangular pattern)	Horizontal and vertical distance between strands	mm
k (in hexagon pattern)	Horizontal distance between strands	mm
v (in hexagon pattern)	Vertical distance between strands	mm
f_b	Base frequency	Hz
d	Diameter of Litz wire strand	mm

Abbreviations

HEV	Hybrid electric vehicles
EV	Electric vehicles
BLI System	Boundary Layer Ingestion System
NASA	National Aeronautics and Space Administration
CNT	Carbon Nano Tubes
IACS	International Annealed Copper Standard
AC	Alternating current
DC	Direct current
PM	Permanent magnet
NI	Number of turns × current (magneto-motive force)
Sm2Co17	Samarium Cobalt permanent magnets
NdFeB	Neodymium Iron Boron permanent magnets
RPM	Revolution per minute
FEA	Finite Element Analysis
1D,2D,3D	1 dimensional, 2 dimensional, 3 dimensional
RMS	Root mean square
Back-emf	Back electromagnetic-motive force
FFT	Fast Fourier Transform
SPM	Surface mounted permanent magnet machine
MW1 and MW2	Two commercial magnetic wedges from literature
LF1	Soft magnetic composite wedge from literature
ms	Millisecond
IEC	International Electrotechnical Commission
AWG	American Wire Gauge
YDK	Korean Litz wire and Litz cable manufacturer
mmf	Magneto-motive force

Chapter 1. Introduction

1.1 Background information

There is a growing world-wide trend to move away from fossil fuels for transportation with the electrification of transport being a key factor in this transition. In the automotive sector, hybrid electric vehicles (HEV) and pure electric vehicles (EV) are becoming ever-more popular. Electrical machines for automotive applications are now a mainstream technology with many manufacturers having products in the market that meet the required performance specification. There remains significant pressure on cost reduction with ambitious targets [1] and an interest in moving away from rare-earth magnets but in general electrical machines have reached the level of power density and efficiency that meet the demands of HEVs and EVs.

In recent years, the deployment of electric hybrid propulsion systems into aerospace industry has attracted much attention[2][3][4][5]. However, the implementation of electrical machines in aerospace as propulsion systems is not as well developed as in the automotive sector. All-electric or hybrid propulsion in aircraft still faces significant performance gaps, particular the constraints on battery storage energy density.

Various roadmaps have identified the need to achieve overall drive-train power densities in the 3 kW/kg range, which includes the energy source. As an example, Figure 1.1 shows the various targets for improvements in power density proposed in the Aerospace Technology Institute technology roadmap [6] for the various components that would make up a fuel-cell drivetrain. As can be seen, the 2026 target is 13kW/kg which increases to 25kW/kg by 2050. It is important to note that whereas these levels of power density have been demonstrated in some very high-performance machines, at least as transient short-term ratings these machines have been focussed on high power density, usually at some penalty in efficiency. Efficiency and power density are often in conflict during the design and hence the challenge of getting to 25kW/kg for propulsion machines is that the range of the aircraft is proportional to the efficiency of the electrical machine since the full propulsive power passes through the machine [7].

		2026	2030	Ultimate Target 2050
Electric motor	Power Density (kW/kg)	13	23	25
Power electronics (Inverter)	Power Density (kW/kg)	22	40	60
Power electronics (DC-DC)	Power Density (kW/kg)	15	40	60
Fuel cell stack	Power Density (kW/kg)	7	9	16
Thermal management system*	Power Density (kW/kg)	6	7	20
Air-supply system*	Power Density (kW/kg)	1	1	3
Electrical propulsion system	Power Density (kW/kg)	1.0-1.5	1.5-2.0	3.0-3.5

For thermal management system and air supply system the power used to calculate power density refers to amount of heat dissipated, and compression power required to support the system.

Figure 1.1 Technology Roadmap targets for power density of various components of a fuel-cell powered electric drivetrain for aerospace propulsion (Source: ATI)

The main advantages of hybrid propulsion systems are lower emission, lower energy consumption and reduced acoustic noise. All-electric aircraft may play a role in small personnel transport such as air-taxis and small aircraft but for the medium-term, studies suggest all-electric propulsion is unlikely to be viable in medium and larger aircraft [8].

Hybrid propulsion, in which a gas-turbine is used in combination with various electrical drives is likely be implemented in stages, starting with small regional aircraft in which electrical propulsors are distributed across the wing as shown in Figure 1.2. In some of these concepts, a gas-turbine is used as a prime-mover for a large generator with the propulsion being all-electric. Another likely medium-term development is the adoption of so-called boundary layer ingestion systems such as that shown in Figure 1.3. In this type of system, the main propulsion is provided by standard gas turbine engines, but the rear of the fuselage is fitted with a duct that contains a series of electrical driven fans [9]. Although they provide some additional propulsion, the main role of the BLI system is to ingest the turbulent air flow over the fuselage resulting in a significant reduction in drag and projected fuel efficiency improvements of up to 10% [10].

Figure 1.2 Distributed electrical propulsors in a small hybrid aircraft (NASA Sceptor concept [11])
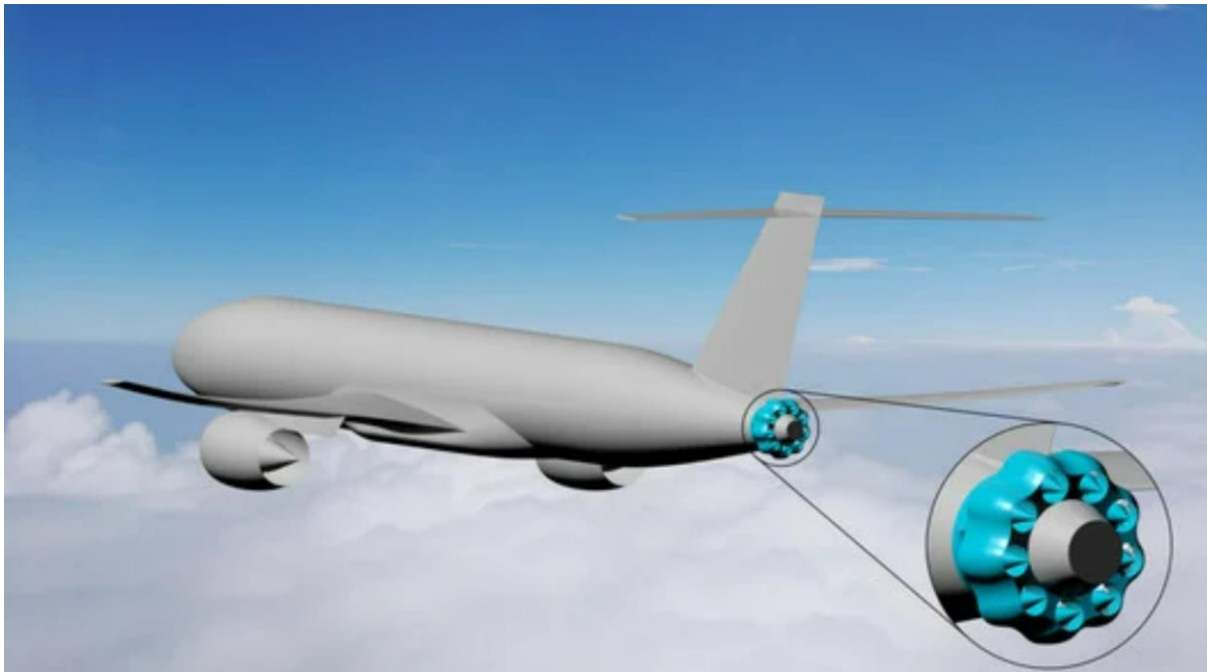
Figure 1.3 Aircraft with boundary layer ingestion system at rear of fuselage (source [9])

The power rating of electrical machines required depends on the size and configuration of aircraft, ranging from 0.5MW for small aircraft to 30MW large aircraft. Typical power ratings for different classes of aircraft are shown in Figure 1.4.
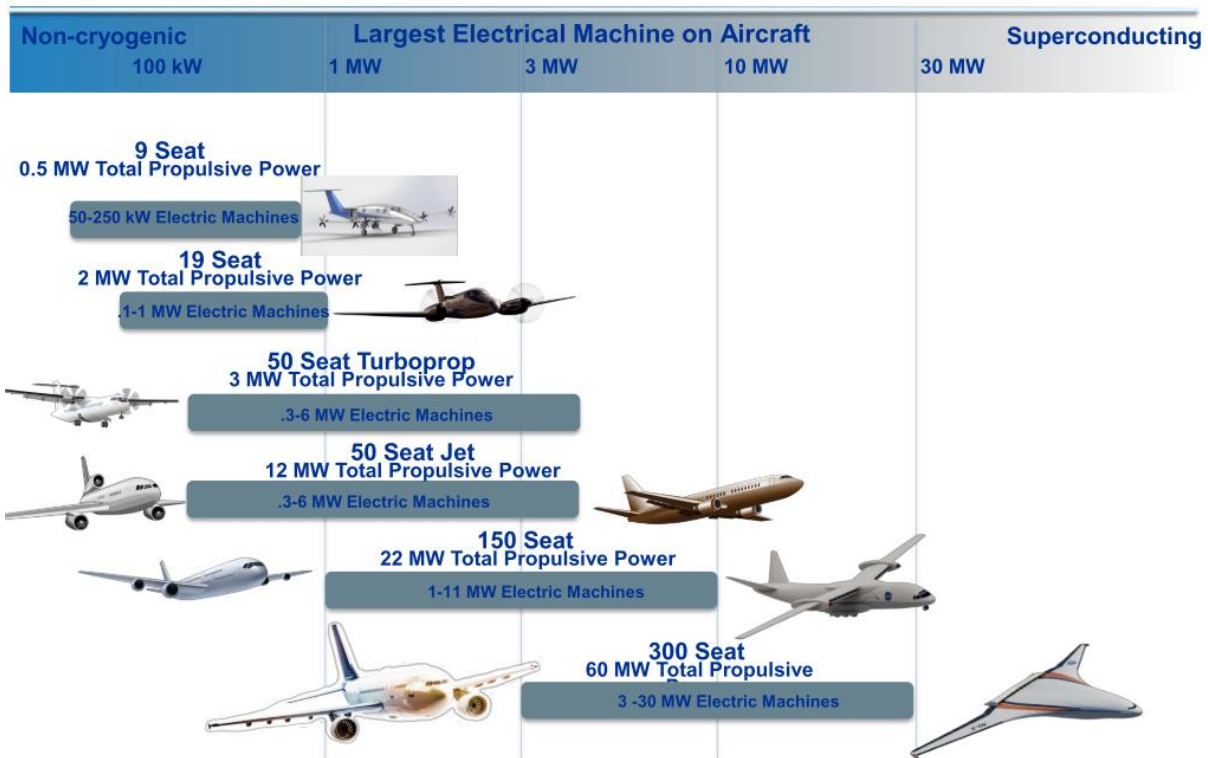
Figure 1.4 Power ratings of different size of aircraft (Source: [11]*)*

As can be seen from Figure 1.4, it is estimated that 0.5MW total propulsive power is needed to power a 9 seat small size aircraft. This can be achieved by implementing a combination of two 250kW machines. Larger aircraft requires power rating in tens of MW range. There are many possible combinations of machine ratings that could be used to achieve a multi-MW overall power rating, distributed propulsion with several 1-2MW electrical machines driven from separate power converters offers a good combination of redundancy and distribution of mass.

A useful measure of machine performance for aerospace applications is gravimetric power density with units of kW/kg. Electrical machines used in aerospace section usually have active power density range to 8 to 23kW/kg [12]. In [13], the design of a 300kW 13,350rpm surface mounted permanent magnet machine for small aircraft is described. This machine achieved active power density (i.e., excluding structural elements) of 10kW/kg and provides some design guidelines for a medium sized machine in aerospace. When power ratings of aircraft increases, the output power of single machines needs to enter the MW range [14][15][16] and this is usually achieved with combination of high speed (up to 20,000rpm) and high power density. Pushing the operating speed near 20,000 rpm inevitably introduces extra demands on rotor design in terms of mechanical stress. In some aerospace applications, there is a preference for fault tolerant capability. This is achieved with various features such as dual-lane windings and multi-phase modular topologies [17]. As an example, the machine reported in [15] split the

stator into six 3-phase modular systems which will also eases the assembly of concentrated winding.

There are two prominent aspects of design which feature prominently in literature, viz. high power density and efficiency. It is worth noting that since many electrical machines for aerospace applications have historically been developed for ancillary applications such as generators, pumps [18] [19], and surface actuators [20] [21], the emphasis has been on power density and not efficiency. It is only with the emergence of concepts for hybrid-electric and all-electric propulsion that greater attention has been paid to efficiency.

1.2 Design features of high-power density machines

As discussed previously, achieving high power density is arguably the critical design objective in terms of releasing a viable solution for hybrid propulsion aircraft although not at the expense of efficiency. To increase the power density of electrical machines, several strategies can be implemented:

1.2.1 Adoption of advanced materials and manufacturing processes

The adoption of advanced materials for magnetic, electrical and structural components can boost machine performance but often with an associated high cost. An example of emerging technologies that one day might play a role in improving both the power density and efficiency of electrical machines is a novel conductor material called CNT-Cu conductor made of composite of copper and Carbon Nano Tubes (CNT) is proposed in [22]. One major advantage of this conductor is that its electrical resistivity is less sensitive to temperature rise than copper itself (a lower temperature coefficient) which makes it competitive for high performance electrical machines. In addition, this material has higher current-carrying capability and lower weight than copper. All these features make it very promising, but its stability and integrity needs further experimental optimisation and validation.

Additive manufacturing has also attracted much attention recently. Additive manufacturing processes involve the creation of three-dimensional objects by depositing materials in layers. There are various additive manufacturing processes depending on how the raw materials are treated (for example, sintering, fully melting of material by electron beam or stereolithography). According to [23], powder bed fusion is the most relevant additive manufacturing techniques in the electrical machine sector. One of the advantages of additive manufacturing is geometric freedom since the shape of an additively manufactured component can be readily customized. In addition, unlike traditional manufacturing process that many small parts are assembled to

form a product, additive manufacturing allows to manufacture a complex device in one piece. In [24], a custom shaped coil was manufactured in which the individual conductor cross-section was shaped using information on the applied field in order to minimise eddy current loss. An additive manufactured conductor material which has a chemical composition of AlSi10MG is proposed in [12]. With help of an additive manufactured aluminium alloy conductor, a customized shape of rectangular hollow conductor was manufactured to accommodate cooling channels and thus allows operation of high current density of 19A/mm^2 and can achieve a high power density of 20.8kW/kg. In addition, by changing build orientation and heat treatment, the conductivity of proposed aluminium alloy can be reduced to 17.4 IACS%, which has attracted much attention for AC loss related topics.

1.2.2 Increased electric loading

Increasing the current density in the windings and hence the electric loading for a machine of a given size will directly boost the output torque but at the expense of increased losses in the winding. Hence, any attempts to increase electric loading requires careful thermal management to maintain the winding temperature within acceptable operating limits [14][25][26][27]. One interesting idea to improve current carrying capability of conductors is to implement hollow copper conductors with circuit duct in the middle [22]. This type of conductor usually has rectangular cross-section, and the cooling fluid flow directly in ducts to improve heat dissipation. With adoption of hollow conductor and aggressive cooling method, current density could be increased over 20A/mm^2. Hollow conductors can be formed using a modified wire drawing method and so can be made from the same alloys and hence achieve the same levels of conductivity. The novelties of adopting hollow conductor are all related to high current carrying capabilities [12]. This type of conductor has not been widely adopted due to its mechanical limitations and manufacturing challenges.

Another method to increase current carrying capability that has been widely adopted, especially in automotive sector, is to use solid rectangular bar conductors instead of wound circular wire. This includes a technology known as hairpin windings which is discussed in more detail. Machines equipped with solid bar conductor tend to be used in combination with rectangular slots whose dimensions are tailored to accommodate a specific size and number of rectangular conductors. The proportion of the slot which is occupied by copper is very high compared to a more traditional winding with circular conductors which yields benefits that can be taken as a reduced loss for a given current or an increased current for a given loss. A higher proportion

of copper in the slot also improves heat transfer in the slot. The proportion of the slot which is occupied by copper is usually quantified by means of a so-called slot-fill factor or coil packing factor. It should be noted that when using high electrical loading, the permanent magnets are vulnerable to irreversible demagnetisation, which means extra care is always required when increase electrical loading.

For machines equipped with rectangular bar conductors, an open slot geometry is usually preferred for easy insertion of pre-formed coils. However, semi-closed slots are an option through either the use of hairpin coils or segmented stator teeth in which the tooth tips are attached after the winding has been inserted [28]. An example of possible arrangements [29] for separate tooth tips is shown in the patent extract in Figure 1.5. This approach can be adopted for solid rectangular bar or rectangular cross-section Litz wire.
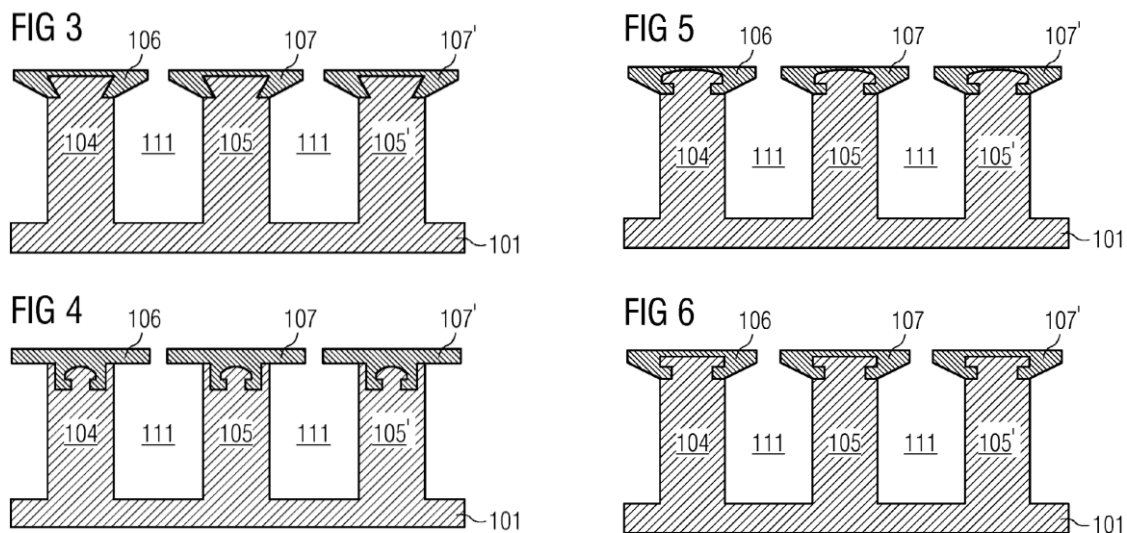
Figure 1.5 Schematics of segmented stator tooth arrangement which allows the insertion of a pre-formed coil into a semi-closed slot (source: [29]*)*

Whereas solid bar conductors offer a route to high slot-fill and hence higher electric loading in a machine, it is important to recognise that large cross-section solid conductors are prone to so-called AC losses caused by induced eddy currents [30]. Indeed, inappropriately selected combinations of conductor cross-section and frequency can result in AC losses which are multiples of the quasi-static conductor losses which more than outweigh the electrical and thermal benefits of the increased slot-fill. By carefully selecting the applications which might benefit from solid bar conductors and following good design practice to mitigate the AC loss, solid bar conductors offer one route to increased power density compared to conventional random wound electrical machines [31].

1.2.3 Increased operating speed

There is an accepted principle in electrical machine design, that the torque fixes the size of the machine rather than the power. Hence, one means of improving power density is to raise the mechanical speed, since the output power is linearly proportional to speed, but size is not greatly affected by speed in many applications. This is a simplified assumption since higher speed and hence a higher electrical frequency will increase the iron loss in the machine, giving rising to loss density in the core and hence exacerbating the problems of removing heat. In addition, increasing the mechanical speed results in increasing centrifugal forces on the rotor magnets. To retain the permanent magnet, a containment sleeve made of either metallic material or carbon fibre is usually implemented to protect the magnet and rotor [15]. A study of the impact of speed on torque density [32] demonstrated that the need to increase mechanical containment progressively decreases the torque density sufficiently that the power density can start to fall with increasing speed. The other factor that limits the maximum speed in many applications is the need to match the speed required by the application without introducing the mass, maintenance and failure modes of adding a gearbox. It should also be noted that as the speed increases, the induced eddy current loss in magnet will also be problematic and hence segmentation of permanent magnet is also required in high-speed applications.

1.3 Efficiency in aerospace electrical machines

For most of electrical machines currently used in aerospace applications such as main generators on a gas-turbine propulsion system, efficiency is not considered as important as power density because the electrical machine only deals with 1-2% of the shaft power. Hence the trade-off of a few percent of efficiency to save mass is usually favourable in terms of aircraft fuel consumption and range. However, this is not the case in hybrid-electric or all-electric propulsion system since the electrical system processes the full propulsive power and hence there is 1:1 relationship between electrical machine efficiency and aircraft fuel consumption. Hence, a well-founded electric propulsion machine design will require a better balance between power density and efficiency than in many existing electrical machines.

These two aspects of performance are often in conflict since efficiency can usually be improved by running the machine less aggressively in terms of magnetic and electrical loadings, which as noted previously is the opposite of what is needed to increase power density. However, where these two performance factors align is the need to minimise losses since power density is ultimately limited by the ability to remove the heat generated by losses. The sources of loss

in a machine include core loss, ohmic losses in the winding (often referred to as copper loss) and various less significant sources of loss such as eddy current loss in rotor magnets and metallic sleeves, aerodynamic losses and bearing frictional drag.

1.4 Machine types for aerospace applications

There are many topologies of electrical machines which find applications across many industry sectors. However, due to considerations of power density, efficiency and technology maturity, only a sub-set of these have been used commercially in aerospace applications for power conversion applications.

1.4.1 Wound-field synchronous machines

Wound-field synchronous machines are the dominant incumbent technology for electrical generators on civil aircraft and have also been adopted as the first commercial starter-generators on aircraft [33] [34]. The stators tend to be fitted with traditional 3 phase AC windings. Voltage regulation in generator mode with respect to both speed and load is realised by controlling the current in the field winding on the rotor, usually using a voltage regulator (AVR) which supplies DC current into the primary of a brushless exciter which in turns feeds the field winding via a diode rectifier on the rotor. When used solely as a generator these machines have the very significant advantage of being connected directly to the three-phase network without the need for a power converter.

Wound-field machines can also be used to provide electrical starting capability, although this requires significant reconfiguration of the machine connections to include a power converter which act as a so-called motor-control-unit. As an example, the Boeing 787 is equipped with a starter-generator which has a starting power capability of ~60kW when driven from a motor-control-unit and a generator capability of 250kVA when directly connected to the aircraft network [35]. Amongst several drawbacks of this machine type are a modest power density, e.g. the state-of-art 250kVA generators on the Boeing 787 achieve ~2.5kVA/kg [36] and the challenge of managing the temperature of the rotating rectifier diodes.

1.4.2 Induction machines

Induction machine has been the dominant machine technology in industrial applications for many decades because of their low cost and high reliability. The main components in an induction machine are a conventional 3-phase stator and short-circuited three phase rotor winding. However, since induction machines are subject high levels of rotor losses, they tend

to have lower efficiencies than PM and wound-field synchronous machines. In addition, since removing losses from the rotor is problematic, the torque density/power density of induction machine is generally lower compared to PM machine counterparts. Induction machines are used in aerospace applications for a variety of ancillary systems such as small actuators, pumps, power drive units, cargo feeders, seat actuators and environmental cooling. In many of the less demanding applications they can be used directly off the AC network with no speed to torque control. A detailed design study based on an aerospace actuator specification [37] demonstrated that an induction machine was not competitive with a PM machine and this fits with the general consensus that PM machines have superior performance compared to induction machines when compared on a like-for-like basis.

1.4.3 Reluctance machines

There are two major categories of reluctance machines, viz. switched reluctance and synchronous reluctance machines. The working principles of both type of reluctance machines are quite similar, as they both rely on tendency of soft magnetic material to align with magnetic field generated by stator winding (reluctance force). A switched reluctance machine is a doubly salient machine with concentrated windings, a simple cruciform rotor structure and a highly salient stator core. Synchronous reluctance machines tend to have non-salient stator with distributed windings and resemble the stator of induction machines and synchronous machines. There is no more constraints on winding configuration and the rotor structure is more complicated than that of switched reluctance machine. Flux barriers which are made of non-magnetic materials are used to block flux path of certain angle and maximize the flux in d (direct) axis. Although reluctance machines have simple rotor structure and potential high fault-tolerant capability, they only achieve modest power density and efficiency and have very poor power factor which in turn results in large converter ratings. The use of reluctance machine in aerospace sector is only seen in early 21st century [38][39].

A high-speed 45kW switched reluctance machine for an aerospace starter-generator was designed, simulated and tested in [40]. This demonstrated competitive power density (quoted at 9.8 kW/L which corresponds to ~ 1.5 kW/kg or so) and a system efficiency of 82%. Several design studies have been published in which the performance of switched reluctance and PM machines have been compared in aerospace applications. As an example, a study in [41] demonstrated that a PM was far superior in terms power density for a demanding actuation application.

1.4.4 Permanent magnet machines

Brushless permanent magnet machines are known for their high power-density and high efficiency, and thus have become the preferred technology for high-performance electrical machines across many sectors. The development of PM machines has built on the emergence of rare-earth magnets in 1970s (SmCo) and 1980s (NdFeB). These materials led to a step-change in the performance of PM machines. However, in the intervening years, material improvements have been more incremental with only modest improvements in the magnetic properties of PM materials [42], albeit that there have been marked improvements in temperature stability and corrosion resistance. There have been many studies published on PM machine design for aerospace applications including actuation [43], starter-generators [44][45] and propulsion [46].

1.4.5 Summary of machine topologies

Figure 1.6 shows a comparison of the key characteristics proposed in [47]. This kind of ranking is subjective and very general, but it is useful in identifying the main strengths and weaknesses on different technologies. This published evaluation indicates that various PM machines tend to be favoured over induction and switched reluctance machines. This conclusion is consistent with most published design studies, although it is important to recognise that this evaluation is focussed on the machine performance and not on the wider system where factors such as fault modes, converter rating, repairability etc.

TABLE 1. Electric Machines Rated by Key Characteristics.

Machine-Type KCs*		Rating[1]					
		IM	SRM	PMM Tooth, Two-Pole	PMM Tooth, Multipole	PMM Toothless, Two-Pole	PMM Toothless, Multipole
KC 1	Rotor losses	6	6	10	10	10	10
KC 2	Stator losses	8	8	9	10	8	9
KC 3	Windage losses	5	1	9	9	10	10
KC 4	Rotor thermal limitations	8	10	4	4	4	4
KC 5	Cooling options	5	5	9	9	10	10
KC 6	Rotor mechanical limitations	5	7	9	9	10	10
KC 7	Torque-to-inertia ratio	5	7	9	9	10	10
KC 8	Torque pulsation	9	3	6	6	10	10
KC 9	Compatibility with bearings	5	5	9	9	10	10
KC 10	High-speed capability	5	7	9	9	10	10
KC 11	Short-circuit behavior	10	10	4	4	3	3
KC 12	Machine complexity	7	10	9	9	8	8
KC 13	Current density	7	7	10	10	8	8
KC 14	Power density	7	8	10	10	8	8
Total		92	92	116	117	119	120

*Descriptions of the KC numbers are provided in the section "Electric Machine Key Characteristics"
[1] 10=best, and 1=worst.
The rotor thermal limitation for PMM is typically 200 °C.

Figure 1.6 Evaluation of key characteristics of different machine technologies for aerospace applications (source [47])

The long development cycles of aircraft means that commercial deployment for a new technology such as PM machines can take many years and so even though PM machines are well recognised for having the best performance amongst competing machines, their market share is still low in aircraft with traditional wound-field synchronous machines still being favoured as generators with some limited electrical start capability. This is likely to change when electric propulsion starts to enter the market in smaller aircraft.

1.5 Rectangular cross-section bar conductors

As noted previously in this chapter, increasing the winding slot-fill is a key factor in improving torque and hence power density and/or efficiency of machines. There are several alternative conductor geometries, types and winding methods that can be considered in the design of an electrical machine. A summary of the main types is shown in Table 1.1.

Table 1.1 Comparisons between rectangular, circular and Litz conductors

	Rectangular bar conductor (form-wound winding)	Circular conductor (random wound winding)	Litz Wire (highly paralleled strands of fine wire)
Conductor shape	Rectangular	Circular	Overall conductor is often rectangular (by rolling) but with circular individual strands
Packing factor	0.6-0.8	0.35-0.55	0.5-0.6
Number of turns in a slot	Usually between 4 and 10 or so	Often 10s or hundreds within a slot	Usually between 4 and a few 0s
Slot shape	Rectangular	Trapezoidal or bulbous	Best suited to rectangular but cross-section can be distorted to fit non-rectangular
Slot opening shape	Open slot for preformed but semi-closed slot possible for hairpin / segmented stator cores	Open or semi-closed	open slot but not limited
Thermal performance	Excellent	Poor	Poor but marginally better than random wound circular

As will be apparent from Table 1.1, based on these top-level characteristics, rectangular bar type conductors would appear to offer the best combination of performance, although as will be discussed in section 2.3.1 of this chapter, AC losses can become a major issue for solid bar conductors. A single slot model equipped with 10 turns of bar conductors is shown in the Figure 1.7 below. These rectangular bar conductors usually have some form of corner radius to manage electric stress and ensure robust coating.

Fill factor about 72%
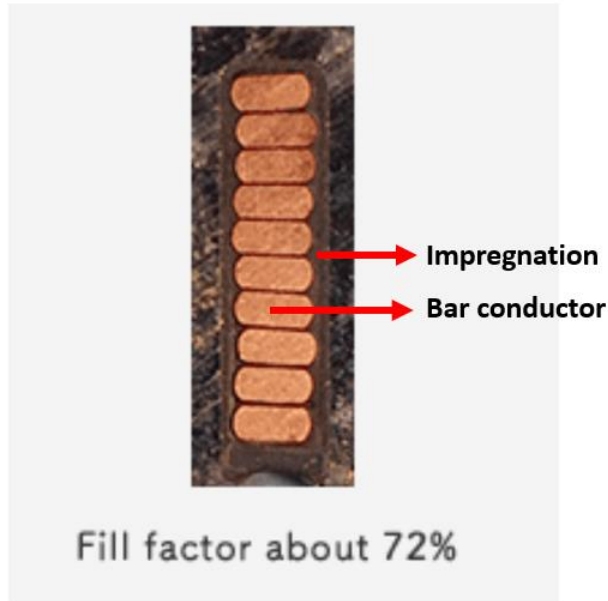
Figure 1.7 Cross-section through the slot of a Mitsubishi Generation 8 traction machine (Source: Mitsubishi Electric)

As is shown in the Table 1.1, the heat dissipation capability of bar conductors is better than that of Litz wire or round conductor. To demonstrate the advantages in terms of thermal performances associated with bar conductor, two simplified single slot model equipped with bar conductor and Litz wire with predefined single direction of heat flux is proposed, see Table 1.2 below:

Table 1.2 Two identical single slot thermal model equipped with bar conductor and Litz wire

Single slot model equipped with bar conductor
Single slot model equipped with Litz wire

13

Zoomed-in view of bar conductor model	Zoomed-in view of Litz conductor model
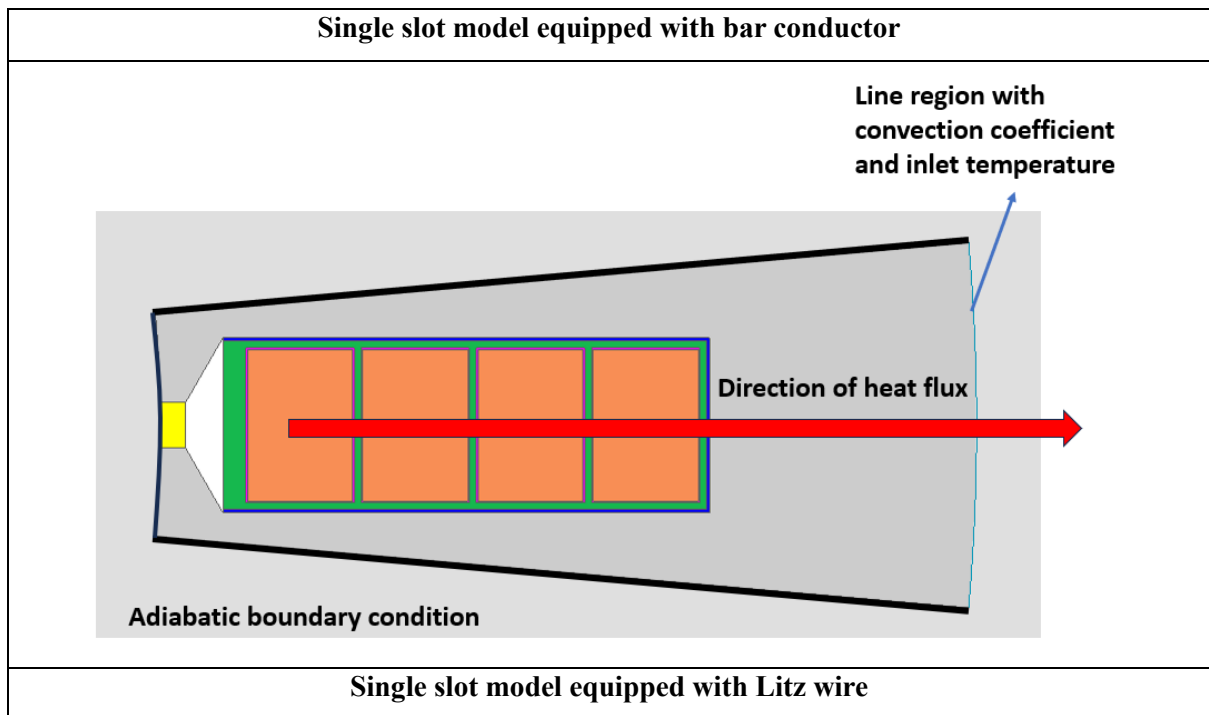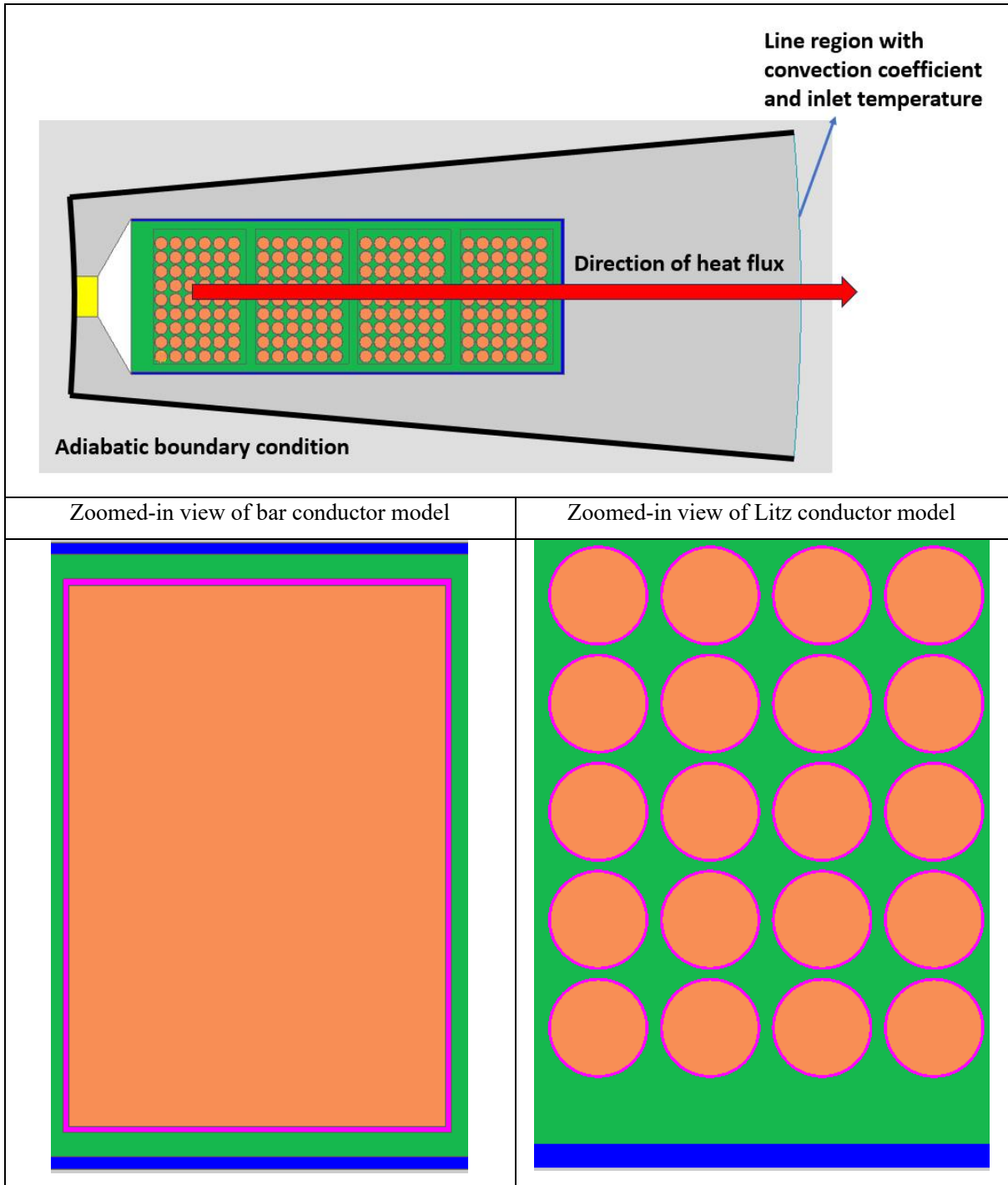
Note that the pink region represents the insulation, and the green region stands for impregnation. While for the blue region, it is the slot liner region. The simulations were performance under steady state thermal context and the detailed thermal material properties are provided in the Table 1.3 below:

Thermal conductivities of different materials k (W/m/°C)	Convection coefficient h (housing water jacket): 1000 W/m²/°C
	Fluid inlet temperature: 70°C
Air: 0.025	Conductor size:
Stator core (hiperco50A): 55	Bar: 8.9mm × 6.2mm
Copper: 394	Litz wire: strand diameter of 0.812mm, 54 strands
Impregnation: 0.2	Insulation thickness: 0.1mm
Insulation: 0.21	
Slot liner: 0.21	

Note that the values of thermal conductivities of various materials are from [48], while for the machines implemented with indirect forced liquid cooling with a current density between 7-20 A/mm², the convection coefficient spans a wide range from 100 to 10000 W/m²/°C [49] and in this case, the convection coefficient is defined to be 5000 W/m²/°C.

These two identical single slot models are simulated under the principle of same overall loss, i.e., the total loss in single turn of bar conductor is defined to be 10W and the equivalent loss per strand in Litz wire bundle is thus 10W/54 strand = 0.19W. While for the losses in stator core, they are defined to be 10W in both models. Note that this amplitude of loss is from simple assumption and these values will only be used as a reference to demonstrate the heat dissipation capability of different types of conductors. The temperature plot of those two models at steady state are provided in the Figure 1.8 below:
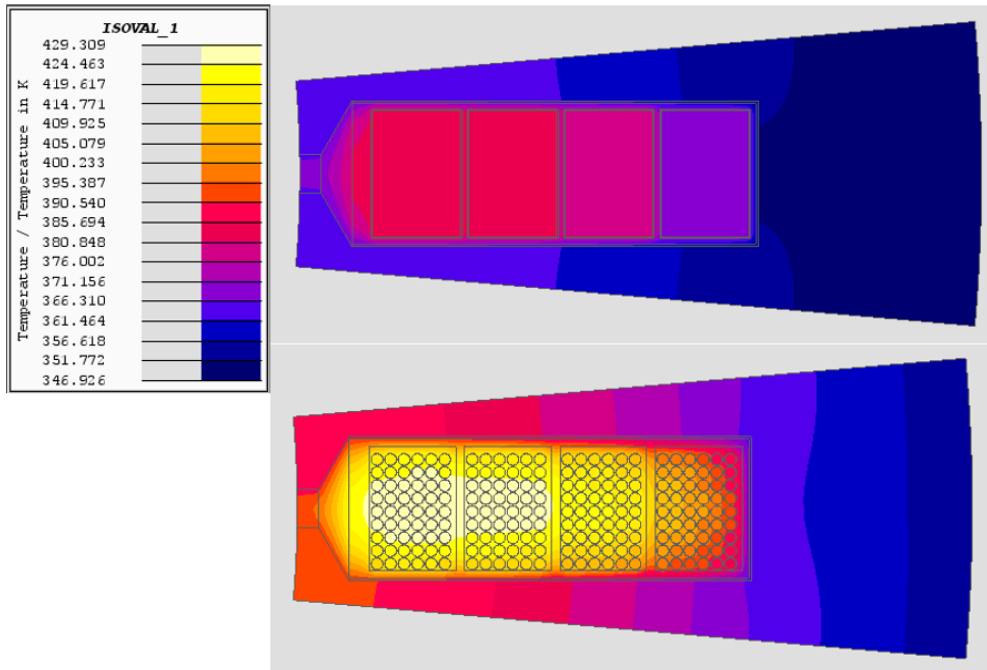
Figure 1.8 Temperature prediction of simplified single slot model equipped with bar conductor and Litz wire

Note that for this simplified thermal simulation, the heat dissipation along axial length is neglected. As can be seen from temperature plot in Figure 1.8 under the constraint of same overall loss, the temperature in a bar conductor model will be lower than that of Litz wire model. This is because for the large section bar conductors, the heat is easier to be dissipated along conductor width, height and axial direction. The findings from the simplified FEA model confirms that the bar conductor outperforms Litz wire/round conductor in terms of heat dissipation capability.

Above investigations give some general understandings about the potential advantages and drawbacks of bar conductor. While for the manufacturing processes of bar conductors, there are 3 main types that can produce rectangular section coils and these are discussed in the next sections.

1.5.1 Hairpin windings

The use of so-called hairpin windings have attracted increasing interest in traction machines for electric and hybrid-electric vehicles [50]. A typical manufacturing steps in manufacturing a hairpin winding [50] are shown in the Figure 1.9 and Figure 1.10. In the first stage short lengths of a bar conductor is preformed into a harpin shape with an open end and then inserted into the slot. After the insertion of hairpin winding, two ends of one single coil are bent outwards by a prescribed degree and then the successive hairpin ends (which have already had the insulation removed) are joined by in-situ welding to form a complete wave-type winding.

16
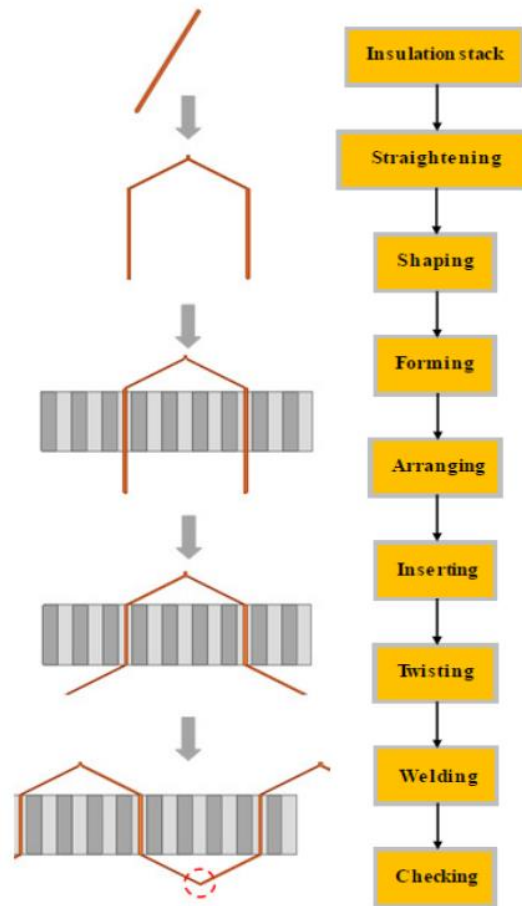
Figure 1.9 Manufacturing and insertion processes of hairpin coil [50]
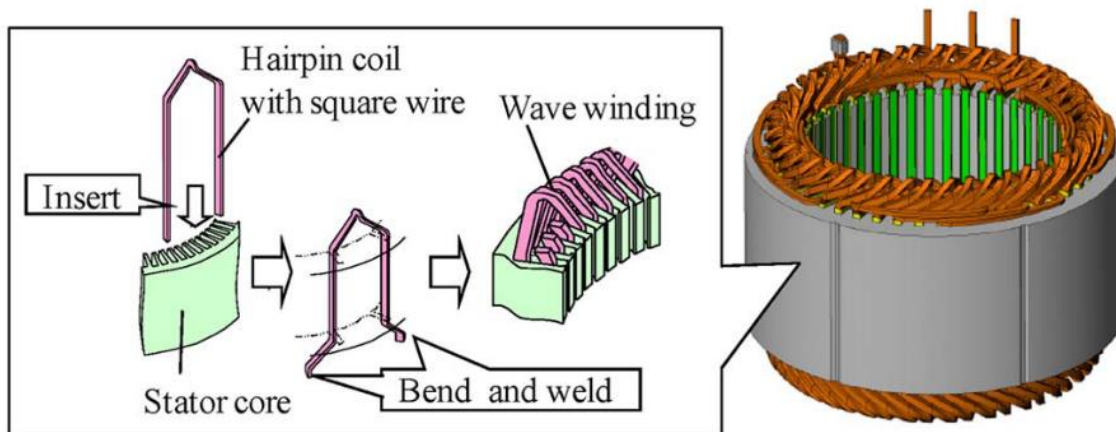
Figure 1.10 Manufacturing and insertion process of hairpin winding with full machine view [51]

As can be seen from Figure 1.9 and Figure 1.10, one clear drawback for machines equipped with hairpin winding is many in-situ welds are required and moreover these exposed welds must be in-situ with an insulating coating such as a varnish. This is complex set of operation, although equipment is now routinely used to automate this entire process. Another

disadvantage is the potential for damage to the insulation of hairpins which are already in the slot as a new hairpin is pushed along the slot. This is particular concern in hairpin windings that involve manual insertion. The main advantages of hairpin winding are the ability to significantly increase the slot packing factor while maintaining semi-closed slots. It also tends to produce a compact and well-defined end-winding.

1.5.2 Form-wound diamond coils

Another more established format for coils with solid rectangular conductors are so-called form-wound concentrated, lap or diamond coils which are manufactured through a combination of various forming, stretching and pressing processes to produce very precise coil geometries [51] [52] [53]. A typical form of a diamond coil is shown in Figure 1.11 along with a series of coils inserted into a stator core in a double-layered three-phase lap winding. This type of coil was initially developed and used for large MW electrical machines operating at very high voltage, where it remains a key winding technology. Coils with overall lengths of several meters are routinely manufactured for large machines using well-developed coil forming machinery.
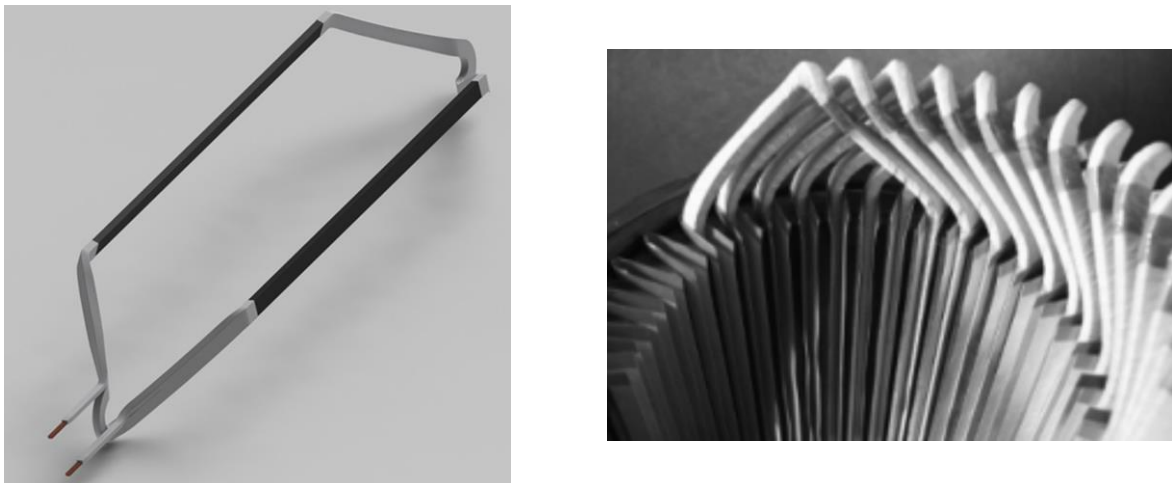
Figure 1.11 Typical form a strip-wound diamond coil

The well-established manufacturing route for the type of coil shown in Figure 1.12 involves winding number of required turns onto a simple bobbin to form a simple loose looped coil. This is then placed on a coil-spreader such as the example shown in Figure 1.12. The coils spreader then performs a series of precision bending operations to produce the near final shaped coil. In this process, the two straight sections are first spread away from each other through a defined angle and then the end-winding regions are lifted and twisted to form a specified angle and form. The formed coil is then lap-wound with a resin-rich fibre-glass tape and placed in a heated coil press such as the example shown in Figure 1.13 to accurately set the final shape and cure the resin. This produces a rigid and precise coil assembly with the correct

18

circumferential span, appropriate alignment of the coil sides to match the slots and the end-turn which is often called the 'nose' of the coil. This diamond coil can then be inserted directly into open slots in the stator core with little or in-situ manual adjustment.
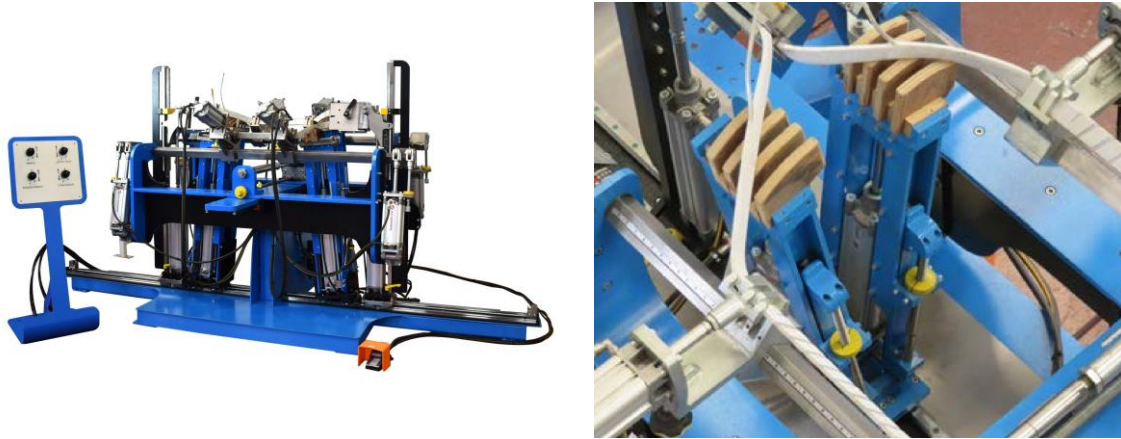
Figure 1.12 Typical commercial coil spreader for manufacturing large diamond coils (Source: Rotary Engineering Ltd)

Figure 1.13 Heated coil-press (Source: Rotary Engineering Ltd)

Although developed for large machines, with the adoption of automation and more precise machinery, diamond coils of much reduced size (lengths in the low hundreds of mm) may offer a good solution for medium sized high-performance machines in terms of form wound coils with rectangular bar conductors. An study reported in [51] evolved the traditional process of manufacturing single diamond coils into a more elaborate muti-slot coil set as shown in Figure 1.14. This was developed in the context of small machines, in this specific case for machines with an active length of 39mm.
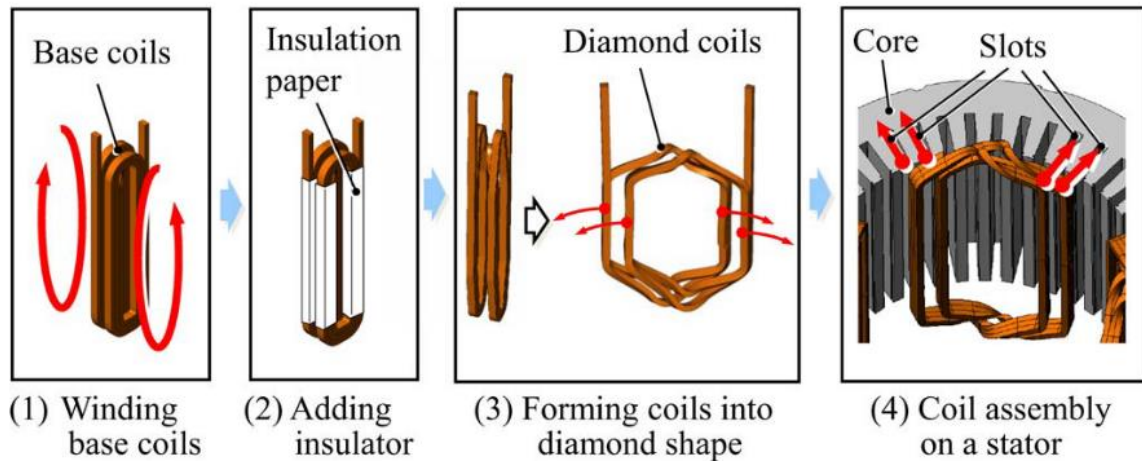
Figure 1.14 Manufacturing and insertion process of diamond coil sets [51]

Compared to hairpin coils, pre-formed diamond coils are particularly well-suited to the demands of aerospace sector high reliability and certification. A major benefit of diamond coils is that the number of welding points is greatly reduced compared to that of hairpin winding, particular using the approach in [51]. This is a desirable feature in terms of confidence in the long-term reliability of the winding. In addition, unlike conventional wound machines or hairpin stators, diamond coils are fully formed, and secondary insulation is applied before insertion into the stator and hence can be fully inspected and tested before insertion with full visibility of all surfaces.

Diamond coils can achieve comparable end-winding lengths compared to hairpin coil and indeed the absence of turn-to-turn welds is likely to make them slightly more compact. The start and end coil sides of one diamond coil are usually in different reference positions in the slot compared to a hairpin winding. For example, for the case of a diamond coil spanning 6 slots with the starting coil side located near slot opening in slot 1 then the corresponding end coil side will be located at the back of slot 7, as is illustrated in Figure 1.15. The change of relative position inside of slot is achieved by twisting the coil at the position of half coil pitch in end-winding region, a feature that is often called the nose of the coil. With all the coils twisted by a predefined length and angle, the end-windings region will be very compact.
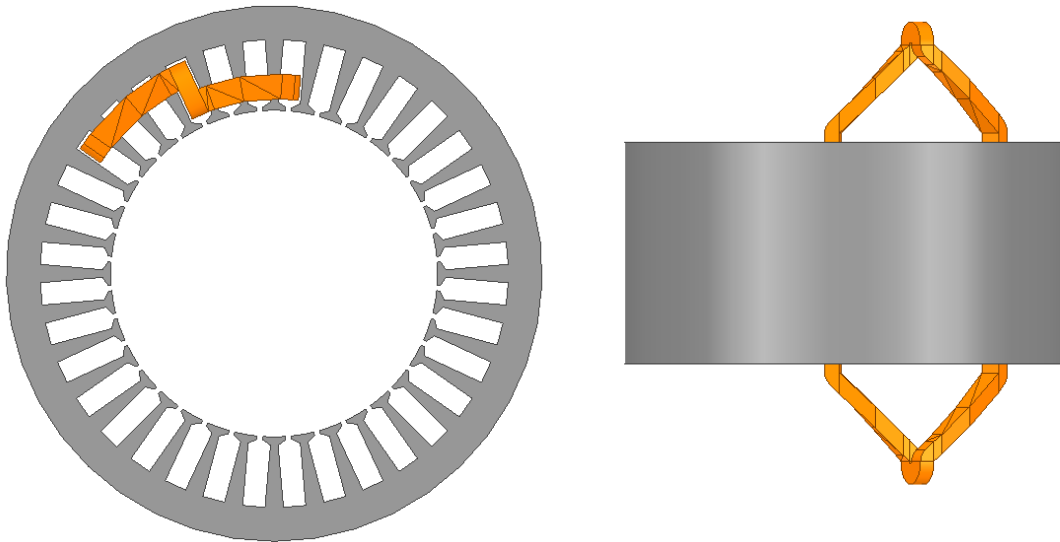
Figure 1.15 A diagram illustrating the starting coil side and ending coil side of diamond coil

As noted previously, one limiting factor of hairpin coils is the number of turns that can be accommodated in to one slot due to the access required for in-situ welding. In hairpin the number of turns is usually 4 although small increases up to 6 may be possible. On the other hand, while for diamond coil, there is essentially no hard limit on number of turns or indeed parallel strips that can be deployed. This feature gives more freedom in the design of the winding, including the possibility of using large number of thin strips to reduce high frequency AC loss.

1.5.3 Strip on edge racetrack coils

For concentrated coils which have compact and non-overlapping end-windings, it is possible to wind a continuous racetrack type coils such as the example shown in Figure 1.16. This type of coil can be used for some types of PM machines with concentrated single-tooth coils but are not directly applicable to distributed windings.

1.6 AC losses in rectangular bar windings

Despite the well-recognized potential advantages of rectangular conductors in terms of increased slot fill and hence lower DC resistance and enhanced heat transfer within the slot, their adoption is often hindered by concerns over so-called AC winding losses [30]. It is entirely possible for AC losses to significantly outweigh the benefits of solid bar conductors unless appropriate measures can be taken to manage their magnitude. Indeed, a winding design based on static considerations only generate unsustainable losses when the machine is eventually put on test due to the neglect or underestimation of the AC losses. A key focus of the research reported in this thesis is to assess in detail the AC loss performance of bar conductor while at the same time evaluate the potential methods to reduce AC losses. A series of studies concerned AC loss minimization processes are reported in chapters 2 and 3.

As mentioned previously, one major threat of high-speed electrical machines is its high level of AC losses. To manage frequency sensitive AC losses, a well adopted solution in high speed application (both automotive and aerospace application) is to use Litz wire [13][15]. Litz wire consists of many turns of thin strands that are properly transposed. Each strand in Litz wire is insulated separately and the profile of Litz wire bundle can be modified to round or rectangular shape. By having transposed and individually insulated thin strands, level of AC losses is very low but near elimination of AC losses comes with much higher cost than that of normal conductors. Another drawback for Litz wire is its inferior thermal performances but this can be compensated by using large number of turns and small current to achieve specified NI.

Alternatively, bar conductor is widely adopted in high-performance electrical machines (or in other words, high efficiency machines) because it has high packing factor and better thermal performances although the level of AC losses associated with bar conductor can be problematic. If the magnitude of AC loss inside of bar conductor can be reduced to a range near DC loss value, the bar conductor can still be regarded as an efficient method to improve efficiency. Based on the previous investigations about how to increase power density and efficiency, a conclusion can be made is that the focus of high performance design is now on the windings. A good design with high power density and high efficiency tends to equip windings that can both withstand high current and with lower losses. Based on this principle, two relatively mature conductor type (bar conductor and Litz wire) will be selected as candidate material for the following evaluation of the thesis.

1.7 Design specification for the research in this thesis

The application context for the research reported in this thesis is a PM machine for hybrid propulsion system for a small-size 9-seater aeroplane. Based on outline specifications provided by NASA [11], the total propulsive power required is around 500-750kW. To meet the demanding requirement of aerospace applications, the final design should have high power density, low weight and high efficiency. Since the total propulsive power can be realised with a combination of two or more electrical machines, the rated power of single machine selected for this study was 350kW. Since this type and rating of machine is used to directly drive a propeller, then the speed required is limited to 6000rpm which is much lower than the 20,000rpm and above speeds which have been reported in previous PM machine studies for aerospace. While for the DC bus voltage, it is defined to be 580V which is based on the voltage specification of existing electrical machines used in aerospace sector.

1.8 Thesis structure

The thesis is structured into the following chapters:

Chapter 1 reviews the demands on and development of electrical machines for aerospace applications and reviews key literature on high power density machines and winding types. It concludes by setting out a top -level performance specification for a machine, the design and analysis of which forms the application context for the research in this thesis.

Chapter 2 is concerned with the detailed design and preliminary modelling of a machine which is in principle capable of meeting the performance specification. The machine is equipped with large section, solid bar conductors. It concludes by demonstrating that as originally designed, the AC loss caused by eddy current are unsustainable.

Chapter 3 provides an in-depth study in the origins of the AC loss issues in this machine and proposes and analyses a number of mitigations to reduce the loss to manageable levels, taking the design from having losses that are almost an order of magnitude too high down to a competitive deign.

Chapter 4 explores the modelling of finely stranded Litz wire and evaluates its performance in the machine design.

Chapter 5 presents some experimental results on a motorette to validate some of the key finding of the research.

Chapter 6 provides a summary of the progression of the design through the thesis, offers some conclusions on the main findings and identifies areas for future work.

1.9 Contributions to knowledge and publications

The key novelties of this thesis are around winding design and can be divided into several aspects:

- The detailed evaluation of solid bar conductors and corresponding AC loss mitigation processes.
- Comprehensive comparisons between different types of conductors (i.e., aluminium bar conductor and Litz wire). Then some novel aluminium substitution strategies are proposed, which is to substitute the copper partially or fully with aluminium.
- Detailed modelling of Litz wire in FEA software and corresponding comparison between Litz and soli bar conductors.

Published papers:

[1] S. Yangyu and G. W. Jewell, "An investigation into the influence of stator tooth and conductor geometry on AC winding losses in a 365kW permanent magnet machine equipped with rectangular bar conductors," IET Conference Proceedings, vol. 2022, no. 4, pp. 52–57, 2022, doi: 10.1049/icp.2022.1072.

[2] Y. Sun, X. Chen, W. Zhu and G. W. Jewell, "An Investigation of Substituting Copper with Aluminium Conductors in a High Power, Medium Speed SPM Machine," *2023 IEEE Transportation Electrification Conference and Expo, Asia-Pacific (ITEC Asia-Pacific)*, Chiang Mai, Thailand, 2023, pp. 1-8, doi: 10.1109/ITECAsia-Pacific59272.2023.10372259.

Chapter 2. A design strategy for achieving high power density in electrical machines

2.1 Initial sizing of a machine design

2.1.1 Introduction to machine sizing

A general process for machine designing usually involves two stages. In the first stage, the priority is to decide constituent materials and the type of machine. There are always trade-offs when selecting materials since improved material performance is associated with increased cost. For example, the cost of high-performance 49% Cobalt-iron for the stator and rotor core is ~100 times higher than that of normal silicon iron electrical steel but only gives improvements in performance of 15-20% [54]. As a consequence, Cobalt-iron tends to only be used in aerospace or motor sport applications where cost can be justified in terms of the increase in power density.

In aerospace applications, the premium on weight saving is very high since reducing aircraft weight has a significant impact on the fuel use and cost over the long lifetime of the aircraft. The lifetime saving of fuel per kg of reduced aircraft weight depends on the aircraft type and flight patten while the lifetime cost saving per kg depends on trends in the price of fuel. However, the significant savings that can be made have a major impact on the material selection since even very high-cost materials such as 49% cobalt-iron cores can be cost-effective even though they are prohibitively expensive for automotive and industrial applications. There is cost pressure on aircraft manufacturers from the airline industry and so there is always a need to justify the performance benefits from high-cost materials. The starting point for this design was a stator with a commercial grade of 49% Cobalt-iron (Carpenter Hiperco50) a silicon iron rotor core (Surahammar NO20) and Sm_2Co_{17} Samarium Cobalt permanent magnets.

Following the initial selection of materials, which can be revisited when a reference design has been established, the next step is to establish the leading dimensions of the machine from the performance specifications. The main elements of the performance specifications are usually rated power and rated speed and in some cases weight limits. However, it is a well-established principle that electrical machines are sized on the basis of torque rather than power. Although the torque rating is sufficient to make a first estimate of the main dimensions, detailed features including the number of poles and slots, the geometry of individual stator slots, magnetic pole-

arc and thickness, stator tooth width, back iron thickness and other parameters usually require more detailed trade-offs and machine specific design equations.

A common approach to electrical machines design is to establish a first estimate of the rotor size from high-level analytical expressions for the torque rating, and then use a combination of design equations and judgement to establish a first set of detailed dimensions and features. This initial design can then be analysed using either a general-purpose finite element analysis package to calculate the torque produced or a machine-specific analysis package such as MOTORCAD. This particular package provides a tool for rapidly and accurately analysing different combinations of machine and is reliant on the user having a good level of understanding of electrical machines in order to modify the input parameters appropriately in response to the predicted performance. It is to be expected that during the process of analytical prediction, misalignment between existing initial model and target model is expected because the analytical prediction is achieved with assumptions.

2.1.2 Sizing methodology

Given the rated operating speed and power, the resulting torque required can be determined using:

$$P = T \times \omega \tag{2.1}$$

Based on a simplified version of the Lorenz force, a well-known equation for the first estimation of the rotor size to achieve a given torque rating is:

$$T = \frac{\pi}{2} D_{ro}^2 L B Q \tag{2.2}$$

As can be seen from (2.2), torque is proportional to the square of the rotor diameter, its axial length, the airgap magnetic loading and the stator electrical loading. To initiate the sizing process, it is common to assume that B and Q can be set as fixed constant. With adoption of this assumption, there are two remaining parameters $D_{ro}^2 L$ in torque equation, which means the rotor volume ($\frac{\pi D_{ro}^2 L}{4}$) is directly proportional to the output torque. The process of selecting values for B and Q will be discussed later in this chapter.

Even with simplifying assumption that Q is a constant, the expression for torque only gives a value for rotor volume rather than any particular combination of D_{ro}^2 and L. Indeed, in principle, any combination of D_{ro}^2 and L could be adopted. A useful starting point is to select an aspect ratio of length to diameter to link these two quantities. To initiate the design synthesis, an aspect

of 1.0 was adopted. This provides a reasonable compromise between the ratio of end-winding volume to active region winding volume and the natural tendency for torque density to improve torque density.

By substituting $D_{ro} = L$ into equation (2.2) to correspond to an aspect ratio of 1.0 and rearranging the equation in terms of stator inner bore diameter yields

$$D_{ro} = \sqrt[3]{\frac{2T}{\pi B Q}} \qquad (2.3)$$

As can be seen from (2.3), to calculate rotor outer diameter, the torque, magnetic loading and electric loading are required. Torque can be calculated straightforwardly from rated power and rated speed. Magnetic loading, which is given by the average airgap flux density falls within a relatively narrow range of values determined by the remanence of the material. As noted in chapter 1, Sm_2Co_{17} magnets tend to be preferred over NdFeB for aerospace applications because of the superior high temperature properties, their much better corrosion resistance and their long-term stability. Grades of Sm_2Co_{17} suitable for use in electrical machines tend to have remanences in the range of 1.0-1.2T depending on the exact composition and operating temperature. In most high-performance machines, the magnetic loading is typically 0.7-0.8T depending on the grade and the pole arc of the magnet. Adopting a conservative starting value of 0.7T and noting that this is an average in the airgap and not necessarily the flux density above the centre of the magnet pole. The last remaining parameter to select in order to size the rotor is the electrical loading, denoted by Q, which is defined as the Ampere-turns per unit of airgap periphery and given by:

$$Q = \frac{\sum I}{\pi D_{ro}} = \frac{N_s k_p A_s J}{\pi D_{ro}} \qquad (2.4)$$

As can be seen from equation (2.4) above, the electric loading is dependent on several parameters and has some diameter related scaling. Whereas the range of current densities in electrical machines is limited to a reasonably narrow range, e.g., 5A/mm^2 for natural convection cooled machines to 15-20A/mm^2 for direct oil cooled machines, the range of electric loadings encountered in electrical machines can span a factor of 10 or more depending on the cooling strategy and size. As an example, Table 2.1 shows a number of electric loading values which have been calculated from published machine performance and dimensional data along with a single case in which the electric loading was provided directly. As shown, there is a very large range of values in published literature with little or no consensus on representative values.

Table 2.1 electric loading values obtained from literatures

Power rating	Speed (RPM)	Electric loading Q (kA/m)	Torque (Nm)	Rotor diameter (mm)	Axial length (mm)	B (T)
250kW[12]	5000	50	477	191	31	0.7
113kW[17]	6000	27	193	253	100	0.7
1MW[16]	20,000	94	477	194	162	0.7
1MW[55]	18,000	24	531	328	223	0.7
1MW[15]	20,000	94	477	191	148	0.7
300kW[13]	13,300	55 (provided)	215	215	75	0.7

As can be seen from the tables above, electric loading values either directly provided or calculated spans a large range from 20kA/m to 100kA/m depending on different power ratings and cooling strategies. Before selection of electrical loading values that can be used for sizing equations, there are several things to note:

- All the references in Table 2.1 are from aerospace related applications.
- For the three high-speed MW machines provided in Table 2.1, the high output power is achieved at high operating speed and adoption of Litz wire. The operating frequency of these machine will be >1kHz and will not be representative of machines for solid bar conductors which are the focus of the research in this thesis.
- While for remaining machines that have similar output capability (several hundred of kW rated power) and similar speed as baseline model, the electrical loading values are more useful for determining initial size of baseline model.

Based on the principles set previously and the remaining electric loading values in the tables, a reasonable starting electrical loading value for initial design was deemed to be 50kA/m. However, to explore the potential for achieving high power density with aggressive cooling and noting the higher packing factor of bar-windings, four values of electric loading from 50kA/m to 200kA/m were considered with 50kA/m increments.

Having set a single value of magnetic loading, four different levels of electric loading, torque, and recalling the assumption of a unity aspect ratio in which $D_{ro} = L$, then rotor outer diameter can be calculated using (2.4). Table 2.2 shows the resulting four rotor diameter and axial lengths for the four selected electric loading levels.

Table 2.2 Calculated rotor outer diameter and axial length for different Q values

Q loading (kA/m)	B loading (T)	D_{ro} (mm)	L (mm)
50	0.7	216	216
100	0.7	172	172
150	0.7	150	150
200	0.7	136	136

Whereas the sizing equations up to this point have proved useful in producing a first estimate of the rotor leading dimension, it is now necessary to start defining the number of slots and number of poles in order to start dimensioning the stator. One factor that has a significant influence on pole number selection was the intention to use solid bar and the likelihood that AC losses would be an important factor. A 6-pole machine was initially identified as potentially offering a good balance between the tendency of PM machine to use higher pole numbers than 6 for reducing stator core mass while retaining a relatively low electrical frequency which nevertheless was likely to generate AC loss behaviour of interest. The choice of pole number is discussed in greater detail in section 2.3.2. A standard 36-slot 6-pole stator with a distributed winding was selected as the starting point for the analysis.

The performance specification and the selected materials which were used as the basis for the more detailed design of the machine are summarised in Table 2.3. As will be apparent, this includes a target weight of 50kg which would give a power density of 7kW/kg.

Table 2.3 Specifications and selected materials for baseline model

Machine specifications	Material selected
Rated power: 350kW	Stator material: Cobalt-iron (Hiperco50 0.15mm)
Rated speed: 6000RPM	Rotor material: NO20 0.2mm
DC bus voltage: 580V	Winding material: Copper (100% IACS)
Target weight: 50kg	Permanent Magnet: Sm_2Co_{17} (Recoma 32)
Number of slots: 36	Rotor containment sleeve material: carbon fibre
Number of poles:6	
Winding pattern: double layer distributed	

Having set the slot/pole combination (noting that this will be revisited in section 2.3.2), the next step was to determine the detailed machine design in terms of the numerous dimensions and features which fully define the geometry and arrangement of the machines. The key

machine design parameters together with notation are shown in Table 2.4 with several defined in Figure 2.1.

Table 2.4 Parameters and notations used for sizing equations.

Parameters	Notation	units
stator outer diameter	D_{out}	mm
Stator inner bore diameter (rotor diameter):	D_{si}	mm
Magnet thickness:	l_m	mm
Airgap length:	l_g	mm
Number of slots:	N_s	-
Packing factor:	k_p	-
Current density:	J	A/mm^2
Slot width	W_s	mm
Slot depth	h_s	mm
Back iron thickness	h_{bi}	mm
Flux density at tooth tip	B_{tt}	T
Flux density at tooth body	B_{tb}	T
Slot cross-sectional area	A_s	mm^2
Tooth tip height	h_{tt}	mm
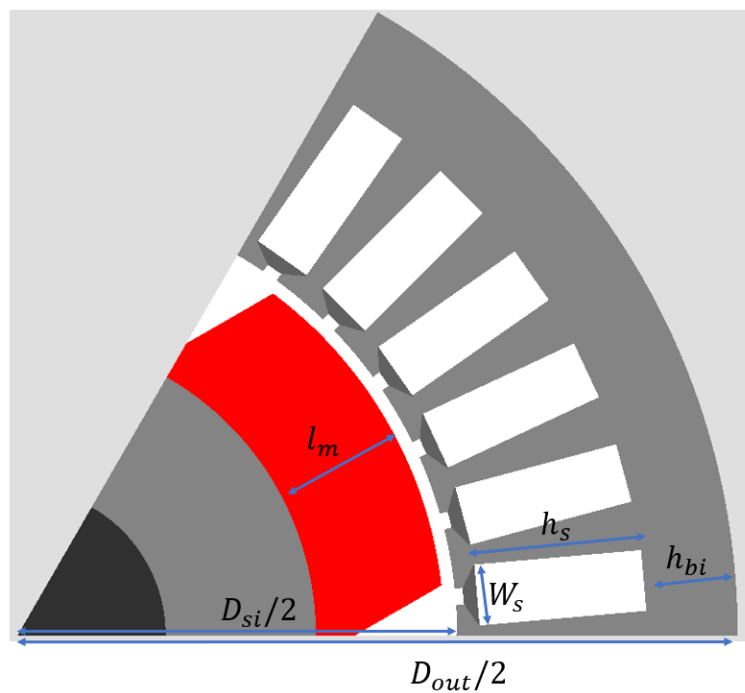
Figure 2.1 Parameters and notations used for sizing equations.

Unlike traditional electrical machines which usually have parallel stator teeth and trapezoidal or bulbous slot shapes, the baseline model used in this thesis (shown in Figure 2.1) is designed to have rectangular slots to accommodate rectangular bar conductors. This type of topology is also referred to as parallel slot stator and has attracted much attention for automotive applications with matched hairpin or diamond coils. It does result in a tapering tooth with the critical region in terms of saturation being towards the front of the tooth.

Another aspect to note about stator geometry is the stator tooth tip geometry around the slot opening region. There are two types of tooth tip geometries that are used frequently: fully open slots and semi-closed slots. The differences between an open slot and a semi-closed slot are shown in the zoomed-in views of Figure 2.2 and Figure 2.3.
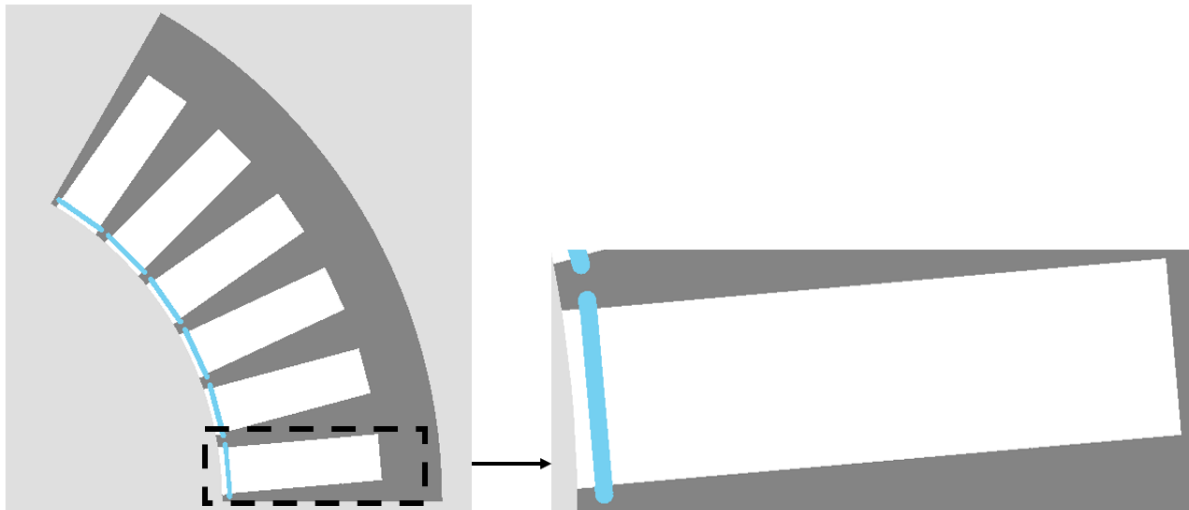
Figure 2.2 Parallel slot geometry with a fully open slot
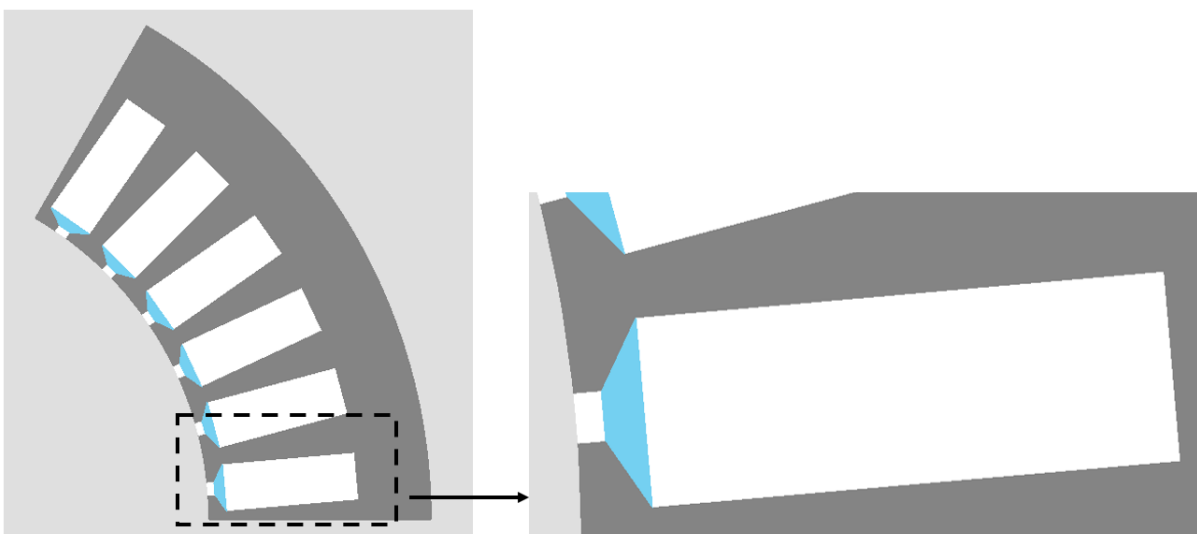
Figure 2.3 Parallel slot geometry with semi-closed slot

Rectangular slots with an open slot geometry are almost always used for rectangular bar conductors to allow insertion of a pre-formed winding. However, there are three potential drawbacks associated with pure open slot geometry. One is that the thickness of tooth tip near airgap can become a flux pinch point. This narrow tooth tip is very likely to become magnetically saturated particularly in machines with high electric loading. The second drawback of a pure open slot is that the PM fringing flux will tend to enter the slot and link the conductors near slot opening hence generating additional eddy current loss in the coil. The third drawback is that an open slot stator gathers less rotor magnet flux than its semi-closed counterpart and hence has a lower torque constant.

Semi-closed slots address many of the electromagnetic drawbacks of open slots and tends to be the preferred arrangement for coils wound from many narrow strands of wire. The coils can be wound either in-situ with a winding needle passing through the slot opening between teeth or preformed as a loose coil and fed in via the slot opening. However, stator tooth tips which form part of a single piece lamination would preclude the insertion of pre-forms coils based on rectangular conductors. This limitation can be overcome using modular stators in which separate tooth tips modules are fitted to captive features such as a dovetail on the main tooth body which itself is part of the main stator core lamination as shown in Figure 2.4. As is evident, this particular variant of so-called modular stators introduces significant complexity to the core assembly and requires the highest levels of precision in the manufacture of the core modules.
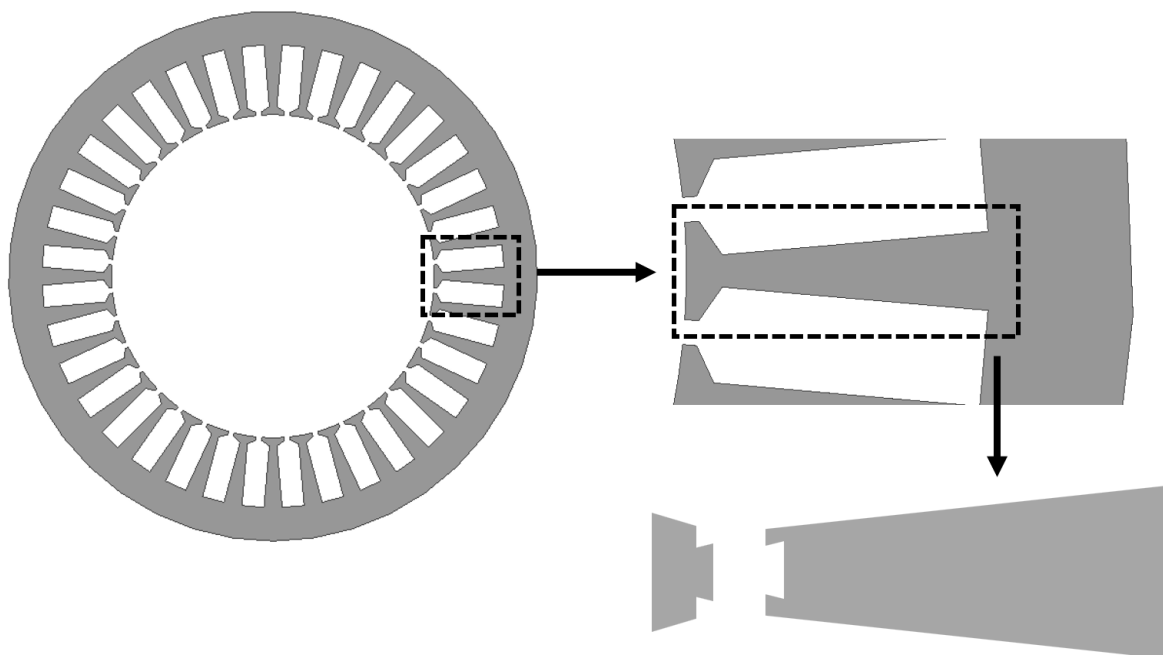
Figure 2.4 Detailed explanation for manufacturing process of segmented stator with semi-closed slot

The stator in Figure 2.4, with semi-closed slot can be manufactured by placing the coils open slots and then sliding on the tooth tip stack from one end of the stator. Similar processes are introduced in [56] and can be used as reference when it comes to final stage of manufacturing. For the initial design stage, the semi-closed stator tooth will be used as baseline and the impact of stator tooth width and substantially the impact of magnetic wedge will be studied in the future.

With all the required parameters and topologies defined properly, next step is to estimate two rotor related parameters: magnet thickness and airgap length. The relationship between the magnet length, the airgap length and the resulting airgap flux density can be established using the simplified magnetic circuit of Figure 2.5 and a simple one-dimensional model of flux based on the concept of a magnetic circuit [35]. It consists of an infinitely permeable iron core with a permanent magnet magnetised in the direction shown with a length in the direction of magnetisation of l_m and cross-sectional area A_m. This produces flux in an airgap of length l_g and cross-sectional area A_g. A coil of N series turns carrying a current I is wound onto the core.
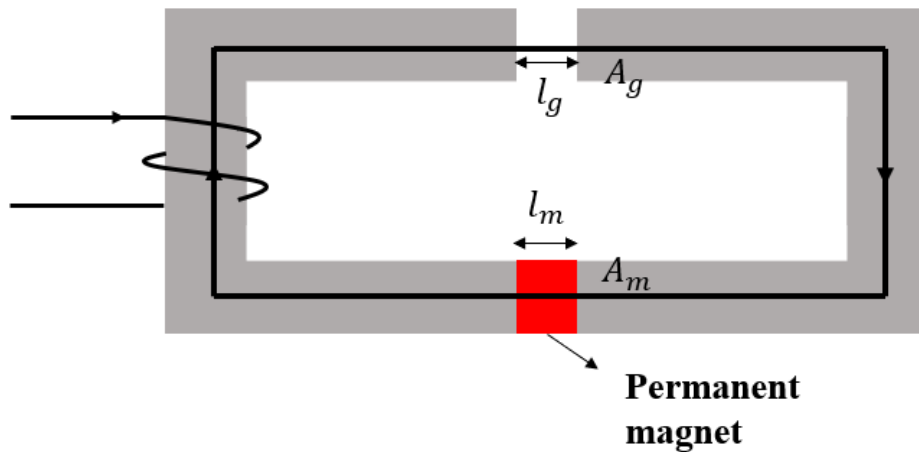
Figure 2.5 Simplified magnet circuit used for estimation of airgap and magnet length

Applying Ampere's law that the integral of H around a closed path equals total current enclosed by that path yields:

$$H_{iron}l_{iron} + H_g l_g + H_m l_m = -NI \qquad (2.5)$$

Since the iron core is infinitely permeable $H_{iron} = 0$ and hence (2.5) becomes:

$$H_g l_g + H_m l_m = -NI \qquad (2.6)$$

Under open-circuit conditions with NI =0 the equation further simplifies to:

$$H_m = -\frac{H_g l_g}{l_m} \qquad (2.7)$$

Applying Gauss' law to magnetic circuit in Figure 2.5 gives:

$$B_m A_m = B_g A_g \qquad (2.8)$$

For the linear region of the magnet demagnetisation characteristic, the flux density in the magnet is given by:

$$B_m = \mu_0 \mu_r H_m + B_r \qquad (2.9)$$

By combining equation (2.7) (2.8) (2.9) under open circuit condition and with some rearrangement, the airgap flux density can be calculated using:

$$B_g = \frac{A_m}{A_g} B_m = \frac{A_m}{A_g} \frac{B_r}{(1 + \mu_r \frac{A_m l_g}{A_g l_m})} = \frac{B_r}{\frac{A_g}{A_m} + \mu_r \frac{l_g}{l_m}} \qquad (2.10)$$

When the cross-sectional area of magnet is equal to that of the airgap, i.e., $A_g = A_m$, equation (2.10) becomes:

$$B_g = \frac{B_r}{1 + \mu_r \frac{l_g}{l_m}} \qquad (2.11)$$

This well-established equation provides a reasonable estimation of the airgap flux density for a given combination of magnet and airgap length. Note that this equation is based on a simplified one-dimensional analysis which neglects fringing and airgap leakage flux. Equation (2.11) can be used to plot the ratio of the airgap flux density to the material remanence as a function of the ratio of the magnet length to airgap length.
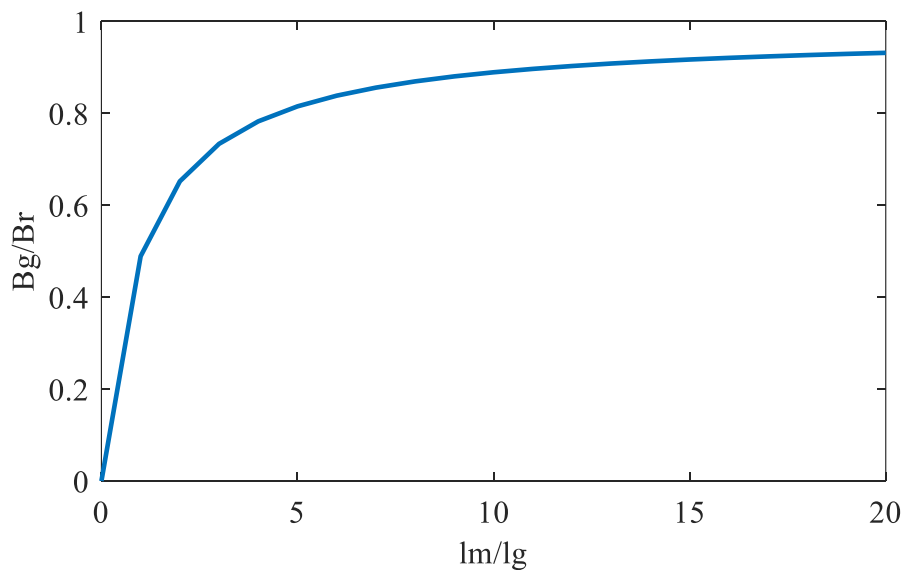
Figure 2.6 B_g/B_r versus l_m/l_g curve

34

As will be apparent, there is a diminishing return in airgap flux density with increasing magnet thickness. It is common in cost sensitive applications to find a balance of performance and cost around a ratio of 4-6. However, if the main objective of the design is power density and magnet cost is a secondary consideration then there is some merit in increasing the ratio beyond 6 up to 10 or so, beyond which the rate of increase on airgap flux density is so small. It should be noted that when curvature is taken into account [57] there is an optimum thickness beyond which the airgap flux density starts to reduce. Furthermore, in machines where the combination of rotor diameter and rotational speed expose the magnets to large centrifugal forces, the extra containment sleeve thickness (and hence larger effective magnetic airgap) required to accommodate thicker magnets can also result in an optimal magnet thickness beyond which the airgap flux density drops.

In order to provide a practical mechanical clearance and sufficient space to accommodate a thin carbon-fibre sleeve, a total magnetic airgap of 2mm was selected as a starting point. The exact thickness of the sleeve required will depend on the magnet thickness selected, but allowing up to 1mm for a sleeve is a good starting point for this relatively small diameter rotor operating at 6000rpm. As will be shown later in section 2.3.5, a 1mm sleeve does indeed prove adequate. A total effective magnetic airgap of 2mm would give a magnet thickness of ~10mm if the usual trade-off points of l_m/l_g=5 from Figure 2.6 was adopted. This was taken as a starting point for the design optimisation, but as shown later in section 2.3.4, a systematic evaluation of the torque benefits of increasing magnet thickness was performed to establish the merits of further increases in magnet thickness beyond 10mm.
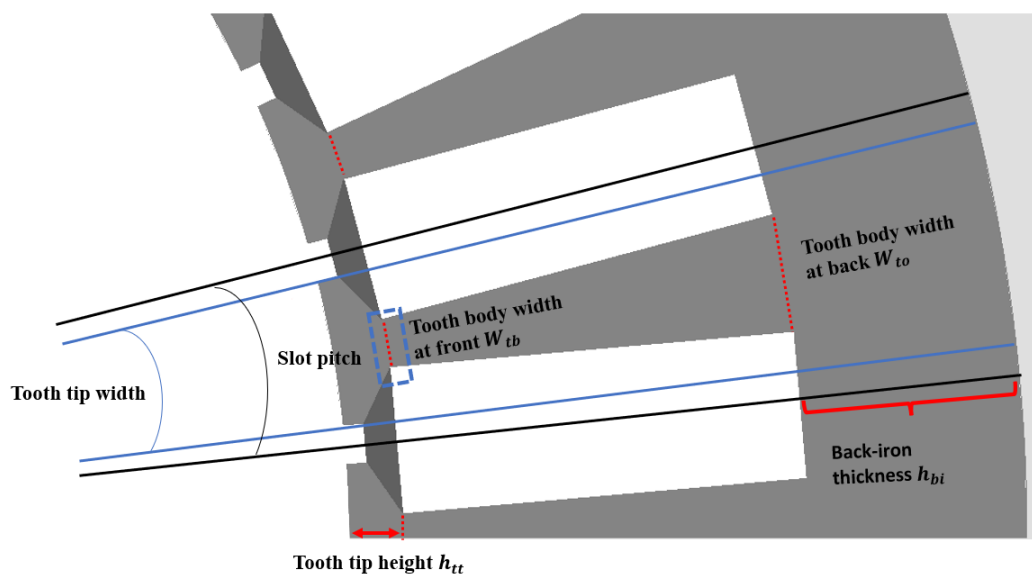
Figure 2.7 Schematic explaining tooth tip width, slot pitch and tooth body

35

The dimensioning of the stator tooth for the case of a semi-closed slot is based on ensuring that the flux gathered at the airgap does not magnetically saturate the main body of the stator tooth. The selection of the tooth tip width involves a compromise between capturing airgap flux, reducing leakage flux from the magnet and the coil through the slot opening. In some cases where there is also a need to ensure a sufficient slot-opening to allow in-situ winding. A typical tooth pitch to slot pitch ratio, λ, at the airgap is $0.7 - 0.8$ for permanent magnet machines [58] and for this initial sizing a value of 0.75 was adopted. The flux density in the tooth tip at the airgap per unit axial length is given by:

$$B_{tt} = \lambda B_g \tag{2.12}$$

As noted previously, the pinch-point in terms of saturation of the tooth body is the region at the transition from the tooth body to the tooth tip. The flux density in this region, B_{tb}, is given by:

$$B_{tb} = \lambda B_g \times \frac{\lambda \pi D_{si}}{N_s w_{tb}} \tag{2.13}$$

Rearranging this gives:

$$w_{tb} = \frac{\lambda^2 B_g \pi D_{si}}{B_{tb} N_s} \tag{2.14}$$

By setting a maximum tooth body flux density then a tooth body width can be calculated. The slot width, w_s, can be approximated using the following:

$$w_s \approx \frac{\pi (D_{si} + 2h_{tt})}{N_s} - w_{tb} \tag{2.15}$$

The electrical loading, Q, is given by:

$$Q = \frac{\sum I}{\pi D_{si}} = \frac{N_s k_p A_s J}{\pi D_{si}} = \frac{N_s k_p w_s h_s J}{\pi D_{si}} \tag{2.16}$$

Rearranging equation (2.16) for slot height gives:

$$h_s = \frac{Q \pi D_{si}}{N_s k_p w_s J} \tag{2.17}$$

Having linked the slot height to stator inner bore diameter D_{si}, its value can be calculated analytically. Two remaining unknown parameters are the slot-fill factor and the operating rms current density. Since this machine was designed to use solid bar conductors in a matched

rectangular shaped slot, a slot-fill factor 0.75 was adopted. As to the current density, a rms value of 10A/mm² was selected as this is representative of high-performance machines in which the conductors are indirectly cooled, e.g., via a liquid cooled jacket or forced air cooling. Fixing these parameters allows the slot depth to be calculated.

As will be apparent from Figure 2.7, the tooth tip has a radial depth h_{tt}. In this initial study this was set at a fixed 1.5mm. The last remaining parameter to determine the stator outer diameter is the back-iron thickness. The back-iron carries a peak flux which is equal to half the flux from one pole. In a 6 pole, 36 slot machine the peak flux over half a pole passes through three teeth. It is common to set the back iron thickness to 2/3 of the effective width of the teeth which collect the flux. Hence, a reasonable first estimate of the stator back iron thickness is to set it equal to twice the width of an individual tooth. As will be apparent, the rectangular shape of the slot means that the tooth gradually widens towards the back of the slot. The tooth width at the back of the slot can be approximated using the following:

$$w_{to} \approx \frac{\pi(D_{si} + 2(h_{tt} + h_s))}{N_s} - w_s \tag{2.18}$$

Hence, the height of the back-iron is given by:

$$h_{bi} \approx \frac{2}{3}\left(\frac{\pi(D_{si} + 2(h_{tt} + h_s))}{N_s} - w_s\right) \tag{2.19}$$

This assumption regarding the back iron thickness is again a relatively aggressive assumption and this value will be further refined in later sensitivity studies. Having set the slot depth and back iron thickness, the stator outer diameter can be calculated by:

$$D_{out} = D_{si} + 2(h_{tt} + h_s + h_{bi}) \tag{2.20}$$

It may also be necessary to include a further smaller allowance to accommodate a slot-wedge. An allowance of 2mm was included to allow for a slot wedge to be incorporated. The topic of slot wedges is discussed in more details is section 3.2.2.

Since setting a value for electric loading is known to be problematic as it depends on the thermal management features of the machine, the size and the acceptable efficiency levels, designs were established using the analytical equations above for four different values of electrical loading. In principle, the design equations developed should yield a design which meet the performance specification in terms of torque and power. However, because the sizing

methods and equations are based on a very simplified representation of the electromagnetic behaviour in the complex geometry of a real machine, there will inevitably be some deviation from the performance of a particular design when it is analysed using more sophisticated methods.

As mentioned previously, three different FEA based software packages have been used in this research. The majority of simulations in this thesis were performed using MOTORCAD from ANSYS, FLUX from Altair and Maxwell from ANSYS.

MOTORCAD is a motor analysis package which has been developed to be used in the design process of machines. It is reliant on the user providing a set of design dimensions and features for which it then uses an in-built template driven finite element solver to predict many different aspects of performance, including thermal performance. In the design of a machine, this package simply provides predictions of performance for the user to iteratively adjust parameters and hence it needs a well-founded sizing study to have been undertaken by the user ahead of inputting dimensions in MOTORCAD. Within this package, the user does not interact directly with the finite element package, with all the geometry and material specifications and the meshing being generated automatically from templates into which the user feeds various machine dimensions and other design parameters. It requires no expertise in finite element modelling and can be used in coupled thermal and electromagnetic analysis. At present MOTORCAD is limited to two-dimensional finite element analysis. Overall, it is a powerful tool for design but is limited in terms of flexibility to explore various non-standard geometries or features.

The FLUX packages FLUX2D and FLUX3D provide comprehensive 2D and 3D finite element simulation tools. They are general purpose tools that can be used with any type of electromagnetic device and can be used with scripts to perform repeated analysis. These packages allow electric circuit coupling but very little coupled thermal / electromagnetic capability. Setting up a problem involves far more efforts and expertise than MOTORCAD although there are now motor templates available in FLUX2D.

The Ansys Maxwell is another well-known FEA software that has been widely used. There are three main advantages associated with this software: 1. The built-in 'RMxprt' package allows user to parameterize the model in 1D context and then automatically generate corresponding 2D and 3D models. With the help of this feature, the modelling time especially with 3D can be reduced significantly. 2. With the help of mechanical modelling and thermal modelling features

embedded in Ansys workbench, the electromagnetic, mechanical, thermal coupled simulation can be easily achieved within the same software. 3. Recently, the Motor-cad and Ansys Maxwell has been emerged, which means the simplified model generated by Motor-cad can be imported to Ansys Maxwell and then further complicated simulations can be done in Maxwell.

Since MOTORCAD has the advantage of a much faster problem set up time, it can be used rapidly as a 'calculator' for electrical machines. Hence, it was adopted for refining the initial analytically sized designs. The previously described sizing equations are sufficient to establish some key stator and rotor parameters but not for detailed winding designs and optimisation of the geometry. Initially a simplified winding design process was adopted, with the detailed winding design described later in this chapter. The basis of the simplified winding design process was to calculate available winding height in the slot based on slot area, slot-fill factor, number of turns per slot, spacing between conductors and enamel insulation thickness. As noted previously, for this bar winding, a slot fill of 75% was specified. When turn height is obtained, the corresponding turn width can be calculated by turn area/ turn height. The information required for simplified winding design process is shown in the Figure 2.8 and Table 2.5 below:
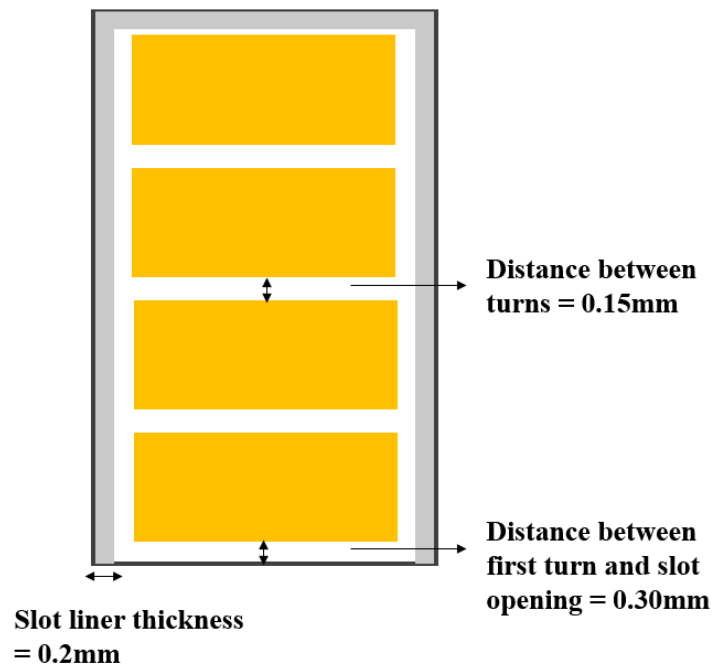
Figure 2.8 Diagram illustrating the parameters required for winding design process

Table 2.5 Required information for simplified winding design process

39

Number of turns per slot	4
Insulation thickness	0.10mm
Distance between turns	0.15mm
Distance between slot opening and front-most turn	0.30mm
Slot liner thickness	0.20mm

2.1.3 Application of sizing methodology

Using four different values of electrical loading from 50kA/m to 200kA/m and following the methodology developed in the previous section leads to the 4 design variants shown Table 2.6 to Table 2.9 below.

Table 2.6 Detailed parameter predicted by sizing equations when Q = 50 kA/m

Initial model 1 with Q = 50kA/m	
Description: surface parallel rotor, parallel slot with distributed winding	
Machine layout: 	Stator dimensions (all in mm unless specified)
	Number of slots: 36
	Stator outer diameter: 296
	Rotor outer diameter: 212
	Axial length: 216
	Slot width: 13
	Slot depth: 13
	Tooth tip depth: 1.5
	Slot opening: 2.67
	Tooth tip angle: 30°
Rotor dimensions (all in mm unless specified)	General information
Rotor outer diameter: 212	Stator back-iron material: Hiperco50 0.15mm
Pole number: 6	Stator winding: copper (100%IACS)
Magnet thickness: 10	Rotor back-iron material: NO20
Magnet arc: 140°	Magnet: Recoma 32
Magnet segments radial: 1	Active weight (incl.end-winding): 114.1kg
Magnet segments axial: 1	Conductor height: 1.7mm
Shaft diameter: 142.6	Conductor width: 12.2mm
Mechanical airgap: 2	Current density: 10 A/mm2
	Torque predicted: 495Nm

Initial model 2 with Q = 100 kA/m	
Description: surface parallel rotor, parallel slot with distributed winding	
Machine layout: 	Stator dimensions (all in mm unless specified)
	Number of slots: 36
	Stator outer diameter: 259
	Rotor outer diameter: 168
	Axial length: 172
	Slot width: 10.5
	Slot depth: 23
	Tooth tip depth: 1.5
	Slot opening: 2.67
	Tooth tip angle: 30°
Rotor dimensions (all in mm unless specified)	General information
Rotor outer diameter: 168	Stator back-iron material: Hiperco50 0.15mm
Pole number: 6	Stator winding: copper (100%IACS)
Magnet thickness: 10	Rotor back-iron material: NO20
Magnet arc: 140°	Magnet: Recoma 32
Magnet segments radial: 1	Active weight (incl.end-winding): 73.7kg
Magnet segments axial: 1	Conductor height: 4.3mm
Shaft diameter: 96.6	Conductor width: 9.3mm
Mechanical airgap: 2	Current density: 10 A/mm^2
	Torque predicted: 583Nm

Initial model 3 with Q = 150 kA/m	
Description: surface parallel rotor, parallel slot with distributed winding	
Machine layout:	Stator dimensions (all in mm unless specified)
	Number of slots: 36
	Stator outer diameter: 250
	Rotor outer diameter: 146
	Axial length: 150
	Slot width: 9.2
	Slot depth: 32.28
	Tooth tip depth: 1.5
	Slot opening: 2.67
	Tooth tip angle: 30°
Rotor dimensions (all in mm unless specified)	General information
Rotor outer diameter: 146	Stator back-iron material: Hiperco50 0.15mm
Pole number: 6	Stator winding: copper (100%IACS)
Magnet thickness: 10	Rotor back-iron material: NO20
Magnet arc: 140°	Magnet: Recoma 32
Magnet segments radial: 1	Active weight (incl.end-winding): 62.1kg
Magnet segments axial: 1	Conductor height: 6.2mm
Shaft diameter: 74.6	Conductor width: 8.0mm
Mechanical airgap: 2	Torque predicted: 533Nm

Initial model 4 with Q = 200 kA/m	
Description: surface parallel rotor, parallel slot with distributed winding	
Machine layout:	Stator dimensions (all in mm unless specified)
	Number of slots: 36
	Stator outer diameter: 253
	Rotor outer diameter: 132
	Axial length: 136
	Slot width: 8.3
	Slot depth: 41.8
	Tooth tip depth: 1.5
	Slot opening: 2.67
	Tooth tip angle: 30°
Rotor dimensions (all in mm unless specified)	General information
Rotor outer diameter: 132	Stator back-iron material: Hiperco50 0.15mm
Pole number: 6	Stator winding: copper (100%IACS)
Magnet thickness: 10	Rotor back-iron material: NO20
Magnet arc: 140°	Magnet: Recoma 32
Magnet segments radial: 1	Active weight (incl.end-winding): 59.7kg
Magnet segments axial: 1	Conductor height: 8.5mm
Shaft diameter: 30.3	Conductor width: 7.0mm
Mechanical airgap: 2	Current density: 10 A/mm^2
	Torque predicted: 506Nm

The dimensions in the tables above were obtained from the sizing equations but these do not necessarily produce the rated torque when analysed using finite element analysis. Hence, for each of the four designs, the torque was predicted using MOTORCAD. The resulting torques are shown in Table 2.10. As will be apparent these fall short or exceed the rated torque. The axial lengths of these designs can be scaled to return to the rated torque. The resulting mass of these scaled designs are shown in Table 2.10 and include an estimate of end-winding mass based on values from MOTORCAD.

Table 2.10 Change in mass required to achieve rated torque of 557Nm

Q loading of the design	Torque predicted for design	Original mass	Mass for machine scaled to rated torque of 557Nm (incl. end windings)
50kA/m	495Nm	114.1kg	127.6kg
100kA/m	583Nm	73.7kg	70.7kg
150kA/m	533Nm	62.1kg	64.5kg
200kA/m	506Nm	59.7kg	64.6kg

As can be seen from Table 2.6, for an electric loading of 50kA/m, a combination of shallow slots, large rotor diameter and hence stator to meet the torque rating results in a very heavy machine. When the electric loading is gradually increased to 100kA/m and 150kA/m, stator geometry looks more reasonable with increased slot depth and considerably reduced mass. The further increase to 200kA/m does not produce a useful decrease in mass but would be associated with increased loss and hence the design with an electric loading of 150kA/m was selected for further optimisation.

2.2 Optimization process on initial model obtained from sizing equations

2.2.1 Introduction to optimisation

Despite the adoption of a high electric loading of 150kA/m, the design does not meet the target mass set out in the specification. Hence, a further optimisation study was undertaken to increase power density. The factors considered were an increase in current density and slot size, sensitivity studies on back iron thickness and magnetic thickness.

2.2.2 Optimization process with respect to current density and slot dimension

In order to meet the target mass of 50kg for the rated torque, various combinations of slot size and current density were evaluated. The optimisation involved establishing the minimum current density which would maximise torque within the current machine cross-section, a process that also involved changing the slot width and conductor size. The final selected design after numbers of iterations is shown in Table 2.11 from which it can be seen that although the optimised design does not meet the 50kg mass requirement, the corresponding torque increase introduced by increased copper volume and current density gives extra space to scale the axial length down to get a further reduction on weight. The scaling process of axial length will be provided in the section 2.2.3.

	Parameters of initial sizing	Parameter of optimised design
Slot width (mm)	9.2	10.3
Slot depth (mm)	29	29
Conductor width (mm)	8.0	8.94
Conductor height (mm)	6.2	6.55
Current density (A/mm^2)	10.0	11.7
Torque (Nm) for original axial length of 150 mm	534	635
Active weight (kg) for design axial length scaled to meet 557Nm torque rating (incl. end winding)	62.1kg	64.4kg

2.2.3 Sensitivity analysis on stator back iron thickness

The next design aspect considered was to evaluate the impact of the thickness of the stator back-iron on machine performance. In this investigation, the rotor outer diameter was kept constant at 146mm (This is equivalent to 150mm stator inner bore diameter) and the stator outer diameter only was varied. The design established in section 2.1.3 had a stator outer diameter of 250mm and hence a split ratio of 0.6. The stator outer diameter was varied over a range either side of 250mm from 220mm to 280mm in 10mm increments. In changing the stator outer diameter, the slot depth was kept constant, and all the change was taken up by back-iron thickness. Figure 2.10 shows cross-sections for the two machines at either end of the range considered. Table 2.12 summarises the variation in torque with back-iron thickness for a fixed axial length of 150mm and a fixed current density of 11.7A/mm^2 rms.

Table 2.12 Impact of split ratio in terms of torque and weight

Stator inner bore diameter (mm)	Stator outer diameter (mm)	Split ratio (D_{si}/D_{out})	Torque (Nm)	Active Weight (kg)
150	280	0.54	636	79.2
150	270	0.56	636	74.1
150	260	0.58	636	69.2
150	250	0.60	635	64.4
150	240	0.63	605	59.9
150	230	0.65	475	55.5
150	220	0.68	271	51.4
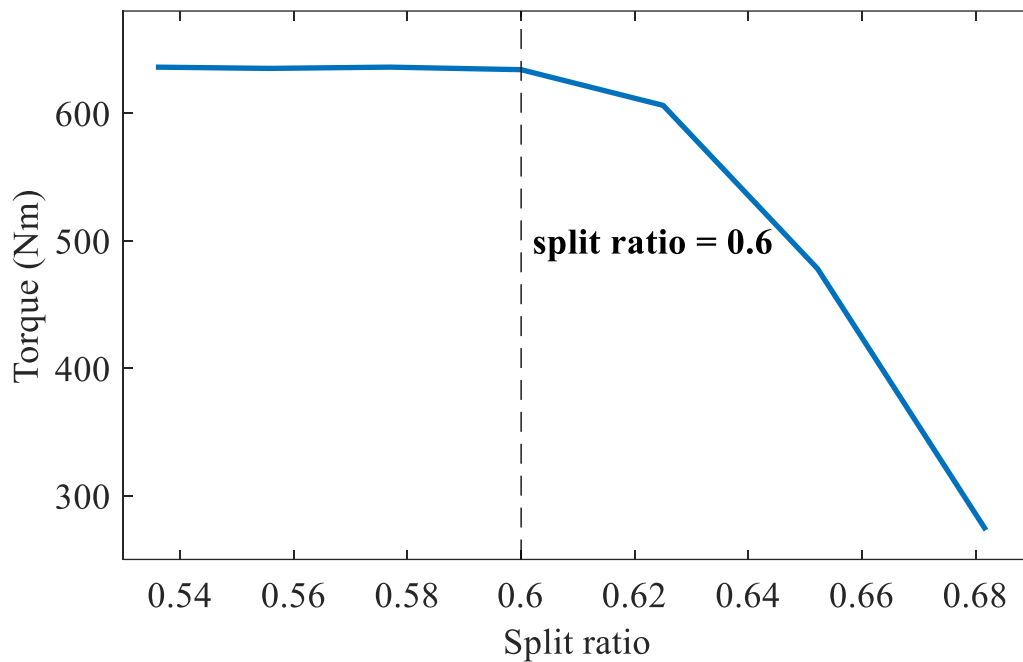
Figure 2.9 Split ratio versus torque curve with variation on back-iron thickness
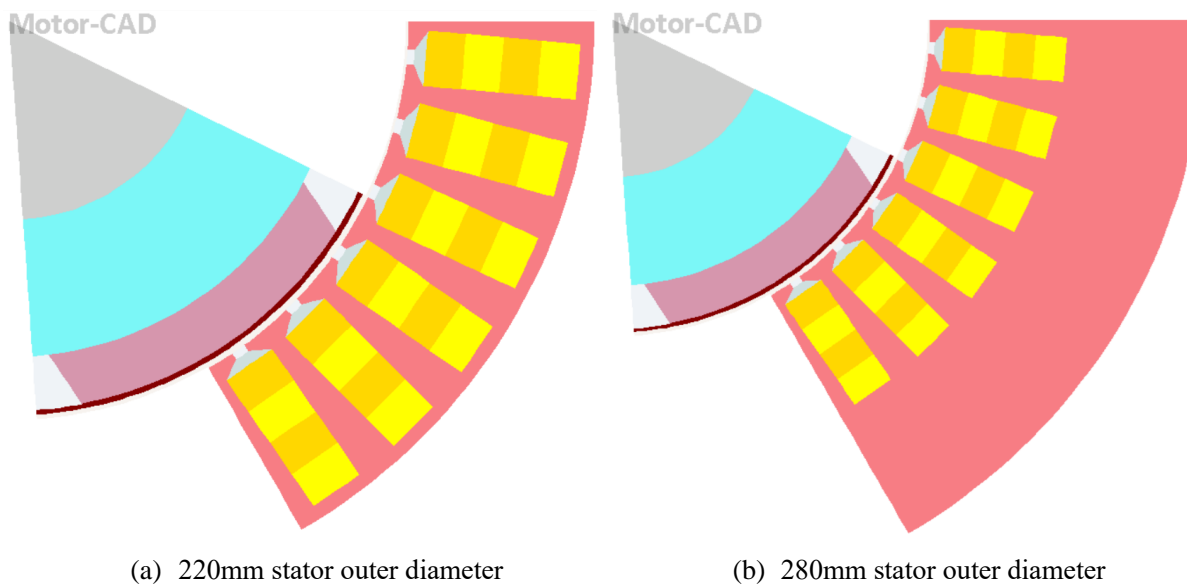
(a) 220mm stator outer diameter   (b) 280mm stator outer diameter

Figure 2.10 Cross-sections of the machines at the extremes of the range covered in Table 2.12

As can be seen from Table 2.12 decreasing stator out diameter from 280mm to 250mm results in little reduction in torque but a significant reduction in mass. However, when stator outer diameter is reduced below 250mm, output torque starts to diminish because the back-iron region becomes highly saturated. This series of designs indicate that any split ratio greater than 0.6 (i.e., any stator outer diameter less than 250mm) should be avoided. Based on the split ratio versus torque curve (Figure 2.9), a 250mm stator outer diameter (0.6 split ratio equivalent) which delivers a torque of 635Nm for an axial length of 150mm and operating at a current density of 11.7A/mm^2 rms was selected for further study.

Since the various refinements to the original design have maintained the same current density and axial length, the torque has increased beyond the 557Nm of the performance specification set out in section 1.7. Hence, there is scope to scale the axial length by a ratio of 635/557 (existing torque/rated torque) to bring the torque back in line with the specification. This will give a slightly less than proportionate reduction in the mass of the machine because the contribution of the end-windings and the elements of the casing such as end plates which do not scale with axial length. Scaling the axial length by this ratio reduces the axial length to 132mm, resulting in mass reduction from 64.4kg to 57.9kg. The calculated end-winding mass for this machine using MOTORCAD is 10.4kg using an assumption based on a simplified semi-circular representation. Hence, in order to meet an active total mass target of 50kg, i.e., including end-windings but excluding casing and shaft, further optimisation of the design is required. Moreover, even if the mass specification was met, there remains values in exploring further mass reductions by optimising other features of the machine.

2.2.4 Sensitivity analysis on magnet thickness

Previous refinements to the design focussed on the stator quantities of electric loading and stator back iron. One of the key remaining dimensions in the machine which can have a significant influence on the torque is the magnet thickness as this directly impact on the airgap magnetic loading. As part of this optimisation, the magnetic airgap length (which has been set to a fixed 2mm up to this point) was also varied between 0.5mm and 3mm. This magnetic airgap must include sufficient space to accommodate a rotor containment sleeve to retain the individual magnets in constant with the rotor core over the full speed range. The sizing of the containment sleeve is closely linked to the selection of the magnet thickness (which determines the mass and hence the centrifugal loading on the sleeve) and the maximum thickness that can be accommodated. Hence, this phase of the optimisation was concerned with understanding the trade-off between magnet thickness and torque for different magnetic airgaps with considering of a containment sleeve in the next section of this chapter.

Figure 2.11 shows the predicted variation in torque rating as a function of magnet thickness and magnetic airgap length for a machine with 146mm diameter rotor, a split ratio of 0.6 and an axial length of 132mm. In all cases, the rotor core radial depth was maintained at a fixed 25.7mm and hence the shaft / non-magnetic hub changed as the magnet thickness was varied.
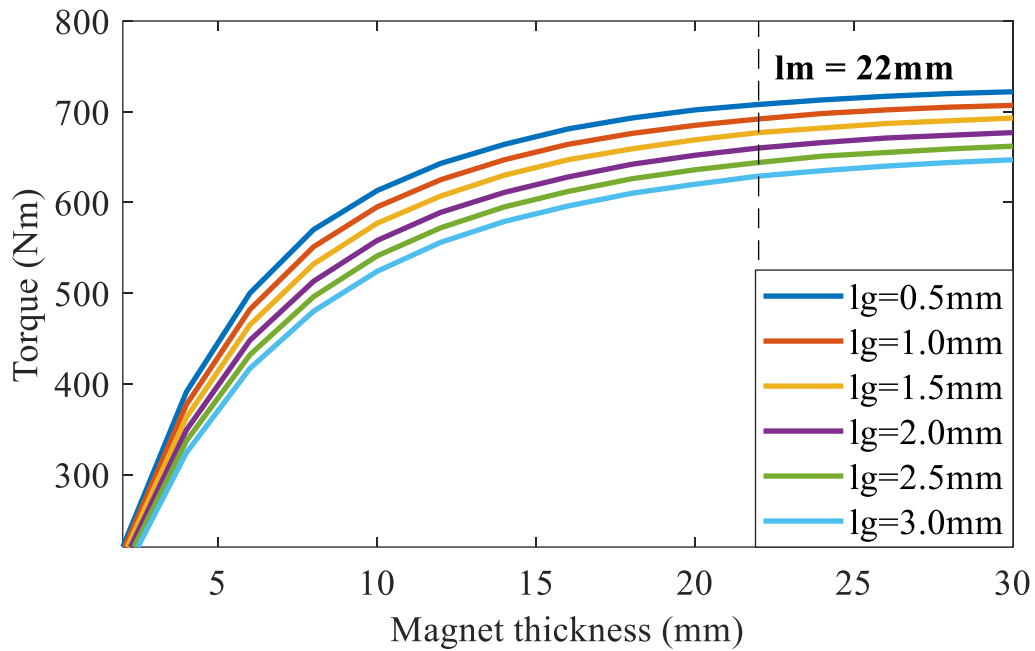
Figure 2.11 Two-dimensional finite-element predicted variation in torque with magnet length for a series of effective magnetic airgaps

As can be seen from the predicted characteristics above, for magnet thickness below 10mm or so, any increase of magnet thickness leads to a significant increase in torque. However, as magnet thickness continues to increase, the corresponding improvement in torque are obtained with diminishing return, and indeed there is little or no benefit in exceeding a magnet length of 22mm. In a cost-sensitive applications such as an EV traction machine, the high cost of the rare-earth magnets means that it would be difficult to justify a magnet thickness greater than 8-10mm depending on the airgap. However, in aerospace applications where mass reduction can often justify increased cost, a magnet thickness of 22mm appears to offer a good solution even though this is thicker than normal for this size of machine. As for the impact of airgap length on torque with a given magnet thickness, Figure 2.12 shows the reduction in torque with increasing airgap for the cases of 22mm and 10mm thick magnets, in both cases for a fixed machine axial length of 132mm.
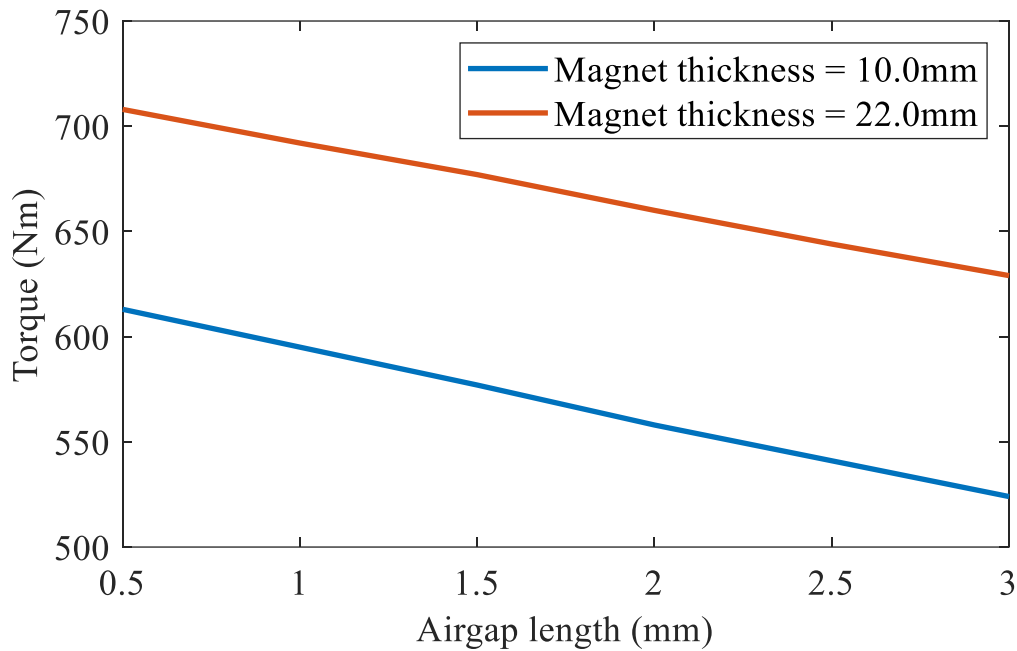
Figure 2.12 Finite element predicted electromagnetic torque as a function of effective magnetic airgap for fixed magnet lengths of 10mm and 22mm.

As would be expected, there is some torque penalty associated with increasing the airgap. At this stage the analysis only takes electromagnetic performance into consideration, which would suggest that an effective magnetic airgap of 0.5-1.0mm would offer a reasonable balance between mechanical clearance and torque capability. However, this does not include the need to incorporate a containment sleeve. The selected 22mm magnet is comparatively thick and is hence likely to require a containment which is proportionally thicker than a 10mm thick magnet. In order to settle on a combination of magnet thickness and effective magnetic airgap length, it is necessary to establish a suitable sleeve thickness and this process will be detailed in section 2.2.5.

Substituting magnet thickness 22mm back into the optimized version of initial model with corresponding change on shaft diameter to keep constant rotor core thickness, this model now gives 658Nm torque and 57.8kg mass. Since the torque of initial model was further increased by adopting thicker magnet, there is extra space for scaling down the axial length with the ratio of 658Nm/557Nm to further reduce total mass of initial model, resulting in a total weight of 50.9kg, torque 561Nm and axial length of 112mm. The performance of initial model is very close to the specifications and by decreasing stator outer diameter from 250mm to 246mm, the requirement of torque and weight can be met.

2.2.5 Determination of rotor containment sleeve thickness

Having identified a preferred combination magnet thickness from a purely electromagnetic point of view, it is important to ensure that this thickness is feasible. Specifically, in terms of whether a sleeve that is thick enough to withstand the centrifugal loading produced by the magnets will not result in an increase in effective magnetic airgap that will outweigh the incremental benefits of a thicker magnet in terms of torque rating. As discussed in chapter 1, some form of rotor containment sleeve is widely used in surface mounted permanent magnet machines to retain the magnet in contact with the rotor hub over the full speed range. Several available materials for rotor sleeve are reviewed in literature review section and carbon fibre with extremely high tensile strength and low density is selected for baseline model. As well as its excellent mechanical strength, carbon-fibre composites in which the fibres are arranged in an epoxy matrix are more or less electrically insulating at a bulk property level despite the individual fibres being conducting. The rotor of the baseline model has traditional topology with shaft, rotor hub and permanent magnet bonded with adhesive hub onto the rotor core. The worst-case assumption in terms of calculating the thickness of sleeve required is to neglect the magnetic force of attraction between the magnet and core and also to neglect any restraining effect from the magnet to core adhesive bond. Hence, the magnets can be regarded as a dead-weight on the sleeve and hence some well-established analytical equations can be used to determine the rotor sleeve thickness.

The minimum rotor sleeve thickness is ultimately determined by the hoop stress limit in the sleeve. This hoop stress can be considered in terms of two contributing components. The first, and usually the smallest of the two contributions is the self-loading of the rotating composite itself. The second and usually dominant component is dead-weight loading from the permanent magnets. The peak hoop stress σ_{max} (which occurs at the inner bore) in a thick-walled cylinder can be calculated by [59]:

$$\sigma_{max} = \frac{\delta_c \omega^2}{8} \left[(3 + v_c) \left(\frac{d_{co}^2}{2} + \frac{d_{ci}^2}{4} \right) - (1 + 3v_c) \frac{d_{ci}^2}{4} \right]$$
$$+ \left(\frac{d_{co}^2 + d_{ci}^2}{d_{co}^2 - d_{ci}^2} \right) \left(\frac{m_{eq} r_{meq} \omega^2}{\pi d_{mo}} \right)$$

(2.21)

The leading dimensions of the rotor are shown in Figure 2.13.
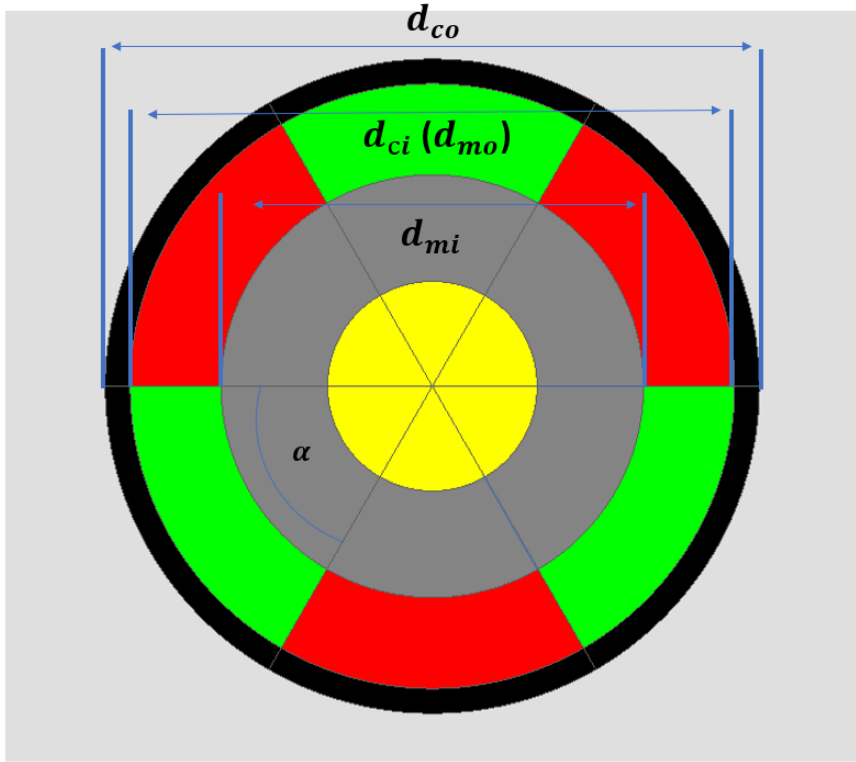
Figure 2.13 Rotor cross-section for surface mounted permanent magnet machine

The equations to calculate to equivalent m_{eq} and the equivalent radius of gyration r_{meq} in (2.21) are:

$$m_{eq} = \frac{\pi}{4}\left(d_{mo}{}^2 - d_{mi}{}^2\right)\left[\frac{\alpha\delta_m}{180} + \left(1 - \frac{\alpha}{180}\right)\delta_{ip}\right] \tag{2.22}$$

$$r_{meq} = \frac{\sqrt{2}}{2}\sqrt{\frac{d_{mo}{}^4 - d_{mi}{}^4}{4\left(d_{mo}{}^2 - d_{mi}{}^2\right)}} \tag{2.23}$$

It is worth noting that equations (2.22) and (2.23) are specific to an arc shape magnet and expressions to calculate m_{eq} and r_{meq} of loaf shaped magnet are provided in [59].

As well as limiting the hoop stress to some defined design stress limit, another design feature that must be taken into account is that the strain needs to be matched in different components of rotor to avoid detachment of magnets from the rotor core at high speeds. This is usually achieved in composite wound sleeve by introducing pre-tension into the fibre if the sleeve is wound in situ or interference fitting of pre-formed sleeves with a specified diametrical interference [59]. A properly designed level of interference does not introduce additional stress into the rotor at the maximum speed and hence although equation (2.21) does not account for diametrical interference, but it remains a useful tool to calculate the sleeve thickness to remain within a specified material stress limit. Given a combination of rotor outer diameter, magnet

51

thickness, airgap length, operating speed and maximum hoop stress, the resulting rotor sleeve thickness can be calculated analytically using (2.21) (2.22) and (2.23).

A key factor in determining the sleeve thickness is the specification of the maximum stress level to which the composite can be exposed. Values of up to 1GPa have been proposed for PM machines in literature [59]. Whereas this is within the range of properties that can be achieved by good quality carbon-fibre filament wound composites, it is common in electrical machines to adopt lower values and increase the long-term safety margin to account for factors such as stress relaxation in composite when exposed to temperature cycling [60]. Furthermore, in-situ winding of filament sleeves directly on to the magnets requires the pre-tensioning of the fibre to manage strain as noted previously. During the in-situ curing, it is difficult to retain very high levels of pre-tension and hence 500-600MPa is often regarded as the upper limit of design stress for in-situ wound sleeves. To provide some over-speed capability the first analysis was performed based on a design stress of 300MPa which is well within the capability of filament wound carbon fibre composites even when temperature cycled.

Figure 2.14 shows the variation in the thickness of sleeve with magnet thickness for a maximum localised stress of 300MPa. This relationship was established with iterative use of equations (2.21) - (2.23). The thickness shown are well within the range that can be accommodated in a 2mm gap between the outer surface of the rotor magnets and the inner bore of the stator. For example, the 22mm preferred value of magnet thickness identified in section 2.2.4, requires only a 1mm thick sleeve which can be readily accommodated and still leave a mechanical radial clearance of 1mm between the outer surface of the sleeve and the inner bore of the stator. Hence, a combination of l_g =2mm and l_m=22mm was selected for baseline reference design.
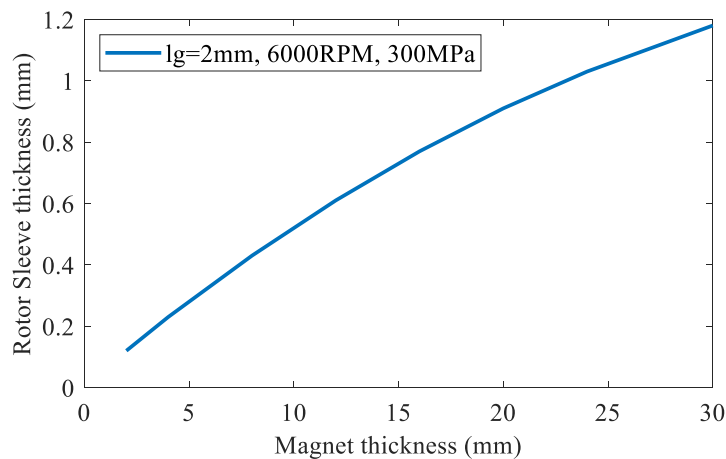
Figure 2.14 Variation in sleeve thickness to limit peak sleeve stress to 300MPa as a function of magnet radial thickness

52

2.2.6 Summary of optimised design

Following the various stages of design refinement and optimisation, the parameters of baseline model that gives rated torque with total weight under 50kg were determined. A detailed design specification for the final reference design is shown in the design sheet in Table 2.13. This final reference design has a stator outer diameter of 246mm, an axial length of 112mm with a total active mass (including the end-windings) of 49.5kg. This gives a power density of ~7kW/kg based on active mass (including an estimate of end-winding mass).

Table 2.13 Design sheet for baseline model

36 slot 6 pole 350kW 6,000RPM	
Description: surface parallel rotor, parallel slot with distributed winding	
Machine layout:	Stator dimensions (all in mm unless specified)
	Number of slots: 36 Stator outer diameter: 246 Stator bore diameter: 150 Axial length: 112 Slot width: 10.3 Slot depth: 32.3 Tooth tip depth: 1.5 Slot opening: 2.67 Tooth tip angle: 30° Winding layout:
Rotor dimensions (all in mm unless specified)	General information
Rotor outer diameter: 148 Pole number: 6 Magnet thickness: 22 Magnet arc: 140° (elec) Shaft diameter: 50.6 Effective magnetic: 2.0 Containment sleeve thickness: 1.0 Residual mechanical airgap: 1.0	Stator back-iron material: Hiperco50 0.15mm Stator winding: copper (IACS100%) Rotor back-iron material: NO20 Magnet: Sm_2Co_{17} (Recoma 32 grade) Active weight: 39.3kg Total machine weight: 49.5kg Conductor length: 8.94mm Conductor width: 6.55mm Current density: 11.7 A/mm² rms DC bus voltage: 580V
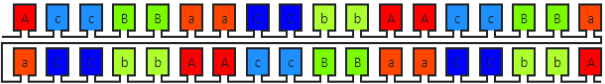
As can be seen from the Table 2.13 above, the stator outer diameter is slightly lower than that of the 250mm identified from the initial sizing process and the sensitivity study reported in section 2.2.3. The 4mm reduction on stator outer diameter was established following a further sensitivity around 250mm with a finer increment of diameters. It was established from this

further study that a 246mm stator provides an optimal solution in terms of additional weight reduction while producing rated torque.

It is interesting to summarise the evolution of the machine during this sizing and optimisation study. Table 2.14 shows a summary of the changes in the leading dimensions and mass as the design optimisation progressed. In each case the axial length was scaled to achieve the desired torque rating.

Table 2.14 The changes of leading dimensions and mass during the design and optimization process for Q = 150kA/m

	Initial sizing	Optimization of current density and slot	Optimization of stator back iron	Optimization of magnet thickness	Final optimization with fine increments
Stator outer diameter (mm)	250	250	250	250	246
Axial length for rated torque (mm)	150	150	132	112	112
Overall mass (kg)	62.1	64.4	57.9	49.5	49.5

2.3 Evaluation of reference machine design performance

The initial design and optimisation were performed using MOTORCAD which includes a built-in customised finite element solver. However, this solver is not a general-purpose finite element package that can be used with specific models to investigate various design features and complex phenomena. Hence, the main analysis tool used in the research reported moved to a commercial finite element package, specifically the FLUX2D and FLUX3D packages from Altair. The first task undertaken was to build a model of the reference design of Table 2.13 in FLUX2D and compares its performance predictions with MOTORCAD.

2.3.1 Comparison between MOTORCAD and ALTAIR FLUX 2D performance predictions

The geometry of the baseline design model in FLUX2D is shown in the Figure 2.15. The symmetry in 6-pole and 36-slot design was exploited to reduce the problem domain to 1/6th of the full machine with anti-cyclic boundary conditions. Two mechanical sets (named stator and rotor) were defined to set-up rotation of the machine with stator fixed and rotor rotating around a defined axis.
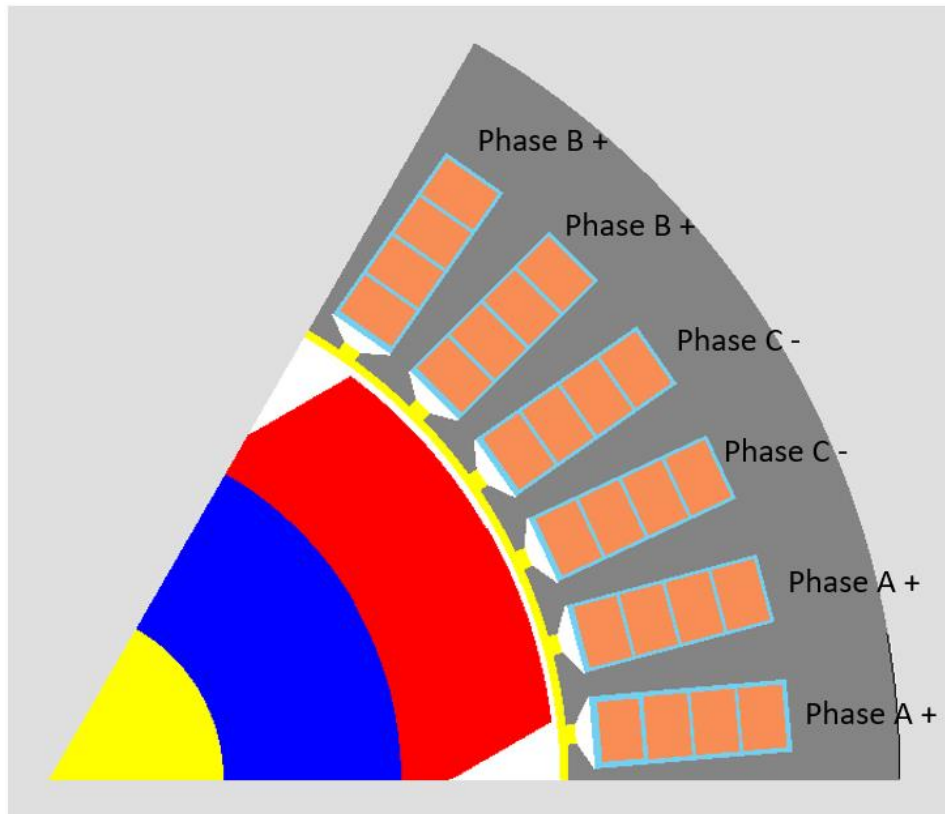
Figure 2.15 Geometrical view of baseline model

An important consideration in the model to note is the direction of magnetization of the magnet. Arc shaped magnet segments of the type shown in Figure 2.15 can be manufactured with one of two different directions of magnetization: parallel and radial. The parallel magnetization of permanent magnet is most straightforward to achieve and can produce an increased flux density in airgap region and hence is often adopted in electrical machines. The radial magnetization on the other hand, is relatively difficult to achieve from a manufacturing point of view and the resultant airgap flux density (which impact torque capability) tends to be lower than model with parallel magnetization. Figure 2.16 illustrates the differences between parallel magnetization and radial magnetization in the reference machine design.

Note that there is a special type of magnet arrangement called Halbach array, which is often seen in high performance electrical machines especially in the format of outer rotor PM machines in aerospace applications. For a Halbach array arrangement, one pole is subdivided into several segmentations with customized magnetisation direction of individual segments. In this way, the flux produced by PMs can be concentrated at the specified side while cancelled at the other side to achieve the flux focusing. Another benefit of Halbach array is that the back iron thickness of rotor can be reduced. Due to the fact that the parallel magnetization can

55

achieve higher flux density in airgap region with reasonably simple manufacturing process, this magnetization method was adopted for the remaining studies reported in this thesis.

Parallel magnetisation   **Radial magnetisation**
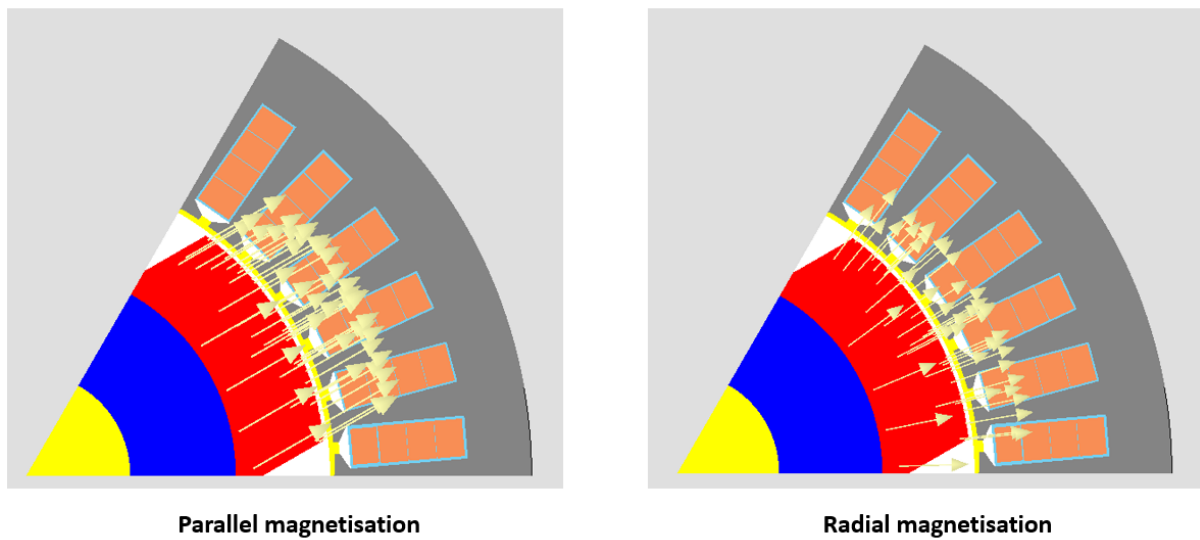
Figure 2.16 Difference between parallel magnetization and radial magnetization

Having defined the geometry and materials, the next step was to specify a finite element mesh for the model. It is well known that mesh equality has a significant influence on the accuracy of a finite element model. The mesh of baseline model with default mesh settings in FLUX2D and the mesh quality assessed by FLUX2D are shown in Figure 2.17.


```
Surface elements :
    Number of elements not evaluated     : 0     %
    Number of excellent quality elements : 99.42 %
    Number of good quality elements      : 0.54  %
    Number of average quality elements   : 0.04  %
    Number of poor quality elements      : 0     %
```
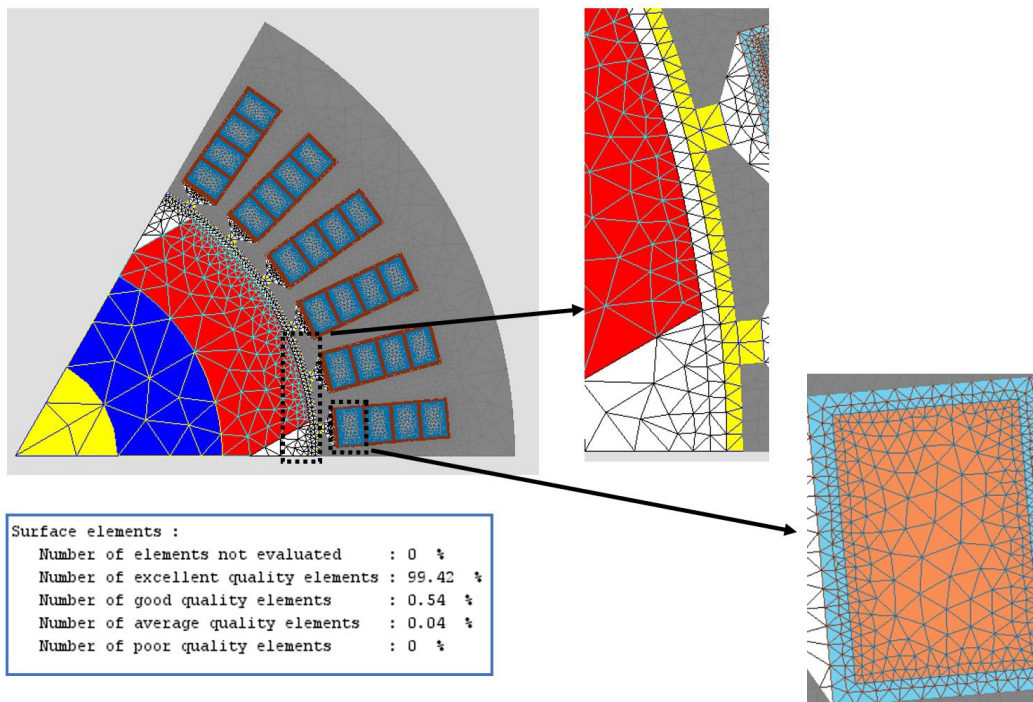
Figure 2.17 Mesh information for baseline model in flux with evaluation of mesh equality

As can be seen from the bottom left of Figure 2.17, the proportion of excellent quality elements evaluated by the software is 99.42%. This assessment, which is automatically done prior to the solution, does not relate to whether there are sufficient elements in the required locations at appropriate discretisation but refers solely to the aspect ratio of the elements. In the case of triangular mesh elements, the ideal element is an equilateral triangle. The requirement on mesh spatial discretisation differs for various regions of electrical machines and arguably two most important regions that need extremely fine meshes in FEA modelling are airgap region and conductor region. The mesh quality of airgap region has major impact on the likely accuracy of the torque prediction while the mesh discretisation in the conductor region is key for calculating eddy current loss.

The FLUX2D mesh shown previously in Figure 2.17, which was auto generated using high level default discretisation, is not optimised in terms of element layout or element type to best deal with eddy currents in the conductors. The issue of custom mesh geometry for improved modelling eddy currents it discussed in detail in section 3.1.5. However, the current mesh of Figure 2.17 is useful in terms of assessing the performance of standard default mesh.

The first simulation performed was an open-circuit calculation to establish the back-emf waveforms at 6,000rpm for each phase. This refers to a condition where the stator windings are un-excited (open circuit), and the rotor rotates as rated speed (6000RPM) in transient magnetic context. The simulation often involves building an external circuit and then linking the circuit to physical representations. Elementary electrical circuit usually consists of different components including current source or voltage source for excitation, solid conductor or stranded coil conductor for winding regions, resistor and ground. The external circuit of baseline model is shown in the Figure 2.18 below:
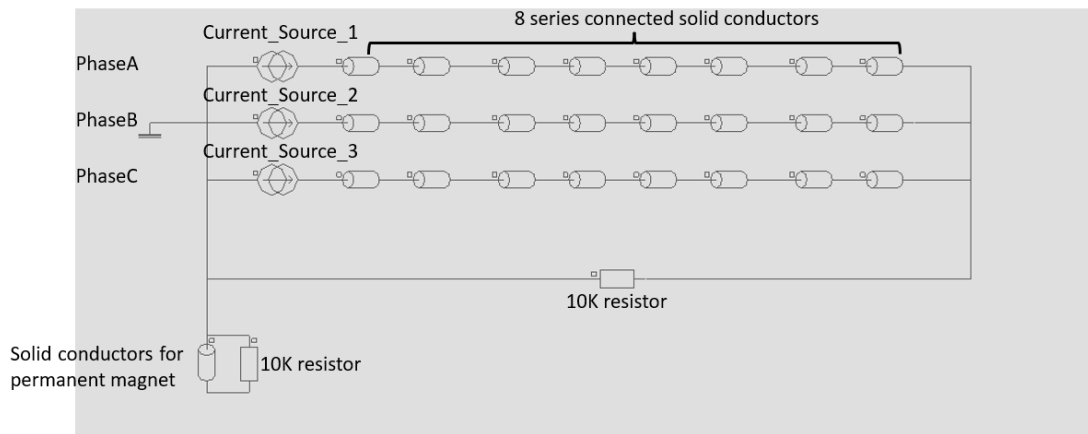
Figure 2.18 External circuit of baseline model

One thing to note is that there are two additional 10K resistors and one solid conductor (representing one pole of permanent magnet) that are connected to the main circuit. This is because Flux 2D does not allow independent components in the external circuit and thus two large value resistors are used to physically connect the circuit but electrically separate the components of three phase and permanent magnets. As can be seen from the Figure 2.18 above, 8 solid conductors are connected in series to represent the winding regions of single phase and three phases are connected in parallel with star connection. While for the solid conductor in bottom region, it represents permanent magnet region and is parallel connected to a large value resistor. The windings are excited by current sources, and the current waveforms are assumed to be pure sinusoidal (no harmonics considered) with parameterized formulas. The equations that define current sources are related to speed, frequency, speed and maximum current and this allows easy control of the input current for future evaluations. The current sources in each phase of the electrical circuit were supplied with the current waveforms calculated using equation (2.24) to (2.26). The term γ in each equation is an angular offset (in elec°) which aligns the zero-time referenced current waveforms with the rotor position (which may contain arbitrary reference angles depending on how the model was drawn).

$$I_a(t) = I_{max}\ sin\left(\omega t + \left(\frac{\gamma\pi}{180}\right)\right) \tag{2.24}$$

$$I_b(t) = I_{max}\ sin\left(\omega t + \left(\frac{\gamma\pi}{180}\right) - \frac{2\pi}{3}\right) \tag{2.25}$$

$$I_c(t) = I_{max}\ sin\left(\omega t + \left(\frac{\gamma\pi}{180}\right) - \frac{4\pi}{3}\right) \tag{2.26}$$

There are two types of regions that can be used to represent windings and other conducting regions in FLUX2D models, viz. solid conductors and stranded coil conductors. It is common in most, but not necessarily all, finite element models to represent a coil as a single homogenous region rather than representing each individual wire within the coil. Stranded coil conductors allow a winding consisting of numerous individual wires (which may be a combination of series and parallel connected) to be represented as a single homogenous region in which the externally driven current is uniformly distributed across the region. In the context of AC losses, the key feature of a stranded coil is that the region is regarded as being non-conducting from the perspective of induced eddy currents and hence is not a source of AC loss.

In cases where the individual to account for both imposed conduction currents and induced eddy currents flowing in the conductors, solid conductor region is usually implemented. There are several things to note for implementation of solid bar conductor. First, the conductor shape needs to be representative of realistic conductors. For example, if to calculate the conductor loss in Litz wire, each strand needs to be reflected in geometry and then connected to its corresponding solid conductors in external circuit. This process introduces extra modelling complexity especially for models with large number of turns. In addition, the mesh quality on conductor region needs to be very fine to fully capture the skin and proximity effect, which means the solving time will be increased. Since the focus of this thesis is to evaluate and compare the losses in different types of conductors, the solid bar conductor will be used in the following analysis.

Open-circuit conditions can be enforced in the finite element model by setting the amplitude of the current sources to zero in the coupled electric circuit of Figure 2.18. The phase back-emf waveforms (i.e., line to star-point) and line to line back-emf waveforms for baseline model are shown in the Figure 2.19 and Figure 2.20.
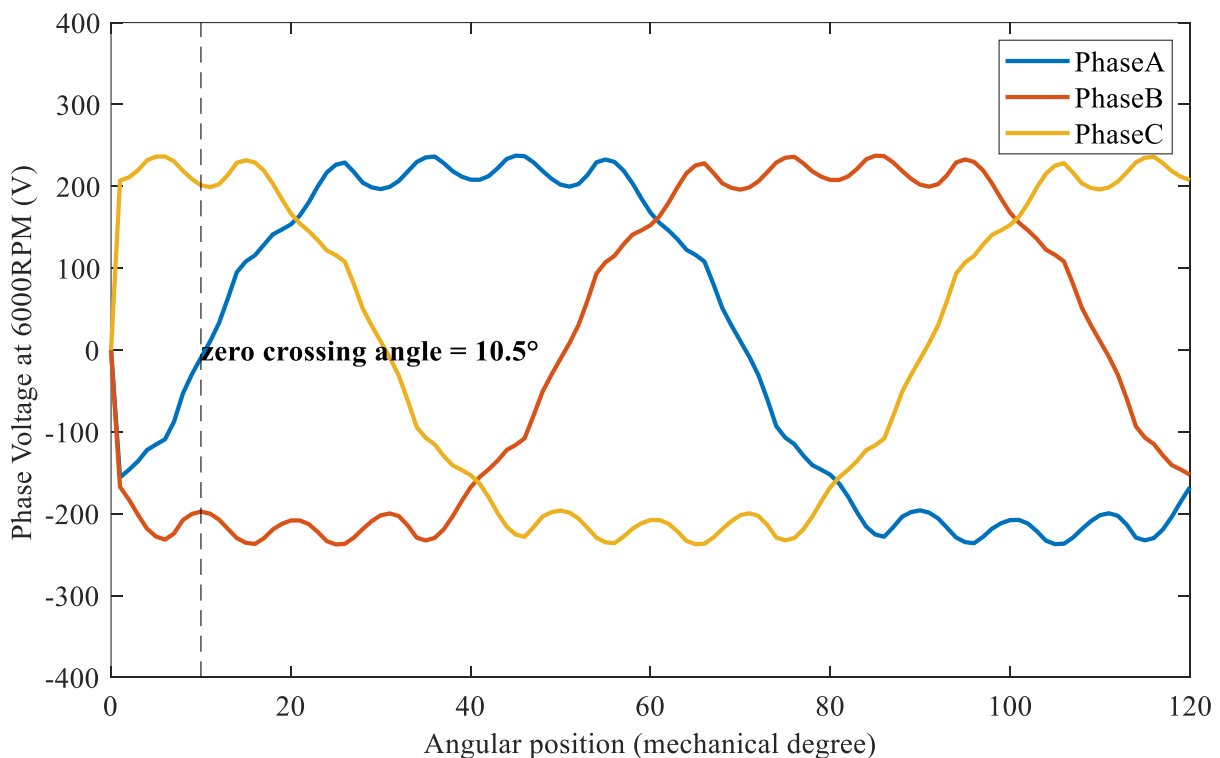
Figure 2.19 Phase (line to star-point) back-emf curve of baseline model
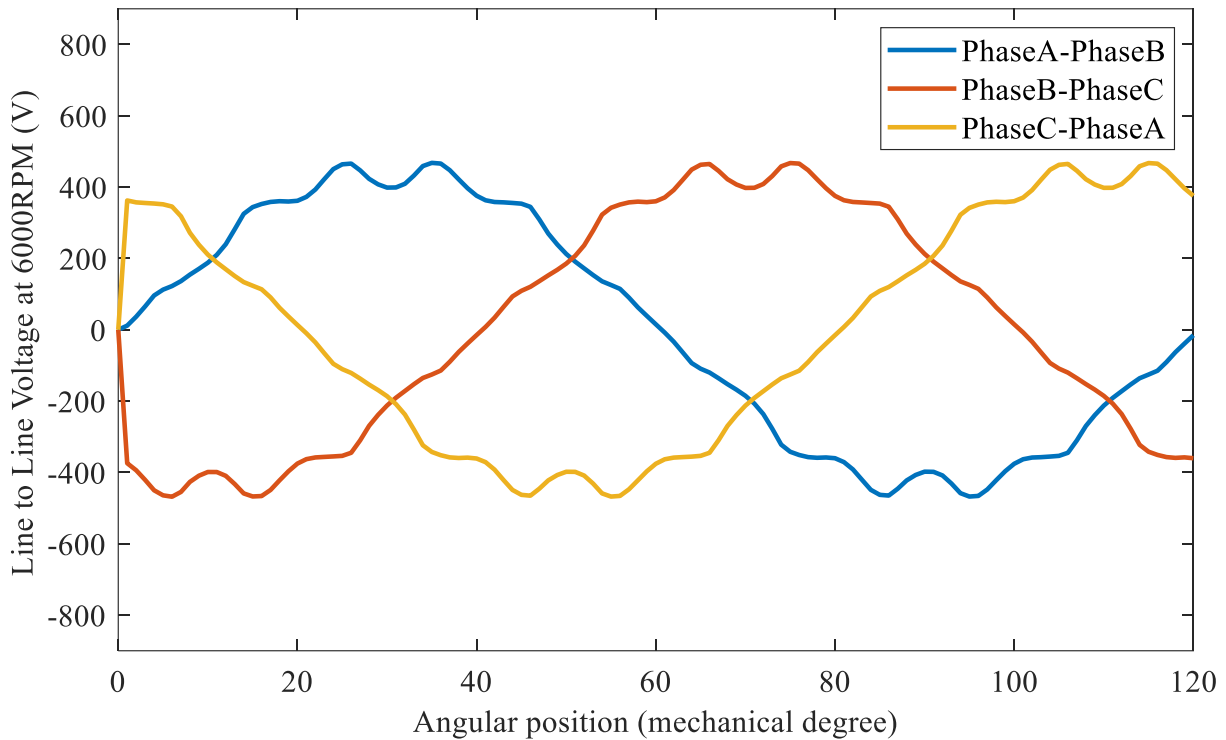
Figure 2.20 Line to line back-emf curve of baseline model

The zero-crossing angle of the back-emf can be used to align the currents with rotor position, i.e., establish a value of γ for (2.24) to (2.26) which control the current sources in the coupled electric circuit. As can be seen from Figure 2.19 and Figure 2.20, both 3-phase back-emf waveforms exhibit significant harmonic content. FFTs of the line to star point and line-to-line back emf waveforms is shown in Figure 2.21 and Figure 2.22. As can be observed, the 5th, 11th and 13th order of harmonic are significant in both waveforms but as expected only the back-emf for the line to star point (which is floating) contains a 3rd harmonic.
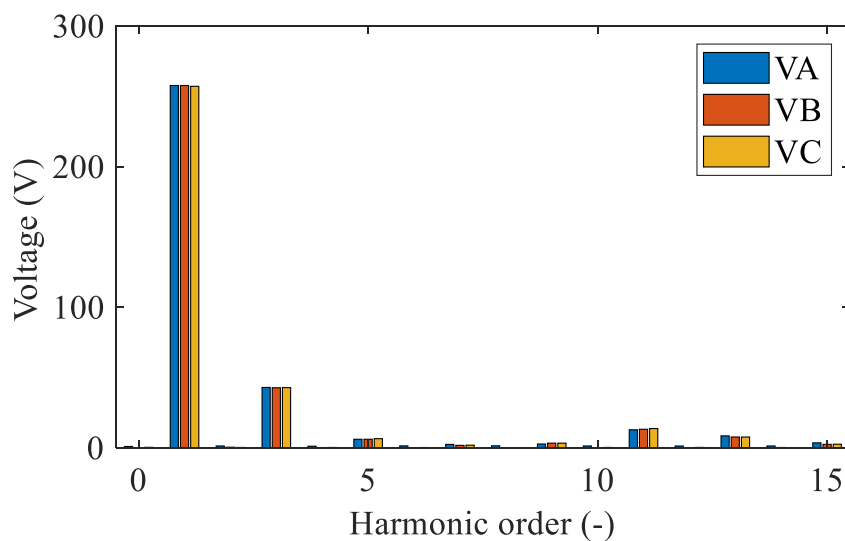
Figure 2.21 Harmonic content of line to star point back-emf waveform

60
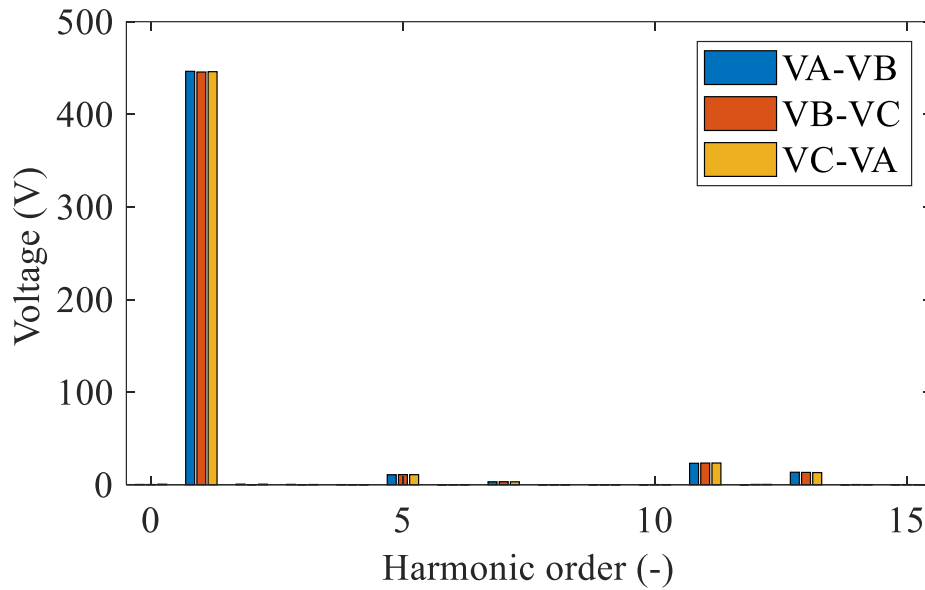
Figure 2.22 Harmonic content of line-to-line back-emf waveform

Following evaluation of back-emfs, the next comparisons were the calculation of electromagnetic torque and the winding losses at rated current and rated speed of 6,000rpm. A comparison of baseline performance between FLUX2D and MOTORCAD is shown in the Table 2.15. As will be apparent, there is good agreement between the electromagnetic torque predicted by both packages. In terms of overall copper loss, it is worth noting that FLUX2D model is a two-dimensional finite element modelling and can therefore only calculate the winding loss in the active region. MOTORCAD also contains a two-dimension finite element solver but also includes an analytical calculation for end-winding loss. Note that the end-winding loss calculated by Motor-cad is pure DC. It should be noted that the differences of total winding loss predicted by two software are relatively noticeable (13.5% taking Motor-cad value as baseline) compared to torque predictions. The difference of loss predictions mainly comes from the mesh differences for two software. Although all the two models use default automatic mesh, the resulting mesh quality among conductor region is significantly different and thus gives misaligned loss predictions as shown in Table 2.15. Since the Motor-cad is only used in early stages to get some quick designs, the processes that align the loss predicted by Flux 2D and Motor-cad will not be provided here. In the following chapter, the evaluations of initial baseline will be carried in traditional FEA software like Flux and Ansys Maxwell. The magnitude of the total loss is some ~10 times higher than the 2214W of quasi-static loss for this machine. This illustrates that for this combination of conductor size and frequency, the AC losses are prohibitive and that significant improvements are required in terms of AC loss to make a bar conductor a viable option.

61

Table 2.15 Torque and loss comparison between FLUX2D and MOTORCAD

	FLUX2D	**MOTORCAD**	**Difference**
Torque	552 Nm	555 Nm	0.5%
DC loss (W)	2214W	2214W	-
AC loss (W)	19,802 W	22,770W	-
Total loss	22,016 W	24,984W	13.5%
Number of sampling points	30	30	-
Solving time	2min	1min	-

2.3.2 Evaluation of variants with different pole numbers

The outcomes of the initial evaluation of the baseline design are that whereas it can produce rated torque, there are prohibitive AC losses for the bar conductor winding selected, i.e., 4 turns per slot, each 8.94mm × 6.55mm. The AC losses are dependent on the electrical frequency. At low frequencies, the losses increase with the square of frequency until skin effect starts to have a significant effect on the eddy currents. One option for bringing down the AC losses while maintaining the same speed range is to reduce the pole number but at the expense of increased weight. On the other hand, increasing the pole number in PM machines tends to result in reduced mass for a given torque rating but at the expense of an increase in the frequency dependant loss mechanisms. The mass savings are obtained from the fact that the rotor and stator back thickness required to maintain a particular peak flux density are inversely proportional to the pole number.

Recall that the baseline model is a 36 slot 6 pole SPM machine equipped with bar conductor and the calculated AC loss at rated working condition is already prohibitive. In order not to exhibit excessive level of AC losses, the emphasis of the pole number investigation was on low pole numbers of 2 pole and 4 pole. However, the evaluation of a 12-pole variant was also included to demonstrate the diminishing return in reducing overall machine mass as the back iron is progressively reduced in thickness. There are three things to note during the process of pole number investigations: 1. stator slot number is kept fixed at 36 for each pole number and 2. stator related dimension are all same as that of 6 pole baseline model and 3. winding pattern will be adjusted accordingly based on the different slot-pole combination.

As different pole number combinations were considered, the principle adopted for scaling the stator back-iron thickness and rotor back-iron thickness was to simply scale the 15.7mm thick

back-iron in the 6-pole design by a ratio of 6/new pole number. For example, if pole number decreases from 6 to 2, the back-iron thickness of stator and rotor needs to be increased by a ratio of 3 (i.e., 6/2) to 15.7*3=47.1mm, thus ensuring equivalent flux density in the rotor and stator back-iron.

Figure 2.23 shows a summary of the initial designs of 2,4 and 12 pole machine based on simple scaling of the back-iron of the baseline 6-pole machine. Also shown is the proposed winding configuration for each pole number. Table 2.6 shows some key design parameters for this starting design.

(a) 36-slot, 2-pole design

(b) 36-slot, 4 pole design

(c) 36-slot, 6-pole design

(d) 36-slot, 12-pole design
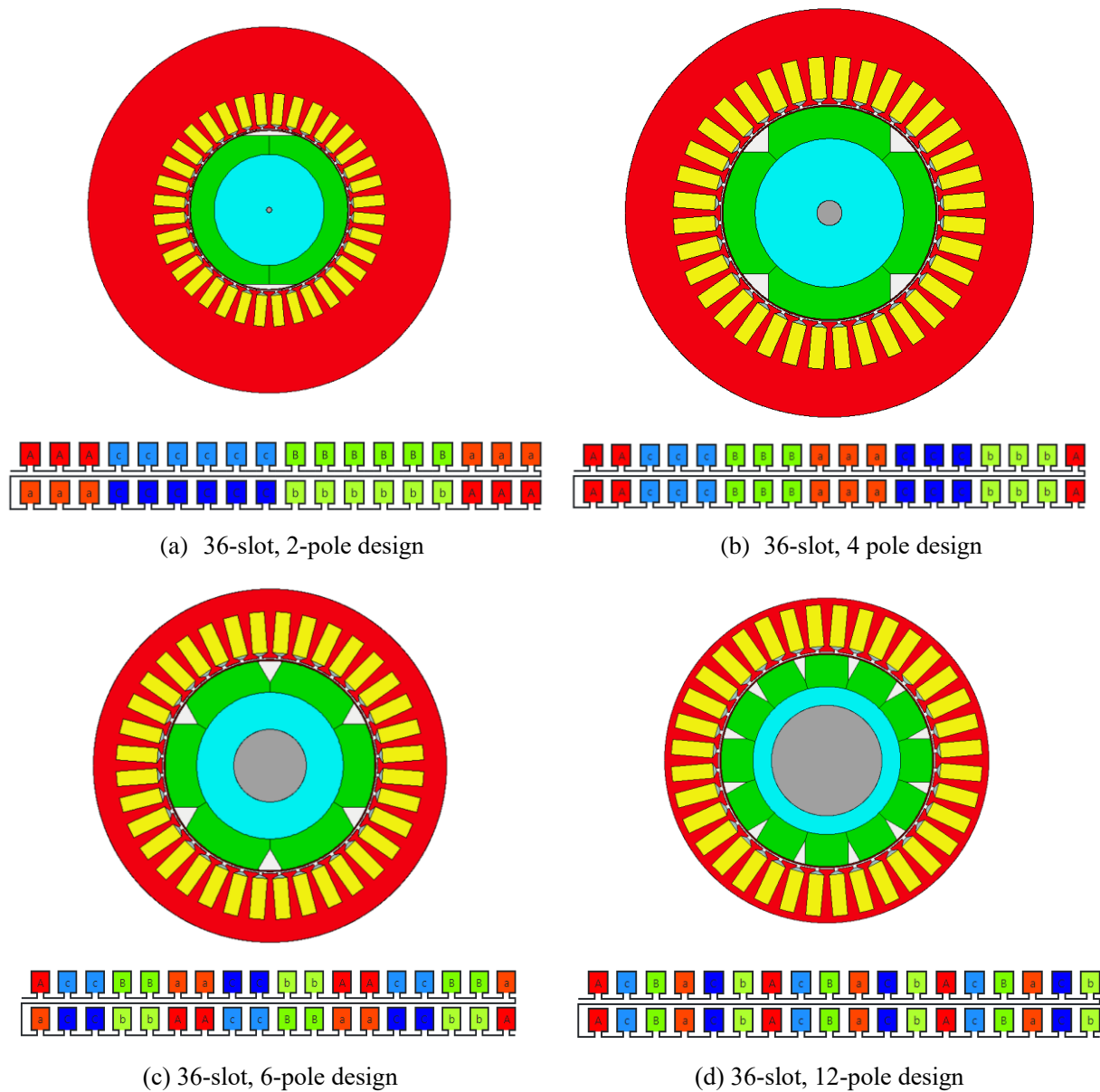
Figure 2.23 Alternative pole number designs with the same rotor outer diameter and 36 stator slots (all cross-sections are shown on the same scale with a constant rotor diameter)

	2-pole	**4-pole**	**6-pole**	**12-pole**
Fundamental winding factor	0.956	0.960	0.966	1.000
Winding type	Single layer distributed	Single layer distributed	Double layer distributed	Single layer distributed
Coil span	18	9	6	3
Stator back-iron thickness	47.1mm	23.6mm	15.7mm	7.9mm
Rotor back-iron thickness	46mm (77.1mm*)	38.6mm	25.7mm	12.3mm

Note that for 2 pole variant the scaled rotor back-iron thickness is 77.1mm. This thickness is impossible to apply to the existing model because the rotor outer radius is only 73mm. To make the scaling process of 2-pole design realistic, the shaft diameter is set to be a reasonably small value of 10mm and will be kept constant during the process, which means the back-iron thickness for 2-pole variant is 46mm (with constant rotor outer radius of 73mm, 22mm magnetic and 5mm shaft radius).

The simple scaling of the rotor back-iron provided a useful means of initially sizing the various designs. However, some optimisation of the stator and rotor back-iron was undertaken using Motor-cad that was able to vary the back-iron around the original scaled value to establish the most appropriate thickness on a more robust basis to ensure a more equitable comparison between the pole numbers.

The detailed scaling process for stator and rotor back-iron thickness is to change the thickness of stator by ±20% and ±40% each time with corresponding change in the rotor back-iron taking nominal thickness as baseline. As an example, Figure 2.24 shows the influence of a ±20% and ±40% variation around the nominal 47.1mm thick back-iron of the 2-pole design on the electromagnetic torque for the nominal axial length of 128mm. Each increment or decrement will be 20% of nominal stator back-iron thickness. This axial length is the value that corresponds to the case with the 54mm thick back-iron achieving a rated torque of 557Nm. For the particular case shown the rotor back-iron was a fixed at 46mm although as part of the optimisation this was also systematically varied.
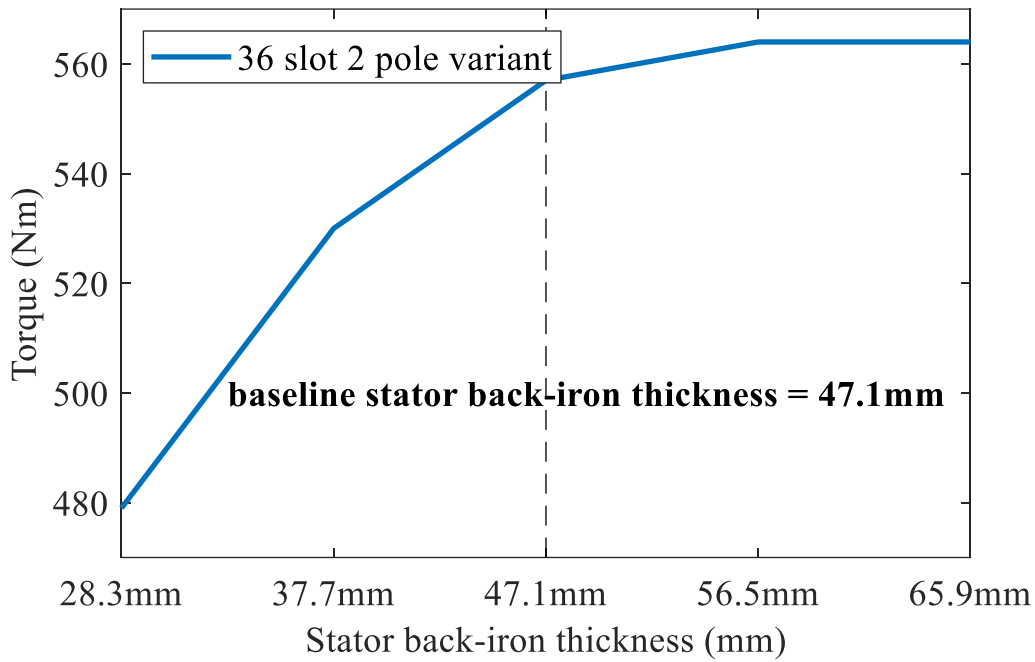
Figure 2.24 The impact of variation on stator/rotor back-iron thickness on torque for 36 slot 2 pole variant

The optimal designs establish for each combination of slot/pole number using this systematic variation of the rotor and stator back-iron are summarised in the

Table 2.17. In each case, the axial length quoted is the value required to produce the rated torque of 557Nm. The torque and AC losses were calculated using only MOTORCAD with no cross-checking via FLUX2D. All the calculations are carried in room temperature (20°C) at rated speed of 6000 RPM over one electrical cycle.

Table 2.17 Summary for optimal designs for different slot/pole combinations

	36 slot 2 pole	36 slot 4 pole	36 slot 6 pole	36 slot 12 pole
Stator outer diameter (mm)	290	253	246	230
Stator back-iron thickness(mm)	37.7	18.9	15.7	7.9
Rotor back-iron thickness (mm)	46	30.9	25.7	12.9
Axial length (mm)	138	115	112	131
Total weight (kg)	95.6	57.1	49.5	45.8
Fundamental electrical frequency at 6000rpm (Hz)	100	200	300	600
Quasi-static copper loss (W)	2,727	2,263	2,214	2,589
AC loss (W)	6,761	13,770	22,800	51,100
Total copper loss (W)	9,488	16,033	25,014	53,689
Winding type	Single layer distributed	Single layer distributed	Double layer distributed	Single layer distributed

Note that all the loss values are obtained with an assumption of 20°C room temperature. As can be seen from Table 2.17 there is the expected progressive reduction in mass with increasing pole number as the back iron thickness is reduced. The problems encountered previously with the 6-pole machine in terms of prohibitive AC loss are reduced with decreasing pole number as would be expected. However, even with a 2-pole machine that has a fundamental frequency of only 100Hz, the combination of large individual bar conductor cross-sections (8.94mm × 6.55mm) and slot leakage means that the AC losses are still almost 3 times the quasi-static loss.

The slot dimensions and conductor cross-sections are the same in each case and hence, other than a small correction for the change in axial length, it would be expected that the AC loss would increase more or less as the square of pole number if the eddy currents were resistance limited. However, the increase in frequency from 100Hz to 200Hz which is a consequence of the increase in pole number from 2 to 4 only results in 2.1 times increase in the AC loss. This suggests that significant skin effects are present at 200Hz, which can be confirmed by the fact that the conductor height is bigger than skin depth at corresponding frequency. The AC loss increase between 2 pole and 6 pole is only a factor of 3.48 as compared to a factor of 9 for a simple square of frequency relationship. This is the consequence of different loss components that are added into together in a non-linear format, i.e., the impact of skin effect and proximity effect from adjacent conductors and the loss generated by rotor PM flux. This again demonstrates the danger of relying of simple analytical expressions for skin effect to size conductors for use in a machine.

In summary, whereas reducing the pole number has reduced the AC loss considerably, it has not reduced to a sufficient level to make even a 2-pole machine viable in terms of loss and in any case, it incurs a very significant mass penalty. Since even a two-pole rotor cannot provide acceptable levels of loss for this particular winding arrangement and conductor size, additional mitigation strategies are required in order to address AC losses in this series of machine designs. Methods for mitigating AC losses are discussed further in chapter 3. These AC loss mitigation strategies are a key novelty of this thesis.

Chapter 3. Investigation of AC losses and method to reduce it

3.1 Loss mechanisms in solid bar conductors

As is discussed in previous chapters, the key efforts on enhancing power density in PM machines are now focused primarily on stator design and in particular enabling at high electric loading through a combination of increased slot fill and improved thermal management of losses. In machines requiring relatively few turns per slot, both of these features can be enhanced through the adoption of solid bar conductors, particularly if slot shape is a close match to the conductor dimensions. Bar conductors are becoming increasingly common in some PM machines, particularly as noted in chapter 1, with development of hairpin coils which are being increasingly being used in electric vehicle traction machines [61]. Whereas bar windings can improve slot-fill, care must be taken in ensuring that high frequency AC losses do not outweigh the benefits of the slot-fill. To manage the AC losses in bar conductors, the principles underlying windings losses need to be understood in order to implement loss mitigation strategies.

From a design point of view, it is useful to separately consider the behaviour of conductors to low frequency time varying currents and the behaviour with higher frequency currents. The quasi-static losses (sometime referred to as DC loss despite applying to AC currents) deals with the case where the current is uniformly distributed over the cross-section of the conductor. With uniform current flow across the conductor the quasi-static loss is relatively easy to calculate because of its linear relationship to resistivity, current and conductor dimension, see (3.1) below:

$$P_{cu} = I_{rms}^2 R = J_{rms}^2 \rho V_{cu} \tag{3.1}$$

To produce the desired torque, a particular product of average current and turns is required. Substituting $J = \frac{NI}{A}$ and $V_{cu} = lA$ back into equation (3.1), yields:

$$P_{cu} = \frac{\rho l (NI)^2}{A_{cu}} \tag{3.2}$$

As can be seen from (3.2), the quasi-static loss in a given slot is inversely proportional to the cross-sectional area of copper which is the reason that the proportion of the slot which is occupied by copper plays such an important role in the reducing ohmic losses. The definition of slot fill factor (sometimes referred to as coil packing factor) is the proportion of the total

available slot area which is occupied by copper. As an example, Figure 3.1 shows a simplified representation of a stator slot that has 18 conductors each with a copper outer diameter of 1.3mm (this diameter does not include the enamel on the wire itself). The slot has a width of 6mm and a useable depth of 10mm after space is made set aside for a slot closure / wedge. In this case, the slot fill is given by $\frac{18 \times \pi \times (1.3)^2}{6 \times 10} = 0.39$. There are several definitions for slot fill depending on whether they use the available slot area (i.e., after subtracting the slot liner) but in this thesis the definition is based on the ratio of copper area to bare slot area.
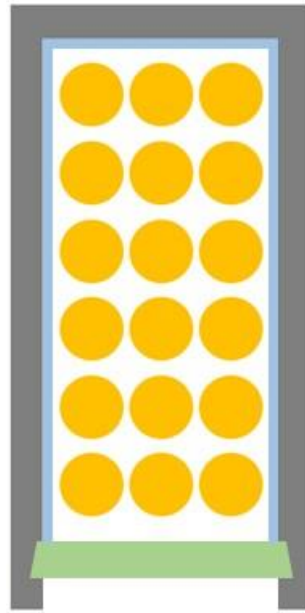
Figure 3.1 A simplified slot diagram illustrating the importance of slot fill factor

The achievable slot fill with circular conductors is not a fixed number and depends on the exact winding technique employed, the slot shape, the number of conductors and the thickness of the slot liner. For a given core geometry, there is significant benefit in increasing the slot fill, not only to reduce loss but also to increase the effective thermal conductivity across the slot to aid heat transfer.

In contrast to the straightforward methods for calculating quasi-static loss, the calculation of AC losses is far more complicated. The additional AC losses are caused by eddy currents which are induced in conductors themselves due to the exposure to time varying incident magnetic fields and results of different mechanisms. The induced eddy currents can be regarded as the direct consequence of Faraday's law of induction, and as a result of Lenz's law as they flow in the opposite direction of source current to create an opposing reaction field (Lenz's law). There

are four types of sources that generate eddy current losses in the conductors of electrical machines:

i)   The influence of imposed time-varying current in a conductor on the flux-linkage of the conductor itself. As the frequency of current increases, the current is increasingly confined to the surface of conductor, a phenomenon which gives rise to the term 'skin effect'.

ii)   Time varying currents flowing in nearby conductors whose time-varying flux links the conductor of interest. This behaviour is often referred to as the proximity effect.

iii)   The time-varying field produced by the rotor permanent magnets which is directly incident on the coil rather than being confined to the stator core. This comprises a proportion of flux which enters the slot via the slot-opening and an additional component of cross-slot leakage flux.

iv)   When bar conductor is subdivided into thinner strips and connected in parallel, there will be circulating currents flowing among the parallel strips due to the impedance mismatch of each strip. This type of eddy current loss is often referred to as circulating current loss.

The aggregate induced eddy currents can cause significant current re-distribution within individual conductors and a consequent marked increase in loss. The eddy current losses are a function of the dimensions of the conductor cross-section, the electrical frequency and the immediate surrounding environment of the conductor in terms of nearby conductors and core regions. All these features will be evaluated in the following sections.

3.1.1 Skin effect

Skin effect is a widely used term to describe the process by which time varying currents flowing in a conductor will increasingly tend to concentrate near the surface and hence flow within a 'skin' as the frequency is increased. This redistribution of current towards the outer regions of a conductor results in an increase in effective resistance which leads to the concept of AC resistance and AC loss. A schematic representation of the mechanism by which induced eddy currents are induced by an externally driven source current is shown in Figure 3.2. This shows a length of circular conductor which has for illustration purposes been sectioned to show the lower half only.
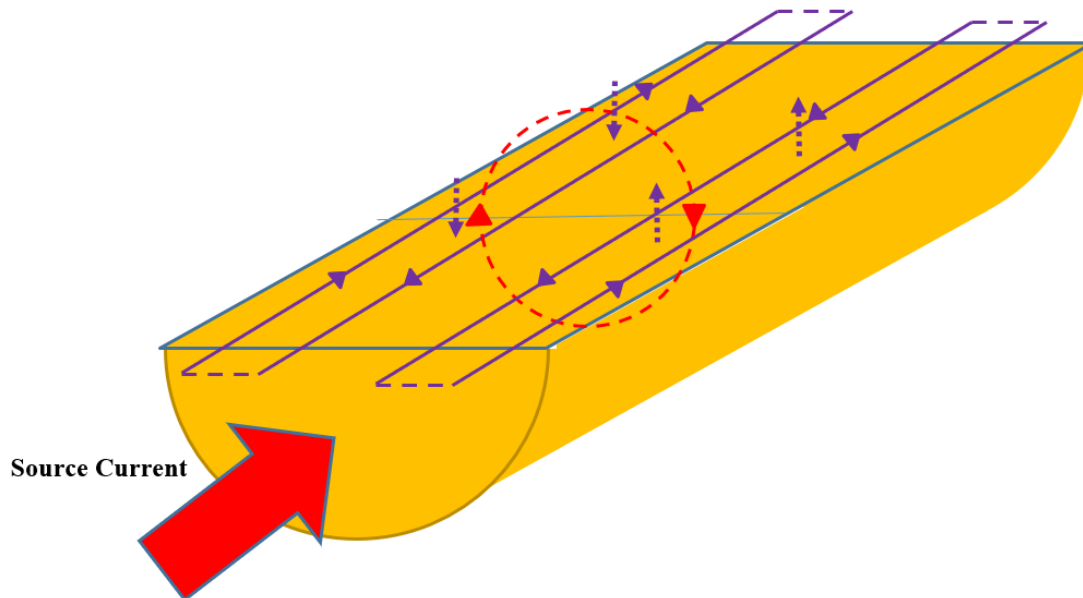
Figure 3.2 Induced eddy current loops and resulting field produced by a time-varying current carrying in a conductor

The large red arrow in Figure 3.2 represents the external AC source current into the conductor. Applying the right-hand corkscrew rule to this source current results in a circumferential magnetic field inside the conductor shown schematically by the red dashed circle. The reaction field produced by the induced eddy currents (highlighted by the dashed purple arrow) will according to Lenz's law be oriented in the opposite direction to the source current field. Lenz's law can be used to establish the eddy current loop directions which produce these reaction fields and are shown as solid purple lines.

As can be seen from Figure 3.2, the two loops of induced eddy current flow in the same direction as the source current at the outer edge of conductor and in the opposite direction to source current in the middle of the conductor. Hence, the net current appears to flow in a skin around the edge, hence the term skin effect. When viewed from the terminals of the coil, the net current is the applied source current since the induced eddy currents sum to zero as they flow in closed loops within the coil. Since ohmic losses are proportional to the square of current density, then confining a given total current to some fraction of the cross-section will increase the overall loss for a given total current. There are well-established equations for calculating various aspects of skin effect, e.g., effective or AC resistance, skin depth and modified ohmic loss both in frequency domain and time domain [62]. One analytical equation for calculating average eddy current loss density in a circular wire in frequency domain from [62] is:

$$P_{skin} = k_s (J_{mz} f)^2 \qquad (3.3)$$

Note that for this equation, the eddy current reaction field is neglected. In addition, this equation is based on the assumption that the current waveforms are purely sinusoidal and thus J_{mz} represents amplitude of exciting current density. The key term in equation (3.3), k_s, is the skin effect eddy current loss coefficient and for circular wire is given by:

$$k_s = \frac{a^4 (\pi \mu_0)^2 \sigma}{96} \qquad (3.4)$$

A comparable expression for a loss coefficient for rectangular conductors has been derived in [62]:

$$k_s = \frac{a^4 (\pi \mu_0)^2 \sigma}{96} \left(\frac{4}{\pi} + \frac{64(k_b - 1)}{15} \right) \frac{1}{k_b} \qquad (3.5)$$

The term k_b is the wire width to wire thickness ratio and when $k_b = 1$, the loss coefficient is equivalent to the format of square wire and when k_b approaches to infinity, equation (3.5) becomes equivalent to (3.4) for circular wires. Equation (3.5) demonstrates that the skin effect is proportional to a^4 and f^2, which means that avoiding significant skin effect requires the use of fine wire, particularly at higher frequencies.

Another concept that is widely adopted for skin effect related issues is that of skin depth. The skin depth provides an approximation for the thickness of current concentration region. The skin depth is proportional to frequency, material resistivity and permeability:

$$\delta = \sqrt{\frac{\rho}{\pi \mu_0 \mu_r f}} \qquad (3.6)$$

Copper has a skin depth of 3.8mm at 300Hz which is the fundamental electrical frequency of the reference machine design. A useful but very simplistic rule-of-thumb is that the skin depth at the operating frequency of the conductor should be greater than half the main dimension of the conductor if serious eddy current problems are to be avoided. According to this very simple guidance, the single piece bar conductor is only slightly beyond this limit in terms of the conductor width and hence eddy currents are likely to be an issue.

In order to both calculate AC losses produced by skin effect and illustrate the nature of current distributions within conductor at different frequencies, a simplified single conductor finite element model was built in FLUX2D. The conductor is supplied with steady state sinusoidal

AC current and hence a complex steady-state formulation can be used in which the time variation is treated as a complex exponential term. This allows a single calculation to be performed for each frequency without the need for time-stepped solutions and their associated transients. The conductor is assumed to be magnetically remote from any other conductors and hence it can be located as an isolated conductor in space with a tangential flux boundary (i.e., vector potential = 0 on boundary). The boundary was located 80mm away from the conductor as shown in Figure 3.3.
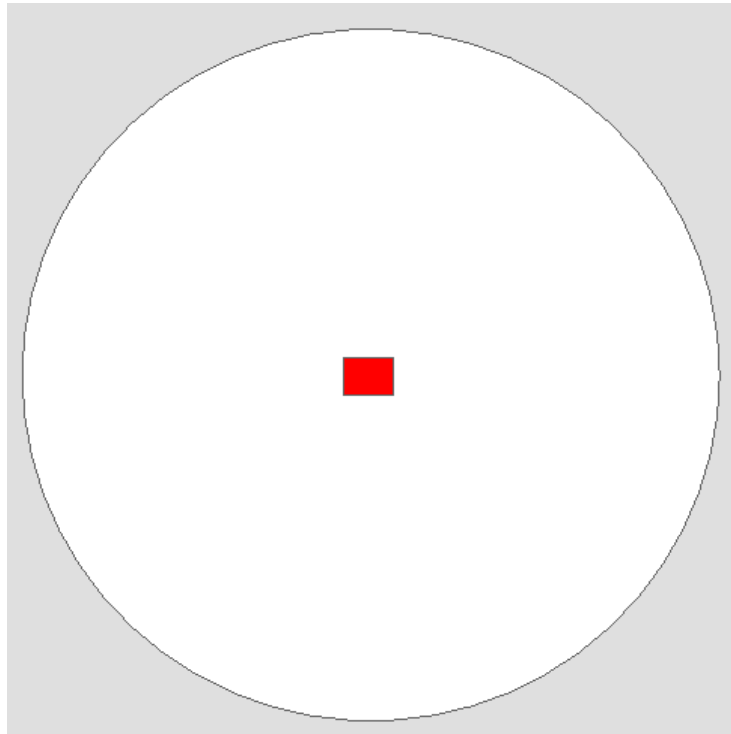
Figure 3.3 Single conductor model in 2D steady state context for illustration of skin effect

The isolated bar conductor considered in this series of simulation has a dimension of 8.94mm x 6.55mm which is same as one series turn conductor in the optimised reference machine design established in chapter 2. The model depth was set to 1m. The model was solved at discrete frequencies between 0.001Hz to 1000Hz with 100Arms (141A peak) injected current. The 0.001Hz solution was used to represent a quasi-static case which is representative of DC conditions. The predicted peak current density distributions in this single isolated conductor are shown in Figure 3.4. These have all been plotted to a consistent colour scale. For the 0.001Hz case, the current density is a uniform 2.4 A/mm^2 (noting that in this complex formulation). As will be evident, at 300Hz (which is the fundamental frequency of the reference design at its rated speed) there is some evidence of eddy current redistribution in the corners,

but the bulk of the conductor cross-section is operating more or less at the same current density as the quasi-static case.
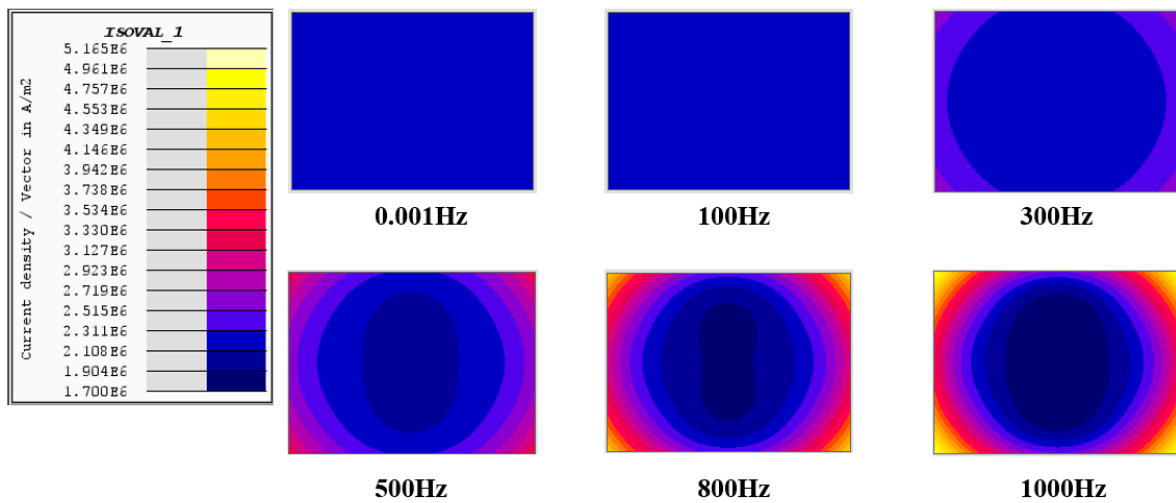
Figure 3.4 Current density plot of isolated rectangular conductor for sweeping frequencies up to 1000Hz

As noted earlier, the increase in loss caused by induced eddy currents leads to the concept of AC resistance which is the effective resistance of the conductor at a particular frequency. The loss predicted by the finite element simulations can be used to calculate the ratio of the AC resistance and DC resistance and they are summarised in Table 3.1. As shown, the increase in effective resistance and hence loss is only 3.7% in this isolated conductor at 300Hz, although it starts to rise rapidly at higher frequencies.

Table 3.1 Increase in effective resistance with frequency for single isolated conductor

Frequency (Hz)	0.001	100	300	500	800	1000
R_{ac}/R_{dc}	1	1.004	1.037	1.097	1.220	1.314

The relatively small increase in effective resistance and hence loss at 300Hz in this single isolated conductor might suggest that the use of a solid 8.94mm × 6.55mm conductor at 300Hz in the baseline machine might only results in a small change in performance. However, it was shown previously in section 2.3.1 of chapter 2 that a 6-pole machine equipped with same dimensions of conductors exhibited AC losses that was many multiples of the quasi-static loss. It will be shown in the following sections, that this isolated single conductor case results in a very significant underestimate of the eddy currents effects at machine level. Indeed, these results demonstrate the dangers of relying on simple guidance around skin depth and conductor

cross-section for judging whether AC losses are likely to be a major problem in a practical machine context.

3.1.2 Proximity effect

Proximity loss is the term used to describe the additional frequency dependant copper loss generated in a conductor when it is part of a closely coupled array of conductors. The currents which flow in adjacent conductors produce a contribution to the localised time-varying field in the conductor of interest. The analysis of a single conductor model described in section 3.1.1 can be extended to include a further three conductors in a 1×4 array, initially again surrounded entirely by air. These four conductors are connected in series and hence carry the same net sinusoidal current of 100Arms. The resulting predicted current density plots over different operating frequencies for a steady-state complex sinusoidal excitation are shown in Figure 3.5. The resulting AC resistance are summarised in Table 3.2. As will be apparent, the presence of additional conductors increases the AC resistance significantly, particularly in the upper and lower conductors compared to the single isolated conductor, e.g., the upper and lower conductors have an AC resistance of 135% of the quasi-static resistance at 300Hz compared to ~104% for a single isolated conductor at the same frequency.
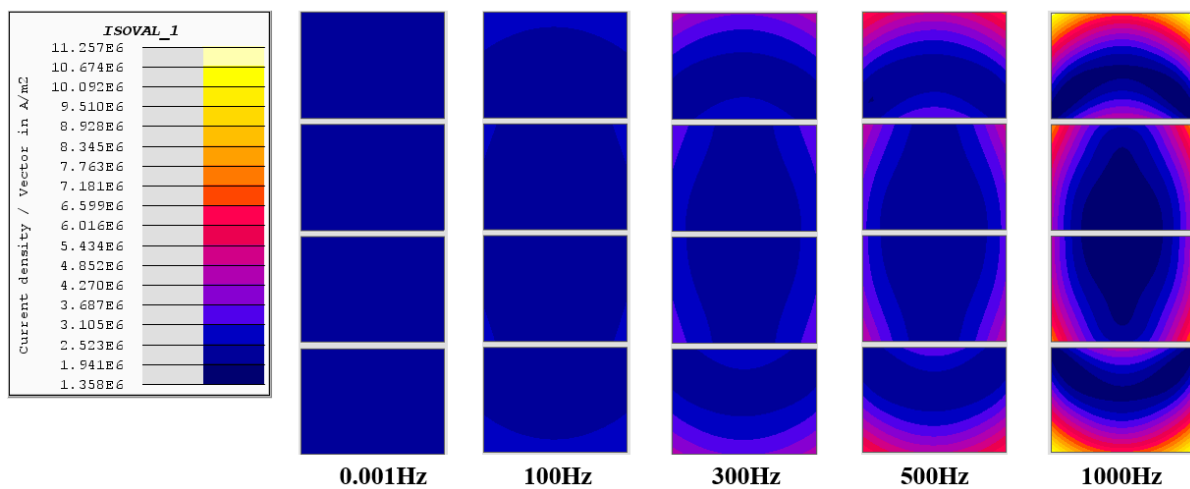
Figure 3.5 Eddy current distribution in 1x4 array of bar conductors in air --- each conductor has a size of 8.94mm x 6.55mm

Table 3.2 Increase in effective resistance with frequency due to proximity effect of adjacent conductors

Frequency (Hz)	0.001	100	300	500	1000
R_{ac}/R_{dc} in lower and upper conductors	1	1.04	1.35	1.82	3.01

R_{ac}/R_{dc} in central pair of conductors	1	1.01	1.11	1.26	1.69

3.1.3 Cross-slot leakage flux

Cross-slot leakage is the term given to the flux that passes across the slot and impinges on the conductors within the slot. The most significant contributor to this leakage field is the flux produced by the conductors in the slot itself. The preceding two sections have demonstrated the increase in eddy current losses which occur between a single isolated conductor and an array of 4 conductors in air due to proximity effect. This increase becomes even more pronounced when the same array of 4 conductors (8.94mm × 6.55mm) is put into a representative stator slot. The simplified rectilinear finite element model of a slot in Figure 3.6 was simulated in FLUX2D using the same steady-state complex AC representation of a sinusoidal current with a rms magnitude of 100Arms. In this case, the same array of four conductors (numbered 1-4 as shown) was surrounded on three sides by a representation of a linear magnetic core which was assigned a linear fixed relative permeability of 5000. The region above the slot is an open region of space.
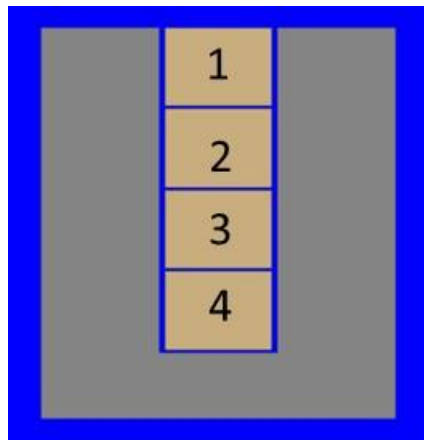
Figure 3.6 Simplified rectilinear model of four series conductors in a slot

The resulting variation in eddy current density at various frequencies up to 1kHz are shown in Figure 3.7, in each case to the common colour scale shown (the maximum of which corresponds to the highest localised current density in the 1kHz case). The corresponding AC resistance variations are summarised in Table 3.3.
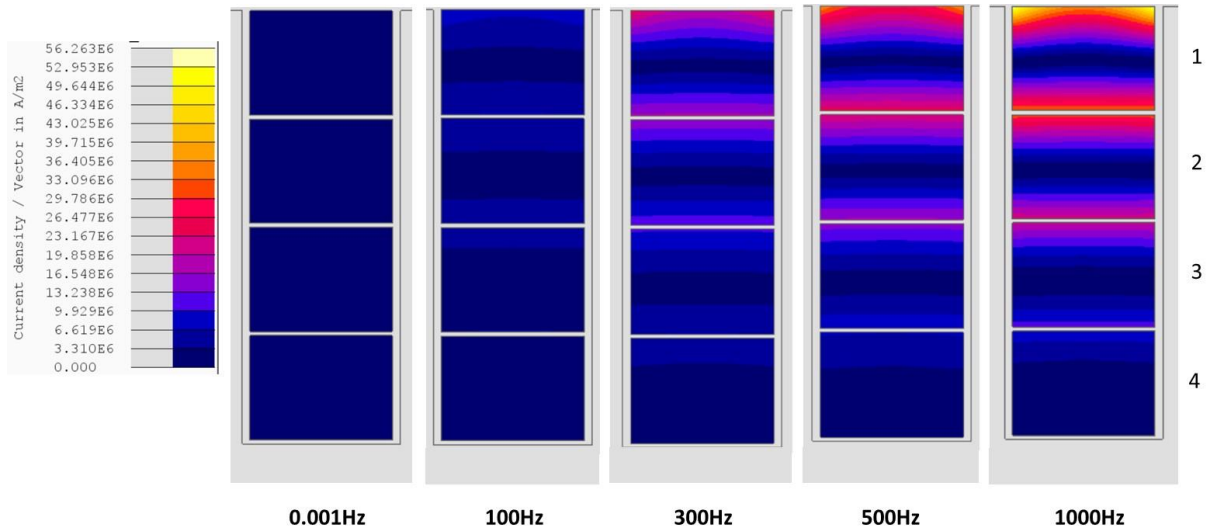
Figure 3.7 The variation of current density for simplified rectilinear model with 4 series connected conductors

Table 3.3 The AC resistance variation of simplified rectilinear model with 4 series connected conductors carrying current of 100A rms

R_{ac}/R_{dc}	Frequency (Hz)				
	0.001	100	300	500	1000
Conductor 1	1.000	3.844	21.80	43.20	77.72
Conductor 2	1.000	2.472	11.76	22.82	40.49
Conductor 2	1.000	1.531	4.889	8.902	15.41
Conductor 4	1.000	1.062	1.460	1.958	2.902

The behaviour observed in Figure 3.7 and Table 3.3, in particular the impact on the conductor nearest the airgap can be understood by considering the fundamentals of cross-slot leakage flux. A useful first order estimate of the variation of flux density in slot due to the conductors in the slot can be obtained by applying Ampere's law to the simplified model of Figure 3.8. This model consists of an infinitely permeability iron core and assumes a simplified one-dimensional field in the slot. Ampere's law states that the integral of the magnetic field strength around a closed path equals the current enclosed by that path.
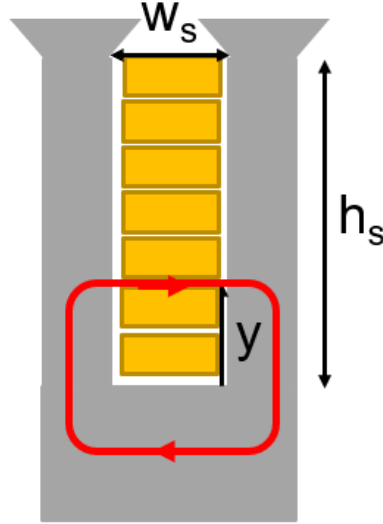
Figure 3.8 A simplified model with infinite permeability of iron core and 1 dimensional field

Applying Ampere's law to simplified model gives:

$$\oint \vec{H} \cdot \vec{dl} = NI \tag{3.7}$$

Assuming permeability of iron core is infinite, and the magnetic flux density is constant around the path, equation (3.7) can be simplified to:

$$H_x(y)w_s = Jyw_s \tag{3.8}$$

Rearranging (3.8) for $H_x(y)$ and multiplying the equation by μ_0 to obtain flux density yields the following expression:

$$B_x(y) = \mu_0 Jy \tag{3.9}$$

This equation clearly illustrates that the flux density will increase linearly from slot bottom to the top of the slot moreover is independent of slot width for a given current density.

3.1.4 Radial flux in the slot

This flux density produced by the rotor magnets is largely oriented in the radial direction in the airgap and hence in the slot area impinges on the conductors in a radial direction as shown in the cartesian approximation in Figure 3.9 where the y-axis is an approximation to the radial direction. The resulting circulating eddy current flows in the direction shown. When a rectangular conductor with width $d_x = 2a$, thickness $= d_y$ and infinite length in axial direction

is subjected to an alternating field in the y-axis (shown in figure), the eddy current loss can be calculated from [62]:
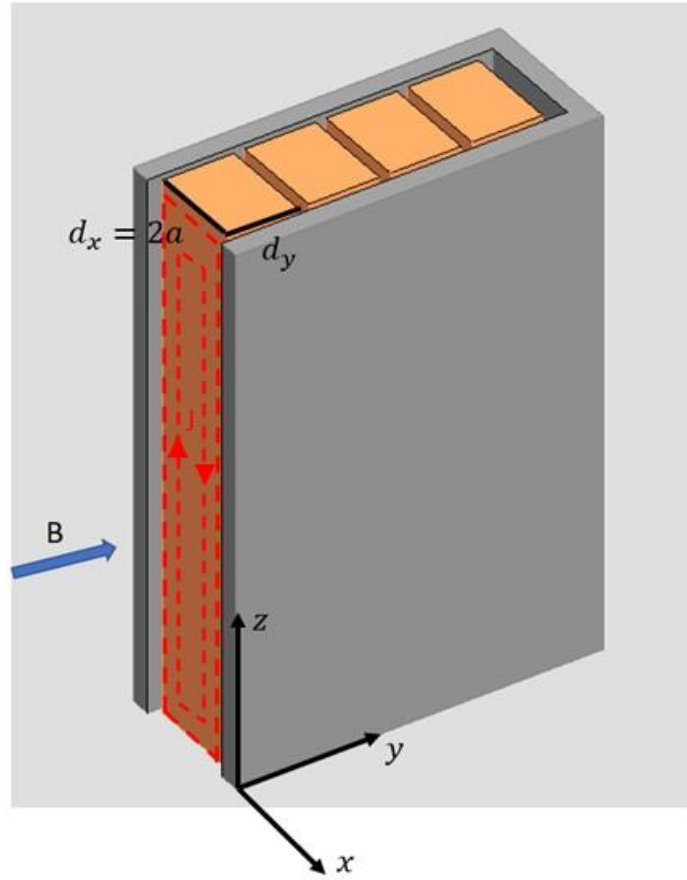
Figure 3.9 A rectangular conductor exposed to a time varying magnetic field normal to axial direction

$$p_c = k_c k_\xi B_{my0}^2 f^2 \tag{3.10}$$

Note that this equation does not take eddy current reaction field into account. Where f is frequency, B_{my0}^2 is flux density amplitude inside the wire when eddy current effects on the field are not considered. While for equation of k_c, it can be determined from:

$$k_c = \frac{(2a\pi)^2 \sigma}{6} \tag{3.11}$$

Where a represents half conductor width and σ is conductivity. The co-efficient $k_{\xi 0}$ can be determined by:

$$k_{\xi 0} = \frac{3}{4\xi^3} \frac{\sinh(2\xi) - \sin(2\xi)}{\cosh(2\xi) + \cos(2\xi)} \tag{3.12}$$

Where ξ is the ratio of rectangular wire thickness over skin depth with a form of:

$$\xi = \frac{a}{\delta}$$ (3.13)

Where δ is skin depth that can be calculated from (3.6). By assuming conductor half width is less than the skin depth, the k_ξ can be assumed to be 1 [62] and thus (3.10) can be further simplified:

$$p_c = \frac{(2a\pi)^2 \sigma}{6} B_{my0}^2 f^2$$ (3.14)

Note that the equation (3.14) can also be used for calculating eddy current losses generated by cross-slot leakage flux by replacing d_x and B_{my0} with d_y and B_{mx0}. As can be seen from (3.14), the proximity loss generated by rotor permanent magnet (or cross-slot leakage flux) is proportional to square of conductor width, the square of magnitude of the flux density in normal direction and square of frequency. As is shown in the Figure 3.9, the eddy current path generated by rotor PM effect is in ZX plane. To reduce this type of eddy current loss, some form of segmentation on Z axis or X axis would be required, but the Z direction corresponds to the direction of normal current flow, which means only segmentation of X axis is feasible.

3.1.5 Modelling of eddy currents in solid bar conductors

The key factor in quantifying AC loss effects and in assessing the benefits of different mitigation strategies is to have confidence in the eddy current simulations. Although finite element methods and commercial packages are well-developed and have been shown to be capable of high levels of accuracy when appropriately applied, it is important to recognise that mesh quality is an important factor in determining accuracy. This is particular the case in eddy current problems since skin effect can result in very rapid spatial changes in field and induced current density. The field gradients over the cross-section of the conductor tend to be larger than in corresponding magneto-static models which means that fine discretisation near the conductor surface is essential.

Localised mesh densities with a finite element model of an electrical machine should have finer meshing in regions of high field gradient. This inevitably results for example in large differences between the mesh discretisation close to the airgap and in the stator core back iron. The research reported in this thesis is focussed on AC winding losses and therefore particular

attention was paid to the meshing of the stator winding region. A good mesh should be able to have the least number of mesh elements to minimise computational efforts but also deliver sufficiently accurate predictions. The balance between number of mesh elements and accuracy of results is important for machine level simulations especially 3D models.

In most regions of the electrical machine, triangular elements provide the best means of representing the mixture of curves and straight lines which define the geometry of the various machine components. However, the nature of eddy currents within a conductor tend to favour elements which can represent the skin and layer type behaviour and hence rectangular element which so-called 'mapped meshing' is recognised as being the preferred approach. In problem domains in which a single surface is exposed to the source of excitation, a graded meshing strategy in which the element size reduces as the surface is approached is often used. Figure 3.10 shows a uniform mesh and a graded mesh, both of which contain several hundreds of rectangular elements. Since the conductors in slots are subjected to fields from all directions and meshes graded in two orthogonal directions are not straightforward to implement, a uniform mesh approach was adopted.

| (a) Uniform meshing | (b) Graded meshing |
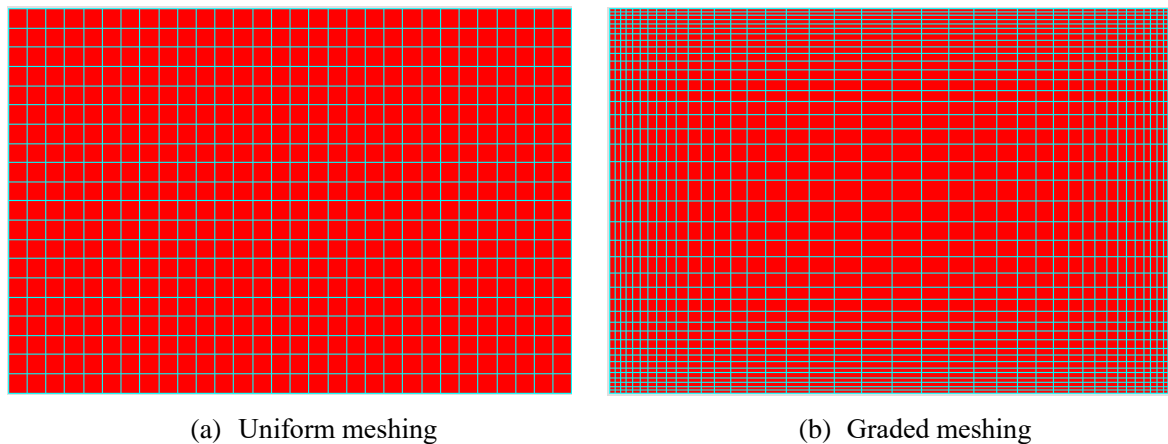
Figure 3.10 Illustration of different meshing strategies for conductor regions

In order to establish the sensitivity of predicted eddy currents to different levels of mesh discretisation, a series of simulations was performed for a single isolated conductor model and 1x4 array of conductors, in both cases with the conductors surrounded by air. The mesh density was systemically varied across a range and the eddy current loss calculated for each case. Figure 3.11 shows one typical mesh, in this case with 30 elements across the width of the conductor and 8 elements across the height of the conductor. In this particular model, the dimensions are those of the conductors in the reference machine design of chapter 2, i.e., 8.94mm × 6.55mm. The FLUX package includes a feature that assesses the quality of the

individual elements. For rectangular elements this is not as significant as triangular elements, but it is still a useful measure to keep an eye on.
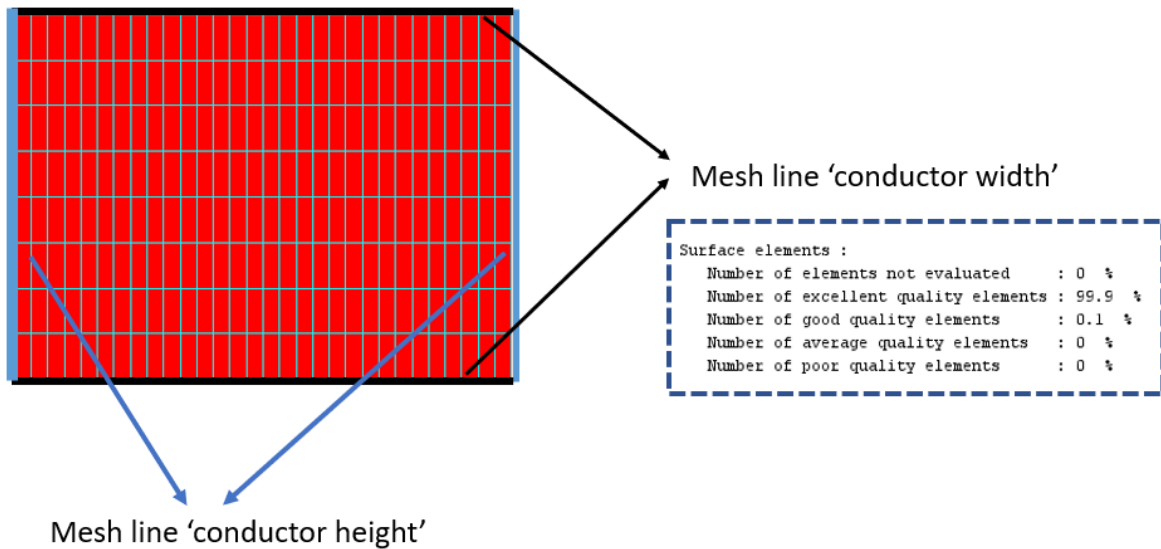
Figure 3.11 Mesh plot of single conductor with 30×8 mapped mesh

To find some equivalent mesh settings that generates fewer number of mesh elements but still gives results that are insensitive at the same time, the numbers of segments along the width and height direction were progressively increased for single conductor model and 1x4 array model. The resulting variation in the predicted loss for various mesh arrangements are shown in Table 3.4. As can be seen from the results, there is no appreciable difference in predicted loss for meshes of 15×9 and above. Although this does not guarantee that a particular mesh density will be adequate in the more complicated circumstances of an electric machine, it nevertheless provides some useful guidance for meshing of electrical machine models.

Table 3.4 Evaluation of mesh quality on losses in 1×1 and 1×4 conductor array at 300Hz with 100Arms injected current

Mesh setting within each conductor (width segments×thickness segments)	Loss in isolated single conductor (W)	Loss in 1×4 conductor array (W)
5×3	3.151	14.934
10×6	3.151	14.932
15×9	3.151	14.931
20×12	3.151	14.931
20×15	3.151	14.931
30×18	3.151	14.931

3.1.6 Sources of AC losses in machines

The time-stepped model of the reference design from chapter 2 was solved for both open-circuit conditions (i.e., zero stator current) and a case with stator currents only but no permanent magnet excitation, in both cases at the rated maximum speed of 6,000rpm. In the first instance, the cross-section of the 8.94mm × 6.55mm series turn was made up of a single bar conductor. The open-circuit simulation provides a means of isolating the effect of the incident field in the conductors which comes from the permanent magnet excitation. For the case of excitation with full rated current only (in which the magnets were set the have a relative permeability of 1.0 and no magnetisation) this provides an indication of the contribution to the overall winding loss from the stator winding. The predicted AC winding losses (note that for open circuit condition, all the losses are generated by rotor PM flux) for open circuit, armature excitation only and a conventional on load simulation are shown in Table 3.5. For comparison, the quasi-static conductor loss at the rated torque operating point is only 2214W.

Table 3.5 Finite element predicted winding loss for the reference design for open circuit, armature only and on load conditions with 120 sampling points over 1 electrical cycle

	Open circuit AC loss	Armature only AC loss	On load AC loss (W)
Baseline model AC loss	1,429W	17,735 W	21,016 W

This series of simulations were carried using Flux-2D with same mesh settings for each solving and with 120 time-steps spanning one electrical cycle. As can be seen from the Table 3.5, the sum of open circuit AC loss and armature only AC loss is less than the on-load case. The open circuit contribution from the permanent magnet excitation, only accounts for less than 10% of total losses. This suggest that the majority of the permanent magnet flux, at least under open-circuit conditions, passes through the stator core with relatively little fringing flux entering into the stator slot region. This is supported by the flux plots shown in Figure 3.12 for open-circuit conditions. The equivalent vector potential plot for armature only condition is provided in Figure 3.13.
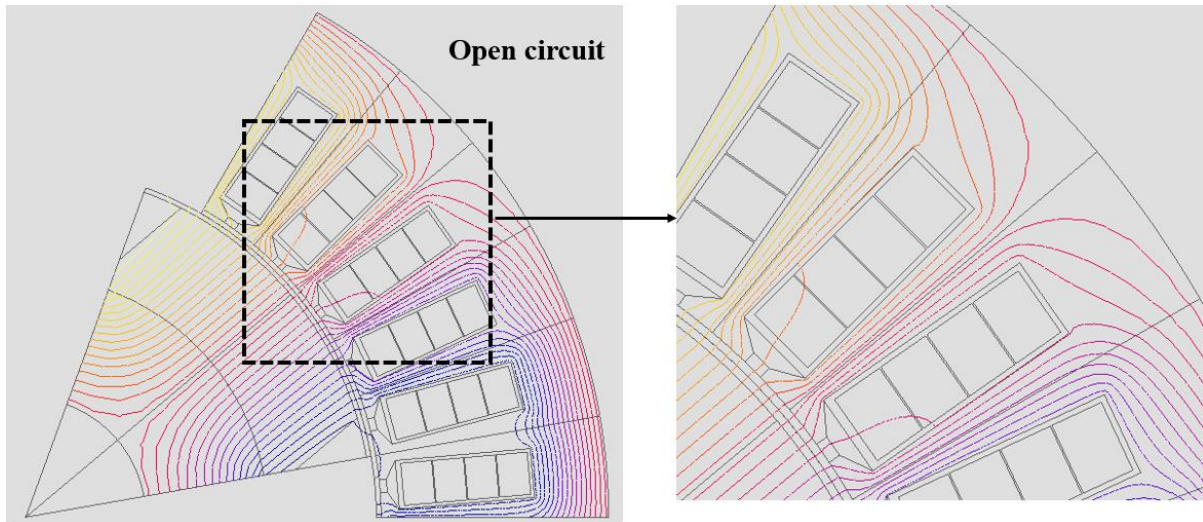
Figure 3.12 Flux lines plot (vector potential plot in 2D context) of baseline model at open circuit condition
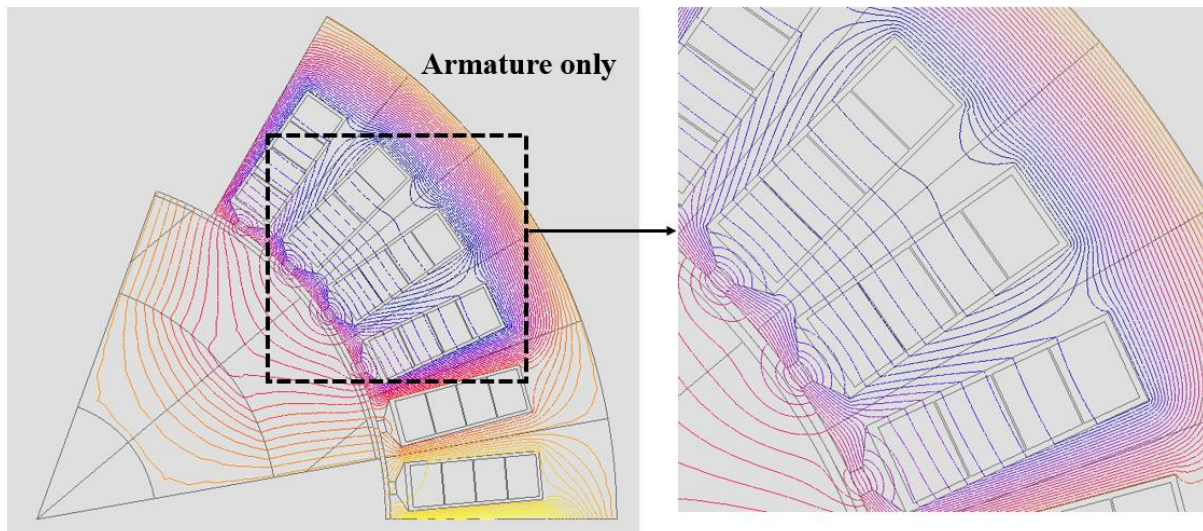
Figure 3.13 Flux lines plot (vector potential plot in 2D context) of baseline model at armature only condition

As can be seen from Figure 3.13, the number of cross-slot leakage flux lines that link conductors is much higher, which in turn generates high level of AC losses in the windings as shown previously in Table 3.5. The flux plot for the corresponding normal rated load condition (which include permanent magnet excitation and rated currents) is shown in Figure 3.14. It is important to recognise that each flux plot is scaled into 20 increments relative to the maximum value of vector potential in the problem domain and hence the magnitudes of fluxes across the three simulations cannot be directly compared.
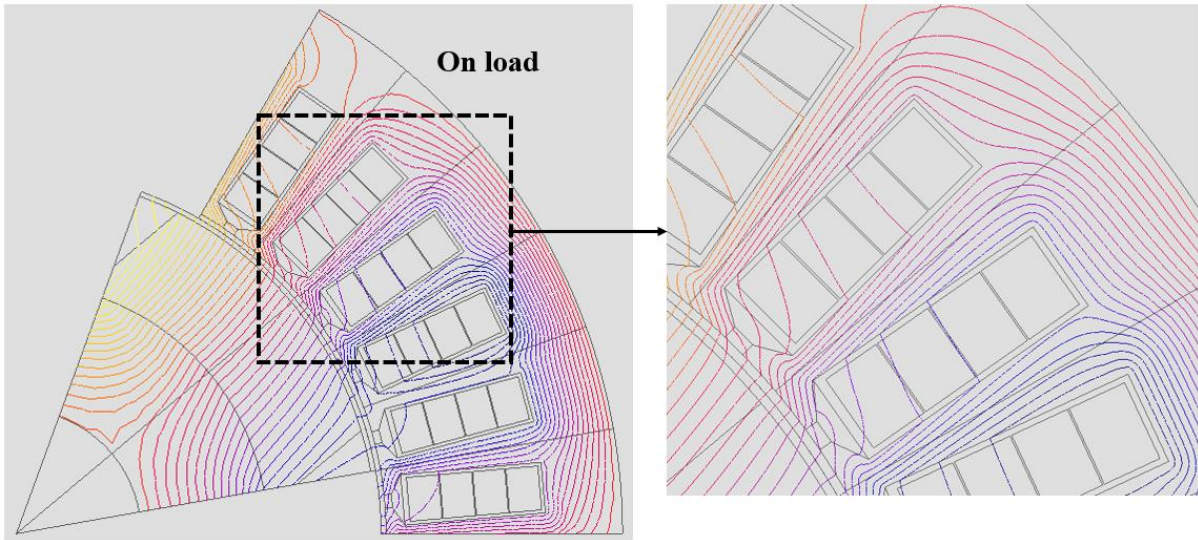
Figure 3.14 Flux lines plot (vector potential plot in 2D context) of baseline model on load condition

It can be concluded from this series of calculated losses and flux plots that most of the conductor AC losses are generated by cross-slot leakage flux while a much smaller contribution is from the PM flux. To investigate the field distributions and their impact on the loss, a series of 17 sensor test points were placed in FLUX2D finite element model along a line in the radial direction of slot 1 to capture the variation of magnetic flux density. The detailed locations of sensors are shown in the Figure 3.15, with the numbering convention starting at 1 at the front of the slot.
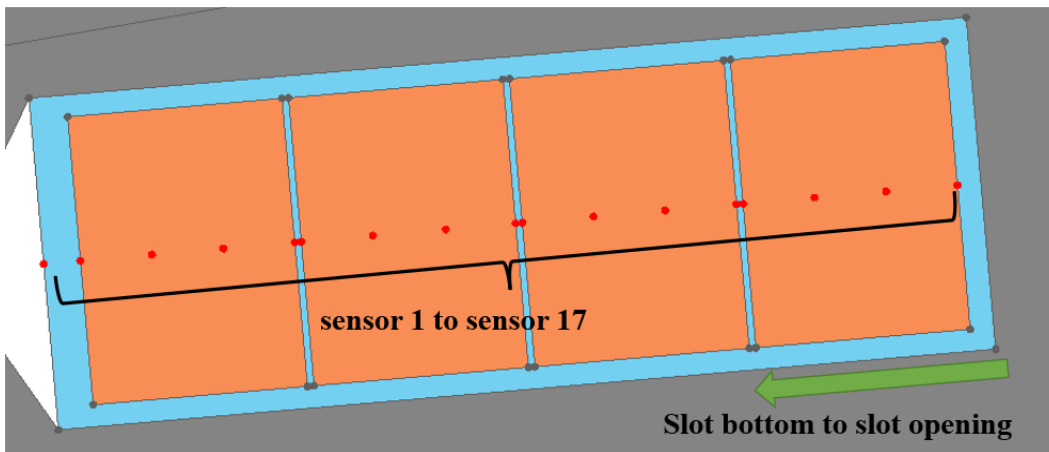
Figure 3.15 Detailed location of sensors in slot 1 for evaluation of flux density variation from slot bottom to slot opening

Figure 3.16 shows the variation over one cycle of the magnitude of the flux density at each of the 17 sensor locations. As would be expected from the earlier analytical model, the flux density variation is much greater at the front of the slot. Since the eddy current loss is proportional to square of rate of change of flux density then this spread in flux densities

demonstrates that not only is the overall excessive with this conductor arrangement, but it is also highly concentrated in the conductors at the front of the slot. In this particular case, the total loss of front-most conductor per slot is 2221W and back-most conductor 128W. It is also worth noting that the open-circuit loss is very concentrated in the front conductor as this is the most exposed to permanent magnet flux entering through the slot opening. From the open-circuit simulation ~96% of the total winding loss is concentrated in the front conductors.
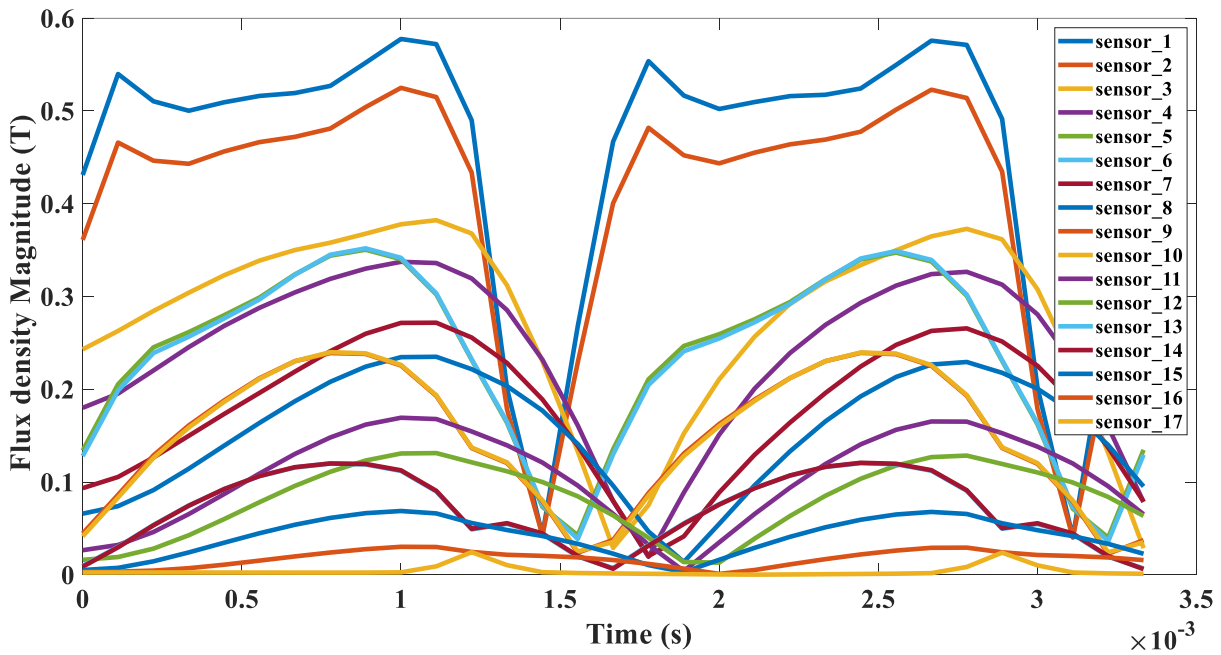
Figure 3.16 Variation in flux density at 17 sensor locations in a stator coil

3.2 Methods to mitigate AC losses

Different types of loss components in bar conductor and the corresponding AC loss mitigation techniques are summarized in the Figure 3.17 below. Note that this diagram only contains the some of the methods for reducing AC losses. For detailed information, they will be introduced in the following sections.

85
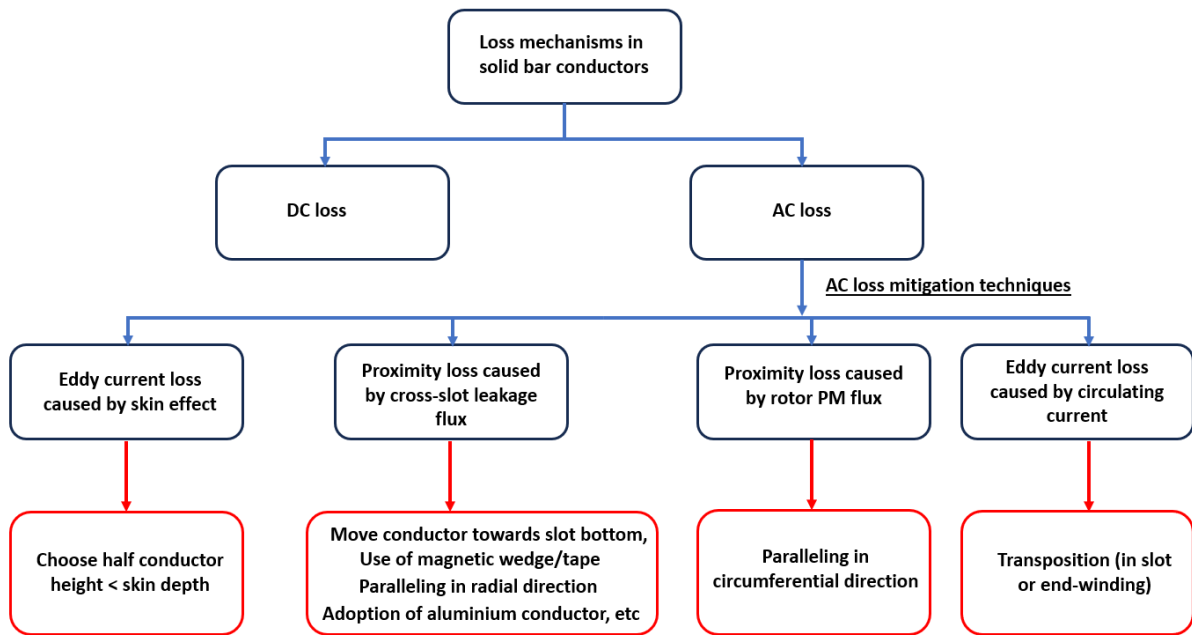
Figure 3.17 The loss mechanisms and corresponding AC loss mitigation techniques

3.2.1 Locating conductors further back in the slot

The concentration of AC loss in the front-most conductor suggests that some benefits could be achieved by moving the front conductor away from slot opening and filling the gap created with non-magnetic supporting materials between main slot wedge at the airgap and the front conductors. This is likely to be effective in terms of reducing the flux from the rotor magnets but not necessarily in terms of the cross-slot leakage flux from the stator winding itself since this is related to width of the total conductor and the total Ampere turns in the slot as shown in equation (3.9). For machines equipped with bar conductor and matched parallel rectangular slot, the slots are tightly packed hence moving the front conductor further away from the airgap requires either a change in the dimensions of the individual conductors or a corresponding increase in the slot depth.

To accommodate such a move, the stator outer diameter needs to be increased so as to allow a deeper slot without compromising the stator back iron [63]. Hence, there will be a significant mass penalty since the mass of the stator core increases with the square of the outer diameter. Despite this penalty, it is still useful to evaluate the impact of distance between slot opening and front-most conductor on the AC losses.

To allow for systematic variation of distance between front conductor and slot the opening, the dimensions D1 defined in Figure 3.18 was introduced. The dimensions D1 was set as a

parameter in the various equations which define the slot geometry in FLUX2D and hence it could be automatically varied to undertake a sensitivity study.
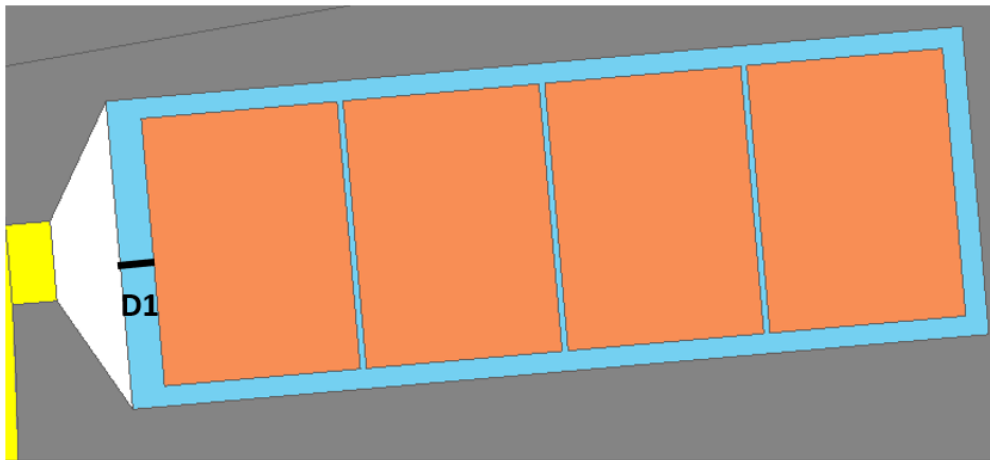
Figure 3.18 Parameter D1 which defines the distance between slot opening and front-most conductors

A series of finite element simulations were performed with D1 varied between 0.2mm to 1.6mm in 0.2mm increments. The individual conductors remained fixed at 8.94mm × 6.55mm and the separating between conductors was kept constant at 0.2mm. All these simulations involved the machine operating at rated torque of 557Nm at 6,000rpm. A summary of the results is shown in the Table 3.6. It is worth noting that since the conductors remain the same size throughout this series of simulations, the quasi-static loss against which the total loss at 6000rpm can be compared remained fixed at 2214W.

Table 3.6 Impact of slot opening clearance --- baseline model

D1 (mm)	Total loss (W)	Loss reduction (W)
0.2	22522	-
0.4	22311	211
0.6	22110	201
0.8	21919	191
1.0	21735	184
1.2	21558	177
1.4	21390	168
1.6	21233	157

As can be seen from Table 3.6, moving conductors away from slot opening has some benefits in terms of reducing the copper losses, e.g. the moving conductors towards the back of the slot

by 1mm reduces the loss by 1000W without the need to change machine geometry. Within the same stator core with the same slot depth, another option is to reduce the radial height of the individual conductors thus reducing the packing factor. Maintaining the same overall slot Ampere turns with smaller conductors will inevitably result in higher quasi-static losses but the savings in AC loss may result in lower overall loss. A series of simulations were performed with the conductor radial height reduced to from 6.55mm to 5mm as shown in Figure 3.19. This reduction in the conductor height frees ~7mm in the slot of the same depth as the baseline reference design. So, a series of studies for evaluation the impact of D1 varying from 0.8mm to 6.4mm with 0.8mm is carried and the results are provided in the Table 3.7 below:
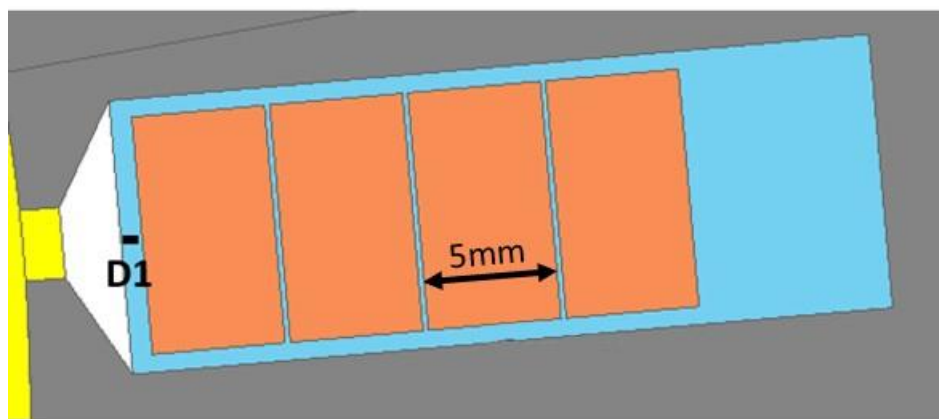
Figure 3.19 Baseline model with reduced conductor height to evaluate the impact of slot opening clearance

Table 3.7 Impact of slot opening clearance --- baseline model with reduced conductor height

D1 (mm)	Quasi-static loss (W)	Total loss (W)	Loss reduction taking 0.8mm clearance as baseline (W)
0.8	2900	15888	N/A
1.6	2900	15160	-728
2.4	2900	14534	-1354
3.2	2900	13990	-1898
4.0	2900	13520	-2368
4.8	2900	13124	-2764
5.6	2900	12790	-3098
6.4	2900	12519	-3369

The impact of slot opening clearance on loss is more significant when the variation range of D1 is increased. By simply increasing D1 from 0.8mm to 6.4mm, the AC loss is reduced by

around 3000W without changing any machine's parameters. This method is regarded as an efficient method to reduce AC losses but is limited to the available space between conductors and slot opening. For the baseline model adopted in this thesis, the rectangular slot is tightly packed with bar conductors and thus there will be little space to change the relative position of each conductor. This means alternative AC loss reduction methods are needed.

3.2.2 Evaluation of the effectiveness of magnetic wedges

Slot wedges are components which close-off the front of the stator slots to restrain the windings within the slot and provide a degree of protection. Most slot wedges are made of non-magnetic material. In smaller machines equipped with random wound mush-coils, the winding is often contained by thin flexible polyester strips that are pushed into the slot and which are sufficiently flexible to adapt to the slot geometry. An example of this type of wedge is shown in Figure 3.20 (a). These are sometimes called slot caps or slot closures and require no features in the stator core to locate and hold the wedge. In larger machines, much stiffer glass fibre wedges of the type shown in Figure 3.20 (b) are used. These are machined to a high tolerance and precisely fit into a corresponding groove in the stator core. These grooves in the stator tooth cause localised saturation and increased iron loss density.
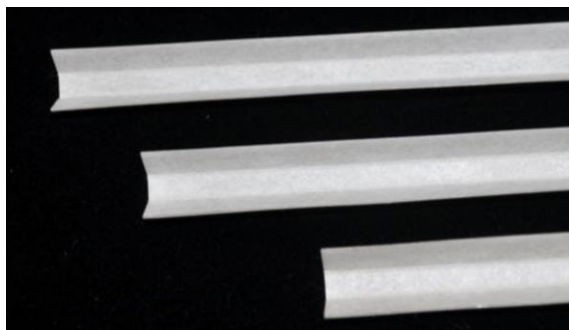
(a) Typical flexible polyester slot wedge   (b) Rigid glass-fibre slot wedge (Source:[64])

Figure 3.20 Examples of different types of slot wedges

In some cases, slot-wedges can be made using magnetic powder in combination with resin and reinforcing fibres. This type of wedge is often referred to as semi-magnetic wedge or a magnetic composite wedge depending on the relative permeability. A wedge with a relative permeability of less than 10 is considered as semi-magnetic wedge while those with a relative permeability higher than 10 are referred to as soft magnetic composite wedge [65]. Conventional magnetic wedges have a composition of 70% iron powder, 10% glass fibre and 20% epoxy resin. Incorporating such a high fraction of iron powder compromises the mechanical strength of wedges [66]. With improvements in material property and

manufacturing process, modern magnetic wedges can be manufactured by rolling and pressing of a special blend of epoxy, glass fibre and iron powder with significant improvements in mechanical strength. One such modern commercial magnetic slot wedges from SPIndustries is shown in Figure 3.21.
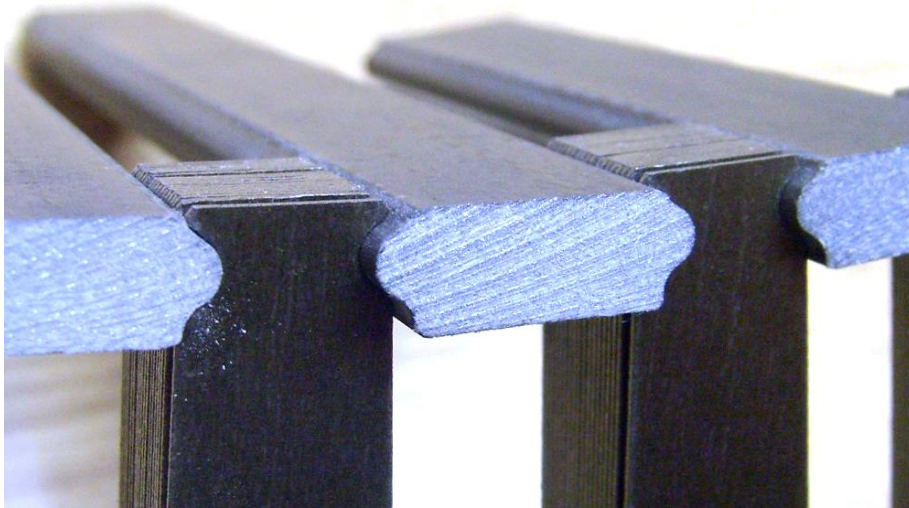
Figure 3.21 Close-up of magnetic wedges manufactured by SPIndustries (source: SPIndustries)

The deployment of magnetic wedge was first seen in induction machines [67][68][69] and have been progressively adopted in other types of machines including permanent magnet machine [65] [70] [71]. With careful design and optimisation of magnetic wedges, the conductor loss can be reduced. Loss reduction due to the adoption of magnetic wedge has only reported in large-scale induction machines [68]. For small and medium sized electrical machines of other topologies, the induced eddy current losses in conductors tends to increase because the flux density near front-most conductor is much higher than the case of non-magnetic wedge. One potential benefit of magnetic wedge is to guide flux generated by the rotor PM away from the slot and towards stator tooth and hence reduced the open circuit loss.

Another interesting feature of magnetic wedge is its ability of reducing pulsations of airgap flux density and thus give smoother output torque. However, one major drawback for machines equipped with magnetic wedge is that the averaged output torque is usually lower than the models with non-magnetic wedge. This is because the use of magnetic wedge introduces a low reluctance path near slot opening region, resulting in more flux passing through wedge region and thus increases slot leakage inductance and reduction on starting torque.

To obtain a comprehensive understanding about the impact of magnetic wedge/ soft magnetic composite on the reference machine design in this thesis, a series of finite element analysis was carried out for three different types of magnetic wedges:

- Linear magnetic wedges with pre-defined permeability less than 10
- Commercial magnetic wedges with non-linear B-H curve and a relative permeability of less than 10
- Soft magnetic composite wedges with non-linear B-H curve

The magnetic material properties of magnetic wedges and their corresponding B-H curves are provided in the Table 3.8 and Figure 3.22 and Figure 3.23.

Table 3.8 Material properties of non-linear magnetic wedge and soft magnetic composite wedge

	Initial permeability	Saturation magnetization (T)
MW1 [67]	6.51	0.98
MW2 [67]	5.24	0.45
LF1 [65]	29.14	1.12
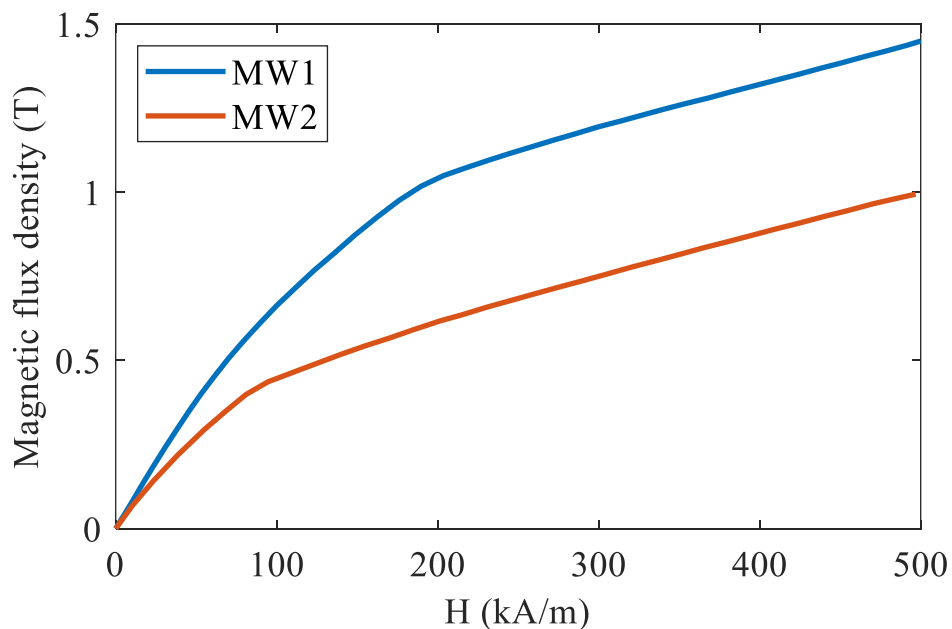
Figure 3.22 B-H curves of semi-magnetic wedge MW1 and MW2
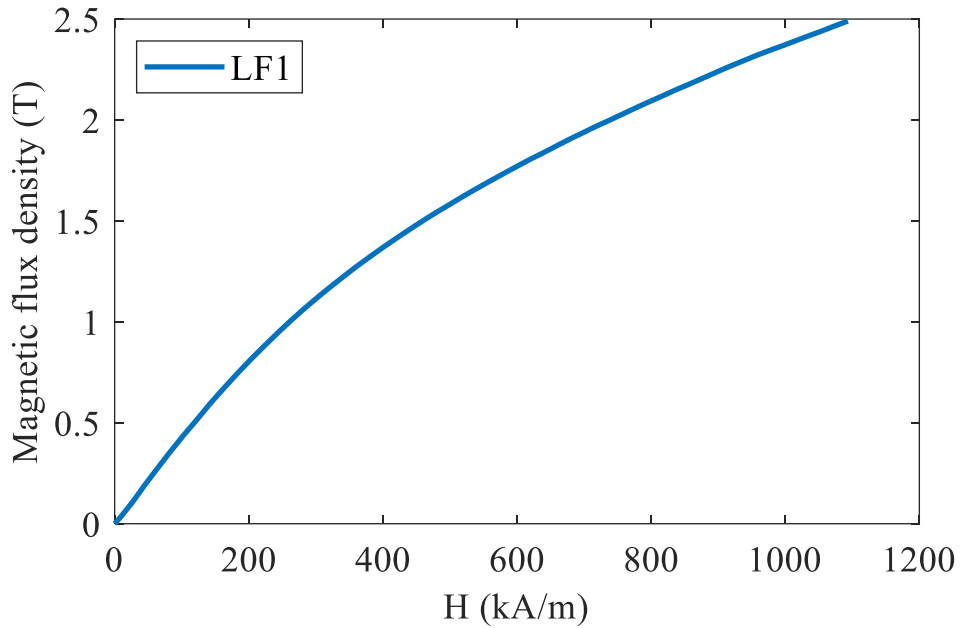
Figure 3.23 B-H curves of soft magnetic wedge LF1

The idealised linear slot wedges were assigned 6 different linear relative permeabilities, specifically u_r = 2,3,5,7,8 and 10. As can be observed from the diagrams, the initial permeability of semi-magnetic wedge materials MW1 and MW2 are less than 10.

Having designed the leading dimensions of baseline models, there is very limited scope to modify the shape of wedge and thus the default wedge shape of baseline model was maintained. Although changing the thickness of the slot wedge have been proven to be beneficial for loss reduction in induction machines [68], this process will not be considered here because the slot is tightly packed with a high packing factor with no space for further increasing wedge height. There are other concepts in terms of using magnetic wedge in electrical machines, such as implementing magnetic wedge with opening in the middle [71] or wedge consisting of different materials [65]. Adopting a wedge with different composition will inevitably introduces extra complexity and potentially higher cost and thus is not considered in the following sections. The wedge shape used in baseline model is trapezoidal due to adoption of semi-closed slot geometry and a zoomed-in view is shown in Figure 3.24.
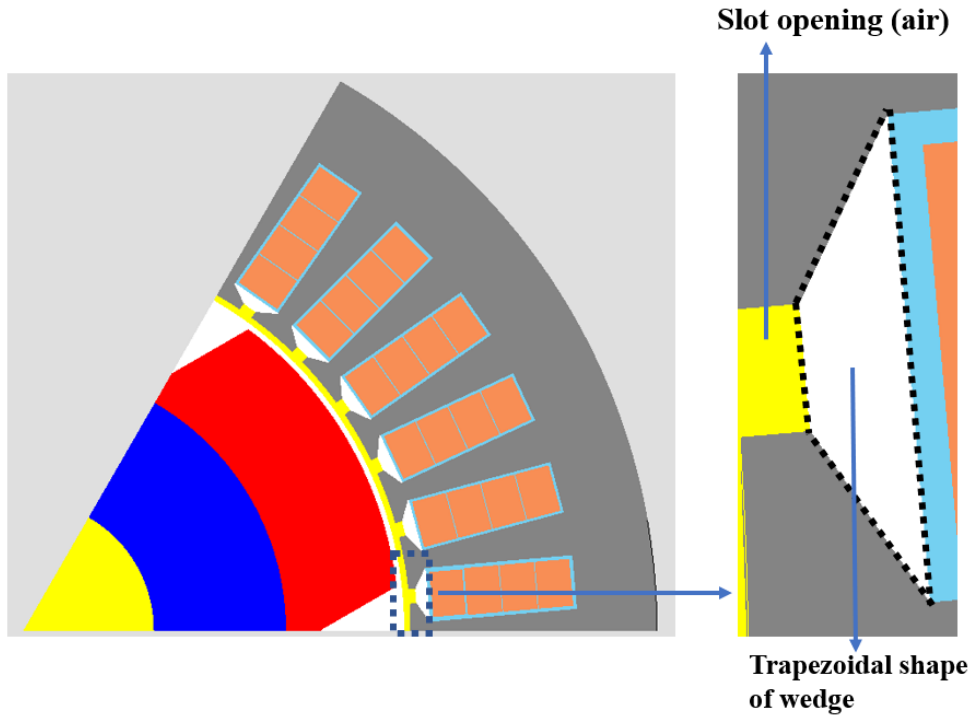
Figure 3.24 Wedge shape of baseline model with zoomed-in view

A series of machine simulations were performed with both the linear and non-linear magnetic wedges. The losses of conductors calculated are shown in the Table 3.9 and Table 3.10 below:

Table 3.9 Loss and torque information for baseline model equipped with linear magnetic wedge

μ_r	Total loss (W)	Torque (Nm)	Induced eddy current loss in magnet (W)
Non-magnetic wedge	22016	550	851
2	22447	540	732
3	22646	532	657
5	22822	519	566
7	22856	509	496
8	22845	505	464
10	22803	497	410

Table 3.10 Loss and torque information for baseline model equipped with non-linear magnetic and SMC wedge

μ_r	Total loss (W)	Torque (Nm)	Magnet loss (W)

Non-magnetic wedge	22016	550	851
MW1	22561	535	708
MW2	22327	543	786
LF1	22556	534	679

As can be seen from the tables above, the incorporation of magnetic wedge tends to increase on-load winding loss. This is because the extra permeability introduced by magnetic materials will create a low reluctance path across slot and thus guide the flux from air gap to wedge and then to stator tooth. The localised flux concentration will cause the flux density near airgap region to increase and thus generate more losses in front-most conductors. As would be expected the designs equipped with a magnetic wedge tend to give a slightly reduced torque.

The incorporation of a magnetic wedge will guide more PM flux into stator tooth and thus reduce the open-circuit conductor loss as evidenced by Table 3.11. On the other hand, the presence of magnetic wedge tends to cause more PM leakage flux and thus cause reduction on amplitude of back-emf and hence the reduction on torque, see Figure 3.25.

Table 3.11 PM flux induced conductor loss at open circuit condition

μ_r	PM flux induced loss in conductors (W)
Baseline model	1265
2	1303
3	1222
5	1057
7	920
8	862
10	763
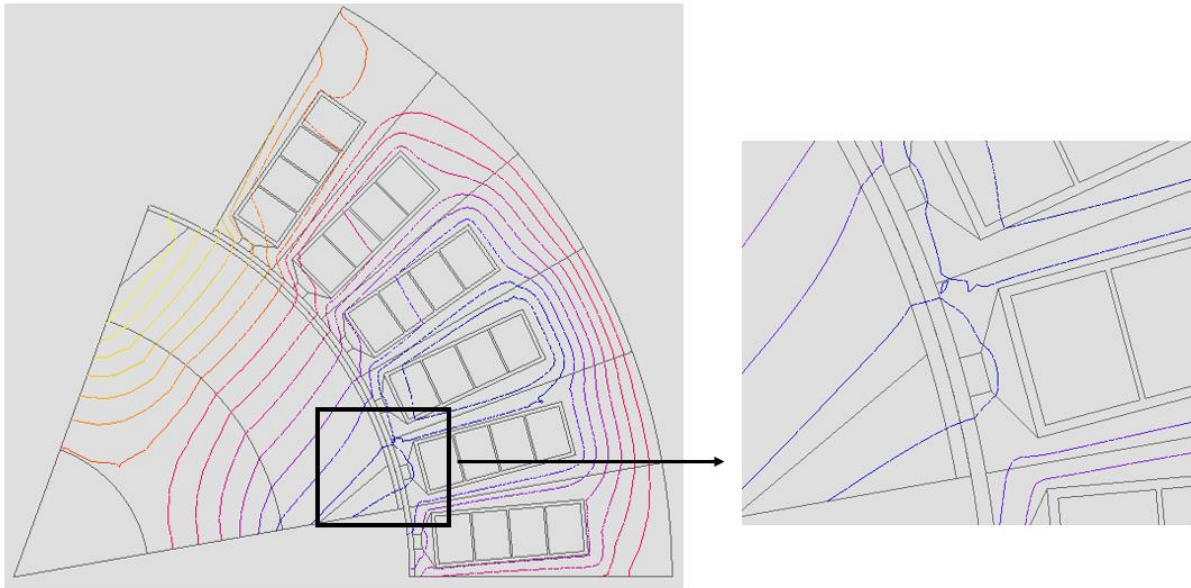
Figure 3.25 PM leakage flux caused by magnetic wedge MW2

As can be observed from Table 3.11, almost all the magnetic wedges have the potentials to reduce PM flux induced eddy current loss. Although the open circuit eddy current loss can be reduced with a magnetic wedge, the increase of eddy current loss in front-most conductor at rated operating point outweighs the decrease on open-circuit eddy current loss and thus lead to overall loss increase. The vector potential plot in Figure 3.25 represent a schematic flux path from which is it evident that the use of magnetic wedge results in increased leakage of PM flux.

To further evaluate the impact of wedge shape on machine's performance, a variant with extra wedge area as shown in Figure 3.26 below:

Original shape   **Modified shape**
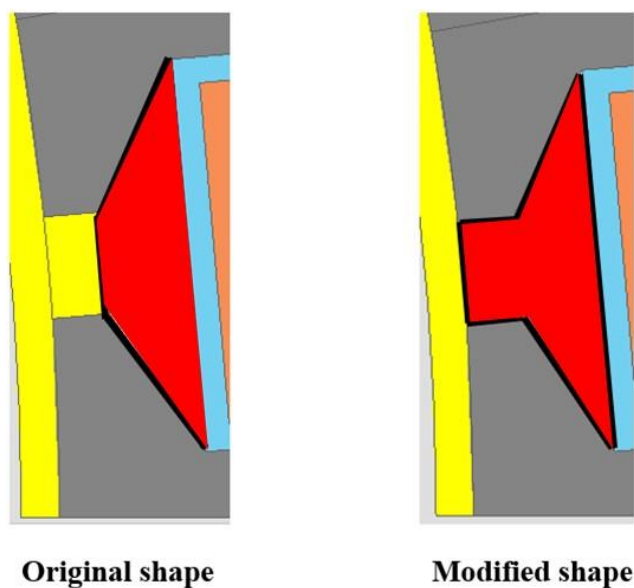
Figure 3.26 Comparison between baseline wedge shape and modified wedge shape (slot wedge regions are red)

95

As can be seen from Figure 3.26, the slot is now fully enclosed by modified wedges. While for the yellow region near wedge, it is one layer airgap region. The fully closed wedge model with linear magnetic wedge was solved at rated on load condition and the result are summarised in Table 3.12.

Table 3.12 Loss and torque comparison for models equipped with original wedge shape and modified wedge shape

μ_r	Total loss (W) --- original	Total loss (W) --- modified	Total loss difference (W)	Torque (Nm) --- original	Torque (Nm) --- modified	Torque difference (Nm)
baseline	22016	22016	0	550	550	0
2	22447	22528	+81	540	536	-4
3	22646	22856	+210	532	522	-10
5	22822	23112	+290	519	508	-11
7	22856	23121	+265	509	497	-12
8	22845	23105	+260	505	493	-12
10	22803	23074	+271	497	486	-11

No benefits are accrued using the modified magnetic wedge shape and indeed the conductor loss is increased, and the average torque is reduced. Based on these findings, the original shape of wedge was used in subsequent analysis.

A set of similar analysis for magnetic wedges was carried out for 2, 3, and 6 parallel path transposed models. Similar behaviour was observed with a slight reduction in torque, slight increase on winding loss and lower torque ripple. Flux density plots of the machine baseline model, with slot wedges have linear permeability of 5,10 and non-linear MW1 are shown in Figure 3.27 to Figure 3.30 respectively.
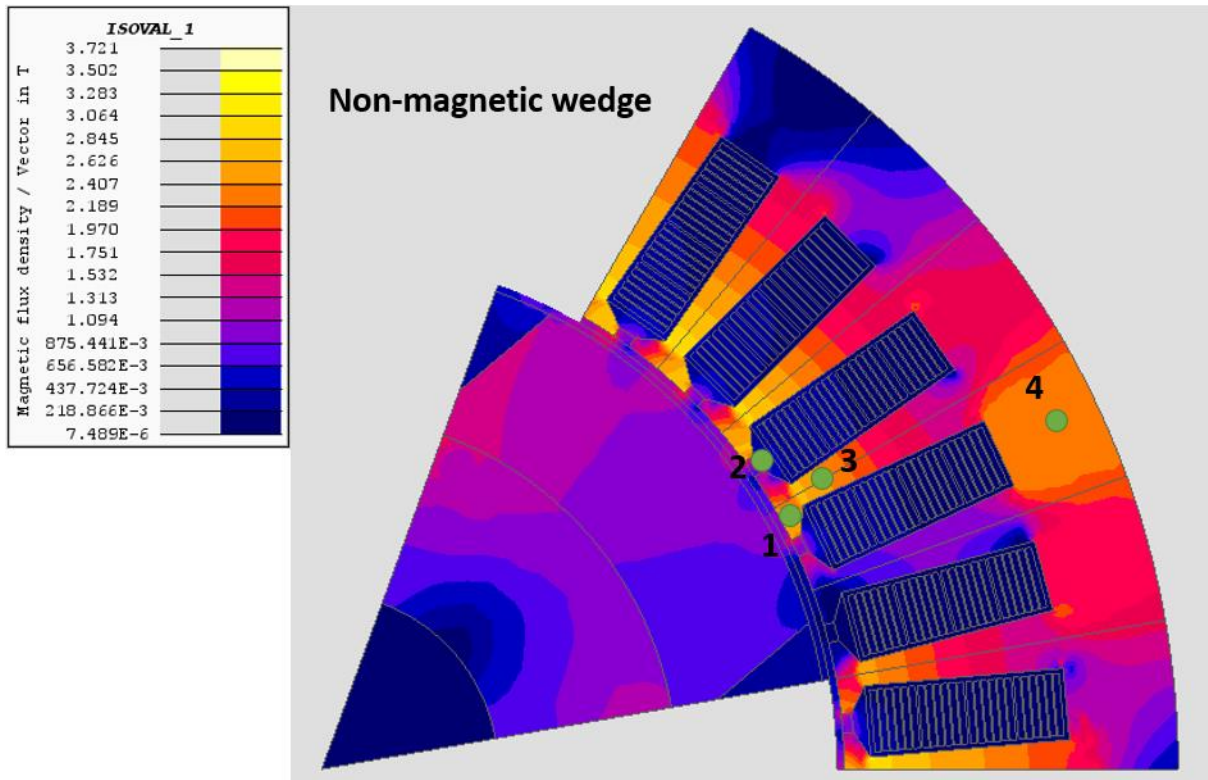
Figure 3.27 Flux density plot of baseline mode with non-magnetic wedge at t = 0.11ms
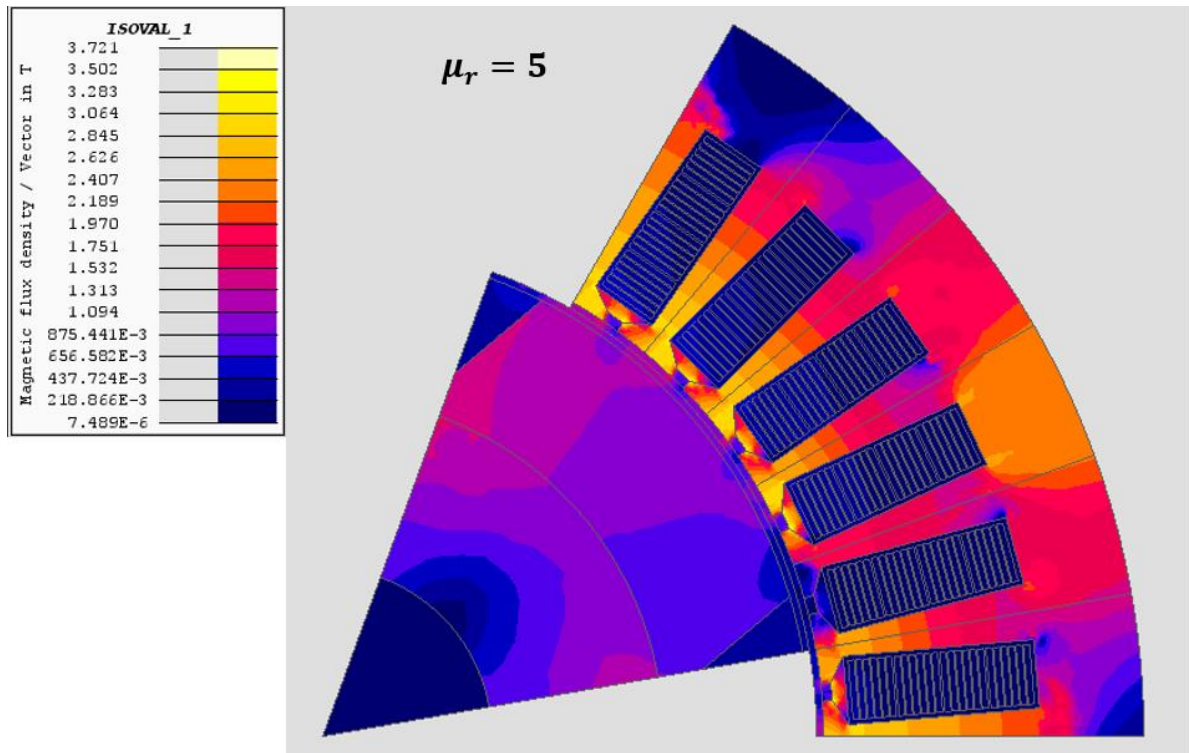
Figure 3.28 Flux density plot of baseline mode with linear magnetic wedge with $\mu_r = 5$ at t = 0.11ms
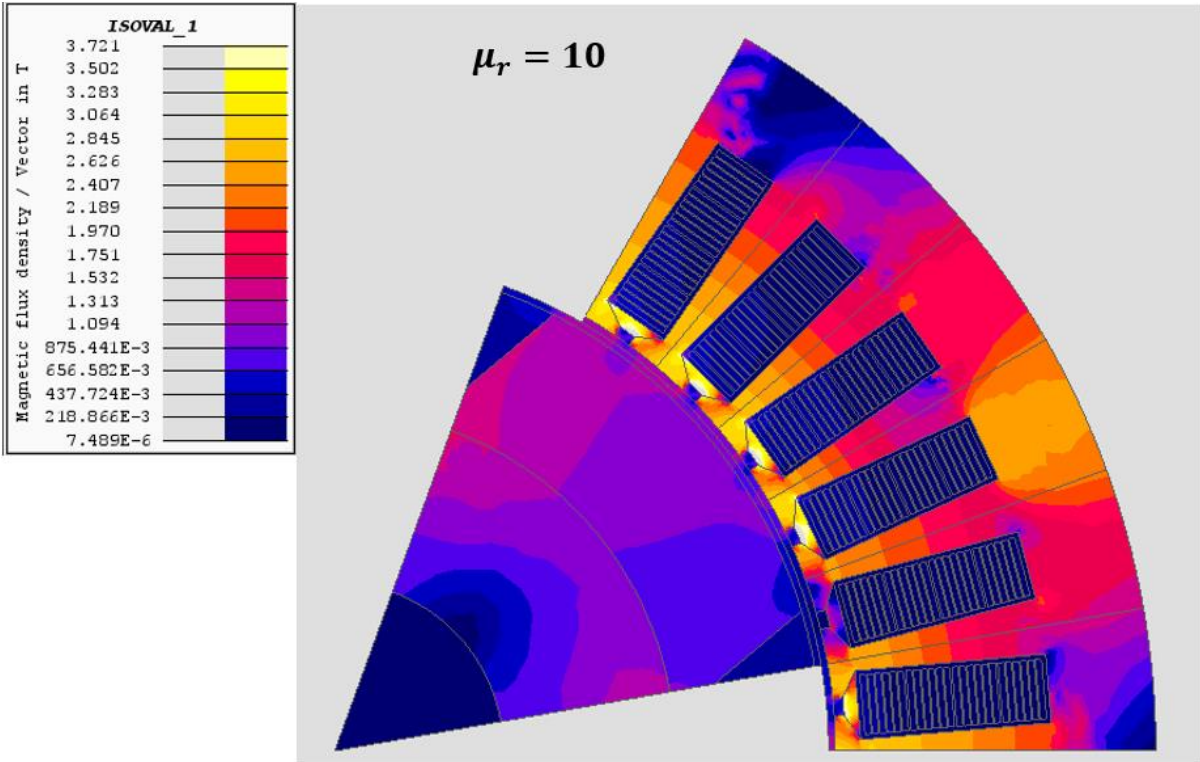
Figure 3.29 Flux density plot of baseline mode with linear magnetic wedge with $\mu_r = 10$ at t = 0.11ms
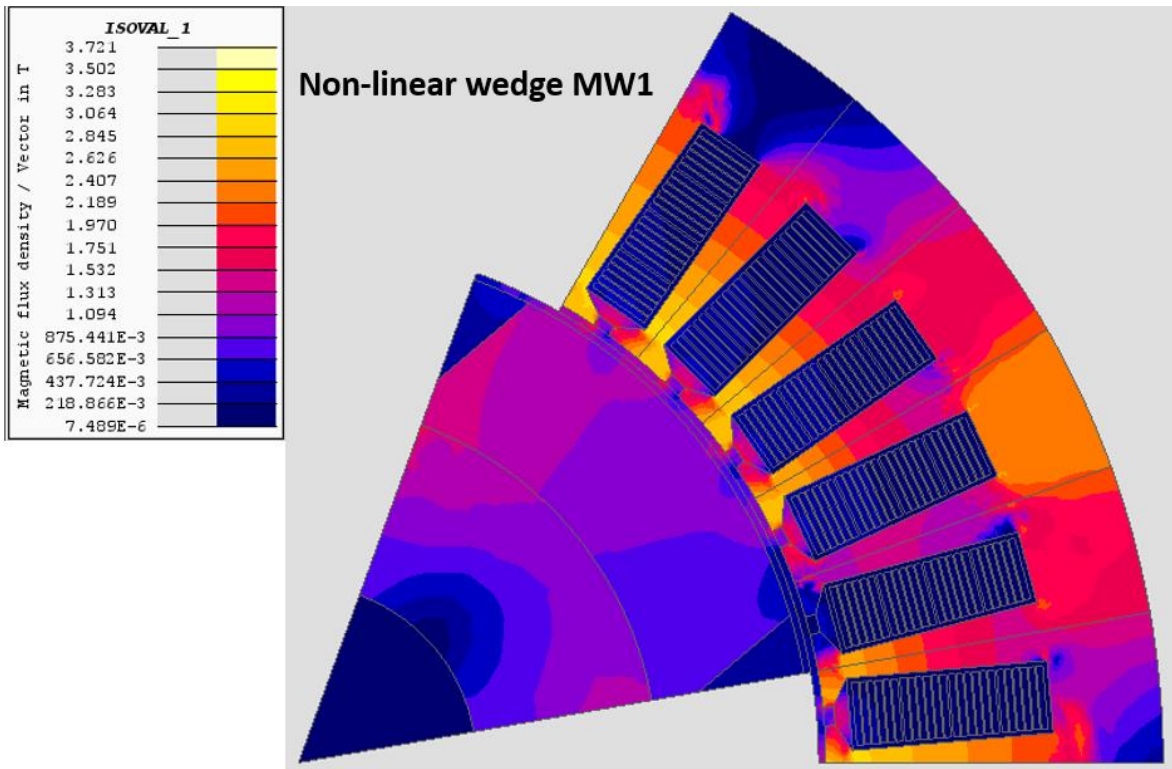
Figure 3.30 Flux density plot of baseline mode with non-linear magnetic wedge MW1 at t = 0.11s

Note that the upper and lower scaling of flux density contours are set to be same for the three different models to provide an equitable and consistent comparison. Four measurement sensor points were incorporated to monitor the magnitude of flux density at the locations as highlighted by green in Figure 3.27. The flux density magnitudes at t = 0.11ms (equivalent to first transient step) are shown Table 3.13.

Table 3.13 FEA calculated flux density magnitude of different positions inside of machine

Flux density (T)	Baseline	$\mu_r = 5$	$\mu_r = 10$	MW1
Point_1	2.52	2.87	2.96	2.7
Point_2	0.70	2.37	3.46	1.44
Point_3	2.46	2.35	2.25	2.43
Point_4	2.26	2.37	2.4	2.32

The highlighted row in Table 3.13 represents the flux density magnitudes in slot wedge region. It is clear that assigning magnetic material to slot wedge will guide more flux through wedge to stator tooth and thus cause flux density to increase. However, the flux density values in Table 3.13 highlight the dangers of assigning linear relative permeabilities to regions even when the relative permeability are low. The flux density values obtained with relative permeability of 5 and 10 are well beyond the saturation flux density of magnetic slot wedges, which highlights the value of using the non-linear characteristics of Figure 3.22 (MW2) for a realistic representation of a slot wedge. Although further refinement of the wedge geometry and material could have been explored, there would have been unlikely to change the main outcomes that torque ripple and no-load conductor AC losses are reduced with magnetic slot wedges, but the on-load AC losses will tend to increase.

3.2.3 Paralleling of thinner strips to make up the turn cross-section

The dominant component of flux density generated by armature currents and hence the main contributor to AC loss in the winding is cross-slot leakage flux. Figure 3.31 shows a schematic of the winding (with the core removed to aid clarity) with the cross-slot leakage component of flux density and the resulting eddy currents (z-direction is the axial direction of the machine).
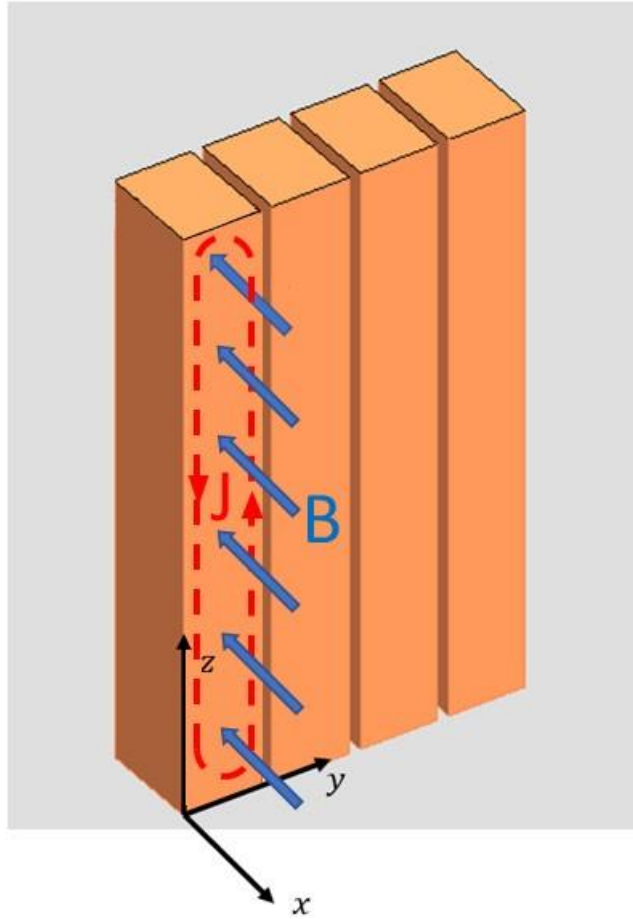
Figure 3.31 Diagram illustrating the effect of cross-slot leakage flux and the induced eddy current path

As can be observed from Figure 3.31 reducing conductor height in radial direction (along y axis in this cartesian representation) would break-up the eddy current path and hence the loss induced by cross-slot leakage flux. This can be done by sub-dividing the original thick bar conductors into several strips and then connect them in parallel as shown schematically in Figure 3.32, in this case for 3 parallel strips.

100
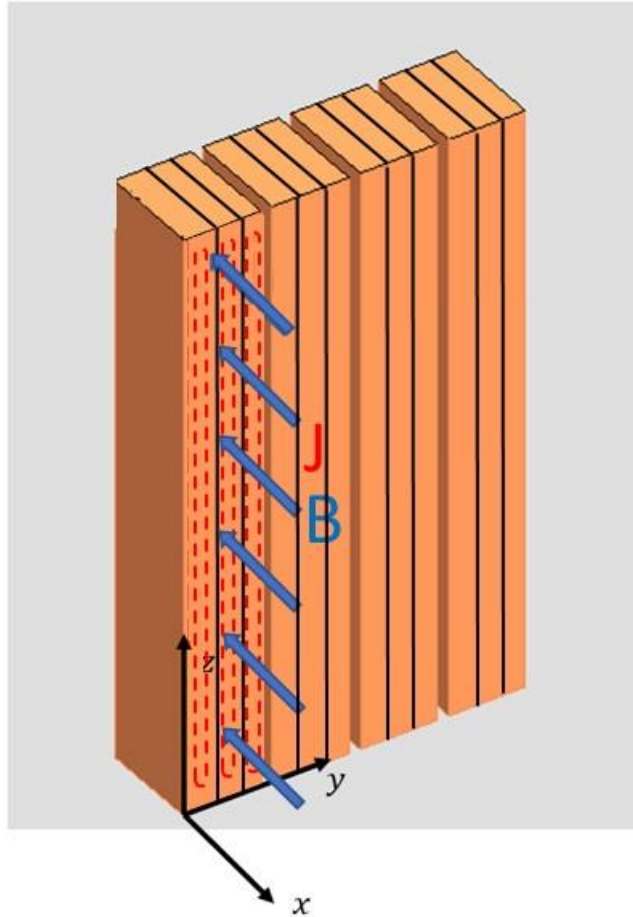
Figure 3.32 Paralleling of original bar conductor into 3 parallel paths to reduce eddy current path

There are two factors which need to be taken into account when paralleling of bar conductors. Firstly, paralleling of conductors will lead to reduction in packing factor due to the presence of extra insulation layer associated with each additional strip. Secondly, as discussed previously in section 3.1.3, the flux-linkage from the stator current tends to increase from the back of the slot towards the airgap. Given the significant difference in slot position between parallel paths of the same nominal series turn there will be impedance mismatches between parallel paths. To ensure that the current is shared equally between the parallel paths and that there are no circulating currents, it is essential to fully transpose the parallel paths in the phase in order to balance the parallel path impedances. Transposition involves interchanging the positions within the slot of each parallel path so that between the points of common connection of the parallel paths, the slot positions are fully evened out. The idea of transposition was first implemented in large scale turbogenerators [72][73] and recently has been adopted in medium power electrical machines [52][74]. Based on the position that transposition is achieved, the transposition strategy can be divided into two categories: the in-slot transposition (also referred to as axial transposition) and end-winding transposition. In the context of in-slot transposition

strategy, there is relatively more freedom on selection of level of transposition including the most traditional 360° transposition [75][76] and less traditional 288° transposition [74]. All the research has confirmed that the proper in-slot transposition is sufficient to reduce AC winding losses with the expense of reduced packing factor and additional complexity in terms of modelling and solving. While for end-winding transposition [73][77], the positions of individual strands are changed at end-winding region and this method is also proved to be effective to reduce AC winding losses. Except for those two well-adopted transposition strategy, a novel transposition strategy which implements both the in-slot transposition and end-winding transposition is proposed in [77] and the existing three transposition techniques are compared.

The baseline model selected is a relatively small machine (compared to turbo generators) with outer diameter around 250mm and 112mm axial length, which manes the axial transposition will be un-suitable and thus the end-winding transposition strategy is adopted. Another benefit of end-winding transposition is that the extra space needed for axial transposition is no longer required, giving the potential of maintaining the original packing factor. This end-winding transposition process can be achieved by systematically changing relative positions of strips in the inter-connects between successive coils. For a given number of stator slots, transposition imposes a constraint on the number of parallel paths into which a series turn can be divided if fully balanced transposition is to be realised. In the case of the 36 slot 6-pole double layer winding, the number of slot pairs per phase is 6 (=36/3/2). Hence, the feasible number of parallel paths is 2,3 or 6 for full transposition.

A series of simulations were performed for windings in which each series turn was sub-divided into 2,3 and 6 parallel paths is achieved at the expense of a reduction in packing factor due to additional enamel layers which must be accommodated. In order to ensure that this important drawback is factored into the finite element models, representative insulation layer thicknesses were factored into the models. The IEC 60317-0-2:2020 standard includes insulation specification for rectangular enamelled copper/aluminium wire. The nominal insulation thickness for Grade 1 and Grade 2 enamelled insulation as set out in section 4.4.1 of this standard is 0.0425mm and 0.072mm respectively [78]. Adopting the nominal insulation thickness for Grade 2 enamel leads to an overall increase in the dimension of conductor of 0.145mm. Conductors which are pressed together in coil forming may also have some residual gap. Adopting an effective separation distance of 0.2mm between adjacent conducting materials provides some allowance for a clearance gap over and above the combined insulation thickness of 0.145mm. Hence, in this study, each additional sub-division of the conductor

cross-section to produce more parallel paths will result in an additional 0.2mm of non-conducting layers, which in turn progressively causes the effective slot-fill factor to diminish.

If successive series turns were also over-wound with an overlapping tape, then a further allowance in the slot-fill would need to be incorporated according to the nominal thickness set out in [79]. It is worth noting that the quantity of this additional taped layer of insulation required is set by the number of turns not the number of parallel strands. In conclusion, the enamel thickness of single strip is defined to be 0.10mm for each surface while for the thickness of polyester glass fibre tape of single turn, it is 0.08mm for each side. As for the other parameters needs to be defined, the slot liner is set at 0.2mm, turn to turn distance is set to be 0.36mm to account for two layers of insulation and one layer of polyester tape, and the distance between front-most turn and slot opening is defined to be 0.5mm. The detailed slot geometry of baseline reference design without paralleling is show in Figure 3.33 while the geometry of 2, 3 and 6 parallel path variants are shown in Figure 3.34.
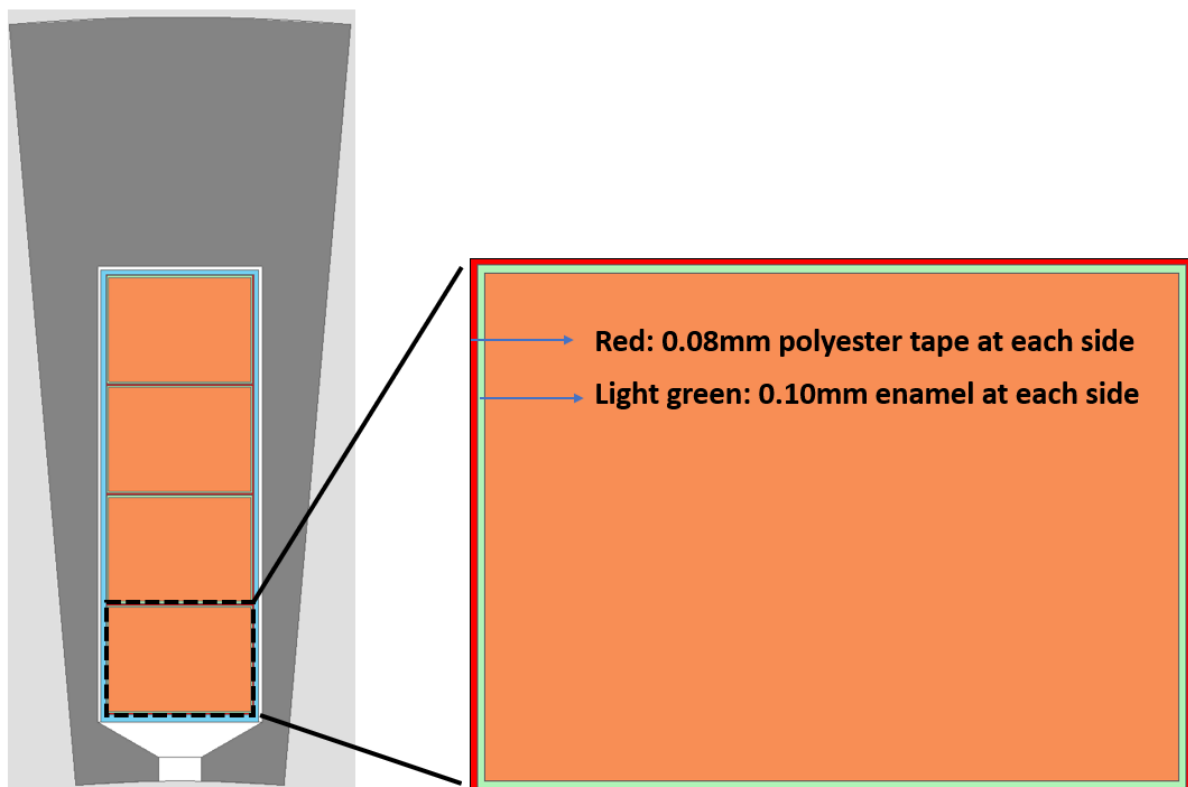
Figure 3.33 Detailed slot view for baseline model accounting for slot liner, enamel insulation and polyester tape
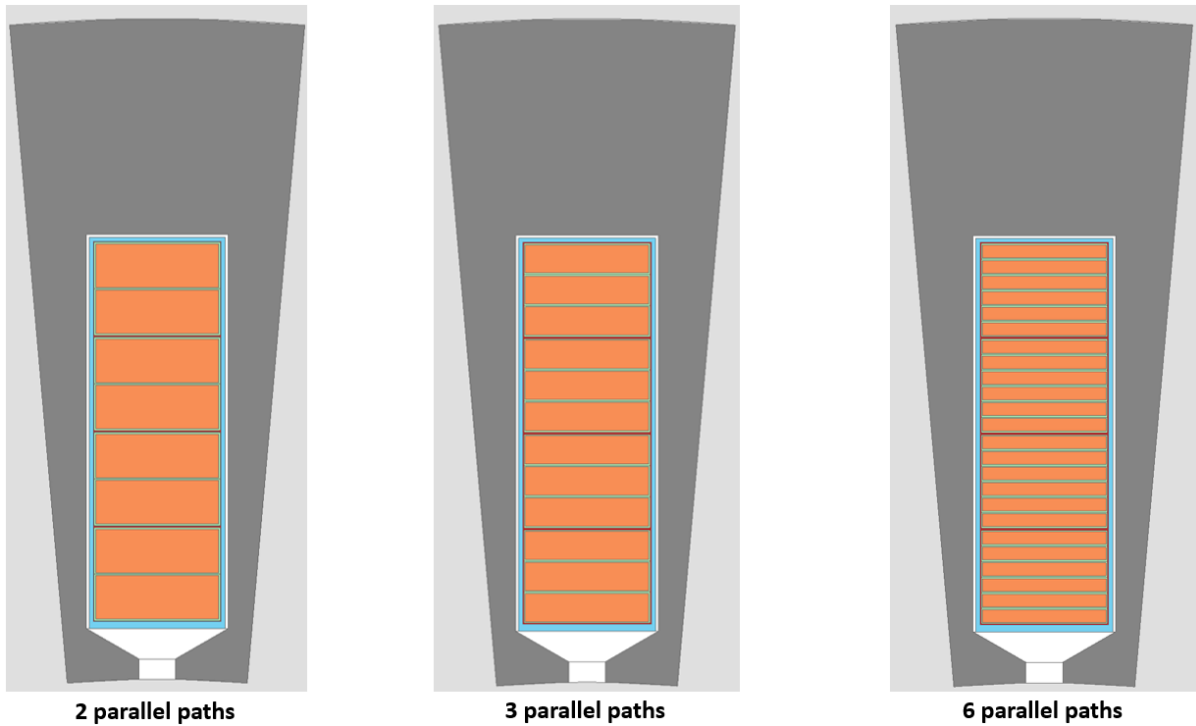
Figure 3.34 Detailed slot view of 2, 3 and 6 parallel path model

It is worth noting that the more rigorous definition of insulation thickness in this section results in a small change in conductor position when applied to the baseline design, which in turn results in a small change in the overall loss for the baseline design compared to earlier simulations in this thesis. These improved definitions of slot insulation were maintained for the remainder of the research reported in this thesis.

In order to represent the paralleling of conductors, the corresponding connections need to be applied to external electrical circuit which is coupled to the finite element model. By way of example, for the case of two parallel paths (designated as A and B) and 4 series turns (designated as 1-4) the machine level geometry view and the associated electrical circuit are shown in Figure 3.35 and Figure 3.36 respectively. This 60° model in which only two slots are represented in the circuit does not include any transposition and hence would not be the preferred practical arrangement. However, it is nevertheless a useful simulation in terms of illustrating the importance of transposition.
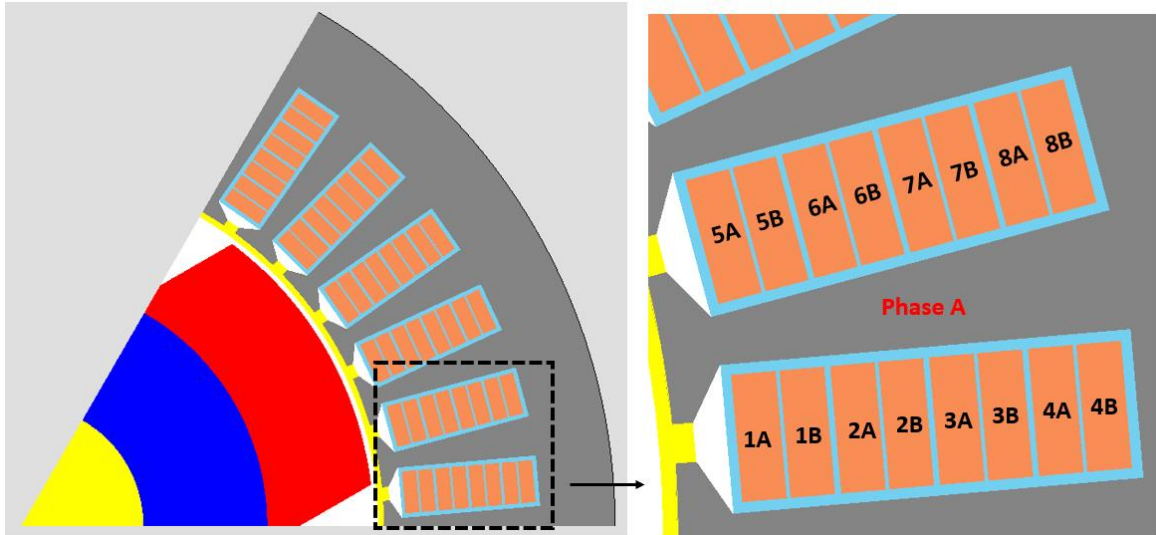
Figure 3.35 Geometrical view of 2 parallel path model with labelling
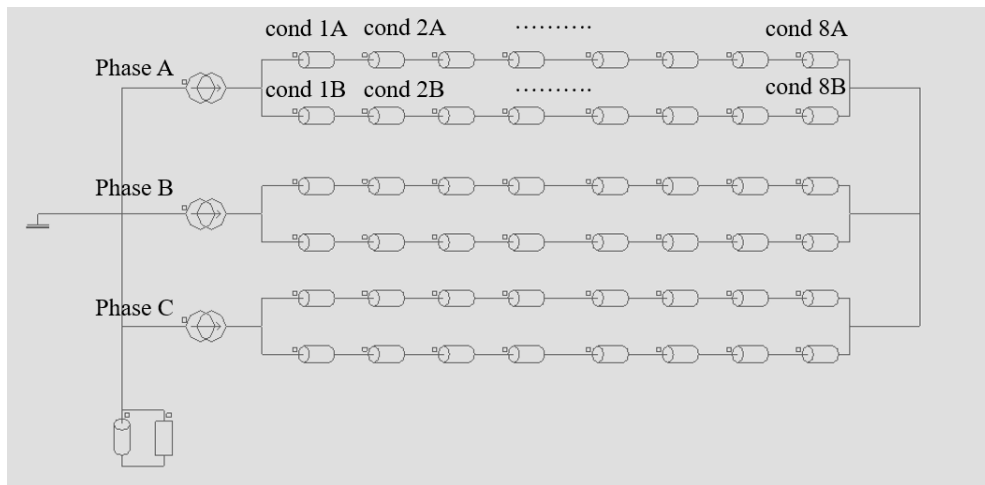
Figure 3.36 Electrical circuit of 2 parallel path model

This non-transposed paralleling strategy was applied to 2, 3 and 6 parallel path variants. Table 3.14 shows the effective packing factors and predicted losses for a speed of 6,000rpm at rated torque.

Table 3.14 Predicted losses for different parallel paths with no transposition

	Packing factor	Quasi-static loss (W)	Total loss (W)
Baseline model	0.79	2214	22016
2 parallel paths	0.77	2284	19570
3 parallel paths	0.75	2358	18695
6 parallel paths	0.67	2613	17712

As can be seen from Table 3.14, sub-dividing thick bar conductor into thinner strips reduces the slot-fill factor with a corresponding increase in quasi-static losses. There is some reduction in the overall losses at this 6000rpm operating point and while there is reduction in loss from the conductor sub-division, the magnitude of the reduction is not sufficient to make any of these bar windings a competitive option. For the most sub-divided case of 6 parallel paths, the overall loss is reduced by ~4.5kW, but the magnitude of the loss at this operating point is still ~8 times that of quasi-static loss for the baseline design. This level of loss in the 6 parallel path version remains prohibitive.

A significant contributor to the excessive loss in the 6-strip variant is circulating currents flowing amongst the non-transposed parallel paths. The current source waveform and the currents in the individual parallel paths of 6 parallel path un-transposed model are shown in the Figure 3.37. As will be apparent there is significant imbalance amongst the currents in the parallel paths, including extended intervals in which the currents in different paths have opposite polarities.
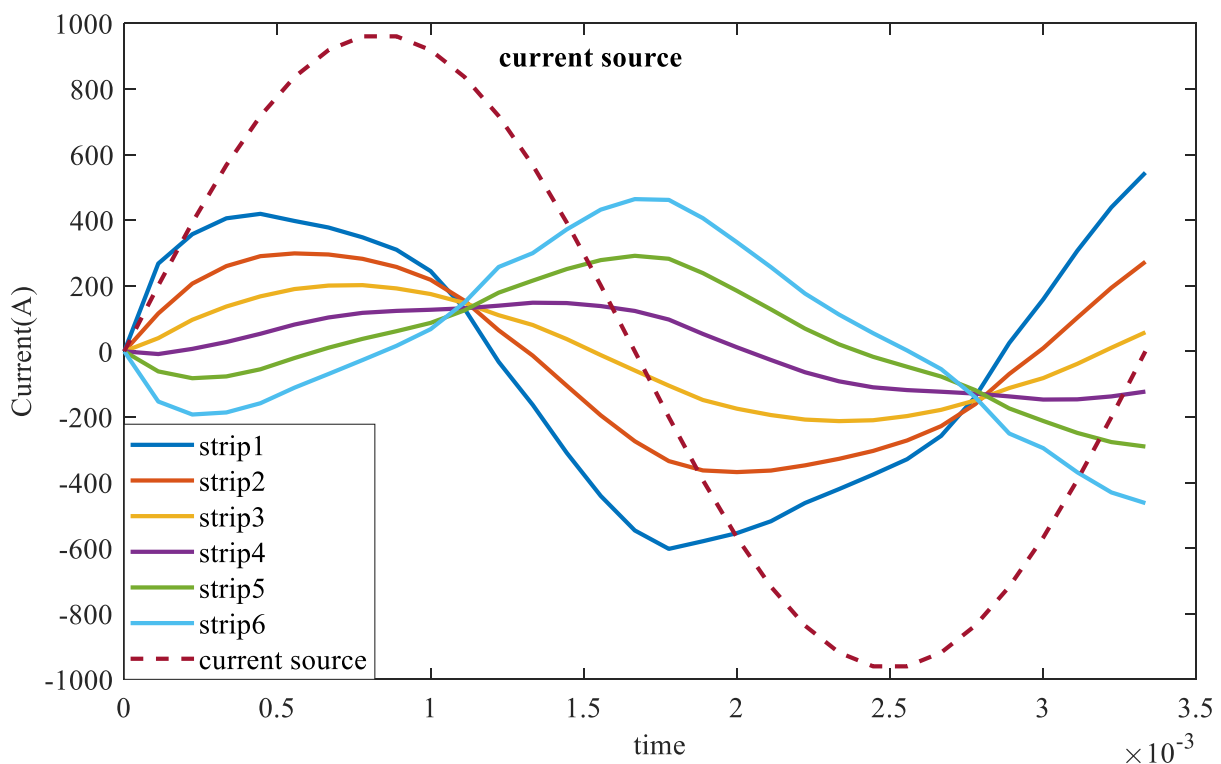
Figure 3.37 Current waveforms of 6 parallel branches of single phase

As noted previously, full transposition of the windings in the end-winding and interconnects can be used to balance the impedance between parallel paths and avoid circulating currents.

106

Figure 3.38 to Figure 3.42 shows schematic representations of the transposition strategies for 2,3 and 6 parallel paths in this 36-slot stator.
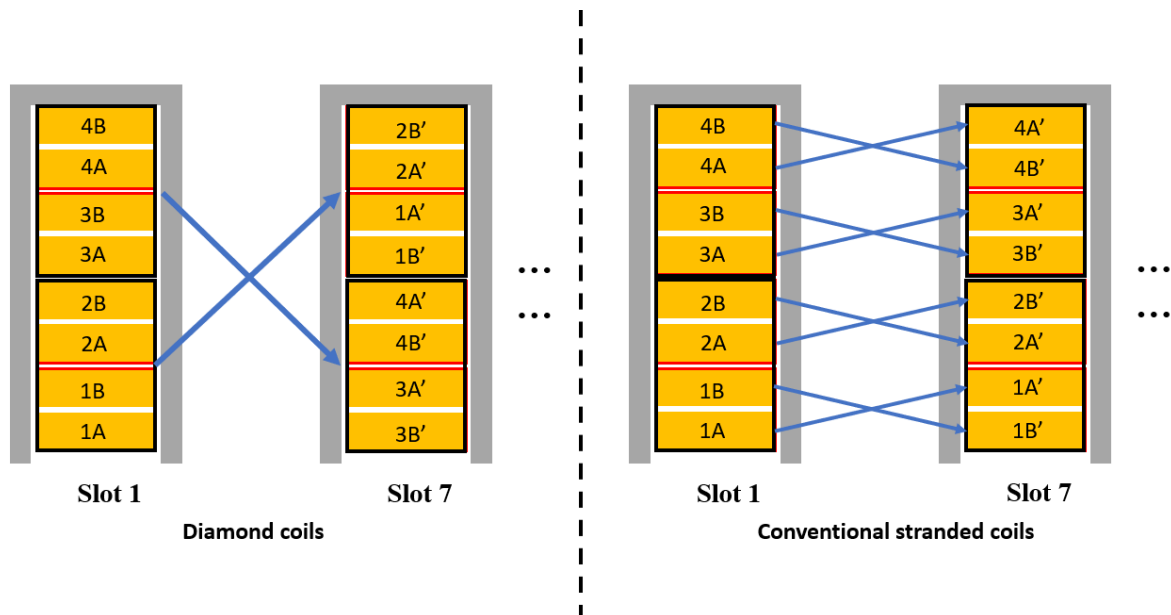
Figure 3.38 Transposition strategy for 2 parallel path model --- for diamond coil and conventional stranded coil
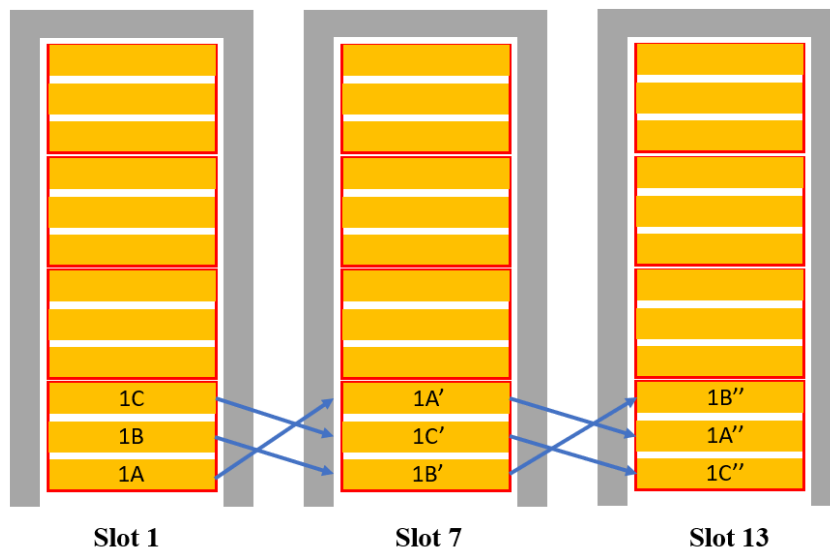
Figure 3.39 Transposition strategy for 3 parallel path model --- for conventional stranded coil only
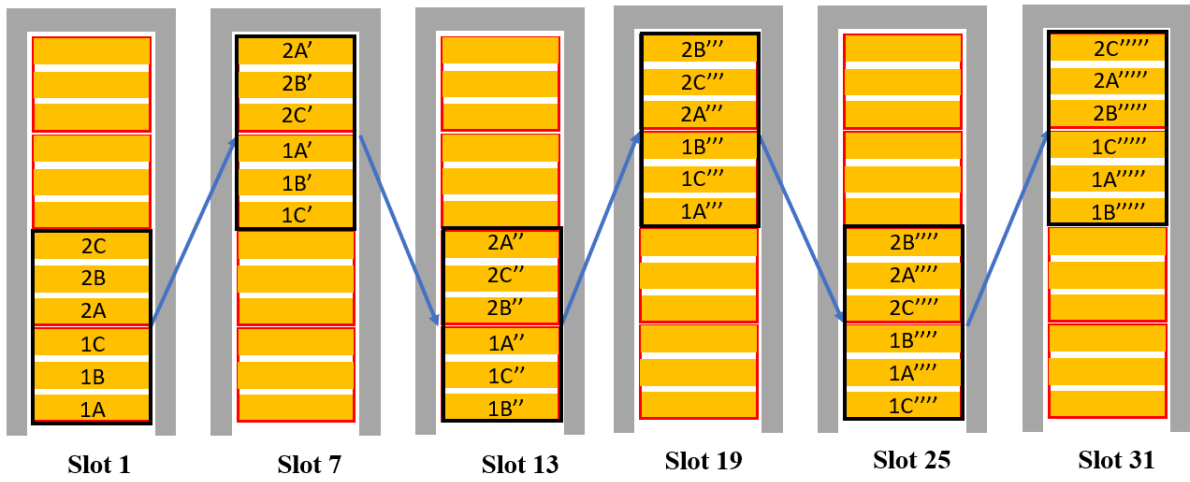
Figure 3.40 Transposition strategy for 3 parallel path model --- for diamond coil only
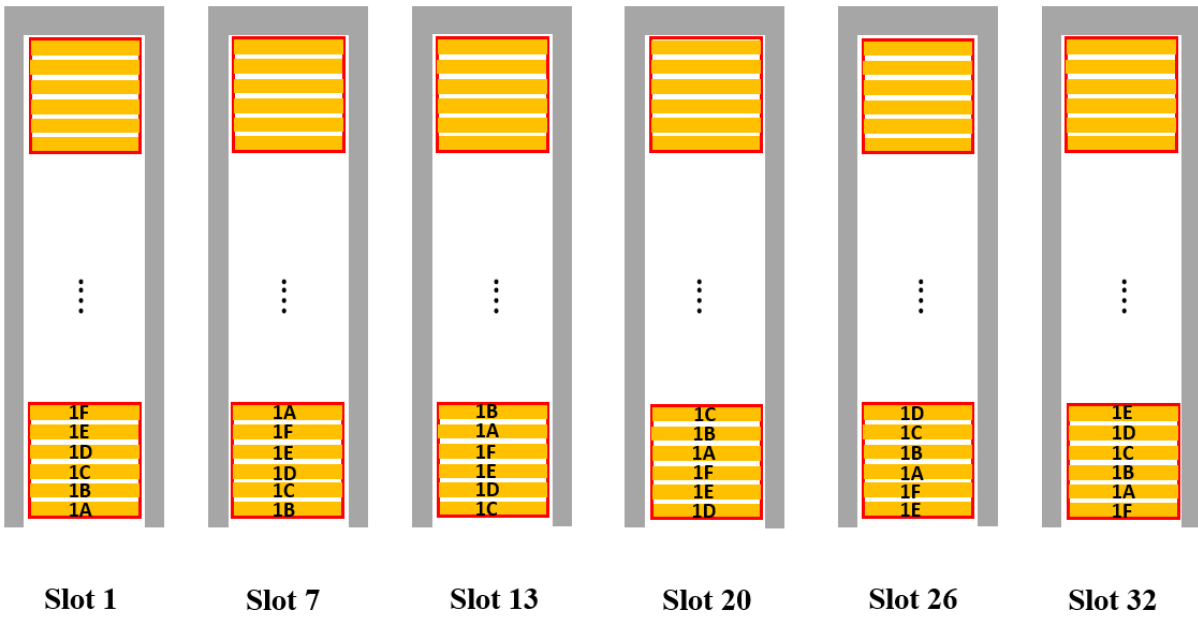
Figure 3.41 Transposition strategy for 6 parallel path model --- for conventional stranded coil

108
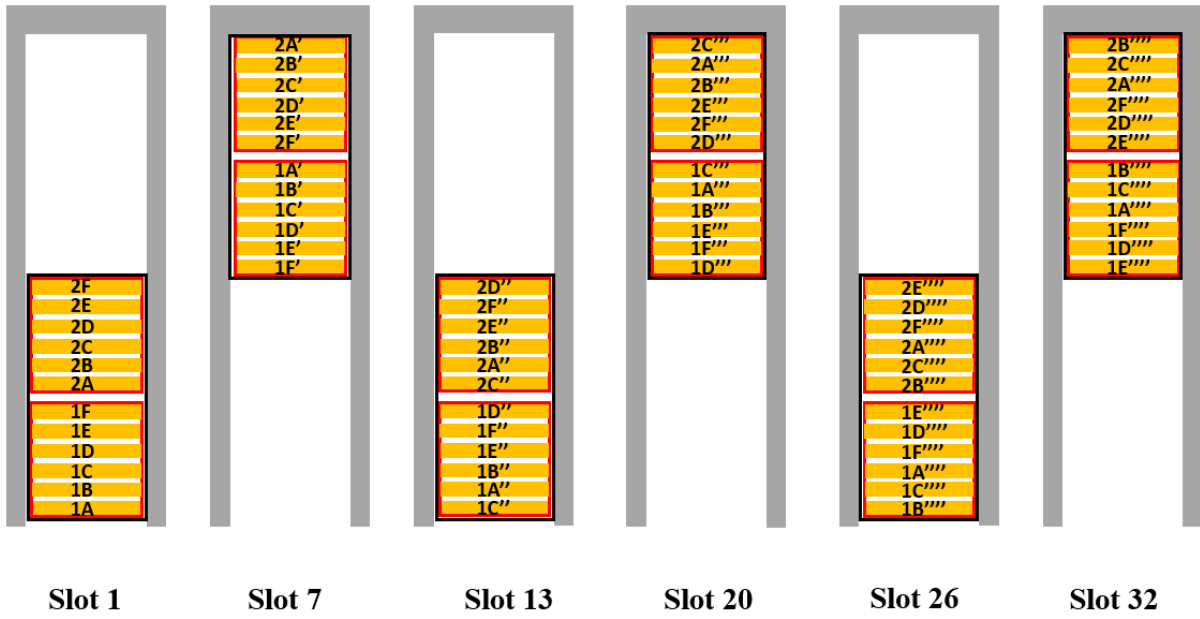
Figure 3.42 Transposition strategy for 2 parallel path model --- for diamond coil

As can be seen from figures above, to achieve full transposition of multi-parallel path models, a greater number of slots must be modelled to capture the symmetry than was the case with the non-transposed model where a 6 slot, 60° segment was able to represent the full machine with appropriate boundary conditions. For example, to model a fully transposed 3 parallel strip machine, three 60° segments are required to achieve the full transposition as shown in the Figure 3.43. While for the associated electrical circuit, it is provided in the Figure 3.44.
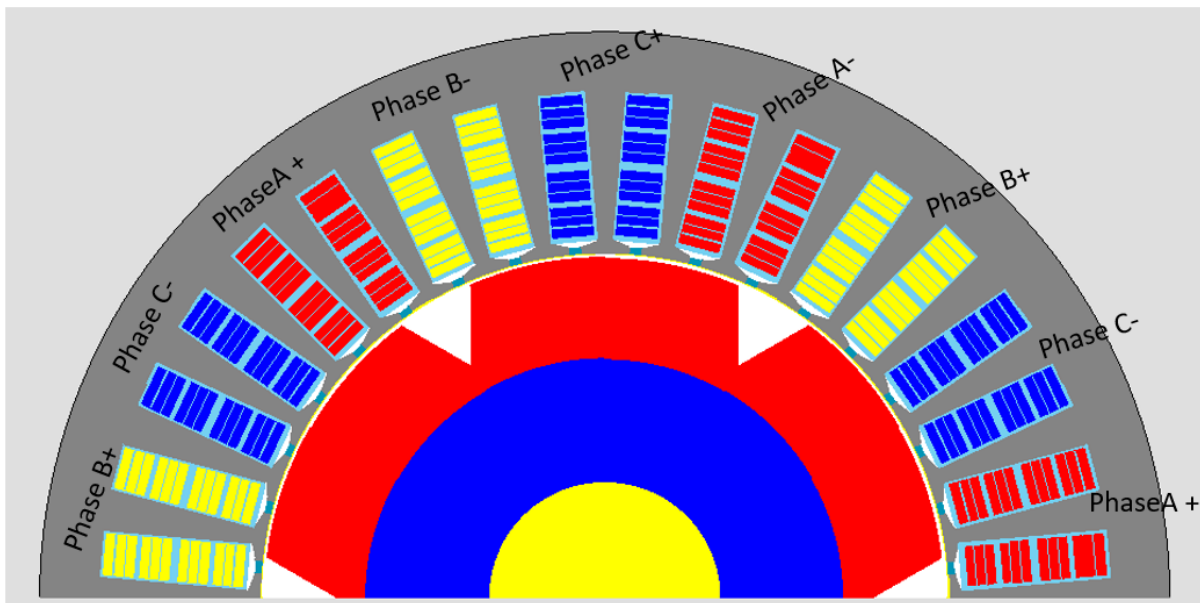
Figure 3.43 Geometrical view of 3 parallel path model
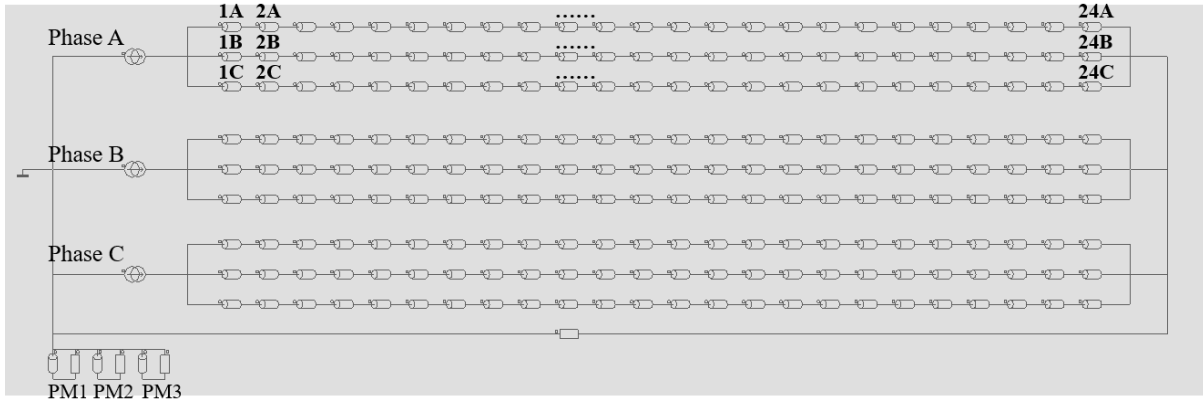
Figure 3.44 Electrical circuit of 3 parallel path model.

A series of simulations was performed for 2,3 and 6 fully transposed parallel paths, in all cases for rated torque at 6,000rpm. The resulting winding losses in the active region (i.e., excluding end-windings) are summarised in Table 3.15.

Table 3.15 Loss comparison between baseline and different parallel path models

		Quasi-static loss (W)	Total loss (W)	Ratio of total loss to quasi-static loss
	Baseline model	2214	22016	9.94
2 parallel paths	Non-transposed	2284	19570	8.57
	Fully transposed	2284	12106	5.30
3 parallel paths	Non-transposed	2358	18695	7.93
	Fully transposed	2358	9275	3.93
6 parallel paths	Non-transposed	2613	17712	6.78
	Fully transposed	2613	7595	2.91

As would be expected, full transposition of the winding results in a marked reduction in the winding loss at this operating points. Furthermore, increased parallelisation results in a progressive reduction in loss. The lowest loss is achieved with 6 parallel strips with a loss of 7595W which is around 1/3 of the loss in the baseline reference design. However, this is still almost three times the quasi-static loss for this 6-strip variant. The effectiveness of the transposition in the 6-strip variant is evident in Figure 3.45 which shows the current waveforms of the current source and 6 individual strips, which are indistinguishable from each other. It is

110

important to note that this equal sharing of the current is an outcome of model solution and not an imposed constrains on the circuit.
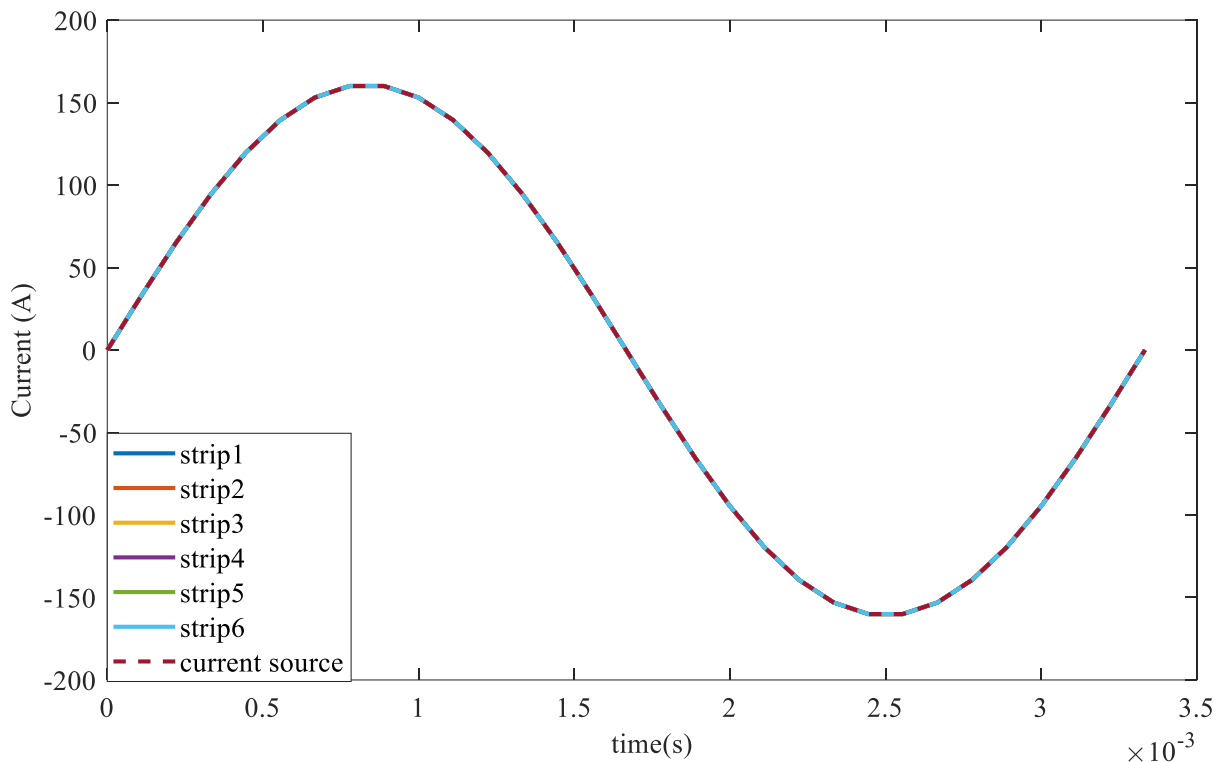
Figure 3.45 Current waveforms of 6 parallel paths model with full transposition

Having demonstrated the behaviour of a fully transposed winding in a model in which equal sharing of the single current source in each phase was not enforced in the circuit, but naturally occurred due to the winding arrangement, further analysis of these winding arrangements can be performed on a simplified model in which 1/6 of the rated current can be enforced in each path with independent current sources in each path. This allows the finite element model to be reduced to a 6-slot, 60° degree domain.

This investigation of paralleling options has identified a machine with 6 parallel paths in a fully transposed arrangement as being the preferred design. Although it results in the lowest winding loss of all the strip conductors considered up to this point, it still has an unsustainable level of winding loss. Hence, further mitigation strategies are considered in the next sections.

3.2.4 Evaluation of magnetic tape

The concept of using magnetic tape to replace the traditional polyester tape to reduce winding loss was proposed in [80]. The magnetic tape with chemical composition of Fe-Si-Al has an initial relative permeability of 16 and saturation flux density of 0.85T. Detailed manufacturing

process can be found in [80]. By changing composition of materials, filling ratio and particle size of the magnetic powder, variation in permeability and electrical and thermal conductivity can be achieved. It has been proposed in the literature [80] that an ideal magnetic tape with a higher permeability and higher saturation flux density (permeability = 100, saturation flux density = 1.6T) would be very effective in terms of windings loss reductions for this particular machine topology proposed (outer rotor PM machine with Halbach array designed for drones). The idea of this tape is that it is wound around the conductors in a similar manner to insulating tape to divert a proportion of the incident flux away from the core conductor. The magnetic properties of the magnetic tape material modelled in this investigation are taken directly from [80]. The magnetisation curve for this material is shown in Figure 3.46. The initial relative permeability up to 0.5T or so is 18.
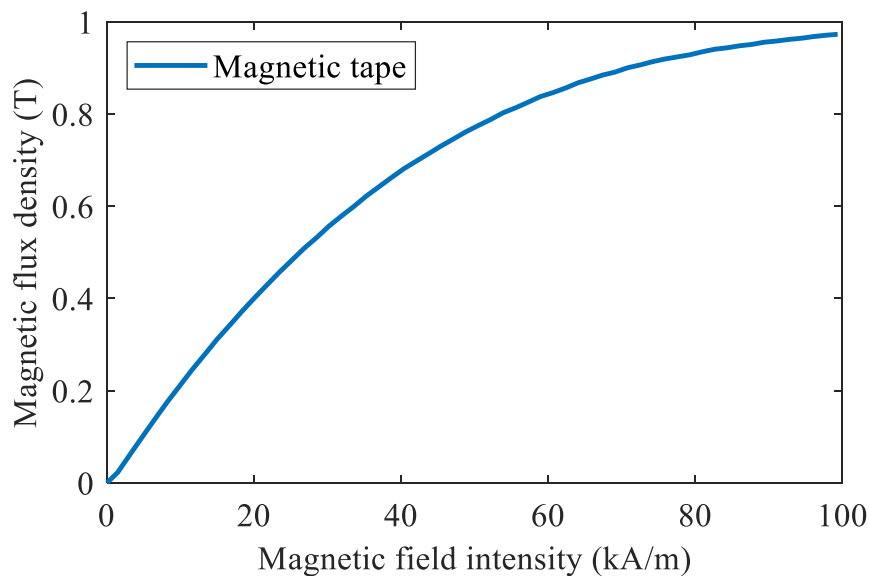
Figure 3.46 Magnetisation curve of magnetic tape from [40]

A series of full machine simulations were performed at rated speed and power with a range of different tape thicknesses. The resulting variation in loss as a function of tape thickness is summarised in Table 3.16. As shown and as would be expected, there is no change in the electromagnetic torque. There is some progressive reduction in the loss as the tape thickness is increased, but even for the thickest tape of 0.14mm the benefit are marginal and even thicker tapes would require a reduction in the conductor cross-section to accommodate a thick tape in the slot. Although the outcomes reported in [80] suggest that magnetic tape has the potential to achieve useful reductions in loss, in this particular machine which has large cross-section conductors, the benefits are marginal and are unlikely to offer a viable option given the cost and the potential impact on the slot-fill.

Table 3.16 Loss and torque information for models with different magnetic tape thickness

Tape thickness (mm)	Total winding loss (W)	Torque (Nm)
No tape	7595	553
0.06	7512	553
0.08	7482	553
0.10	7452	553
0.12	7423	553
0.14	7394	553

With processes of sub-dividing the original thick bar conductor into 6 parallel strips, full transposition and implementation of magnetic tape, the total winding loss has been reduced significantly compared to original model obtained from sizing equations. However, the magnitude of total winding loss is still very high and thus additional AC loss mitigation processes are required in the following sections.

3.3 Evaluation of alternative conductor materials

3.3.1 Pure Aluminium conductors

There is growing interest in the automotive sector in the adoption of aluminium windings formed with stranded conductors for reasons of cost. However, it remains at present rarely used in mainstream electrical machines due to its higher resistivity per unit volume. Key properties of aluminium and copper conductors are compared in Table 3.17.

Table 3.17 Key material properties of Copper and Aluminium

	Copper (100% IACS)	Aluminium (1350EC grade)
Electrical conductivity at 20°C	5.8×10^7 Sm^{-1}	3.54×10^7 Sm^{-1}
Temperature coefficient of resistance at 20°C	0.00393	0.0043
Density	8890kgm^{-3}	2700kgm^{-3}
Specific heat capacity	376 J kg^{-1}K^{-1}	921 J kg^{-1}K^{-1}

As can be seen from the Table 3.17, the main obstacle to deploying aluminium conductors is its higher resistivity per unit volume. For a fixed winding volume, the quasi-static loss in an aluminium coil will be 1.63 times higher than the equivalent copper coil. Nevertheless, there

are several reported machines equipped with aluminium conductors. In [81], the stator outer diameter and axial length of a 6kW induction machine were increased to accommodate a larger volume of aluminium conductor to match the DC loss of a copper counterpart. However, the penalty of increased core size to accommodate the larger winding outweighs corresponding benefits associated with aluminium conductors. Similar scaling process for aluminium conductor is proposed in [82] but again, the overall trade-offs tend not to be particularly favourable.

One idea which has been reported to make aluminium conductors competitive with their copper counterparts, is to exploit their mechanical properties to increase the slot-fill without changing the core geometry. One method proposed is to deform round aluminium conductors with a custom bobbin, punch and die set [83]. With carefully controlled compression of aluminium windings, the packing factor inside of slot can reach 78%, resulting in lower DC loss, lower mass, and slightly higher AC loss compared to conventional round wire copper counterparts. However, it is worth noting that this compression approach has also been applied to copper windings [84]. The low density of aluminium is another interesting feature when comparing aluminium with copper, especially in the aerospace [56] and drone sectors [80]. As noted several times already in this thesis, in aerospace applications the main design criterion is usually high power density and lower weight, making aluminium conductors a potential option for future hybrid propulsion systems. The integrity of aluminium conductors from a manufacturing standpoint is reviewed in [85]. This identified no clear problems that would prevent designers from deploying aluminium windings, although it is well recognized that extra care needs to be taken with joining and terminating coils. As reported in [86], the higher electrical resistivity of aluminium conductors makes them less prone to AC loss in high-speed applications than an equivalent copper conductor although at low frequency a like-for-like aluminium replacement will have higher loss. It is proposed in [87] that through the adoption of appropriate design and optimization processes, machines equipped with aluminium windings have the potential to outperform copper counterparts in terms of losses while still retaining the benefits of lower weight, lower cost and easier recyclability. It is important to stress that the relative merits of machines with copper and aluminium windings will depend on the specifics of the geometry and electrical frequency, and that in the vast majority of mainstream specifications, copper windings are likely to be favoured.

The focus of this section is to take advantage of the lower electrical conductivity of aluminium conductors which make them less prone to AC losses than an equivalent copper conductor.

Through careful design and optimisation, there is some potential for some machines designs equipped with aluminium windings to outperform copper counterparts in terms of lower AC loss, reduced mass and hence higher power density and high efficiency. Whether any benefits are derived will depend to a great deal on the specific size, geometry and electrical frequency of the machine.

3.3.2 The influence of material electrical conductivity on AC losses

It is recognised that the material conductivity determines both the quasi-static loss and AC loss in a conductor. For a specified operating speed and hence electrical frequency, a material with lower conductivity will produce a higher quasi-static loss but on the other hand results in lower AC losses. When material conductivity is varied, the resultant proportions of quasi-static loss and AC loss changes correspondingly, which means there is likely to be an optimum material resistivity that gives the lowest combination of total losses at a particular frequency. The investigation of optimal conductivity is not without some practical value since there are many alloys with levels of conductivity of interest depending on the frequency. Furthermore, there are processing routes that open up some scope to manipulate electrical conductivity. For example, Aluminium composites produced by additive manufacturing have achieved electrical conductivities between 27.0% IACS and 30.3% IACS with different build orientation and heat treatment [88].

In order to explore the relationship between electrical conductivity and losses, a series of machine level simulations of overall winding loss were performed for the reference machine using time-stepped finite element analysis. During the extensive set of simulations, the speed of the machine was varied between 3,000rpm and 10,500rpm (150Hz to 525Hz) in 1500rpm increments (75Hz increment) and at the same time, the electrical resistivity is varied between 50% and 225% of the resistivity of copper in 25% increments. As an example of the data generated, Figure 3.47 shows the variation in total winding loss as a function of normalised electrical resistivity at 3 different rotational speeds, in all cases for rated torque. As can be observed from the diagram, at 6000rpm, the lowest loss is achieved with a resistivity that equals that of room temperature copper, albeit that this optimum is rather shallow. As the speed is increased, the normalised resistivity which gives rise to the lowest loss moves up to higher resistivity range. It is worth noting that the optimum normalised resistivity, even at 9000rpm does not reach the value of 1.63 which is normalised resistivity of Aluminium at room temperature. Indeed, the resistivity of Aluminium does not become the optimal resistivity.
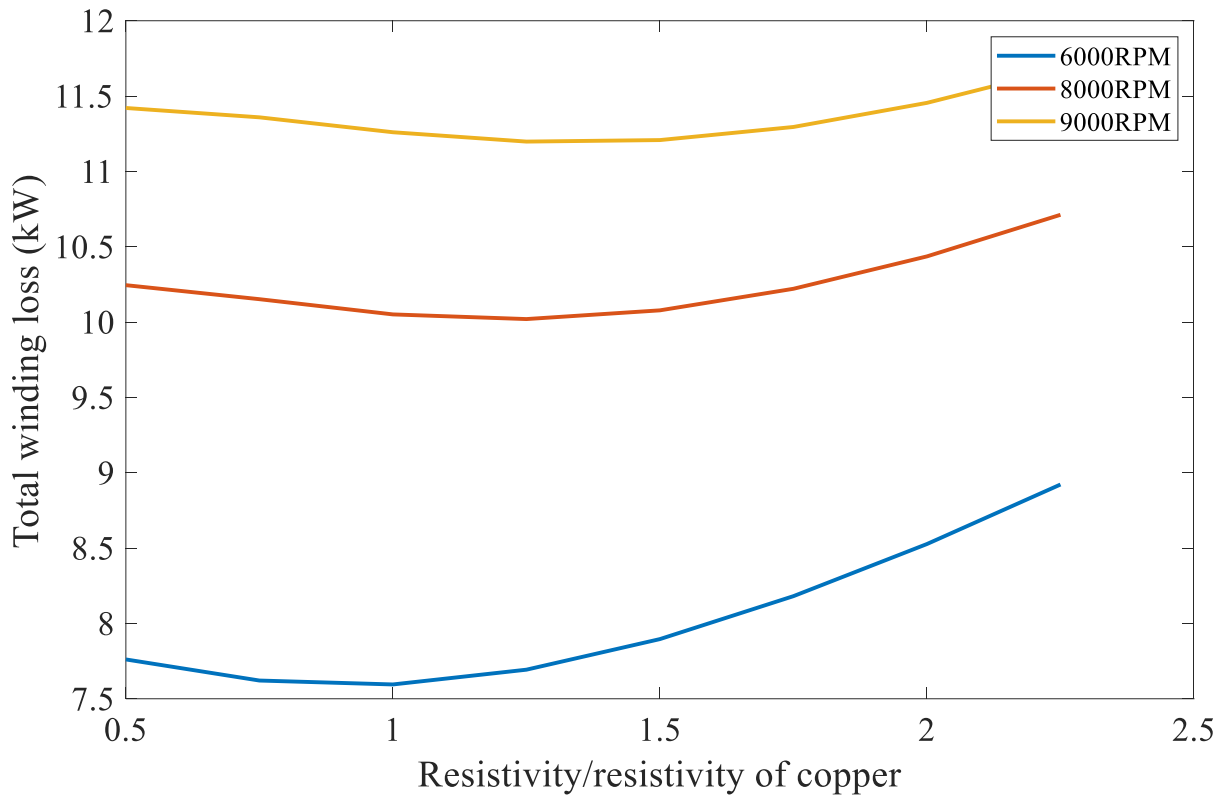
Figure 3.47 Resistivity/ resistivity of copper versus total loss curve at 6000RPM

If to plot the total winding loss curve versus different resistivity at 9,000RPM solely, one can find that the optimal material resistivity at this particular speed is close to aluminium resistivity. To validate the findings that around 9,000RPM direct implementation of aluminium conductor will give lower loss than copper model, the model was simulated over a speed range from 3,000rpm to 12,000rpm at rated torque for both copper and aluminium windings. The resulting total loss comparison between copper and aluminium windings is shown in Figure 3.48. As would expected, copper has the advantage at lower frequencies but the gap between the performance of copper and aluminium narrows as the speed increases and eventually crosses at 450Hz which corresponds to 9000rpm. This suggests that aluminium is not competitive for this machine whose operating speed range is limited to 6000rpm. The benefits of AC loss reduction due to the higher resistivity becomes more evident as frequency increase, but by 300Hz (6000rpm) these benefits are not sufficient to overcome the significant penalty in quasi static losses.
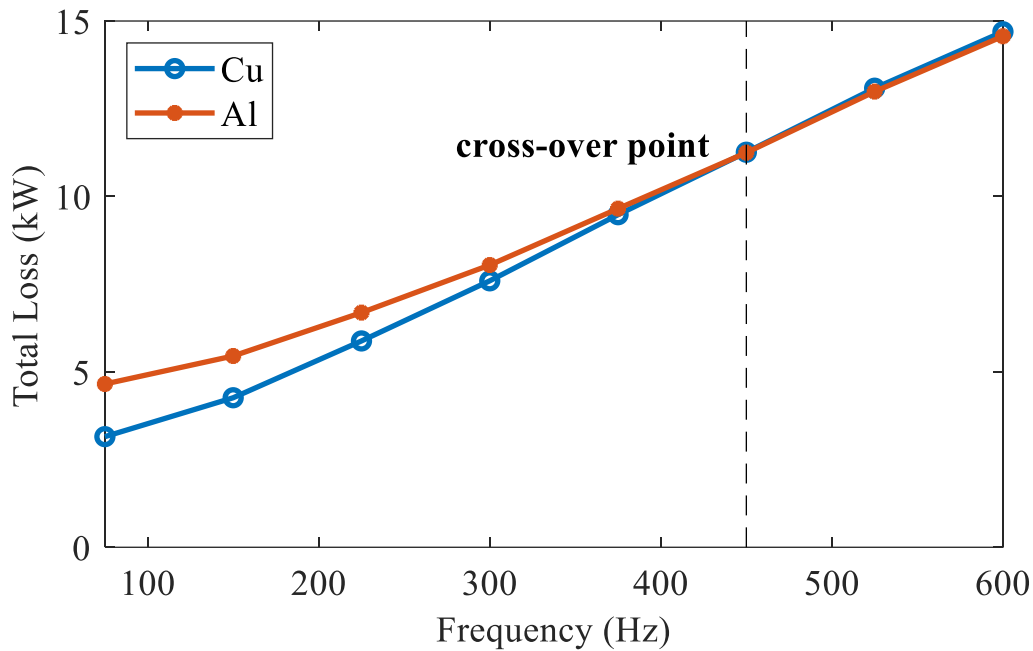
Figure 3.48 Finite element predicted winding loss with pure copper and pure aluminium as a function of fundamental electrical frequency

The results in Figure 3.47 and Figure 3.48 suggest that at 6000rpm, a copper winding offers the optimal conductivity and that no benefit would be gained by alloying the copper with another element to slightly increase its resistivity or moving to aluminium or indeed if a lower resistivity conductor material were available to be used. It is also worth noting that some of the operation of the machine may well be at speeds below the maximum speed where the benefits of copper over copper alloys or aluminium are even greater. However, the conclusion that copper offers the best option in this machine is based on the entire winding being copper and as was shown previously, the level of AC loss varies depending on the location within the slot and hence there may be some value in having hybrid windings made up of more than one conductor material. The next section explores the options and benefits of such hybrid windings.

3.3.3 Hybrid aluminium and copper winding with uniform sized conductors in each turn

The reference design is equipped with 4 series turns per slot, each of which is subdivided into six fully transposed parallel paths. One potential option for further reducing the AC losses is to split the original windings into separate aluminium and copper three phase winding sets and connect them in series at the end of their respective phase windings. The rationale for using hybrid aluminium and copper conductors is based on using aluminium conductors towards the front of the slot where AC losses are most pronounced and copper towards the back of the slot where AC loss is less pronounced. One of the consequences of using two sets of three phase windings with different materials are the manufacturing challenges of series connection. This

said, there is only one copper to aluminium connection point per phase and in practice this could be made via a terminal box connection rather than a direct joint. Three alternative hybrid winding arrangements which involve the progressive substitution of successive series turns of copper with aluminium are shown in Figure 3.49 to Figure 3.51.
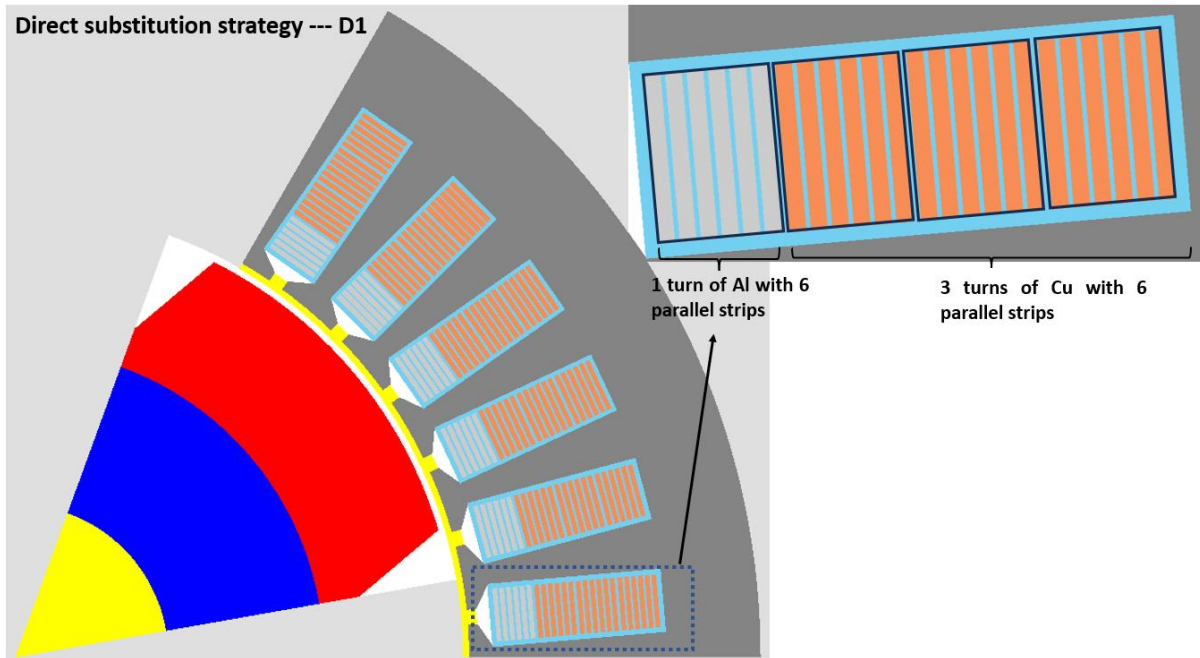
Figure 3.49 Geometrical view of direct substitution strategy 1 --- 1 turn of aluminium and 3 turns of copper
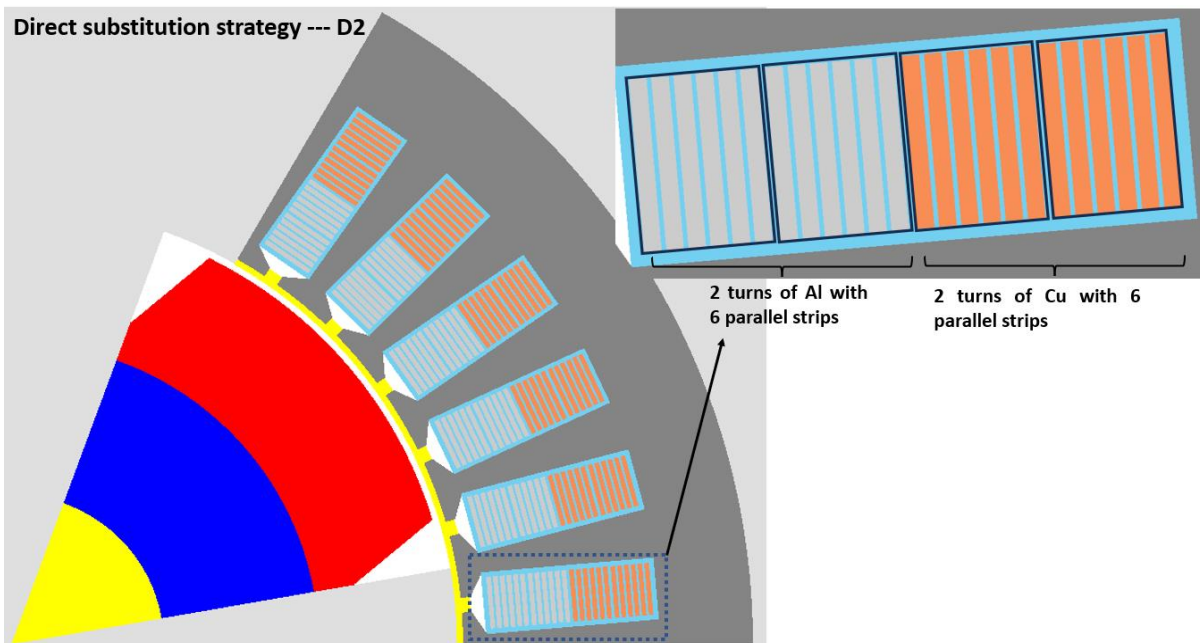
Figure 3.50 Geometrical view of direct substitution strategy 1 --- 2 turn of aluminium and 2 turns of copper
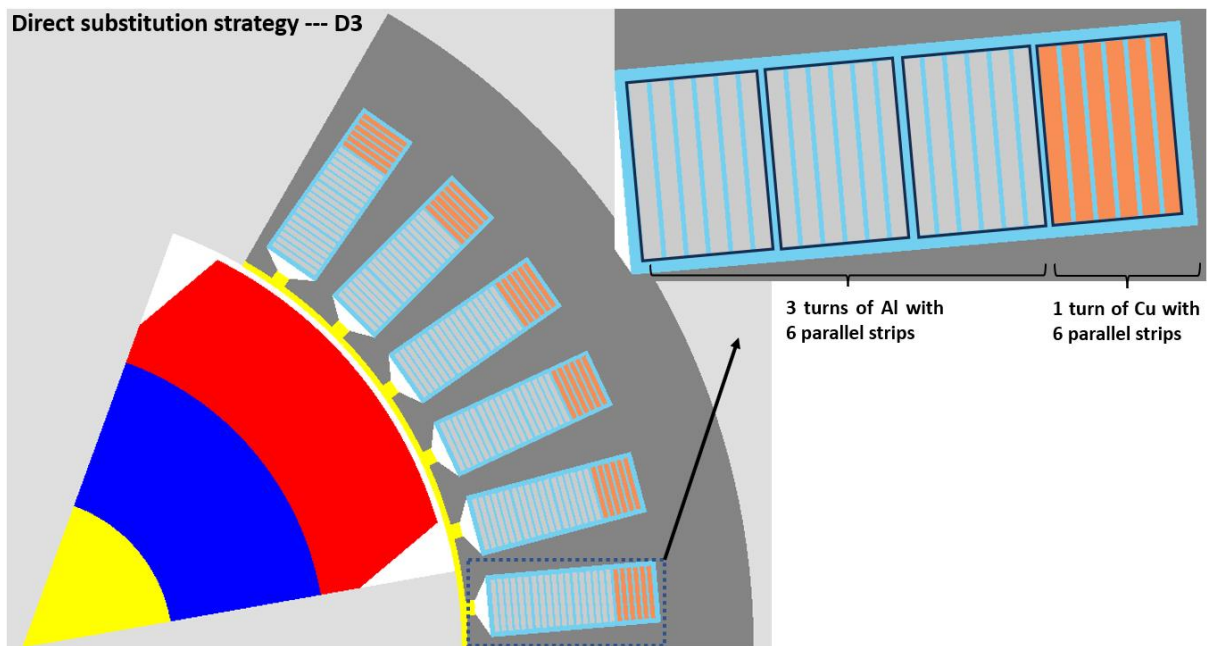
Figure 3.51 Geometrical view of direct substitution strategy 1 --- 3 turn of aluminium and 1 turns of copper

Simulations were performed at rated speed and at 50% and 75% of rated speed to establish the penalties or benefits of this simple hybrid winding approach. The resulting total conductor losses predicted by finite element analysis are summarised in Table 3.18 for winding arrangements D1-D3 including a breakdown between the aluminium and copper windings which would make up a phase. As can be seen from Table 3.18, at 6000rpm there is a significant benefit with winding arrangement D1 compared to the equivalent all copper winding. This benefit reduces with winding arrangement D2 but is still a significant improvement over the equivalent all copper winding. However, D3 incurs a small penalty compared to the equivalent all copper winding at 6000rpm since the conductors towards the back of the slot are less affected by AC loss and so in these conductors the higher resistivity of aluminium increases the total loss. This trend becomes more pronounced at the 3000rpm operating point where the significantly reduced AC loss effects means that the lower resistivity of copper is more beneficial. Indeed, at 3000rpm where the AC losses become less of a feature, all three hybrid windings have a higher loss than the equivalent all copper winding. Hence of all the simple fixed conductor size hybrid windings considered, arrangement D1 is the best performing at all speeds outperforming all copper winding at 6000rpm and 4500rpm at rated torque and incurring a small penalty at 3000rpm. It is worth recalling that at all three of these operating speeds, the all-copper winding outperforms the all-aluminium winding as shown previously in Figure 3.48.

119

Table 3.18 Summary of finite element simulations on uniform conductor sized hybrid windings

Speed	Hybrid winding designation	Total loss (W)	Loss in aluminium winding (W)	Loss in copper winding (W)	Difference from full copper winding
6000rpm	D1	6955	4134	2821	-640
	D2	7233	5835	1398	-362
	D3	7631	6968	663	+36
4500rpm	D1	5559	3032	2527	-322
	D2	5869	4505	1364	+12
	D3	6273	5614	659	+392
3000rpm	D1	4275	2013	2262	+13
	D2	4626	3289	1364	+391
	D3	5036	4380	656	+774

Note that all the above simulations were conducted with material properties at room temperature of 20°C. Assuming the steady state working temperature of this machine is 150ºC, then the resistivity increase of aluminium will be higher than that of copper (because aluminium has larger temperature coefficient of resistance). The resistivity increase of aluminium results in higher DC loss and lower AC loss, which means the extra benefits introduced by hybrid winding model at lower speed range is likely to be compromised. To fully assess the benefits and drawbacks of hybrid winding model, the best method is to perform some electromagnetic thermal coupled simulations. However, the focus of this thesis is on electromagnetic modelling and optimisation, which means the detailed thermal modelling is not considered here but will be investigated in the future.

3.3.4 Asymmetrical substitution strategies

The simulations of hybrid windings detailed in section 3.3.3 above were based on maintaining the same uniform conductor size throughout the winding with only a simple substitution of conductor material. The idea of adopting non-uniform conductor cross-sections for successive turns, sometimes referred to as an asymmetric winding, was originally proposed in [89] for copper hairpin coils and has been proved to be efficient in reducing winding losses. This approach can be extended to hybrid aluminium and copper windings, albeit with some constraints on the cross-section of each individual turn. In order to recognise practical considerations and allow systematic variation of key parameters, it is necessary to impose some constrains and parameterise the model in the following regards:

Uniform strip thickness within a given material: To make hybrid winding more practical and eliminate the need for joints between successive turns, all the conductors of a given material in the winding should have same cross-section, which allows the portion of the overall

winding made up of that material to be wound continuously with the same conductor cross-section.

Conductor cross-sectional area: Since the slot depth, slot width, thickness of slot liner, thickness of enamel and polyester tape are predefined and fixed, the remaining area which can be occupied by the conductor and any primary insulation coating can be readily calculated and hence the total area of conductor per slot is a fixed constraint when determining the height of different combinations of aluminium and copper strips.

Number of series conductors per slot: Any arrangement of conductors must result in four series turns per slot.

Number of parallel strips: As discussed previously, for this 36-slot, 6-pole stator, the number of parallel strips which ensure complete transposition across the phase winding can be 2,3 or 6. There is a degree of freedom in that the two winding sets, i.e., copper and aluminium sets, are not constrained to have the same number of parallel strips since they are only connected at the ends of the phase. However, they must individually have 2,3 or 6 parallel strips.

The freedom to employ 1, 2 or 3 aluminium turns and the scope for the copper and aluminium sections to have 1,2,3 or 6 parallel strands leads to 48 design combinations, even without considering the ability to vary the dimensions of each strip. To narrow this down to a manageable number of options, the investigation was focussed on approaches that have already been proved to be efficient to reduce AC losses, i.e., the replacement of the copper conductors with aluminium for the conductors nearest the airgap, i.e., the asymmetric equivalent of arrangements D1 and D2 for the uniform conductor size. These arrangements are designated A1 and A2 and the slot view of those two examples are shown in Figure 3.52. The winding arrangement A1 in Figure 3.52 representing a case where aluminium strip height is scaled by a factor of 1.2 its original height which in turn means that the copper strip height is decreased to 0.9 of its original height to fit within the fixed slot depth.
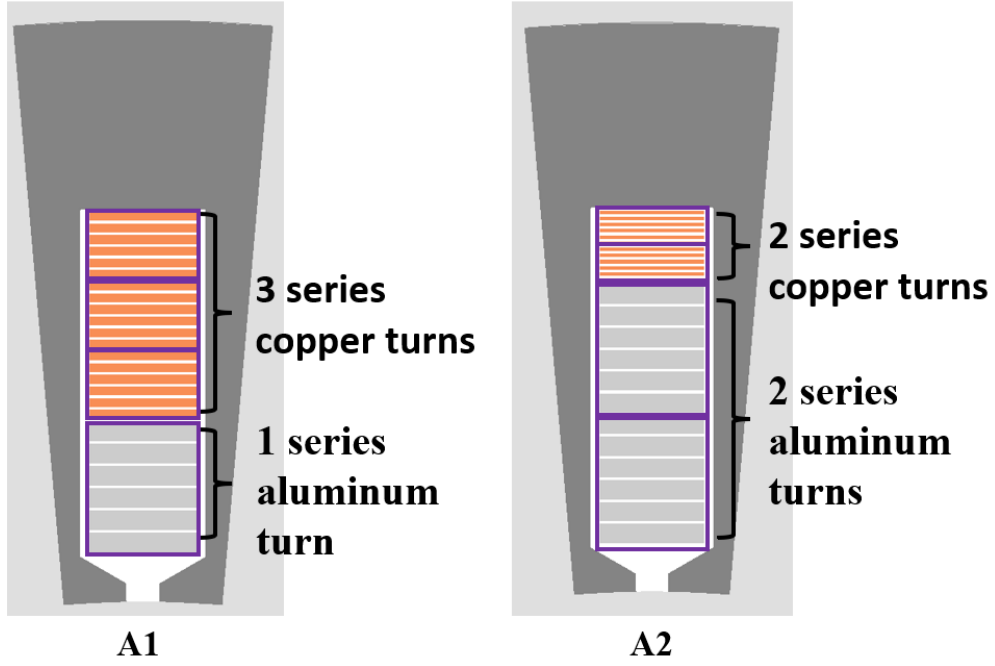
Figure 3.52 Methodology for scaling processes of asymmetrical substitution strategy

To systematically quantify the scaling strategy adopted, a scaling factor can be defined which is normalised against the original 4 turn winding with equal division of the slot between individual turns. A scaling factor of less than 1 results in a small overall series turn cross-sectional area than the original baseline design and vice-versa for scaling factors greater than 1. The normalised heights of the 4 turns must necessarily sum to 4.0. Given the degree of paralleling, the number of turns of aluminium and copper, the height of slot available to accommodate the conductors (h_{total}), the height of the individual aluminium and copper strips can be related by the following equations:

$$h_{Al\_turn} = h_{Al\_strip} \times s \times N_{Al} \times S_{Al} + (N_{Al} \times S_{Al} \times 2 \times h_i + N_{Al} \times 2 \times h_t) \tag{3.15}$$

$$h_{Cu\_turn} = \frac{h_{total} - h_{Al\_turn}}{N_{Cu}} \tag{3.16}$$

$$h_{Cu\_strip} = \frac{h_{Cu\_turn} - (S_{Cu} \times 2 \times h_i + N_{Cu} \times 2 \times h_t)}{S_{Cu}} \tag{3.17}$$

Where h_{Al_turn} and h_{Cu_turn} are aluminium turn height and copper turn height, h_{Al_strip} and h_{Cu_strip} are aluminium strip height and copper strip height, s is the scaling factor, N_{Al} and N_{Cu} represents aluminium turn number and copper turn number respectively, S_{Al} and S_{Cu} are number of parallel paths for aluminium and copper, h_i and h_t are insulation thickness and

polyester tape thickness defined previously. Since the height of single strip of baseline model (i.e., 6 parallel strips in each of 4 equally sized series turns) is already relatively small at ~1mm, in order to maintain mechanical integrity and avoid extremely thin strips of aluminium and copper, the variation of minimum scaling factor was set at 0.6. Furthermore, the fixed insulation coating thickness of 0.1mm on each face increasingly impacts on the slot-fill as the conductor height is reduced. The strip height of aluminium and resulting copper with asymmetrical scaling strategy A1 and A2 are shown in the Table 3.19 and Table 3.20 below:

Table 3.19 Conductor height information for asymmetrical substitution strategy A1

Uniform winding strip height for 6 parallel strips (mm)	Scaling factor for Aluminium strip	Aluminium strip height (mm)	Copper strip height (mm)
0.92	0.6	0.55	1.05
	0.8	0.74	0.99
	1.0	0.92	0.92
	1.2	1.11	0.86
	1.4	1.29	0.80

Table 3.20 Conductor height information for asymmetrical substitution strategy A2

Uniform winding strip height for 6 parallel strips (mm)	Scaling factor for Aluminium strip	Al strip height (mm)	Cu strip height (mm)
0.92	0.6	0.55	1.29
	0.8	0.74	1.11
	1.0	0.92	0.92
	1.2	1.11	0.74
	1.4	1.29	0.55

Two further arrangements shown in Figure 3.53 and Figure 3.54 were considered and designated A3 and A4 respectively. In A3, the number of parallel strips in the front-most aluminium turn is maintained at 6 as was the case with A1 and A2 but the copper conductors at the rear of the slot were only divided into 3 parallel paths. In arrangement A4, this is reversed and the aluminium turn is divided into 3 parallel strips and the copper turns are divided into 6 parallel strips. The feasible scaling ratios for arrangements A3 and A4 are different because the strip height after scaling must meet the requirement of minimum manufacturable thickness.

Specifically, the scaling ratio for arrangement A3 is from 0.8 to 1.6 while for scaling ratio range for arrangement A4 is from 0.4 to 1.2.
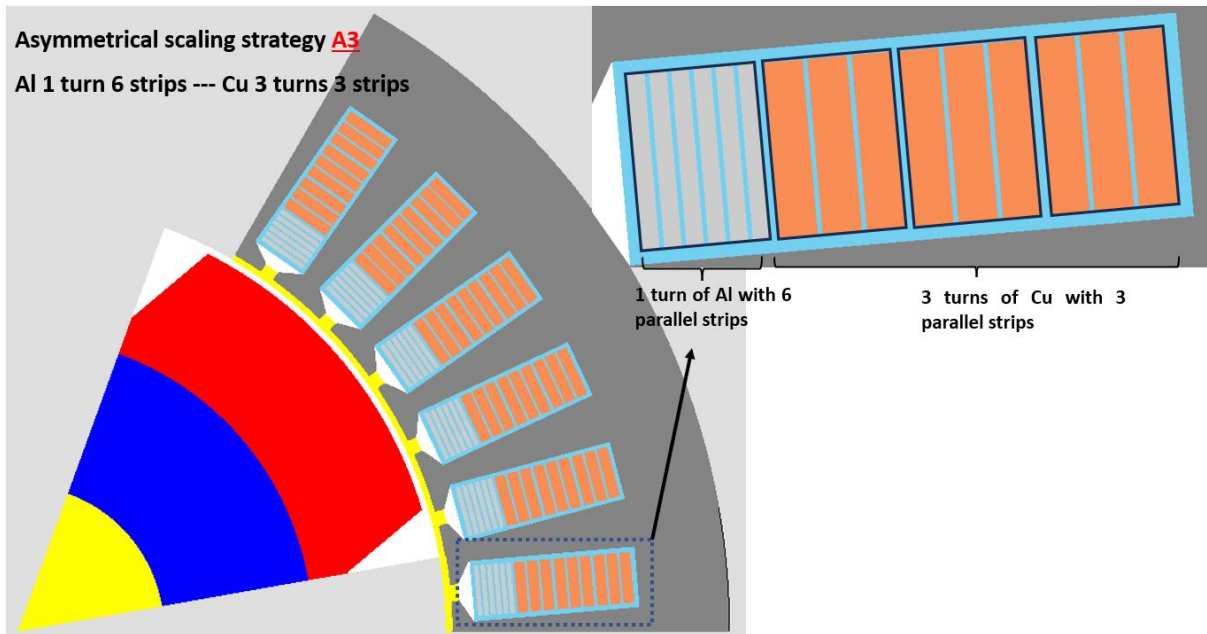
Figure 3.53 Geometrical view of asymmetrical scaling strategy A3 --- Al 1 turn 6 strips and Cu 3 turns 3 trips
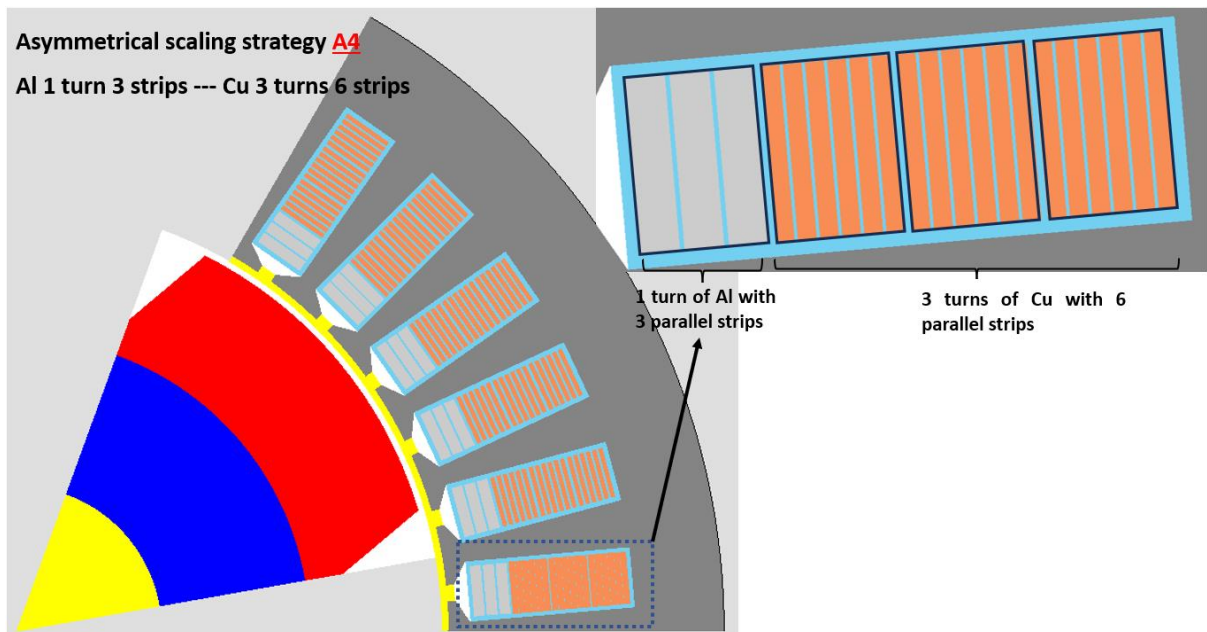
Figure 3.54 Geometrical view of asymmetrical scaling strategy A4 --- Al 1 turn 3 strips and Cu 3 turns 6 trips

Variants of winding arrangements A1, A2, A3 and A4 were solved over a range of scaling factors at rated torque and speeds of 6000rpm, 4500rpm and 3000rpm. The resulting FEA predicted total conductor loss are summarised in Figure 3.55.

124
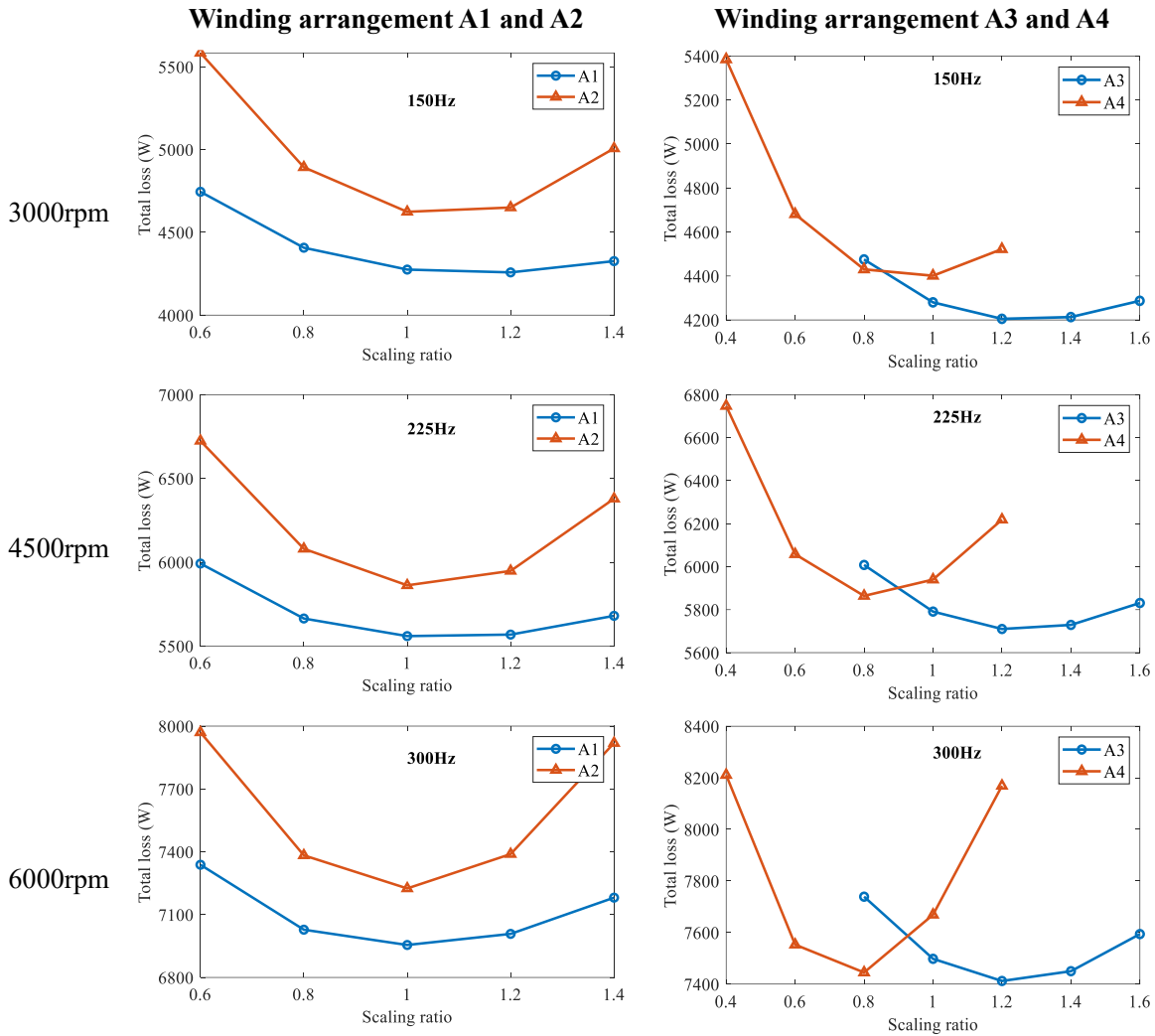
Figure 3.55 Variation in predicted loss versus scaling ratio for coil arrangements A1, A2, A3 and A4 at various speeds and rated torque

As shown in Figure 3.55, the optimal scaling ratio tends to be in the range 1-1.2 for both strategies, although A3 tends to favour slightly higher scaling ratios. In terms of the key operating point of machine at rated torque, then a scaling ratio of 1.0 (i.e., equal sized turns) with arrangement A1 results in the lowest loss at 6955W. Hence, whereas some benefits have been obtained by replacing the front-conductor with aluminium the design freedom of having different sized aluminium and copper turns generated no real benefit in this particular machine with its maximum rated speed of 6000rpm.

3.4 Impact of tooth width in winding losses

As described in previous sections, when paralleling and transposition are implemented to 6 parallel paths model, the total winding loss has been reduced significantly compared to that of baseline model obtained from sizing process. However, the AC loss of this model is still around 2 times higher than quasi-static DC loss. Although the idea of using hybrid aluminium and

copper winding can further reduce the winding losses, the remaining winding loss is still prohibitive and thus further AC loss mitigation strategies are required.

Dividing the original baseline conductor into multi-parallel paths was effective in breaking up the paths for eddy currents caused by circumferential cross-slot leakage flux, albeit with diminishing return as more strips are used and with a slot-fill penalty. However, the flux to which the winding is exposed is not purely circumferential and there is a radial component of flux density which is incident on the conductors. This flux is oriented at such that conductor sub-division into parallel strips is not effective in reducing the induced eddy currents. This could be tackled by dividing the conductors into parallel paths across the width of the slot but this sub-division would significantly complicate coil manufacture and lose the packing factor advantage of a strip winding.

Hence, a re-appraisal of this design was undertaken, since as noted earlier the baseline model was optimised purely for static torque capability and resulted in significant levels of saturation in the stator teeth, particularly near the front ends of the teeth due to the tapering nature which is a consequence of the parallel slots and the high airgap flux density which resulted from the use of a thick magnet. Although this was not a major issue in terms of torque density, saturation of the stator teeth has the potential to modify the field in the stator and increase the radial flux within the slot. To explore whether reducing stator tooth saturation would lead to a reduction in winding losses, a series of adapted designed were considered in which the slot width and corresponding conductor width are progressively reduced. The baseline reference design has a slot and conductor widths of 10.3mm and 8.9mm respectively. Reducing the slot width results in a corresponding increase in the stator tooth width which will tend to alleviate saturation.

The decrease in slot width will necessitate a corresponding decrease in the conductor width. If the same slot Ampere turns are maintained, this will result in an increase in the current density and hence the quasi-static loss. However, it might also lead to an increase in the torque constant due to the reduced tooth saturation and hence an increase in torque for the same Ampere turns. The study of the influence of the tooth width on winding losses was performed for two different design criteria. In the first the same slot Ampere turns as the original baseline design was maintained which led to some increase in torque. In the second, the magnitude of the current was iterated to achieve the desired output torque and the losses calculated for this modified current. Note that this analysis is initially based on 6 parallel paths transposed model equipped with pure copper. When the evaluation of copper conductor is finished, the optimal stator tooth

126

width and slot/conductor width can be determined and then the impact of non-linear magnetic wedges and hybrid windings will be evaluated again based on the new optimal designs.

A series of finite-element, time-stepped simulations were performed at 6,000rpm for a range of slot conductor widths between the original 8.94mm down to 5.94mm in 0.5mm steps. A summary of the results is shown in Table 3.21. The values of current density quoted are the nominal mean current densities in the conductors, i.e., externally driven rms current divided by the cross-sectional area of each series turn.

Table 3.21 Loss information for models equipped with pure copper and with reduced conductor width

Conductor width = 8.44mm					
	Quasi-static loss (W)	Total loss (W)	Ratio of total: quasi static loss	Torque (Nm)	Conductor rms current density (A/mm^2 rms)
Same current	2768	5997	2.17	575	14.6
Same torque	2557	5574	2.18	555	14.0
Conductor width = 7.94mm					
	Quasi-static loss (W)	Total loss (W)	Ratio of total: quasi static loss	Torque (Nm)	Conductor rms current density (A/mm^2 rms)
Same current	2941	5022	1.71	592	15.5
Same torque	2538	4334	1.71	555	14.4
Conductor width = 7.44mm					
	Quasi-static loss (W)	AC loss (W)	Ratio of total: quasi static loss	Torque (Nm)	Conductor rms current density (A/mm^2 rms)
Same current	3140	4523	1.44	606	16.5
Same torque	2578	3704	1.44	555	15.0
Conductor width = 6.94mm					
	Quasi-static loss (W)	Total loss (W)	Ratio of total: quasi static loss	Torque (Nm)	Conductor rms current density (A/mm^2 rms)
Same current	3366	4353	1.29	615	15.8
Same torque	2666	3427	1.28	555	17.7
Conductor width = 6.44mm					
	Quasi-static loss (W)	Total loss (W)	Ratio of total: quasi static loss	Torque (Nm)	Conductor rms current density (A/mm^2 rms)
Same current	3627	4408	1.21	622	19.1
Same torque	2801	3387	1.21	555	16.8
Conductor width = 5.94mm					

	Quasi-static loss (W)	Total loss (W)	Ratio of total: quasi static loss	Torque (Nm)	Conductor rms current density (A/mm² rms)
Same current	3933	4622	1.18	626	20.7
Same torque	2987	3502	1.17	555	18.1

As can be seen from table above, reducing conductor width and slot width and hence increasing the stator tooth width has significant beneficial impact on reducing winding losses despite the increase in the quasi-static losses. In terms of the effectiveness of reducing eddy currents, the 5.94mm wide conductor is the most effective, the difference between the total winding loss at 6000rpm and the quasi-static losses being only 17%. However, the lowest AC loss achieved is the 3387W of the 6.44mm wide conductor since although this is not quite as effective as reducing eddy currents loss it provides a better balance between reducing eddy currents and reducing the cross-sectional area. Compared to the quasi-static loss of 2214W for the baseline reference design, the increase is 51%.

The optimal conductor width and hence tooth width involves a balance between maximising the cross-sectional area of the conductor to minimise the quasi-static losses and reducing the induced eddy current losses. This is likely to result in the optimal tooth width being dependant on the fundamental electrical frequency and hence the rotational speed. To further evaluate the impact of different operating speeds, designs with the different conductor widths were solved from 1500rpm to 6000rpm in 1500rpm increments (equivalent to 75Hz to 300Hz in 75Hz increments). The variation of total stator copper loss as a function of conductor width is shown in the Figure 3.56. As can be observed, the optimal conductor width is 6.44mm at 6000rpm but increases to 6.94mm at 4500rpm.
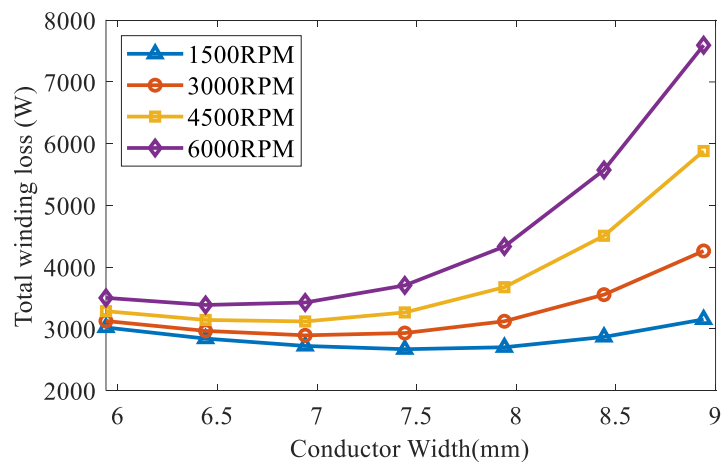
Figure 3.56 Predicted variation in total loss with various conductor width at different rotational speeds

In summary, adopting a combination of transposed and parallel strip conductors and a conductor width of 6.44mm has resulted in a design which now only has a 51% penalty when AC conductor loss is accounted for rather than the almost order of magnitude increase observed for earlier designs. This improvement in AC loss through various features has been achieved while maintaining the same torque and within the same volume envelope as the baseline reference design.

3.4.1 Revisiting the impact of magnetic wedge and hybrid winding based on existing optimal model

As found from section 3.3.4, the conductor width of 6.44mm gives very low AC/DC ratio of 1.21. In this section, two sets of simulations will be carried based on this optimized model, including the direct implementation of non-linear magnetic wedge MW2 introduced in section 3.2.2 and the hybrid aluminium and copper winding substitution strategy D1 introduced in section 3.3.3. The two variants are solved under rated condition and the loss comparisons are provided in the Table 3.22 below:

Table 3.22 The loss and torque comparison for optimized model equipped with magnetic wedge and hybrid windings

	Quasi-static loss (W)	AC loss (W)	Total loss (W)	Torque (Nm)
pure copper	2801	586	3387	555
magnetic wedge MW2	2801	626	3427	552
hybrid aluminium and copper	3248	455	3703	555

The progression of the design through the incorporation and optimisation of various features has necessarily meant that not all features were considered in the context of the optimised final design. As an example, magnetic wedges were considered for a non-transposed winding in section 3.2.2 which had unsustainable levels of loss. Although the drawbacks for inclusion of magnetic wedges far outweighs the benefits, for completeness, the performance of optimal design with 6.44mm conductor width was simulated with magnetic wedges made from MW2 which proved to be the most effective material in the studies of section 3.2.2. The resulting predicted total loss for this combination was 3427W which is higher than the same design without magnetic slot wedges. While for the case of implementing hybrid aluminium and

copper winding into optimized design, the increase of DC loss outweighs the reduction on AC loss, resulting total winding loss higher than that of pure copper model.

3.5 Summary of progression in total winding loss

The machine design established at the end of chapter 2 had an unsustainable level of winding loss of 22,016W at 6000rpm and rated torque, with induced eddy currents increasing the losses by a factor of ~9 from the quasi-static loss. By applying various AC loss mitigation strategies in this chapter, the lowest level of loss achieved at this operating speed for a machine with the same overall size is 3,387W, which is a near seven-fold reduction. Table 3.23 summarised the improvements made by the various design features.

Table 3.23 A summary for the variation of winding loss variations for different AC loss mitigation processes

	Design Stage	Total winding loss at 6000rpm and rated torque	Benefit from modification (all taking baseline from sizing stage as reference)
1.	Original baseline at end of the chapter 2	22,104 W	N/A
2.	Move conductor towards slot bottom from 0.6mm to 1.6mm	21,227W	-877W
3.	Implementation of magnetic wedge MW2	22,325W	+211W
4.	Paralleling of conductors and transposition		
	2 parallel paths fully transposed	12,106W	-9,908W
	3 parallel paths fully transposed	9,275W	-12,739W
	6 parallel paths fully transposed	7,595W	-14,419W
5.	Implementation of 0.14mm magnetic tape	7,394W	-14,620W
6.	Hybrid aluminium and copper winding substitution strategy D1	6,955W	-15,149W
7.	Increase stator tooth width and reduced slot width and conductor width (optimal conductor width =6.44mm)	3,387W	-18,717W

As can be seen from Table 3.23, except for one particular case of magnetic wedges, all the proposed AC loss mitigation processes are able to reduce the AC loss to some extent. Two strategies have been proved to be efficient to reduce AC losses: 1. The paralleling and transposition and 2. Widening the stator tooth and reducing the conductor width. With adoption

of widened tooth, the saturation level in stator tooth region has been reduced and hence the loss. One thing to note is that the nominal current density of widened tooth model has increased from 11.7A/mm^2 used in the sizing stage to 16.8A/mm^2 because of the reduced conductor size. But it still gives the lowest winding loss among all the proposed models.

In conclusion, the final optimized design is the 6 parallel paths fully transposed model with reduced conductor width. This model gives total loss of 3387W and the AC/DC loss ratio of 0.17.

3.6 Contributions to knowledge and publication

The ideas of adopting semi-magnetic wedge or magnetic tape were directly from literatures to evaluate its impact on the baseline machine proposed in this thesis. While for the novelties in this chapter, there are mainly three aspects:

- The concept of using diamond coil to reduce AC winding loss in medium size traction motor in aerospace application. Although the diamond coil was well-adopted in large size generator, its use in traction motor with reduced coil size has not been well researched and thus can be regarded as one of the major novelties.
- The investigation of alternative conductor materials including the use of pure aluminium bar or hybrid aluminium and copper diamond coils. It should be noted that using hybrid aluminium and copper hairpin coil in automotive section has been studied and published in several literatures. However, the adoption of hybrid aluminium and copper diamond coil which gives further freedom to mitigate AC losses remains not well-researched. It is thus another novelty of this thesis.
- The investigation of asymmetrical diamond coils. The concept of adopting asymmetrical coil was originally derived for hairpin winding in automotive sectors. However, the use of asymmetrical diamond coil is not well-researched and thus serves as another novelty of this thesis.

Based on the novelties introduced above, two papers were published:

[1] S. Yangyu and G. W. Jewell, "An investigation into the influence of stator tooth and conductor geometry on AC winding losses in a 365kW permanent magnet machine equipped with rectangular bar conductors," IET Conference Proceedings, vol. 2022, no. 4, pp. 52–57, 2022, doi: 10.1049/icp.2022.1072.

[2] Y. Sun, X. Chen, W. Zhu and G. W. Jewell, "An Investigation of Substituting Copper with Aluminium Conductors in a High Power, Medium Speed SPM Machine," *2023 IEEE Transportation Electrification Conference and Expo, Asia-Pacific (ITEC Asia-Pacific)*, Chiang Mai, Thailand, 2023, pp. 1-8, doi: 10.1109/ITECAsia-Pacific59272.2023.10372259.

Chapter 4. Litz wire

4.1 Introduction

Litz wire, which consists of a bundle of many fine parallel and transposed circular wires, is regarded as the most straightforward solution to AC losses. This type of wire was initially designed for high frequency transformers and applications such as induction heating but has found increasing favour in high-speed electrical machines recently because it can almost eliminate AC losses when the parameters of the Litz wire are carefully selected [55][15][13]. With the ability to almost completely eliminate AC losses, the fundamental frequencies can be pushed into the kHz range and hence operating speed of electrical machines can be set at well beyond 20,000RPM which in turn enables high power density over 20kW/kg to be achieved. Litz wire is often rolled and compressed to different types of profiles as shown in Figure 4.1:

Figure 4.1 Different types of Litz wire with different bundle shape (source: OSCO)

There are 8 different categories of Litz wire depending on winding pattern and bundle shape. One of the most popular types of Litz wire for electrical machines is the type 8 Litz wire which are rolled to have a rectangular cross-section. This type of Litz wire is well suited to rectangular slot geometry that is often seen in high-performance electrical machines. As well as offering a good solution in service, Litz wire can also act as a useful baseline for bar conductors by taking the dimension of bar conductor. The specifications of commercial Litz wire are made up of many parameters which variously indicate overall cross-section, number of parallel strands,

individual strand diameter and thermal class. As an example, Figure 4.2 shows a typical designation of a commercial Litz conductor.

Figure 4.2 Specifications of one particular type of 8 Litz wire from OSCO wires

The type 8 indicates that this Litz wire bundle has a rectangular cross-section. The AWG refers to the American Wire Gauge designation for wire dimensions from which the cross-sectional area of bare copper can be obtained from a standard look up table. In the example shown in Figure 4.2, the designation 22 x 20 means that this Litz wire bundle consists of 22 parallel strands of 20AWG wire, which from standard tables corresponds to an individual strand diameter of 0.812mm. The designation MW35-C indicates the wire meets thermal Class 200C NEMA MW 35-C/73-C and IEC Specification 60317-13 with a thermal rating 200°C. The 0.358" width (9.09mm) by 0.063" height (1.6mm) correspond to the overall rectangular cross-section of the conductor. Given this information of strand number, strand size and overall conductor size, the resulting packing factor within the cross-section of the Litz conductor can be calculated to be 78.2% in this case. Hence, this Litz wire has a 128% of the DC resistance of a solid copper bar conductor of the same overall dimensions.

An essential feature of Litz selection is the individual strand diameters which make up the conductor. In general, the effective packing factor of the conductor reduces as the number of strands increase and hence the DC resistance deteriorates with increased stranding. Moreover, increasing the number of strands is likely to have some cost implications. The selection of strand diameter is therefore a trade-off that depends on the operating frequency. In simple terms, selecting a strand diameter which is smaller than skin depth at the particular frequency of interest while noting the presence of harmonics, the resulting AC loss can be minimised. Several Litz conductor manufacturers also provide guidelines on the selection of strand diameter of Litz wire for a particular given frequency. By way of example, the guidelines for strand diameter selection from YDK (Korean Litz wire manufacturer) are shown in the Table 4.1.

Table 4.1 Guidelines on Litz wire strand sizing from YDK

Frequency	Individual strand diameter (mm)	Recommended wire gauge

60Hz to 1kHz	0.32	28 AWG
1kHz to 10kHz	0.25	30 AWG
10kHz to 20kHz	0.18	33 AWG
20kHz to 50kHz	0.12	36 AWG
50kHz to 100kHz	0.10	38 AWG
100kHz to 200kHz	0.08	40 AWG
200kHz to 350kHz	0.06	42 AWG
350kHz to 850kHz	0.05	44 AWG
850kHz to 1.4MHz	0.04	46 AWG
1.4MHz to 2.8MHz	0.03	48 AWG

As can be seen from the table, the guideline for strand diameter selection from YDK covers a very wide frequency range from 60Hz to 2.8MHz. It should be noted that for electrical machines in most applications, the fundamental operating frequency is unlikely to exceed 2kHz or so, although there may be significant harmonics present in the current waveform, including high frequency minor loops. Hence, guidance on frequencies into the several tens and 100s of kHz are of little relevance to electrical machines.

It should be noted that the benefits of Litz wire in reducing AC loss comes at the expense of diminished coil packing factor compared to a solid bar, which means establishing some standards that accounts for this change in packing factor is the key underpinning requirement for any analysis of the relative performance of Litz wire against solid bar conductors. The specifications for all the possible strand diameter and strand number combinations for type 8 Litz wire were gathered from a stock list and plotted as internal packing factor within the rectangular bundle (solid bar being close to 100% on this measure) versus the number of strands per unit area. The resultant plot is shown in the Figure 4.3 along with the corresponding second-order polynomial curve fit through the data. It is important to note that this measure of conductor packing within the rectangular profile is not the same as the net slot-fill which also accounts for slot liner, any separators, secondary tapes and an allowance of gaps.
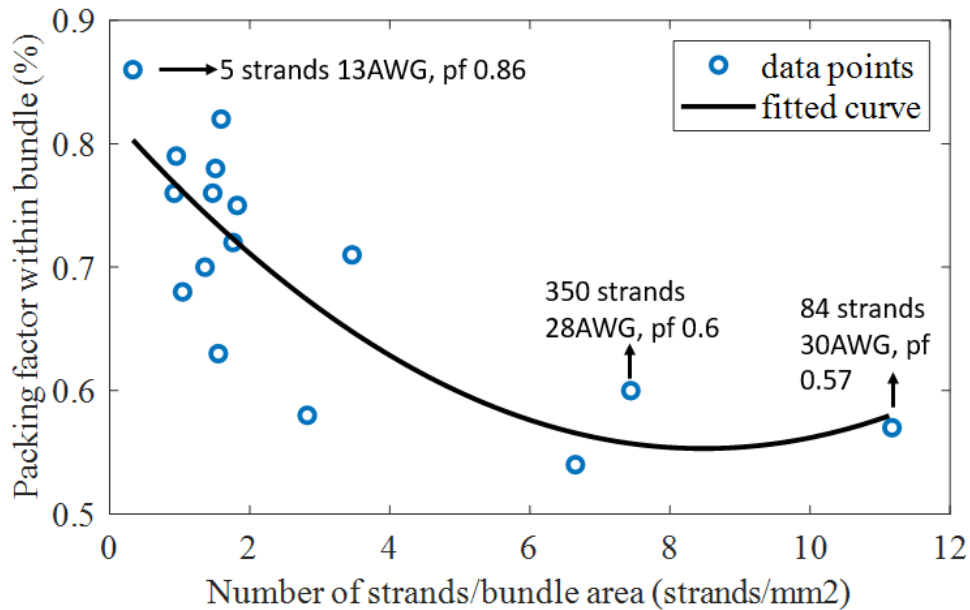
Figure 4.3 Different combinations of packing factor and strand diameter for type 8 Litz wire

Although based on data from a single supplier and there are significant departures from the resulting curve fit, this diagram nevertheless provides a quantitative means of establishing the impact on internal packing factor. Note that three data sets of type 8 Litz wire which has combination of extremely large strand number and small diameter are discarded because they are specifically designed for transformers. As can be seen from Figure 4.3, the abscissa represents the number of strands per bundle area. An increase of strand number will tend to cause a reduction in packing factor due to the additional spacing between strands and extra layers of insulations.

A long-established, if slightly simplistic, principle for selection of a particular composition of Litz wire is that the strands diameter should be less than skin depth at the frequency of interest. For the baseline machine operating at 300Hz, the selection of Litz wire is relatively unconstrained because the skin depth in copper is large (3.8mm) and requirement for strand diameter to be smaller than skin depth can be easily met. Based on the principle that strand diameter should be smaller than skin depth, the strand diameter is defined to be 0.4mm (similar diameter to AWG26). The selection on this particular diameter is mainly because the Litz wires with same dimensions are available from lab stock and hence gives potentials of future experimental validation.

With adoption of 0.4mm type 8 Litz wire, the assumption that no AC loss in Litz wire bundle is valid and thus the direct comparison between bar conductor and Litz wire can be made. The

packing factor within Litz wire bundle was calculated to be 0.6 from Figure 4.3. Given this estimate of conductor arrangement, the resulting DC loss can be readily determined. To demonstrate the penalty and benefits of Litz wire, Table 4.2 shows the two-dimensional, magneto-dynamic, finite element calculated losses for a variety of conductor arrangements from which the very significant, and indeed unsustainable AC loss penalty of employing a solid copper bar winding is clearly evident.

Table 4.2 Loss and packing factor comparisons for models equipped with different paralleling number and Litz wire

Parallel paths	Quasi-static loss (W)	Total conductor loss (W)	Overall slot-fill factor
1	2214	22016	0.79
2	2284	12106	0.77
3	2358	9275	0.75
6	2613	7595	0.67
Litz wire	3690	3690	0.40

It is interesting to note that the total winding loss in Litz wire is 3690W, which is based on the simplified assumption that the AC loss can be reduced to zero is comparable to the best-case bar winding as seen in section 3.4 when an all-copper winding was configured with 6 parallel paths of 6.44mm wide strips.

The previous analysis is based on a simplified assumption that the AC loss in the Litz wire bundle is zero. However, in a realistic Litz wire, the AC loss in Litz wire bundle cannot be assumed to be zero. To establish comprehensive understanding of loss behaviour in Litz wire, the various sources of different loss components in Litz wire need to be considered in turn. The induced eddy current loss inside of Litz wire can be divided into four different categories:

- Strand level skin effect
- Turn level skin effect
- Strand level proximity effects within a turn
- Inter-turn proximity effect

It should be noted that in a commercial Litz wire, all the strands are assumed to be insulated and continuously transposed along length direction with full transposition over a specified pitch. This means that in most cases all strands share the injected current equally. However, there may be some uneven current sharing if the pitch of the transposition is longer than the axial

length of the stator core since there is a significant difference between the reactance of the end-winding and the slot region. In this chapter, the perfect Litz wire is assumed and thus the bundle level skin and proximity losses are neglected. To fully capture the induced eddy current loss in Litz wire bundle, there are various methods available, including:

- Pure analytical models
- Numerical analysis with detailed FEA modelling
- Semi-analytical models
- Homogenisation methods

There are numerous published analytical models for estimating the loss behaviour of Litz wire. One-dimensional Dowell's equation was proposed in [90] to predict AC winding resistance in a transformer. An equivalent square conductor sheet is used to approximate round conductors. J. Ferreira [91] and M. Albach [92] used Bessel functions to account for curvature and thus directly calculated the eddy currents for round conductors when they are exposed in air with a two-dimensional (2D) analytical solution. Based on the above methods, several other papers further improved the analytical methods by accounting for slot leakage, fringing effect, 3D effects etc [93] [94] [95].

Numerical models, specifically an FEA model with a full representation of the winding geometry that accounts for every strand is generally regarded as the most rigorous and accurate method to predict loss behaviour in Litz wires. However, there are two well recognised problems associated with detailed modelling of Litz wire using FEA. Firstly, a fully representative model in FEA software could consist of thousands of strands, which makes the modelling very challenging in terms of model build time, memory requirements, solution time. Secondly, to fully capture the induced eddy current loss in Litz wire, the mesh quality of each strand needs to be sufficiently fine to faithfully represent the steep field gradients which can occur within an individual conductor. Achieving an appropriate level of discretisation in Litz wire is already challenging in a 2D context. When end-winding region is also accounted for in a 3D simulation, the modelling is even more challenging.

To reduce the modelling and computational complexity associated with a fully representative FEA modelling model and yet approach the accuracy of a full FEA solution, the idea of semi-analytical has been proposed in [62][96][97] amongst others. Such methods are based on using field solutions which neglect the stranded nature of the winding to extract localised flux density variation and then substitute those flux density waveform into analytical equations to predict

winding losses. One drawback of such semi-analytical methods is that the eddy current reaction field is not taken into consideration, which means that there is a limited frequency range over which such approach provides a reliable representation of the loss.

Another set of methods to simplify the loss prediction process in Litz wire are so-called homogenisation methods. The idea of homogenisation was first developed in frequency domain calculation [98][99][100]. In the homogenisation process, the Litz wire bundle is modelled as homogeneous region using frequency dependent resistivity and complex permeability. This allows the AC loss in the bundle to be calculated using a steady-state AC solver. Time domain homogenisation techniques have been proposed in [101][102]. This is an attractive approach since the eddy current reaction field is accounted for and there are no demands on strand level mesh quality. One constraint to note is that homogenisation technique requires winding to have a specified minimum number of strands among width and height direction to satisfy the boundary conditions.

The homogenisation method has been implemented in commercial packages, including the Altair FLUX package used extensively in the research reported in this chapter and a semi-analytical model has been adopted in ANSYS Maxwell. An evaluation of these two computationally efficient methods is provided later in section 4.3 and 4.4.

The focus of this section is to evaluate potential benefits and drawbacks of three Litz wire modelling techniques, viz. a detailed strand model, a homogenisation model and a semi-analytical model. It is reasonable to assume that a model which accounts for every strand of Litz wire individually is likely to provide the most accurate method to predict the AC loss providing the individual strands are represented with suitably fine mesh. However, as will be demonstrated in this chapter, such an approach results in very large numbers of mesh elements which in turn make computation very onerous, especially in 3D where it is currently prohibitive. The results generated by a 2D detailed strand-by-strand model were used as reference to make comparison with homogenization and semi-analytical techniques.

4.2 Direct FEA modelling of a 2D motorette model

The detailed modelling of Litz wire accounting for every strand is very time-consuming and challenging to implement in FEA software. A full machine equipped with Litz wire often consists of several thousand or even tens of thousands of individual strands, which means the geometrical representation of those strands will be problematic even when periodicity is exploited. In addition, to fully capture the skin and proximity effect, each strand of Litz wire

needs to be finely discretised. This combination of a very large number of finely discretised conductors poses significant computational challenges because of the very large mesh size. Moreover, the building of a corresponding coupled electrical circuit can also be extremely demanding when the number of solid conductors is high.

An alternative method is to establish some generic understanding of Litz wire modelling on reduced and often simplified problem domains and then apply the arising findings and principles to machine level simulations. The simplified model used in this study consists of two slots, one complete stator tooth and two half tooth sections. This type of arrangement and is often referred to as motorette model. Such motorette models are often solved with a steady state sinusoidal AC excitation. The stator core of motorette model used in this study is shown in Figure 4.4.
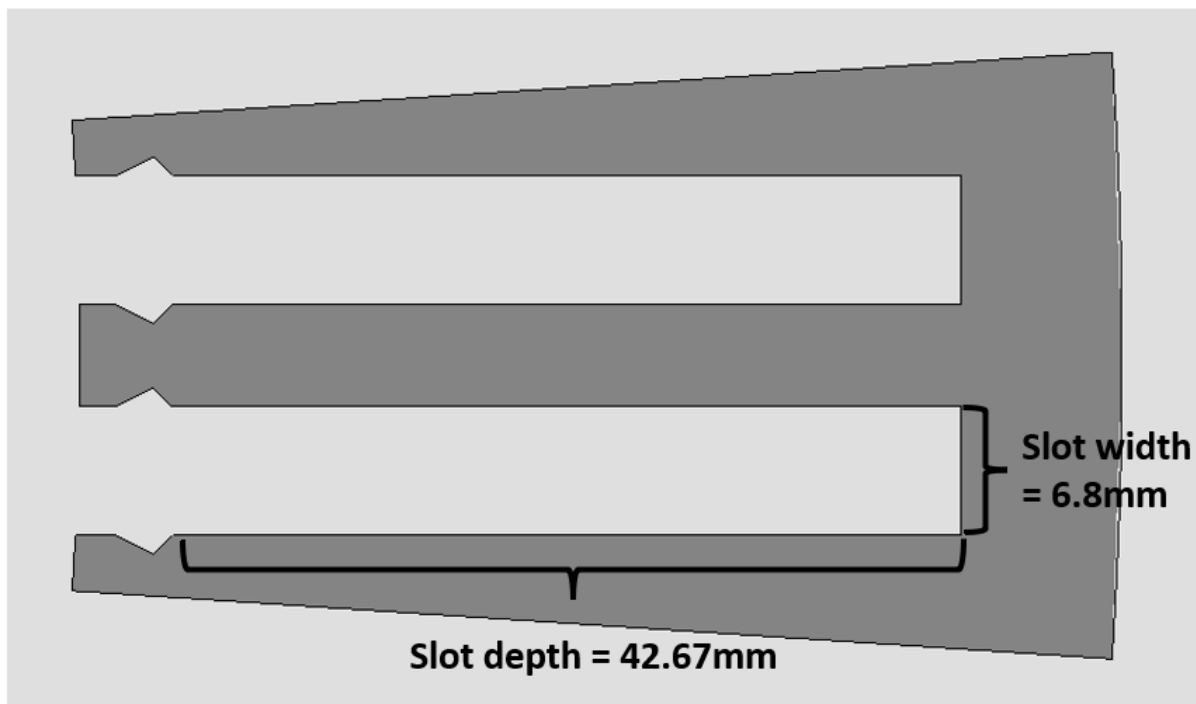
Figure 4.4 Geometrical view of proposed motorette stator core

There are two things to note for this motorette stator core:

- The form of a standard motorette for experimental testing is usually 2 slots and 2 teeth as shown in Figure 4.4 but the minimum repeating unit which best represents the full machine depends on the winding pattern. For baseline reference design which has a 36 slot 6 pole distributed winding with coil pitch of 6 slot, the minimum number of slots for a fully representative motorette model would consist of 7 slots instead of the 2 slots

of the geometry of Figure 4.4. To simplify the initial modelling process, the motorette stator core of Figure 4.4 was assumed to be fitted with a concentrated winding. Although the stator dimensions and winding pattern of motorette model are different from the baseline geometry, the corresponding modelling skills and AC loss analysis still serve as a good reference for further evaluation of the machine level strand model.

- This motorette stator core was available as existing item of hardware which was made available to this project for experimental validation.

- The axial length of the motorette hardware is 300mm long which makes it well suited to 2D analysis and ensures that the quasi-static loss is of sufficient magnitude to be reliably measured.

The Litz wire bundle to fit this motorette needs careful design. The guiding principles adopted were that that bundle should have sufficient cross-section to achieve relatively high packing factor and the strand diameter should be smaller than skin depth. However, it is important to recognise that customised Litz is often difficult to source because the set-up cost for a particular combination of number and diameter means that large minimum orders are often in the 100s of kg. Fortunately, a large drum of existing Litz wire which was a good fit to the motorette stator was available. This was a legacy on old project [103] and had a bundle size of 5.6mm×3.8mm. The bundle is comprised of 115 strands of 0.4mm diameter and 10 turns of Litz wire bundle are necessary to fill the slots in the motorette.

To build the detailed strand by strand model, the winding pattern and spacing between strand are required. In principle a stochastic model could be deployed [104] which includes a simplified representation of randomness within the conductor cross-section, but in this case, the scripting of the model was more conveniently done with a regular winding layout. There are two types of winding arrangement that provide a simple but still reasonable representation of a multi-strand bundle, viz. rectangular or hexagon patterns, as shown schematically in Figure 4.5 and Figure 4.6.

Rectangular pattern
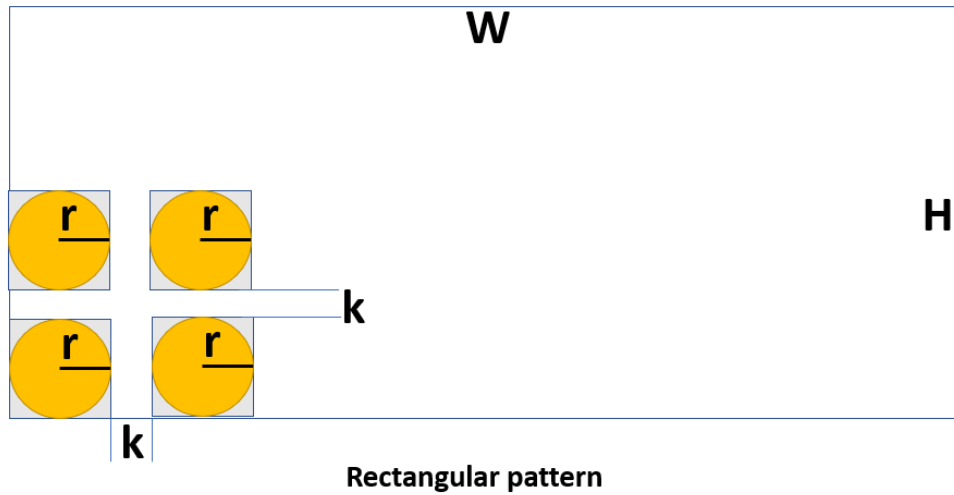
Figure 4.5 Rectangular pattern for type 8 Litz wire
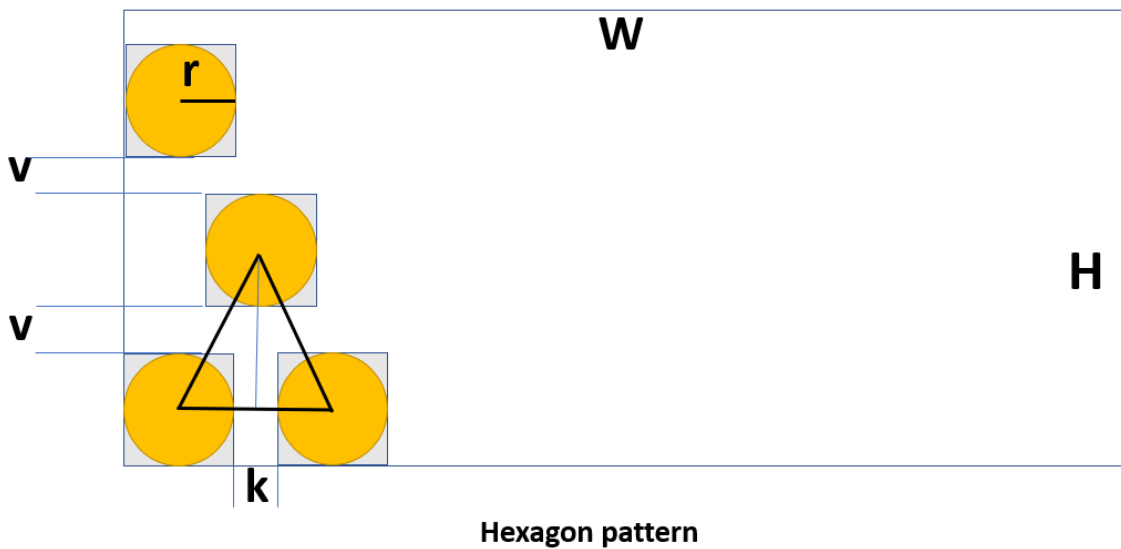
Hexagon pattern

Figure 4.6 Hexagon pattern for type 8 Litz wire

The symbols W and H represent bundle width and height respectively. The parameter k in rectangular pattern represents both the horizontal distance and vertical distance between strands, while in the case of hexagonal pattern, k represents horizontal distance only and the vertical distance is denoted by the parameter v. With all the parameters defined properly, given a bundle cross-section (W×H), strand diameter (2r), distance between strand (k and v), the maximum number of strands per bundle can be determined for both rectangular and hexagon pattern. For rectangular pattern, the theoretical maximum number of strands per bundle can be obtained by setting k=0. While for hexagon pattern, the theoretical maximum number of strands per bundle can also be determined by setting k=0. The vertical distance v can be expressed as a function

of k, which is $v = \frac{\sqrt{3}\times(2r+k)}{2} - 2r$. It should be noted that when setting k=0 for achieving maximum number of strands, the vertical distance could be a negative value.

The maximum number of strands that can be put into a specified bundle size for different winding pattern is parameterized in MATLAB and this program is also capable of accounting for insulation layers of each strand and variation of spacing between strands. The predicted maximum number of strands for 5.6mm × 3.8mm bundle size and 0.4mm strand diameter with different spacing between strands for rectangular and hexagonal patterns are shown in Table 4.3 and Table 4.4. The detailed winding arrangements for a specific case of h=0 for rectangular and hexagon pattern are plotted in Figure 4.7 and Figure 4.8, respectively.

Table 4.3 Predicted maximum number of strands per bundle with different distance --- for rectangular pattern

k (mm)	k (mm)	Total strand number per bundle (N)	Strand diameter (mm)	Bundle area (mm²)	Total strand cross-sectional area (mm²)	Effective packing factor
0	0	117	0.20	21.28	14.70	0.69
0.02	0.02	117	0.20	21.28	14.70	0.69
0.05	0.05	96	0.20	21.28	12.06	0.57
0.07	0.07	96	0.20	21.28	12.06	0.57
0.1	0.1	77	0.20	21.28	9.68	0.45

Table 4.4 Predicted maximum number of strands per bundle with different distance --- for hexagon pattern

k (mm)	v (mm)	Total strand number per bundle (N)	Strand diameter (mm)	Bundle area (mm²)	Total strand cross-sectional area (mm²)	Effective packing factor
0	-0.0536	130	0.20	21.28	16.34	0.77
0.02	-0.0363	125	0.20	21.28	15.71	0.74
0.05	-0.0103	108	0.20	21.28	13.57	0.64
0.07	0.007	104	0.20	21.28	13.07	0.61
0.1	0.033	84	0.20	21.28	10.56	0.50
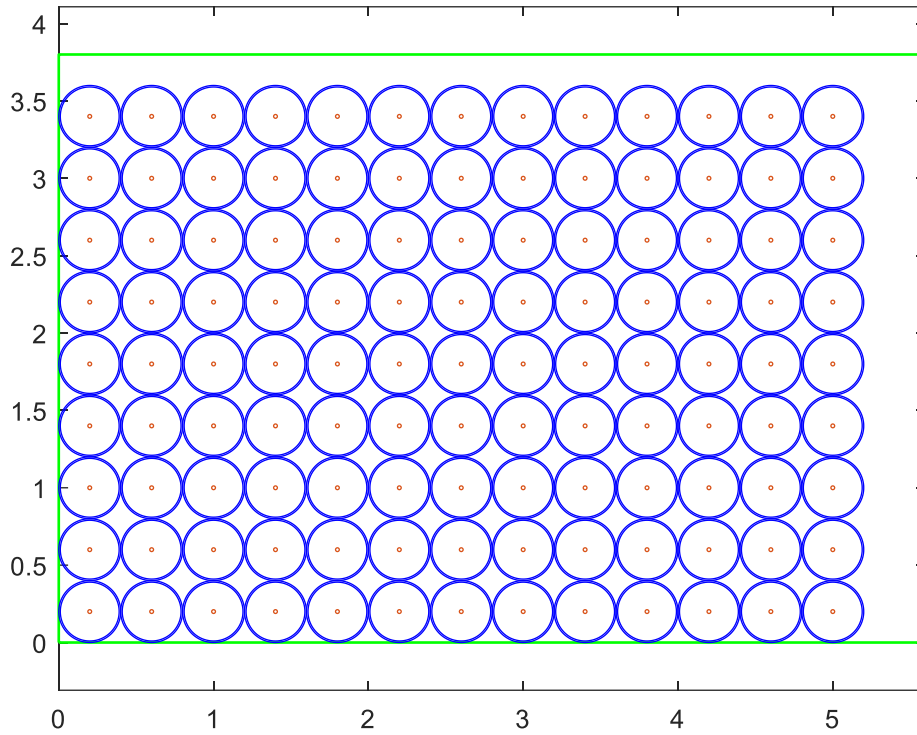
Figure 4.7 Theoretical maximum number of strands for bundle size of 5.6mm×3.8mm with rectangular layout
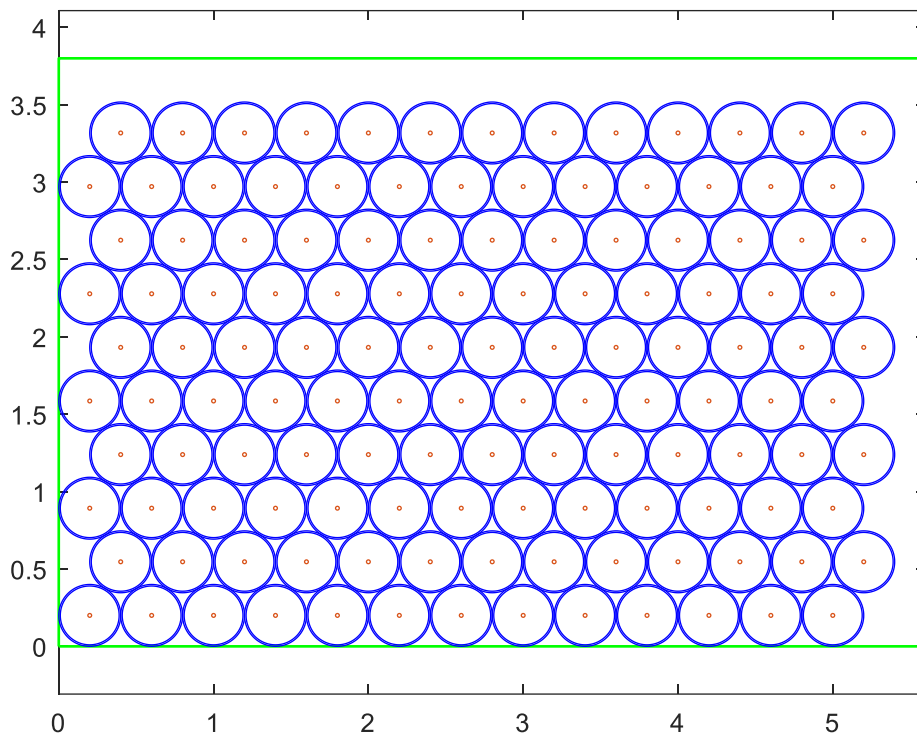
Figure 4.8 Theoretical maximum number of strands for bundle size of 5.6mm×3.8mm with hexagon layout

There are several observations can be made from the analysis of the winding pattern:

- The theoretical maximum number of strands achieved by hexagonal arrangement is higher than that of rectangular arrangement. For example, when distance between

strands is zero, the number of strands for hexagon and rectangular layout are 130 and 117 respectively. The values compare with the actual number of strands in the available Litz wire is 115.

- There are certain cases in hexagon winding layout that the vertical distance between strands is negative.
- To build the detailed Litz wire bundle, either rectangular pattern with horizontal distance of 0.02mm or hexagon pattern with horizontal distance between 0.02mm to 0.05mm can be used.
- The insulation coating of each strand can be accounted for by adding one extra layer of thickness into the original strand, see Figure 4.9 below:
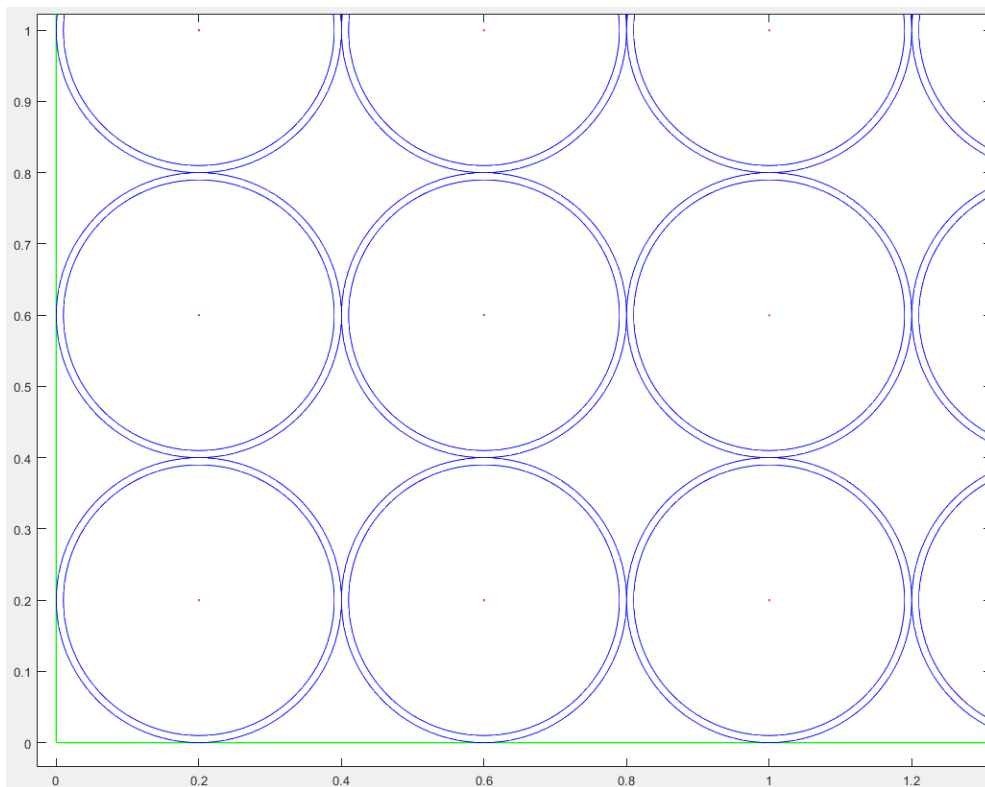
Figure 4.9 A zoomed-in view of Litz wire bundle with consideration of insulation layer

The rectangular layout is selected for building detailed model in FEA software. The motorette model equipped with 10 turns of Litz wire together with its specifications are provided in the Table 4.5 below:

Table 4.5 Geometrical view of proposed motorette model and its specifications

Specifications
Strand diameter (pure copper): 0.400mm
Number of strands per bundle: 115
Number of turns per slot: 10
Bundle size: 5.6mm×3.8mm
Winding layout: rectangular
Axial length: 300mm
Current injected per strand: 0.5A rms
Stator material: M250_35A_50Hz
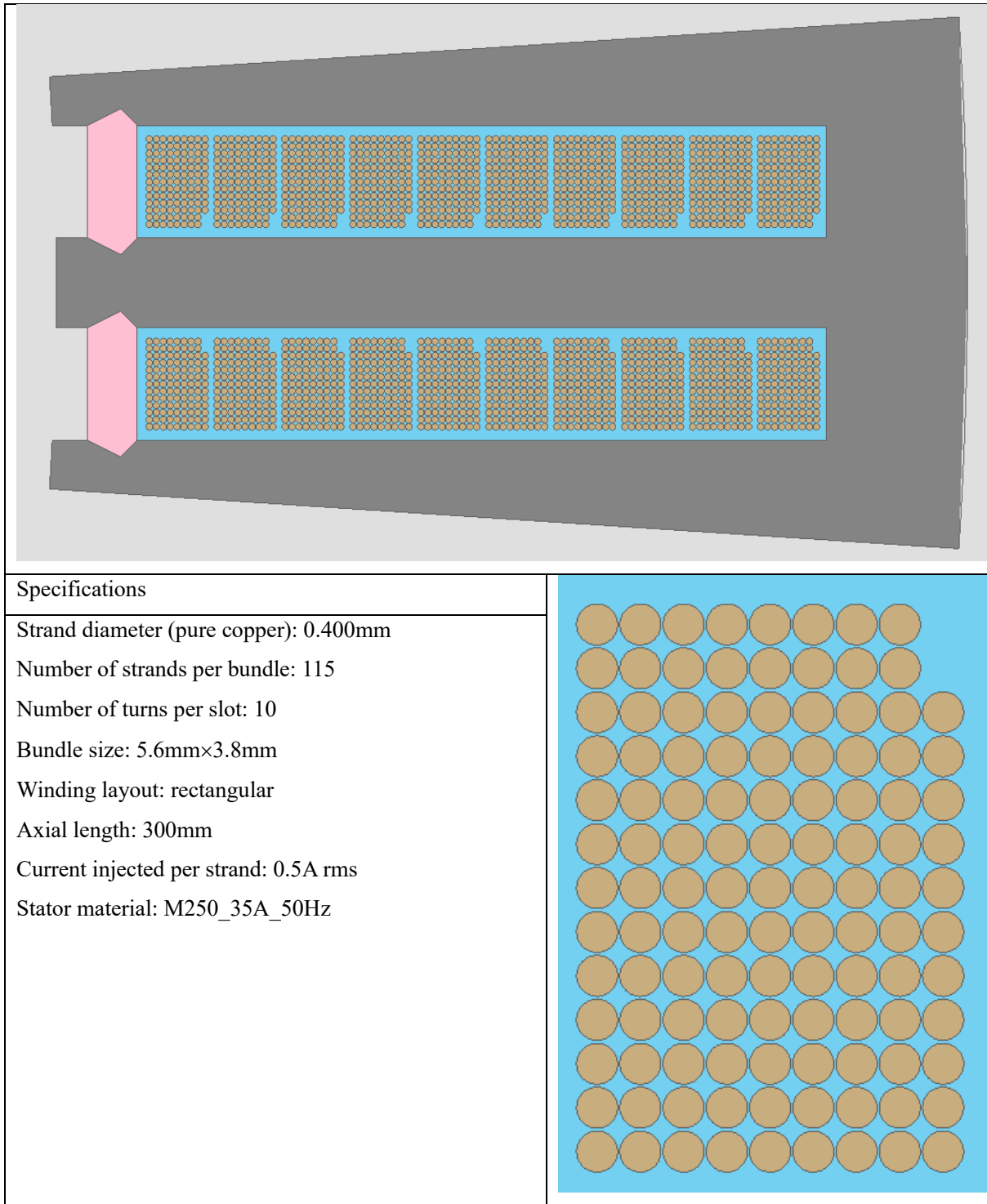
Note that the stator material used in this motorette model, viz. M250_35A_50Hz, is not same as baseline model from previous sections (Hiperco50). This is because this motorette model is based on a prototype that has already been manufactured for experimental validation using Silicon iron. Strand level insulation is not accounted for in electromagnetic FEA modelling to reduce computational time because it has no impacts on prediction of AC losses. Although the

motorette model is already a simplified representation, the total number of strands is still very high at 2300 (115×10×2). The high number of strands gives further challenge in building the finite element coupled electrical circuit because same number of solid conductors are required, and every single circuit element needs to be linked to its corresponding geometrical region in the finite element model. To perform this repetitive task in a reliable manner the built-in Python script feature in FLUX2D was used to code an automated task. The electrical circuit associated with the motorette model is shown in the Figure 4.10, which consists of 2300 solid conductor circuit elements and 115 current sources.
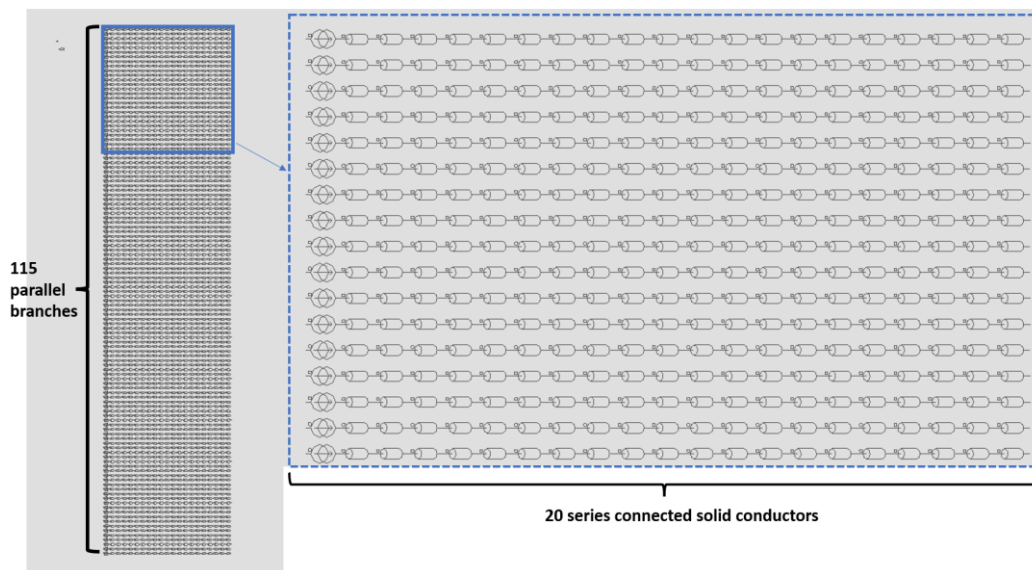
Figure 4.10 Electrical circuit of motorette model

The 10 turns of Litz wire are connected in series. To ensure equal current sharing among strands, the 115 strands of specified Litz wire bundle are connected in parallel with corresponding current sources in each branch. In this way, the current in each branch is forced to be same and thus the requirement of equal current sharing is satisfied. In each case, the current in each branch is 0.5Arms which corresponds to an equivalent current density of ~5A/mm^2.

Following the configuration of the coupled electrical circuit, the next step was to generate the finite element mesh that can capture skin and proximity effect within the 2300 strands. There are two ways of meshing in Flux software: automatic mesh and manual mesh. The automatic mesh option will generate reasonably good mesh for the whole model depending on the size of various face regions. While for the manual mesh, it allows for accurate control of mesh density in certain regions with the help of mesh points and mesh lines. The manual mesh method gives possibility of modifying the meshing setting based on the objective of simulations. For example,

if the focus is on cogging torque, then the airgap region can be meshed manually to have extreme fine discretization while for the other regions, the mesh quality can be reduced slightly. In this way, the simulation accuracy can be guaranteed with reduced solving time. But this method requires additional knowledge and familiarity of software and is thus not friendly to new users. In this analysis, the automatic mesh which gives good mesh quality is adopted and the mesh plots are provided in the Figure 4.11 and Figure 4.12 below:
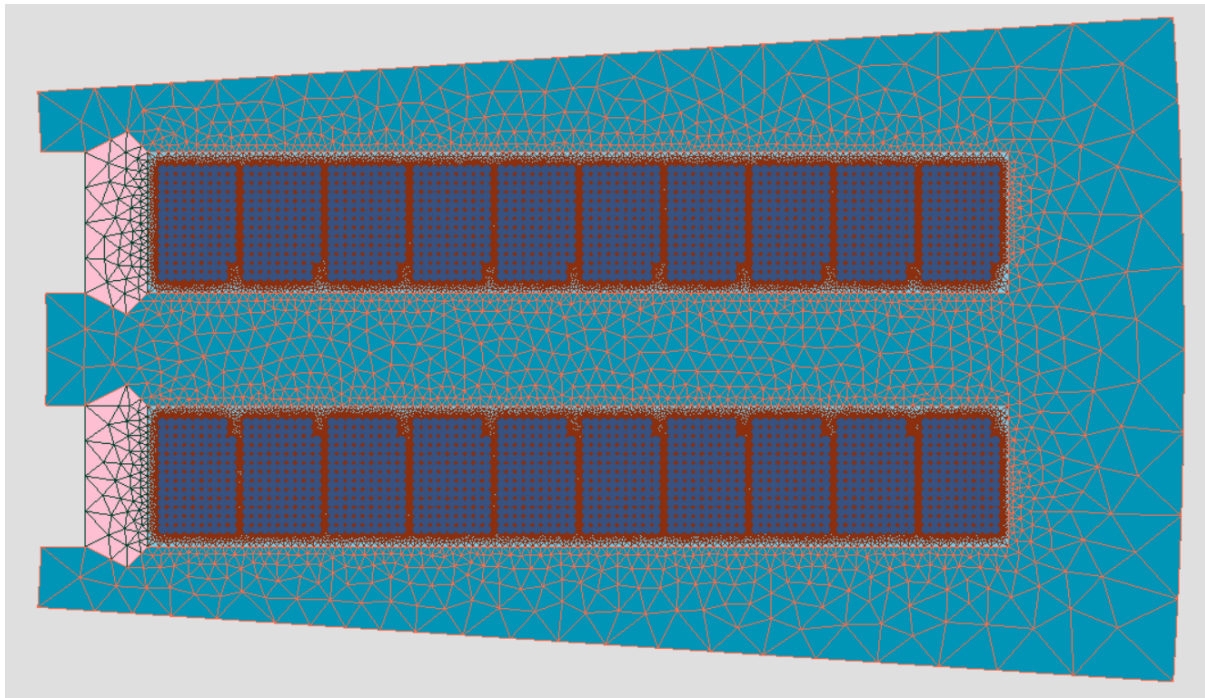
Figure 4.11 Mesh plot of motorette model
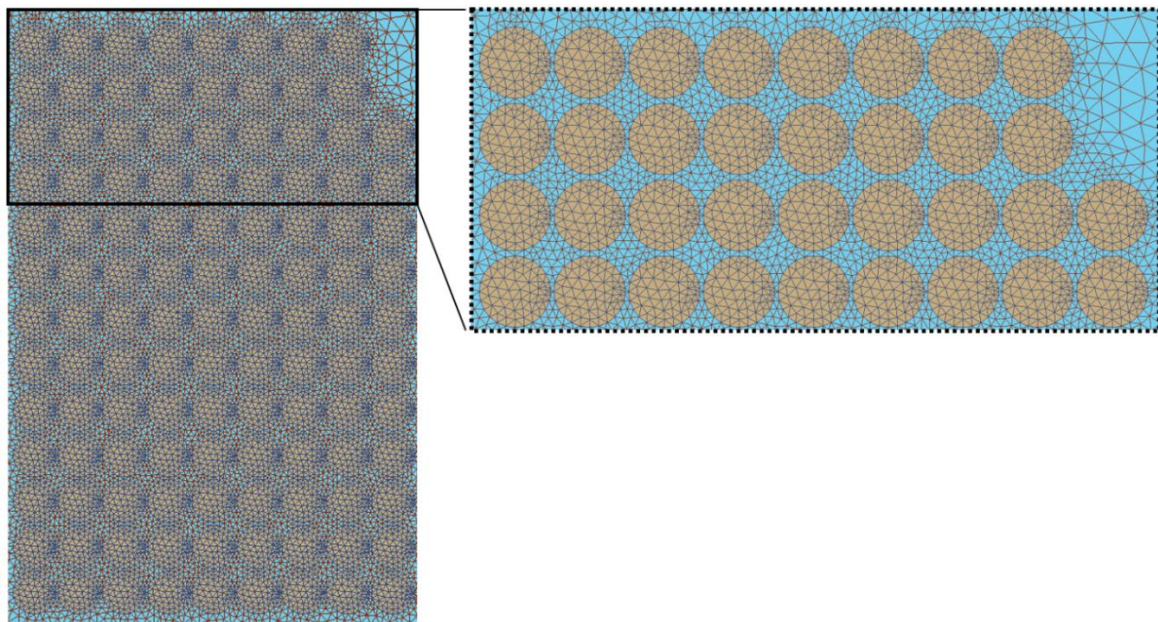
Figure 4.12 Zoomed-in view of mesh plot for one particular bundle

148

The model was simulated with steady state AC excitation model in which the stator core was assumed to be non-conducting and with imported B-H curve from manufacturer. The frequency of the excitation was varied between 0.001Hz (DC) and 2000Hz in 100Hz increments. The resulting winding losses are shown in Figure 4.13. The only quantity calculated directly by the finite element simulation is the total loss. The 'DC loss' is calculated from the conductor cross-section and length and resistivity and remains constant throughout the frequency range and the quantity 'AC loss' is simply the difference between the total loss and the DC loss. It is recognised that this superposition of components is rather simplified given the complex nature of reaction fields etc and non-uniform current distribution, but it is nevertheless useful in terms of drawing out the frequency dependant contribution to the loss.
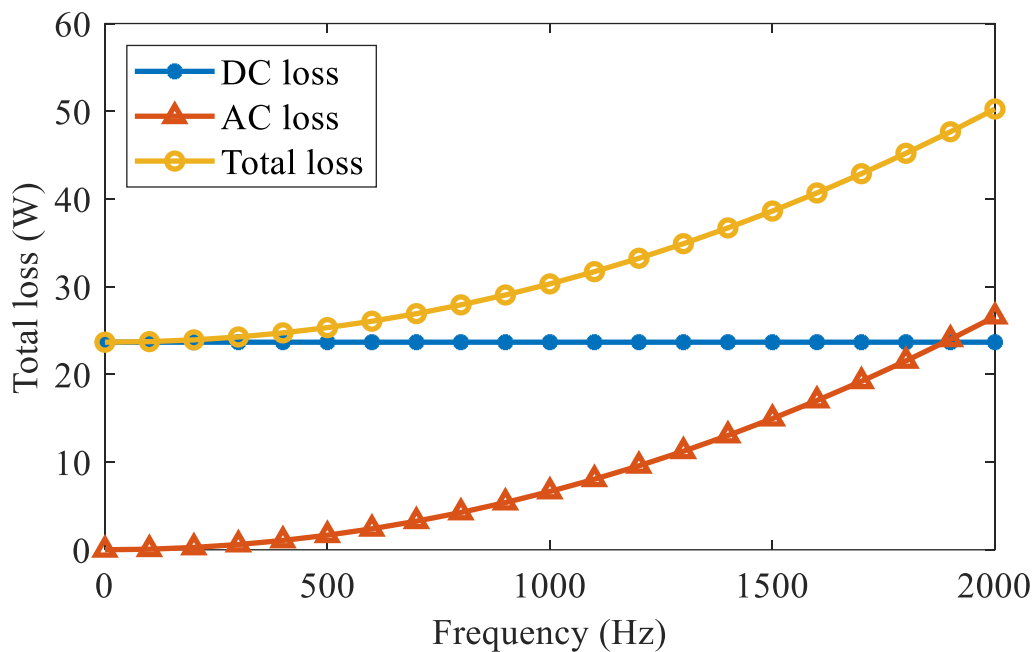
Figure 4.13 Frequency versus total loss curve for 2D detailed motorette model

The current density distribution at the baseline reference rated frequency of 300Hz is shown in Figure 4.14. The turn number is indexed from 1 to 10 from slot opening towards the back of the slot. The zoomed-in view of current density distribution of turn 1,4 and 10 are shown and it is evident that the current density distribution within strands is not uniform. As would be expected, the effect of non-uniform current density distribution is more significant in the conductors near slot opening due to the higher cross-slot leakage flux. It is interesting to note that event at 300Hz (which corresponds to the rated speed of the baseline reference design), the loss in this particular Litz wire model is 103% of the quasi static loss, which demonstrates that the zero AC loss assumption for Litz used towards the start of this chapter is rather

optimistic and that adopting a Litz wire is by no means guaranteed to eliminate AC loss penalties.
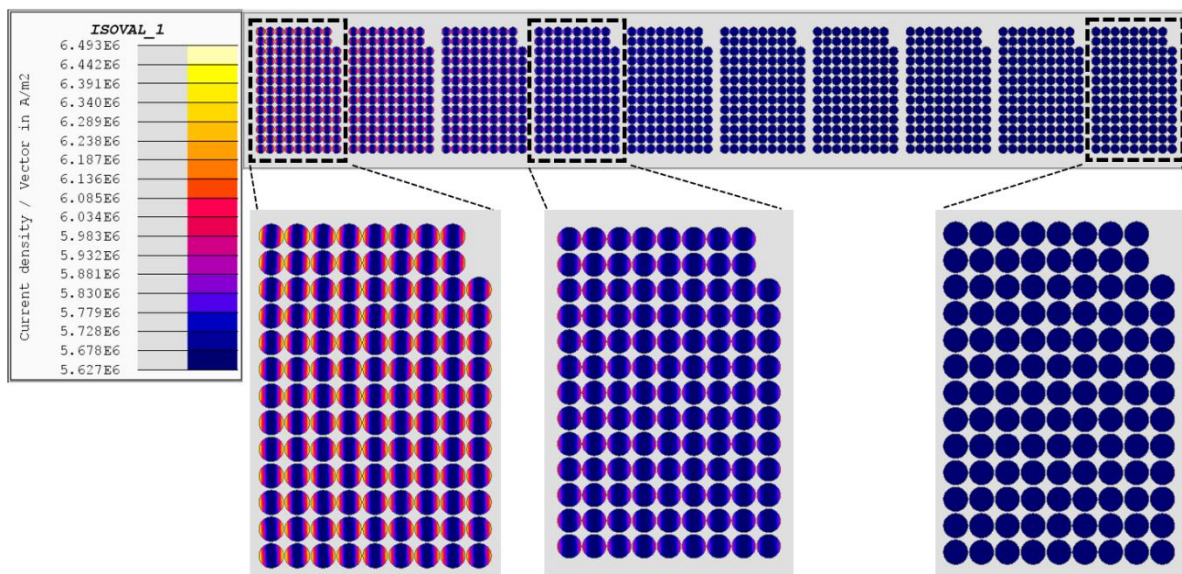
Figure 4.14 Current density plot of motorette model at 300Hz

4.3 Two-dimensional homogenisation model

The homogenisation method represents Litz wire as a homogeneous region with frequency dependent resistivity and complex permeability and has been adopted for models equipped with large number of strands. The homogenisation is based on the fact that the large number of strands in a Litz wire is arranged in the bundle with specified pattern, which means the resultant eddy current reaction field must exhibit periodic patterns. With adoption of this model, the Litz wire region can be considered with homogenised resistivity and complex permeability and hence discretisation at strand level is no longer necessary.

The implementation of homogenization techniques usually comprises two stages: pre-processing followed by corresponding FE analysis of the homogenised model. In the pre-processing stage, a single conductor model with periodic boundary conditions is used to calculate the skin effect loss and the corresponding R_{AC} to R_{DC} ratio is used to determine equivalent resistivity. For the complex permeability, a quarter of strand conductor model is used with a specified external H field as boundary condition and the resultant ratio of B and H is used to determine the complex permeability. Both of the models are performed using a steady state AC solver. In the second stage of homogenisation method, the complex permeability properties are assigned to coil material property and the model is ready to solve for proximity loss. When the calculation of proximity loss is completed, the previously calculated skin effect

150

resistance is added into the diagonal elements of resistance matrix to fully assess the skin and proximity loss in the homogeneous region.

As mentioned earlier, Altair FLUX2D has dedicated built-in homogenisation feature for Litz wire AC loss calculations. To use this feature and fully capture the skin and proximity effect, a stranded coil conductor is used to couple the region and the circuit element instead of the solid conductor element used in the FEA detailed strand model used in the previous section. The detailed setting of homogenised coil conductor region is shown in Figure 4.15.
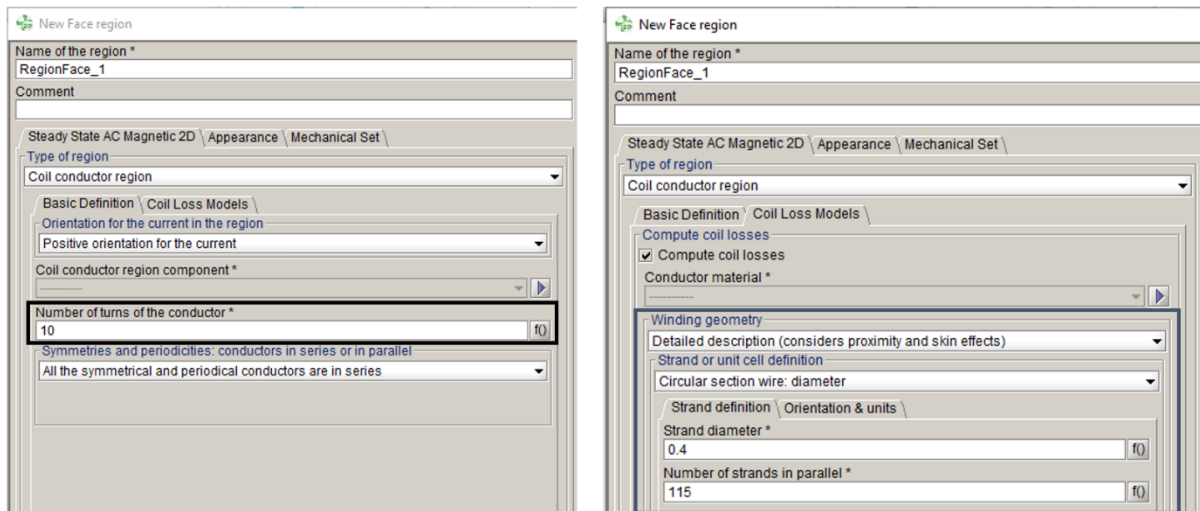
Figure 4.15 Detailed setting of homogenization method in Flux

One interesting feature of homogenisation method is that unlike a detailed strand model where the precise position of strands and bundles is essential, the relative position of strands and bundles are not required. Instead, the only requirement for coil conductor region is to have sufficient area to accommodate all the specified strands. The geometrical view of equivalent homogenisation model is shown in Figure 4.16.
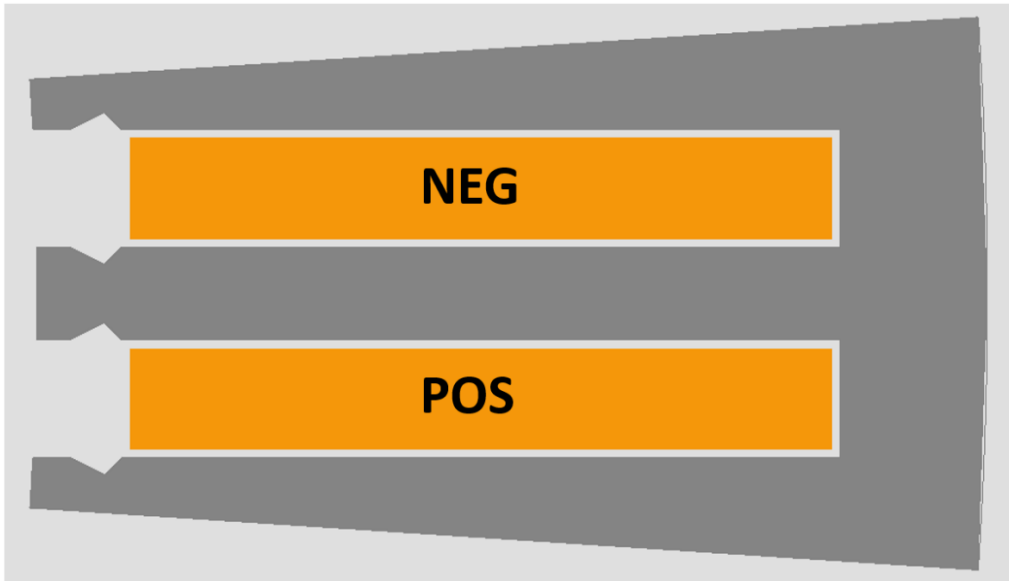
Figure 4.16 Geometrical view of equivalent homogenization model

Since detailed strand representation is not required in homogenization method, the corresponding electrical circuit has been simplified significantly as shown in Figure 4.17.
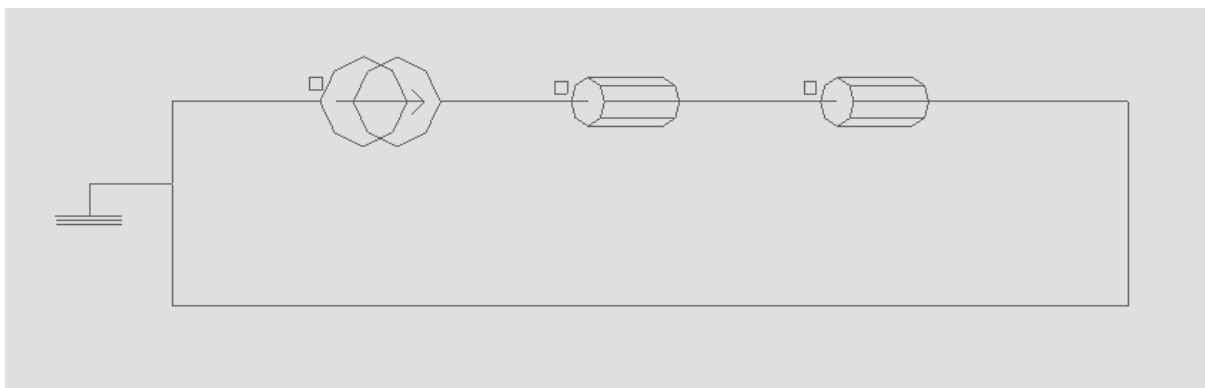
Figure 4.17 Electrical circuit of homogenization model

The electrical circuit for homogenization method only contains one current source and two coil conductors. Note that the amplitude of injected current needs to be multiplied by the number of strands, in this case 115, to ensure same current in each strand. The mesh requirements for a homogenisation model are not very demanding in terms of fine discretisation and hence the automatic meshing tool can used to generate the mesh shown in Figure 4.18.
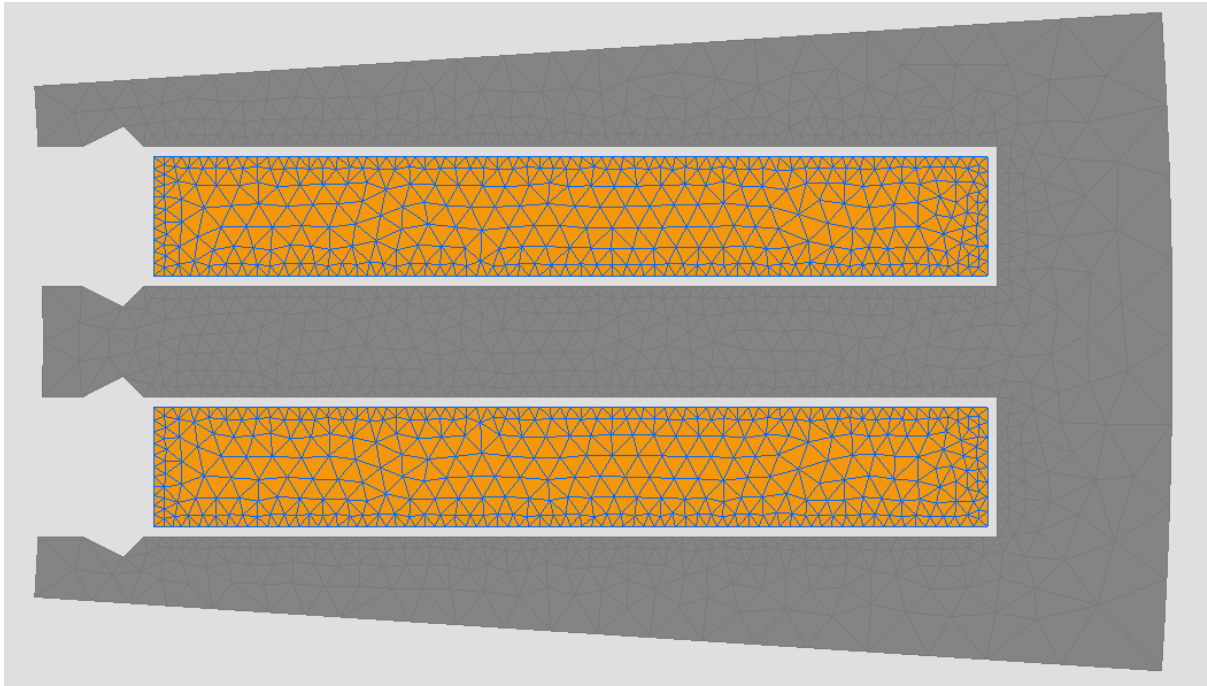
Figure 4.18 Mesh plot of homogenization model

It is apparent that the adoption of homogenisation method reduces modelling and solving time significantly by reducing the efforts associated with geometrical modelling, the specification of an electrical circuit and the overall number of mesh elements. However, there are several things to note about this method:

- One major limit for Flux v2022.0 is that it only works with steady state AC solver and is not compatible with a time-stepped transient magnetic solver. Although the official documentation claims it can be used in transient solver, this feature has been checked and the results are unreliable, which means this feature should only be considered in steady state AC solver at this stage.

- To deliver accurate prediction of winding losses, the coil conductor region must have sufficient number of elementary cells in the coil width and height direction. Specifically, the number of elementary strands needs to be more than 10 in those directions. This condition is largely satisfied in most of electrical machines equipped with Litz wire because both the number of strands is usually relatively large because of the high currents involved.

- The equivalence between non-homogenised and homogenised representation is not exact. Although the homogenization preserves the Joule losses and the stored magnetic energy, the evaluated eddy current density varies from that of detailed strand model. In

153

other words, the current density computed in a homogenization coil conductor region is not directly comparable to the detailed strand model.

A series of simulations were performed with the homogenised model with a 2D steady state sinusoidal AC solver using exactly the same the model geometry, boundary conditions, current settings as used in the detailed strand-by-strand FE model. The frequency was varied between 0.001Hz (representing quasi-static loss) and 2kHz. The resulting total winding loss as a function of frequency is shown in Figure 4.19 alongside the corresponding predictions from the detailed strand-by strand FEA model. As can be seen, the winding losses predicted by homogenization method is in excellent agreement with that from the detailed strand-by-strand model. It is interesting to note that the total solving time over all the frequencies for detailed strand model and homogenization models are 2 hours and 5 minutes respectively. This reduction in solving time is expected because of simplification in the geometrical representation of winding and hence and mesh. The total number of elements in the finite element meshes are 416,344 and 5,040 for the detailed strand-by-strand model and the homogenised model respectively.
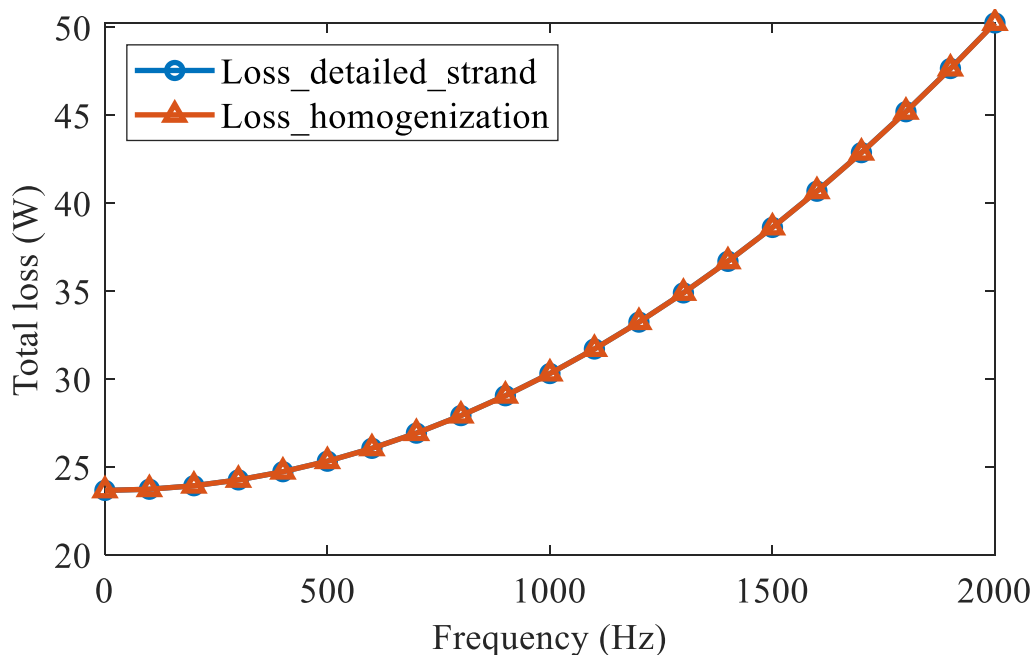
Figure 4.19 Loss comparison between detailed strand model and homogenization model over sweeping frequencies

The predicted current density distribution in the homogenised model is shown in Figure 4.20. As can be seen, there is a uniform current distribution in the homogenised model which is equal to the externally driven current divided by the conductor cross-sectional area. This is to be expected because the resulting Joule loss is accounted for by frequency dependent resistivity

154

and complex permeability, both of which will not affect the source current density in FEA predictions.
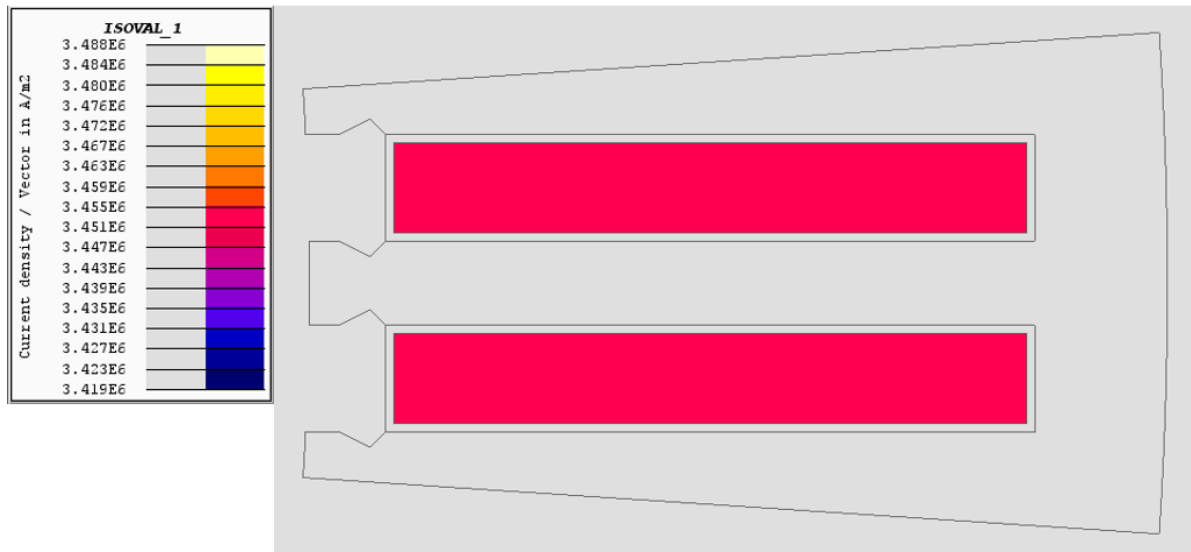
Figure 4.20 Current density plot of homogenization model

4.4 2D semi-analytical method

It is well-recognised that both the strand diameter and operating frequency have an impact on winding losses. To link these two parameters, the terminology base frequency has been proposed. The definition of base frequency is the frequency when skin depth equals the strand diameter, and can be calculated by the equation below:

$$f_b = \frac{1}{\pi \mu_0 \sigma d^2} \tag{4.1}$$

Equation (4.1) is obtained by simply rearranging the well-known equation for skin depth. The concept of semi-analytical model is based on the rather simplified principle that when the operating frequency is below base frequency, the eddy current reaction field can be neglected and thus the analytical equations proposed in [62] can be used to calculate the AC losses. These equations have been already provided in previous sections (sections from chapter 3) and hence will not be repeated here. The semi-analytical model is based on extracting localised flux density variations from solved FEA models (either in frequency domain or time domain). Then these values are substituted back to the analytical equations to calculate AC loss. This technique has already been implemented in the commercial finite element package ANSYS Maxwell and hence the following analysis on semi-analytical model will focus on this software package. To use the built-in capability in Maxwell, a similar process to homogenisation is required. The built-in semi-analytical feature can be activated by changing the material composition to Litz

155

wire, which allows for defining wire composition, wire type, strand number and strand diameter as shown is Table 4.6.

Table 4.6 Geometrical view of semi-analytical model in ANSYS Maxwell with its detailed settings
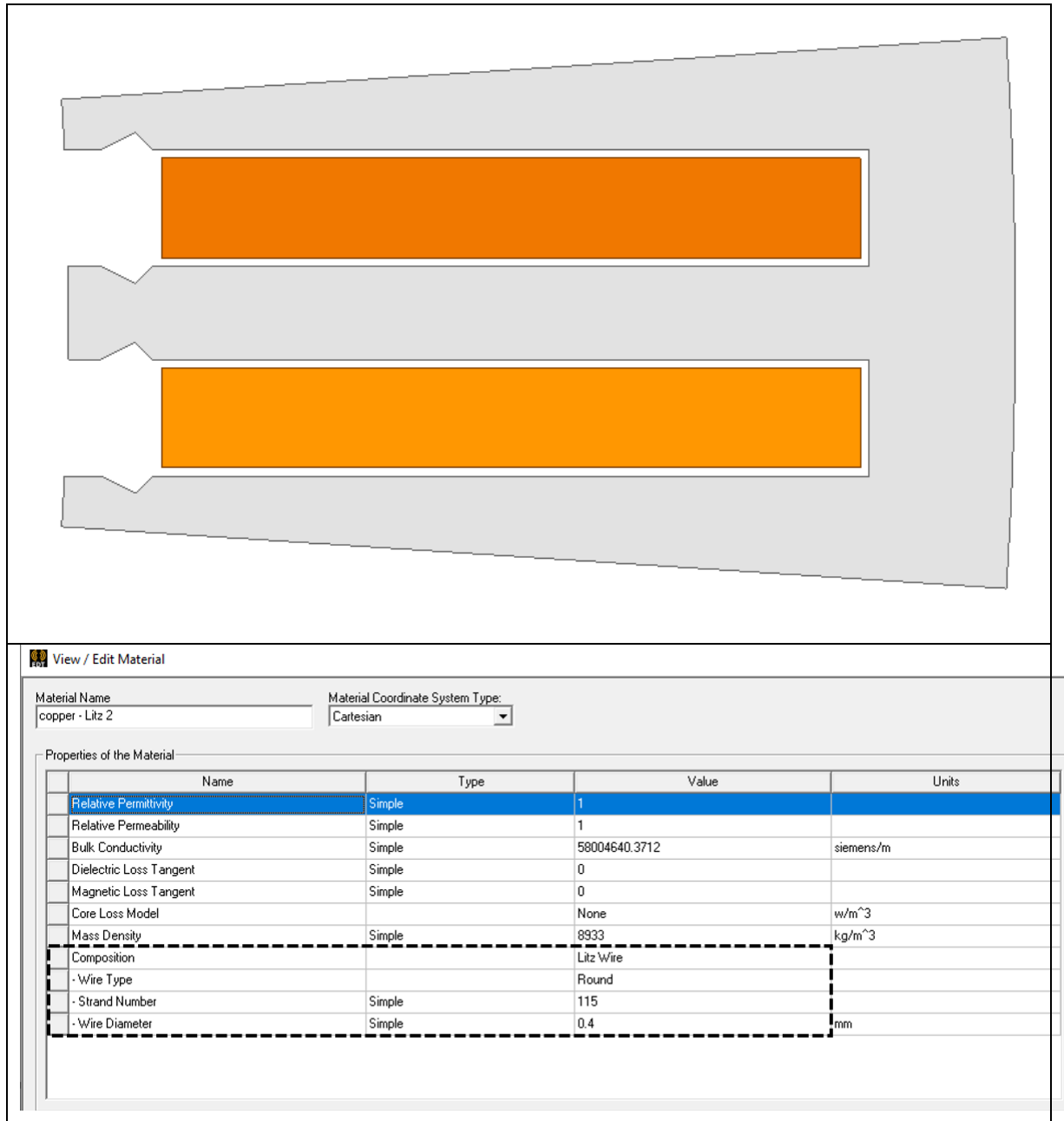
As was the case with the homogenisation model, the requirement on mesh quality across coil conductor region is not onerous as it is modelled as a non-conducting region with uniform current density. When the model is solved, the predicted DC loss and total winding loss can be obtained via the post-processing tools. This approach was applied to the motorette model over the same frequency range and the resulting total winding loss are shown in Figure 4.21

alongside the corresponding curves for the detailed strand-by-strand model and the homogenised model.
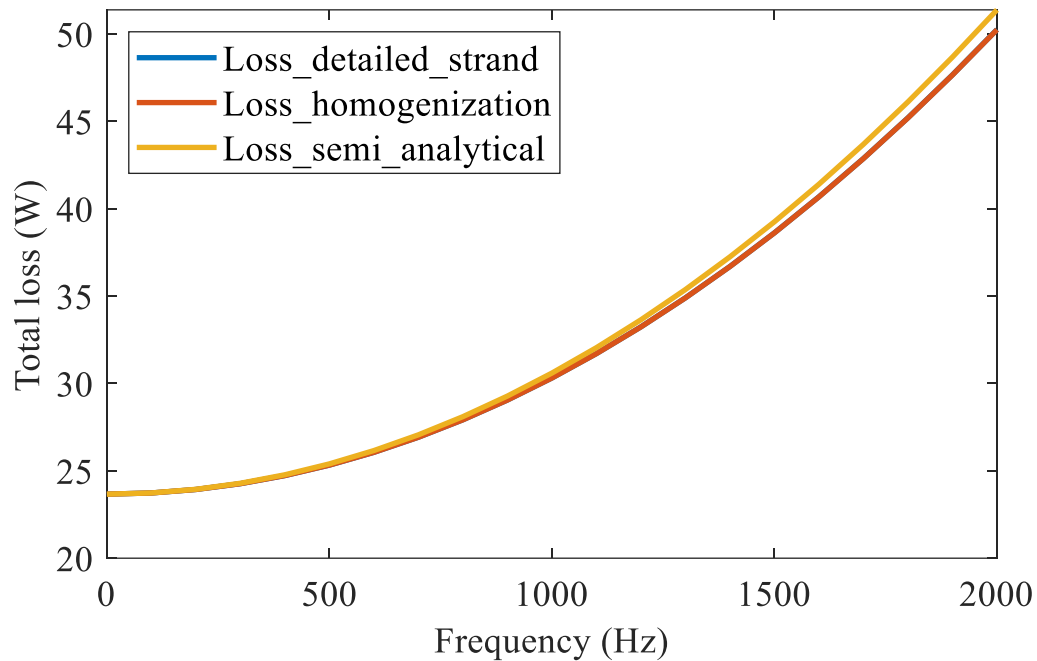
Figure 4.21 Winding loss versus frequency plot of 3 different models: detailed strand model, homogenization, and semi-analytical

As can be seen from Figure 4.21, the total winding losses predicted by the three different techniques show good agreement. The loss curves predicted by homogenisation method and detailed strand-by-strand model align well with each other across the full frequency range. Given that the semi-analytical model is based on a magnetostatic analysis which does not account for the eddy current reaction fields and has no frequency dependant factors in the post-processing, this technique tends to overestimate the winding loss at higher frequency ranges although the magnitude of the discrepancy remains relatively small at ~2.2% at 2kHz. Hence, for the frequencies that are likely to be encountered in electrical machines, all three methods provide comparable estimates of loss, at least for two-dimensional representations.

To evaluate the performances of three techniques at higher frequency range, the three methods were applied from 2730Hz to 81900Hz (upper limit being the equivalent to 3 times the base frequency f_b) in 2730Hz increment giving a total of 30 sampling points. The variation in total winding loss over this extended frequency range curve for the 3 techniques is shown in Figure 4.22.

157
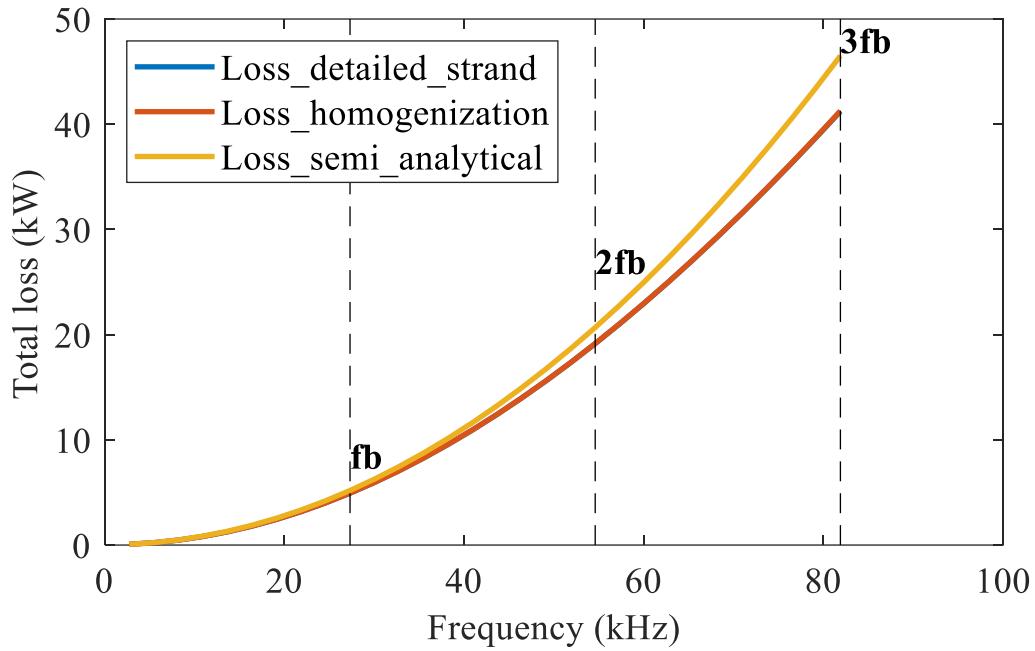
Figure 4.22 Predicted winding loss for 3 different methods over higher frequency ranges

As can be seen from Figure 4.22 above, very good agreement is achieved between all three methods especially when operating frequency is below base frequency of 27.3kHz. As the frequency exceeds the base frequency, the loss predicted by semi-analytical model becomes higher than that of detailed strand model and homogenization model with difference of 5% at $2f_b$. The homogenisation method gives overall better agreement with the detailed strand-by-strand performance over all the frequencies because the eddy current reaction field is accounted for by frequency dependent complex permeability. The magnitude of AC losses at f_b, $2f_b$ and $3f_b$ are shown in Table 4.7 and the computation times for each technique are shown in the Table 4.8.

Table 4.7 Total loss comparison between proposed 3 techniques at f_b, $2f_b$ and $3f_b$

Frequency	Detailed strand model loss (W)	Homogenised model loss (W)	Semi-analytical model loss (W)
f_b	4934	4934	5188
$2f_b$	19148	19154	20681
$3f_b$	41218	41260	46502

Table 4.8 Solving time for 3 different techniques

	Detailed strand model	Homogenization	Semi-analytical
Solving time for 30 sampling points from 2730Hz to 81900Hz with 2730Hz increment	2h38min	7min	2min

It can be concluded that both the homogenization and semi-analytical models can yield AC loss predictions that exhibit good agreement with a detailed strand-by-strand AC loss model over a wide frequency range for this combination of strand number and strand diameter. They achieve this agreement with a very significant saving in solution time and in particular model formulation time. The homogenisation approach shows agreement at frequencies that would be of interest for modelling high frequency converter switching events, i.e., several tens of kHz.

4.5 Three-dimensional modelling of motorette model

The analysis undertaken up to this point has been based on two-dimensional models. It is well-recognised that two-dimensional models tend to overestimate the loss in the slot region (due to the infinitely long eddy current paths with no return regions) and neglect the end-winding region completely. To predict the loss in end-winding regions and make a direct comparison with experimental results, a full three-dimensional model was implemented in FLUX3D. In addition, the end-winding loss can be estimated by subtracting the loss in the 2D model from those predicted by 3D model.

This 3D model of the motorette with a concentrated coil consists of the core, the active region of the coil with the slot, a short end-winding extension region beyond the end of the core and the semi-circular end-winding region as shown in Figure 4.23. The inclusion of a short end-winding extension region is common practice to ease the forming of the end-winding without risking damage of the winding on the sharp edge formed by the end of the core.
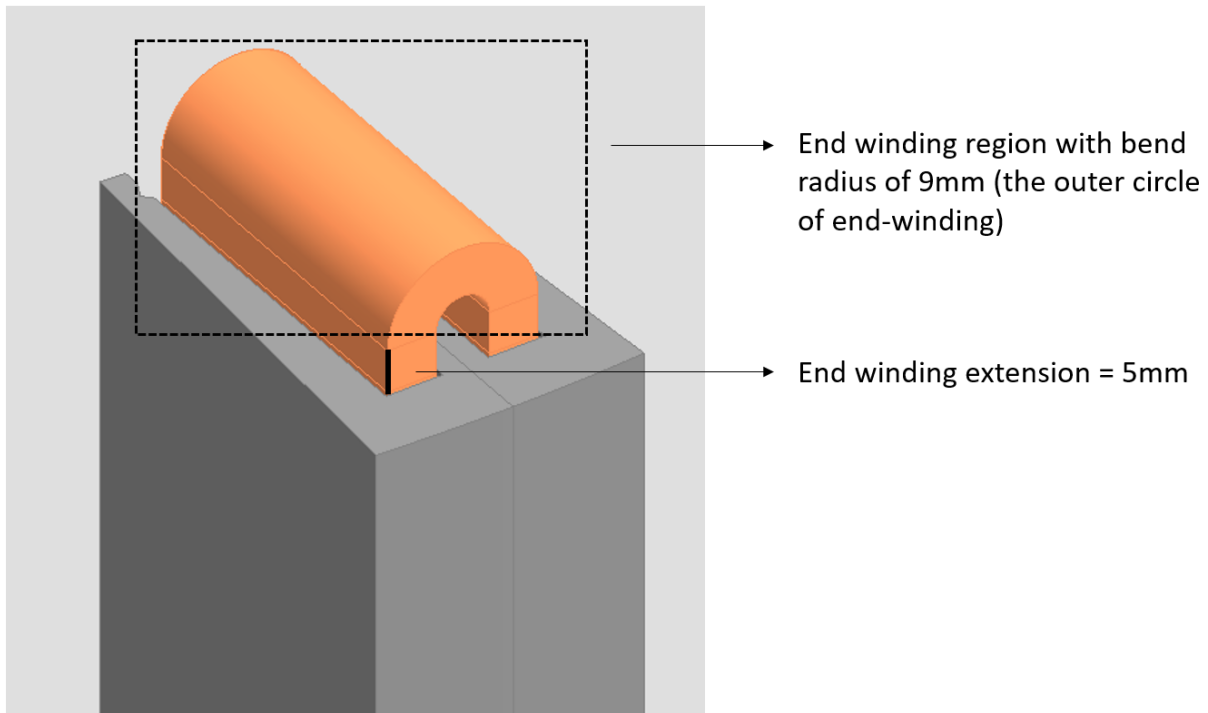
Figure 4.23 Geometrical view of 3D model with end-winding extension region and end winding region

Building and solving for a detailed strand-by-strand 3D model consisting of 10 series turns and hence 2300 strands will be very demanding and time-consuming because of the excessive number of mesh elements that would be involved in a full 3D model. To simplify the investigation of 3D models equipped with Litz wire, the following analysis was divided into two activities:

- A comparison between a 3D homogenised model and a 3D semi-analytical model. Both models represent the full 300mm long core active length (no symmetry settings) and the end-winding.
- A simplified 3D detailed strand-by-strand model which is focussed on the end-winding region with a significantly shortened core length of only 2mm. The idea of using this simplified model with a very short core length comes from the fact that the active region has little impact on end-winding regions and hence the active length can be minimised to reduce the number of mesh elements.

4.5.1 3D homogenization and semi-analytical model

The geometry of the active region of the 3D model was obtained by a simple extrusion of the existing 2D geometry. The physical settings of homogenised and semi-analytical model were simply mapped across from the 2D model. Note that the mesh settings of the 3D homogenised model were changed from that of 2D to realise a better balance between computational time

and accuracy. Specifically, unlike the 2D models which relied on automatic meshing, the mesh of 3D homogenization model and semi-analytical model were controlled manually. The settings of 3D homogenization model and its corresponding mesh information are shown in Table 4.9.

Table 4.9 The mesh plot of 3D motorette model in Flux and its corresponding settings

Machine level mesh	Mesh plot in end-winding region
	Mesh plot in active region
Mesh plot in baseline 2D geometry used for extrusion	
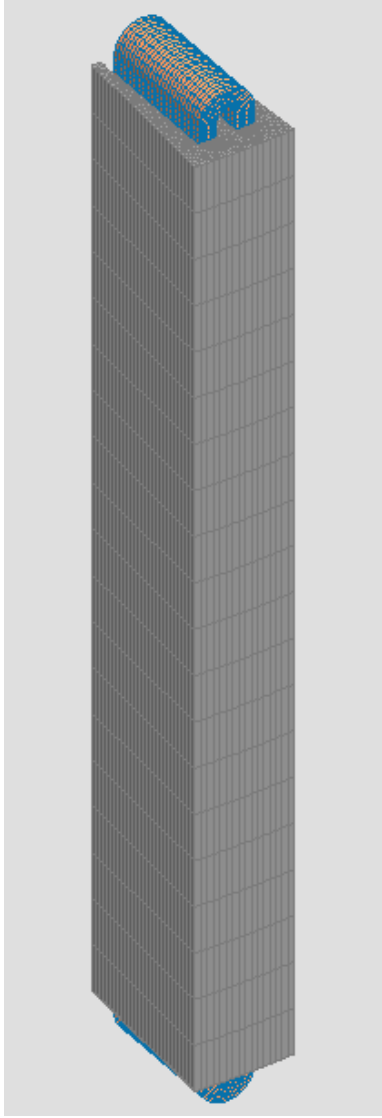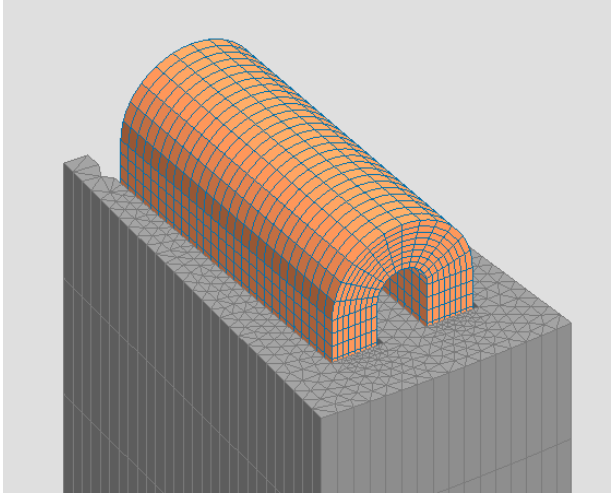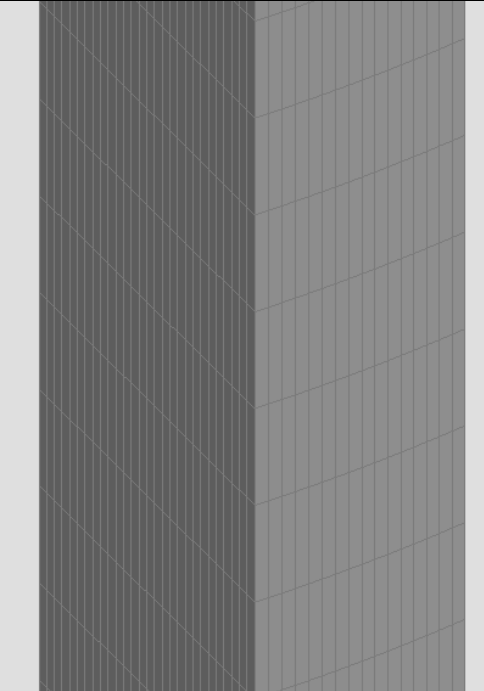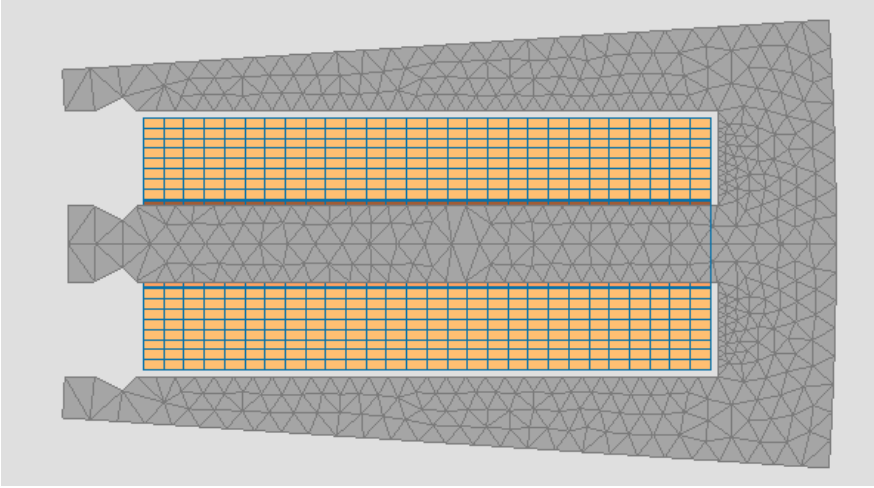
Dimensions for full length motorette model	Settings for homogenisation model
Active length: 300mm	
Stator material: M250_35A_50Hz	Number of turns:10
Copper conductivity: 58004640 S/m	Number of strands per turn: 115
Frequency of interest:	Strand diameter:0.4mm
1. 100Hz to 2000Hz (low range)	Strand shape: round
2. 2730Hz to 81900Hz (high range)	Current injected to each strand: 0.5A/mm^2

Although the mesh requirement for a homogenised model is not particularly demanding in terms of discretisation, the coil regions were still meshed using a mapped mesh. The mesh quality along axial region is important to ensure accurate results and thus a mesh definition line which divides the axial length into specified segments was implemented. Similar mesh settings are applied to different parts of the model. With 20 mesh segments along the active region, 12 mesh segments in end-winding region and 28 x 8 mapped mesh in coil region, the number of mesh elements is 249,083. The winding exhibits axial symmetry about the mid-point of the core and such symmetry is usually exploited to reduce the problem domain and computational time. However, due to the nature of both the homogenised model and semi-analytical model the total computational requirement is not demanding and hence the full-length model was used for these cases. The symmetry was however exploited later in this section for the detailed strand-by-strand model.

The motorette conductor loss was predicted using both the homogenised model and the semi-analytical models, initially over a frequency range between 0.001Hz and 2kHz. The resulting variations in total winding loss as a function of frequency are shown in Figure 4.24.
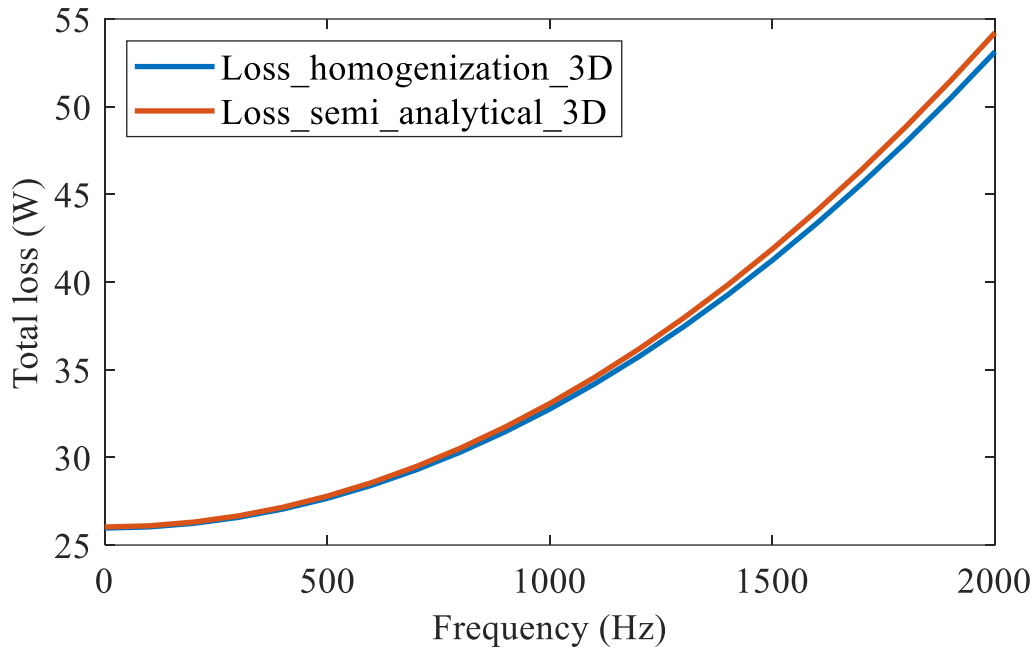
Figure 4.24 Loss comparison between 3D homogenization model and semi-analytical model at lower frequency range

The same model was used over the extended frequency range up to 3 times the base frequency of the strand. The resulting conductor losses are shown in Figure 4.25.
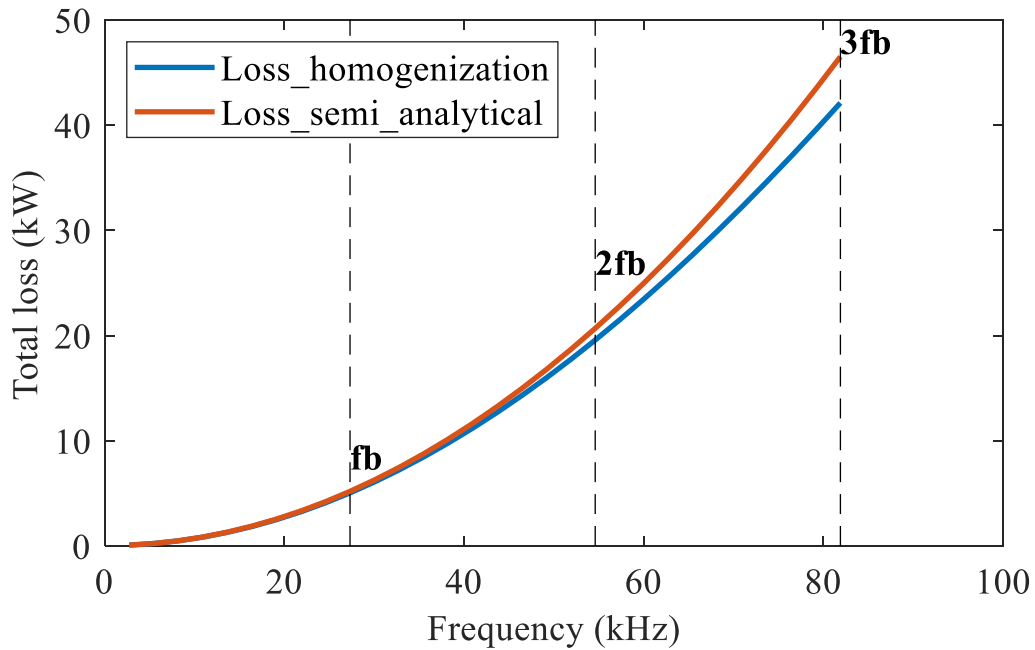
Figure 4.25 Loss comparison between 3D homogenised model and semi-analytical model over higher frequency range

As can be seen from the figures above, the 3D homogenization and semi-analytical models predict very similar losses and even at three times the base frequency, the difference is only 10% taking the values of homogenization model as baseline. The total solving time for the 30

simulations performed across the frequency range are 1h10min for homogenization and 30min for the semi-analytical model.

Figure 4.26 shows a comparison between the losses predicted by the 2D and 3D homogenised models. As will be apparent, there is only a small difference of ~3.5% even at 27.3kHz. A combination of the end-effects in the active region towards the end of the core and the additional end-winding contribution loss can be estimated by subtracting 2D loss from its corresponding of 3D model value. The estimated end-winding loss and end effects are shown in Figure 4.27. It is important to note that this motorette is 300mm long while the end-windings including the 5mm extension are only 64mm long at each end and so the impact of the end-winding is likely to be modest as a fraction of the overall loss even if the loss densities were comparable. In fact, there is a significant loss density difference with the winding loss density of the active region being 4,341W/kg while that in the end-winding region is 452W/kg at base frequency.
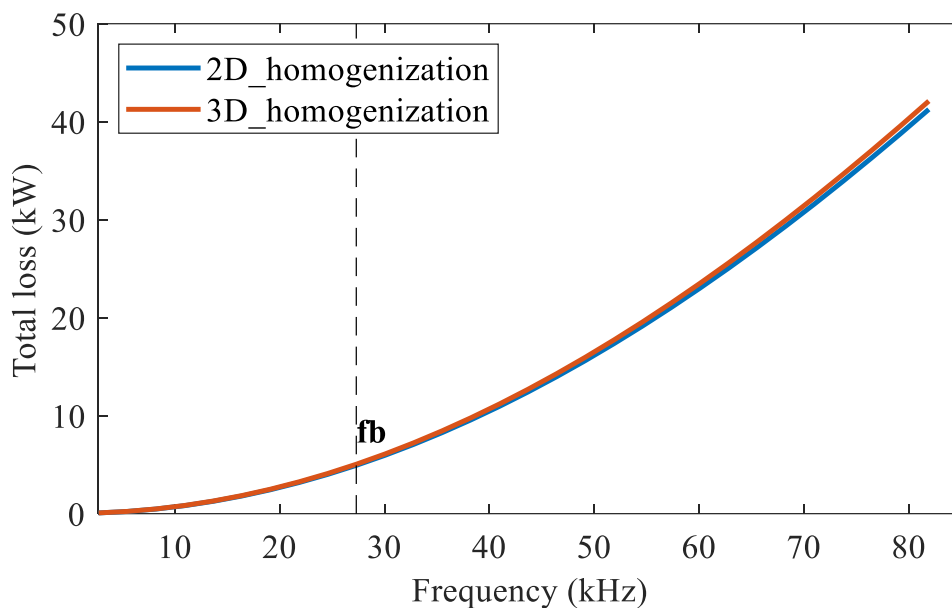
Figure 4.26 Comparison between 2D and 3D homogenization model
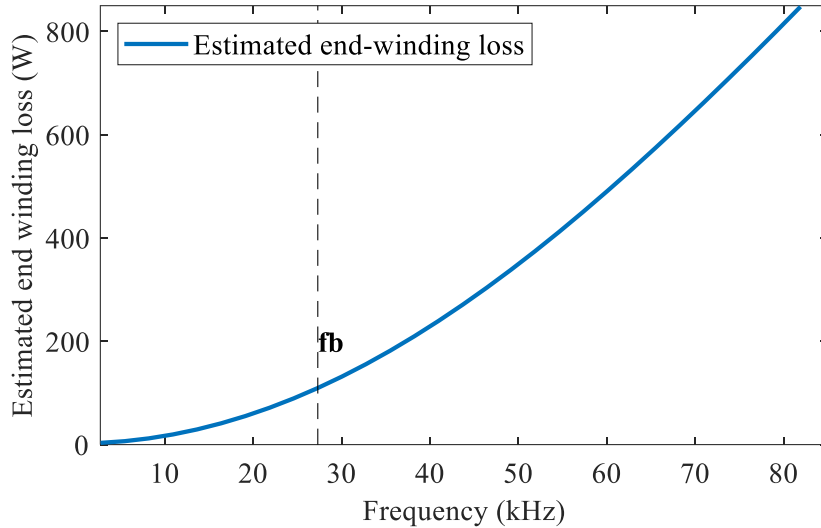
Figure 4.27 Estimated end-winding and end-effect loss

The flux density distribution on the middle plane of 3D homogenised winding at base frequency is plotted in Figure 4.28. As will be apparent, the magnitude of flux density in end-winding region is much lower than that in the active region. Since the associated eddy current loss is proportional to the square of the flux density at a given frequency, it is evident that the end-winding loss density will be much lower than in the active region. Indeed, it is arguable that in this particular coil, the end-winding loss can be neglected and that a two-dimensional finite element model is adequate. It should be noted that the assumption of no AC loss in end-winding is valid with the combination of long active length and concentrated winding. In the case of shorter active length or larger end-windings (e.g., in distributed windings), the assumption of no AC loss in end-winding region is no longer valid and the 3D model with detailed end-winding pattern is required to calculate the losses in end-winding region.
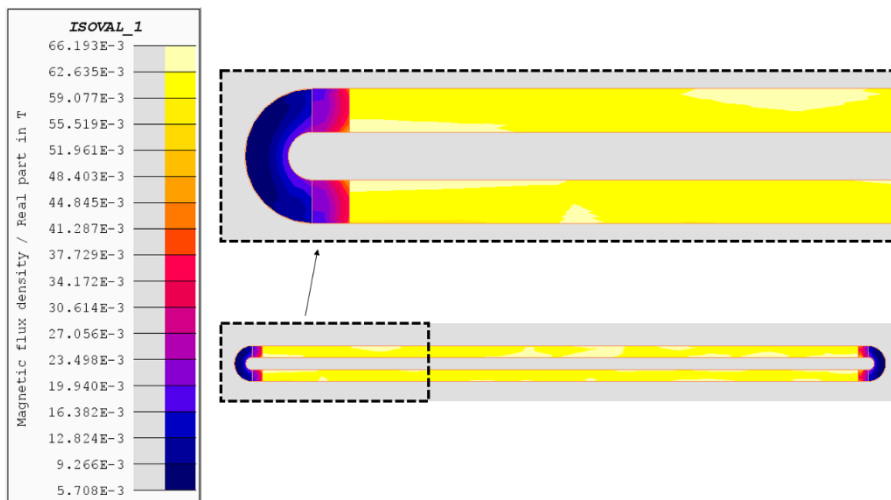
Figure 4.28 Flux density plot in the middle plane of 3D homogenization model at base frequency with 0.5A rms current each strand

165

4.5.2 Three-dimensional detailed strand-by-strand model

The preceding 3D analysis focussed on models with homogenised and semi-analytical techniques. Although the accuracy of those computationally efficient models has been cross-checked with a detailed strand-by-strand model in 2D for this particular motorette geometry and Litz bundle composition, a direct comparison between 3D detailed strand-by-strand model and homogenised/semi-analytical model is very demanding because of the immense computational effort required to take the fine detail of an individual strand model of a motorette equipped with 11 bundles 2300 strands into a third dimension. However, based on the fact that the end-winding region is essentially located outside the of stator core, the active region can be assumed to have limited impact on end-winding regions and thus the detailed strand model with 2mm active length and progressively increased number of bundles was investigated to explore whether the end-winding region can be modelled almost in isolation from the active region.

However, even modelling the end-winding region only of a full-slot involves a very significant computational effort and so the 3D detailed strand baseline model initially focussed on a single Litz wire bundle near the slot opening with the number of bundles being progressively increased as staged comparison with the homogenised and semi-analytical model. This is not ideal compared to a full model, but it does offer a practical means of assessing the utility of the homogenised and semi-analytical models for end-winding regions. The specification of 1 bundle 2mm active length initial strand-by-strand model is shown in Table 4.10.

Table 4.10 Geometrical view and specifications for 1 bundle 2mm active length model

Geometrical view
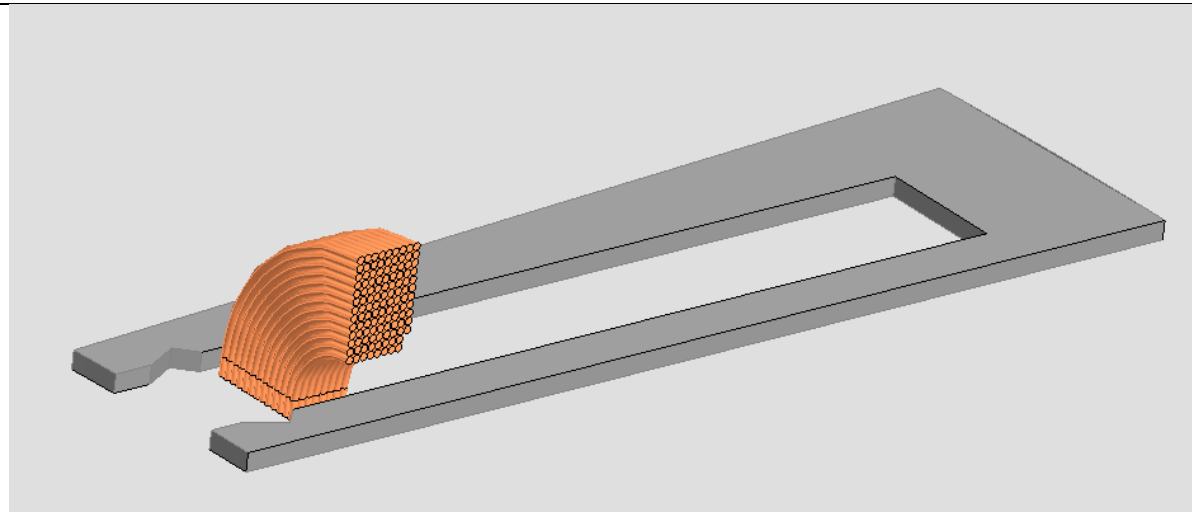
Specifications	Symmetry settings

Axial length = 1mm	XY plane symmetry: tangent magnetic field, normal electric field
Strand diameter = 0.4mm	
Number of strands per bundle: 115	
Number of bundles: 1 (will be progressively increased)	ZX plane symmetry: tangent magnetic field, normal electric field
Current injected to each strand: 0.5A rms	
Stator material: M250_35A_50Hz	
Copper conductivity: 58004640 S/m	

Note that for 3D detailed strand model, the symmetry was fully exploited to reduce total number of mesh elements and the detailed symmetry settings are shown in Table 4.10. The mesh of 3D detailed strand model is controlled in the same manner as that of 3D homogenization model to reduce computational time and give the accurate result at the same time. Every strand in Litz wire bundle is built from propagation and extrusion of baseline strand and thus they have linked and consistent mesh settings. In this way, the control of strand level mesh becomes easier because change the mesh of baseline strand will lead to automatic mesh change on other related strands. The active region is divided into 3 segments because the length in this half-symmetry model is only 1mm. The end-winding arc region is divided into 8 segments. The detailed mesh information is provided in Figure 4.29.
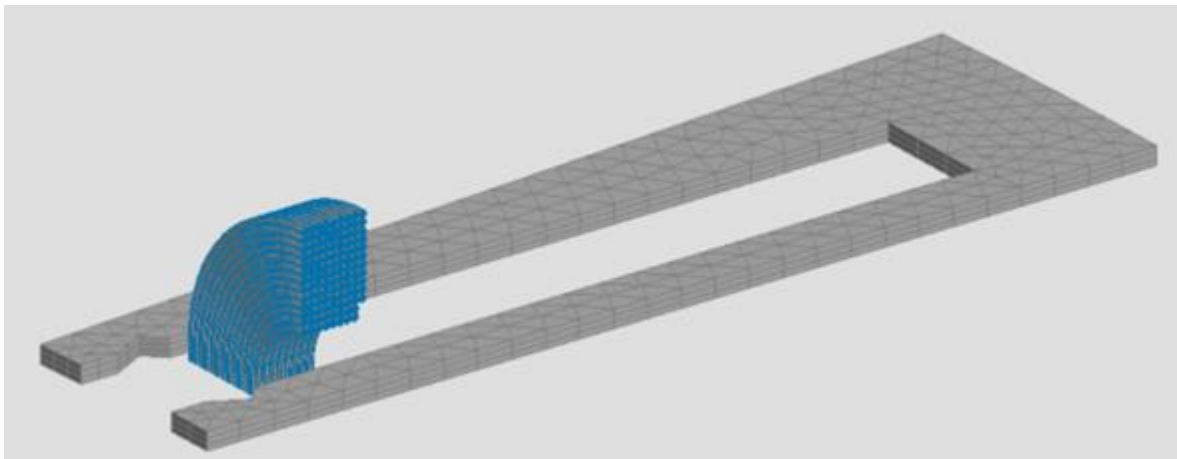
(a) Full model mesh plot
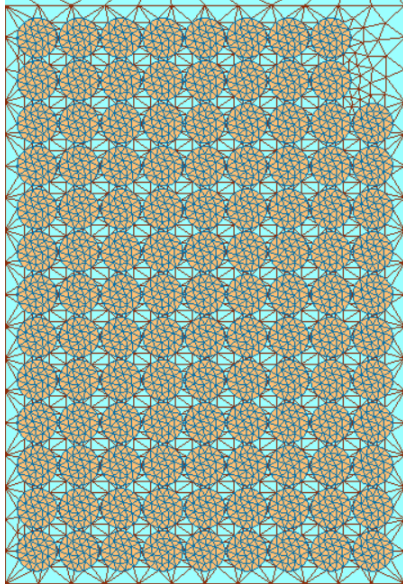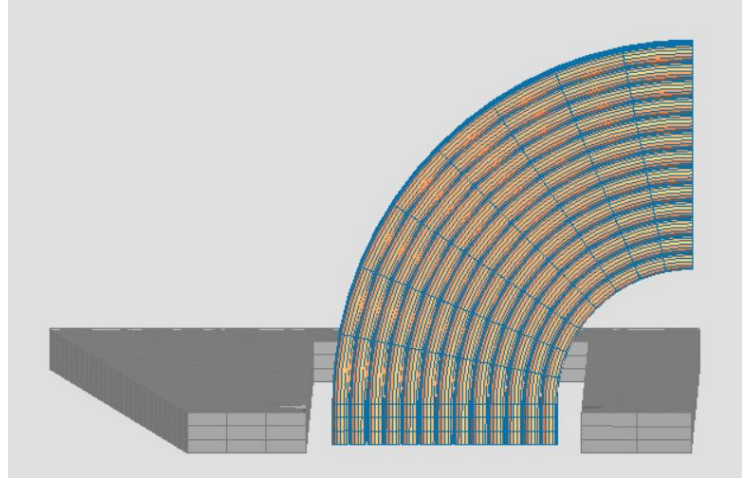
| (b) Strand mesh plot | (c) End-winding bending region mesh plot |

Figure 4.29 Detailed mesh information for 1 bundle detailed strand model: (a) full model mesh plot (b) strand mesh plot and (c) End-winding bending region mesh plot

The electrical circuit has 115 parallel connected solid conductors and separate current sources in each branch to ensure equal current sharing. The frequency range was reduced from 2730Hz to 54,600Hz (twice the base frequency) with 20 sampling points to reduce total computational time. The predicted DC loss and total loss of 3D detailed strand-by-strand single Litz conductor bundle model is shown Figure 4.30 alongside the inferred AC loss contribution which is the difference between the total loss and the DC loss.
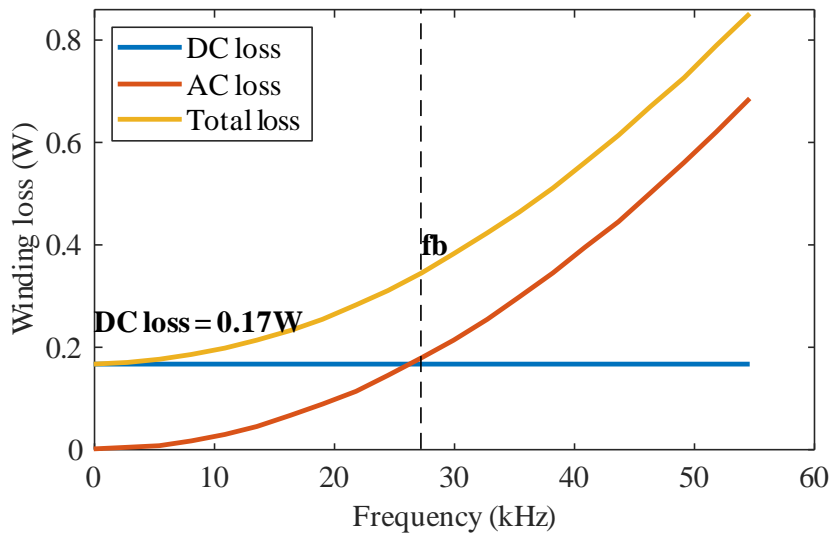
Figure 4.30 Different loss components in detailed 3D 2mm active length 1 bundle model

As can be seen from Figure 4.30, the DC loss is higher than that of AC losses for most of the frequency range below the base frequency. Indeed, even at 10kHz which is well beyond the

range expected in a machine unless high frequency switching events are included, the contribution from the inferred AC loss is very small in comparison with the DC loss. The magnitude of overall winding loss is relatively small (0.34W at base frequency) because the active length has been reduced from 300mm to 2mm. As a point of interest, the cross-over frequency where AC loss becomes higher than DC loss is around base frequency for this particular combination of dimensions.

To compare the results between 3D detailed strand model and homogenization model, an equivalent homogenised model was constructed. The geometry of 3D 2mm homogenised model is shown in Figure 4.31 and the loss comparison as a function of frequency is shown in Figure 4.32.
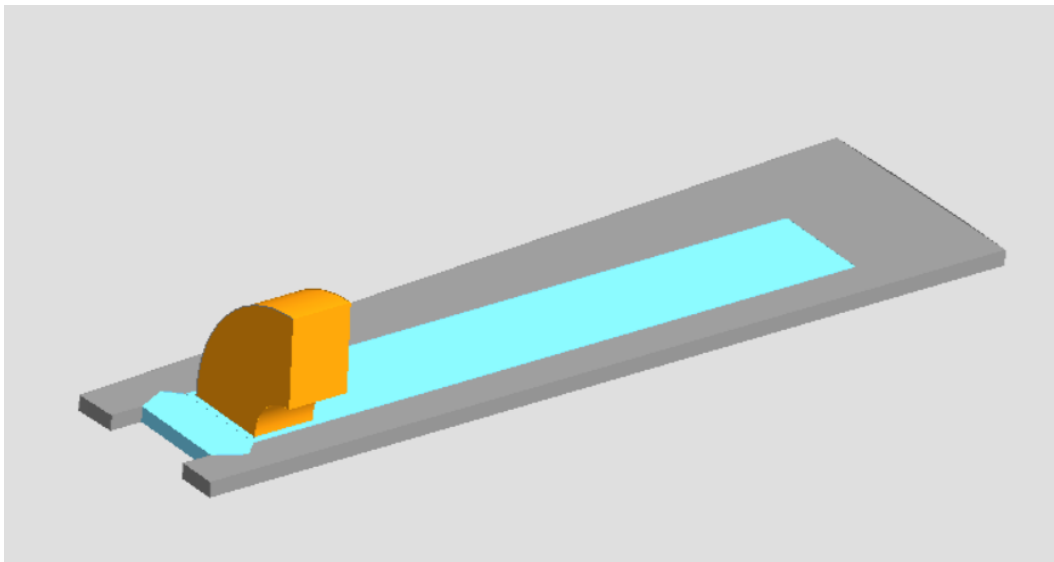
Figure 4.31 The geometrical view of 3D 2mm active length homogenization model
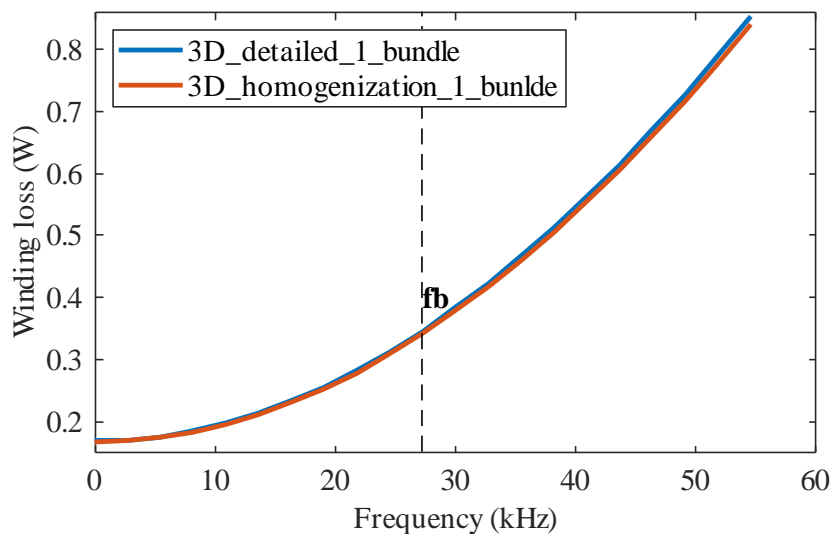
As can be seen from figures above, there is excellent agreement between the two methods. To further evaluate the performance of the 3D homogenised model, the number of turns in detailed strand model was increased to 2 and 3. The geometrical view of the 2 and 3 turn 2mm active length models are shown in Table 4.11.

Table 4.11 Geometry view and symmetry settings of 2 bundle and 3 bundle 3D models

2 turn detailed strand model and homogenization model	3 turn detailed strand model and homogenization model
Specifications	Specifications
Axial length = 1mm	Axial length = 1mm
Strand diameter = 0.4mm	Strand diameter = 0.4mm
Number of strands per bundle: 115	Number of strands per bundle: 115
Number of bundles: 2	Number of bundles: 3
Current injected to each strand: 0.5A rms	Current injected to each strand: 0.5A rms
Stator material: M250_35A_50Hz	Stator material: M250_35A_50Hz
Copper conductivity: 58004640 S/m	Copper conductivity: 58004640 S/m
Symmetry settings	Symmetry settings
<u>XY plane symmetry</u>: tangent magnetic field, normal electric field	<u>XY plane symmetry</u>: tangent magnetic field, normal electric field
<u>ZX plane symmetry</u>: tangent magnetic field, normal electric field	<u>ZX plane symmetry</u>: tangent magnetic field, normal electric field

Those 4 models were assigned the same mesh settings as that of the single turn model and solved over same frequency range from 2,730Hz to 54,600Hz in 2,730Hz increments. The loss comparison between detailed strand and homogenization model is shown in Figure 4.33.
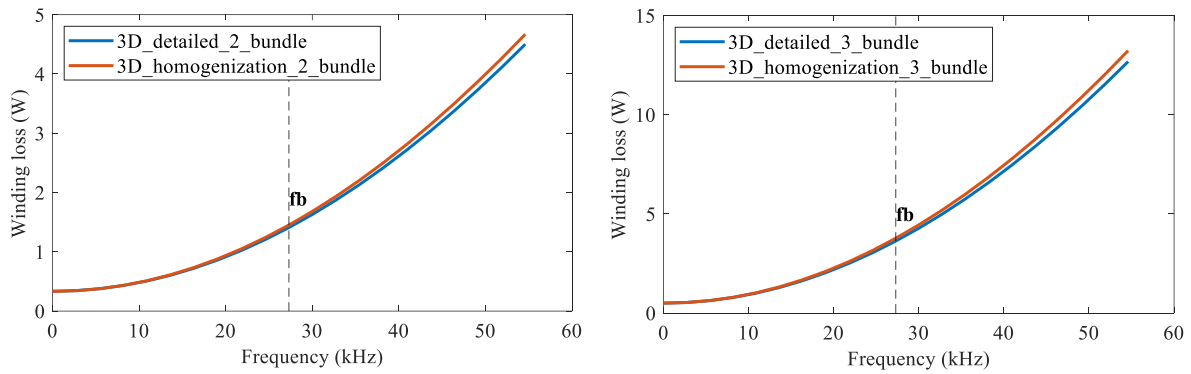
Figure 4.33 Loss comparison between 2 and 3 bundle detailed strand-by-strand models and homogenised models

The solving time of 3 sets of models for all the sampling points are provided in the Table 4.12 below:

Table 4.12 Solving time of homogenization model and detailed strand model with different bundle numbers

	1 turn	2 turns	3 turns
Homogenization	4 min	5 min	5 min
Detailed strand model	3h 22min	14h 35 min	44h

Although the results presented in Figure 4.33 above do not represent a full slot, the number of turns could not be increased further as the available PC struggled in terms of computational time and memory requirement to solve for more turns. Nevertheless, these results provide useful validation of the usefulness and accuracy of the homogenised model and over a much greater frequency range than is required to model this machine.

4.6 Two-dimensional machine level modelling with strand-by-strand model

Previous analysis and simulations are all carried in steady state AC conditions without consideration of rotor movement. In this section, a 2D machine level detailed strand-by-strand model is developed, and the losses are calculated using a 2D simulation. The topology used in this section will be same as that of baseline un-transposed design from section 2.3.1. While for the Litz wire used in this analysis, it is type 8 Litz wire with a 0.4mm strand diameter. The overall Litz conductor bundle has a cross-sectional area of 8.94m ×6.55mm (equivalent to dimension of baseline bar conductor) with an internal packing factor of 60% which results in

280 strands within the cross-section. The spacing between strands is determined by the method specified in section 4.1. To reduce the modelling and computational time, 1/6 of full machine with anti-cyclic boundary condition is implemented which results in 6 slots and hence a total of 6720 strands (each turn accommodates 280 strands and there are 4 turns per slot 24 turns for 1/6 model) to be modelled. The specification of machine level detailed strand model is summarised in Table 4.13 below:

Table 4.13 The specifications of machine level strand model in 2D transient magnetic context
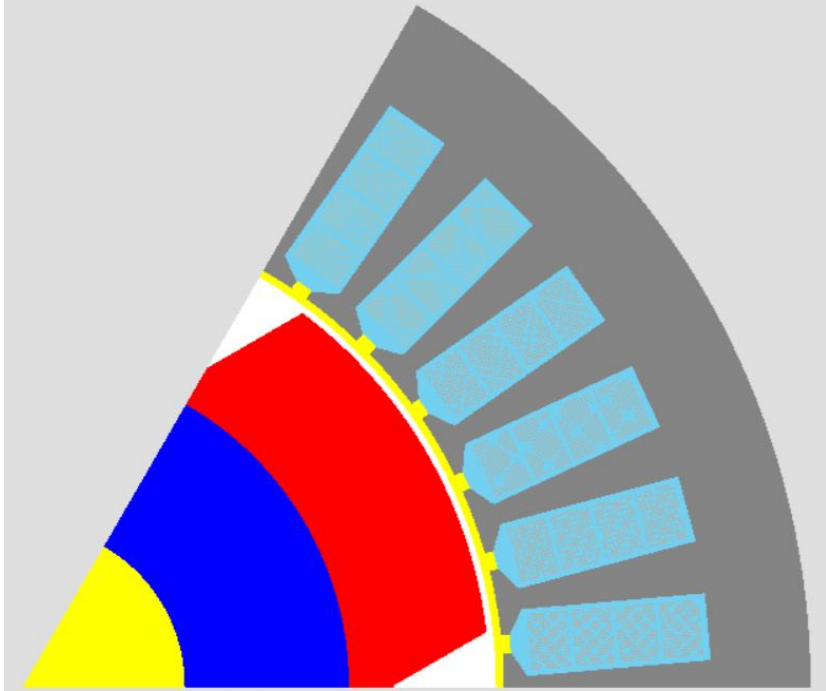
Geometrical view of baseline model
Slot view of machine level strand model
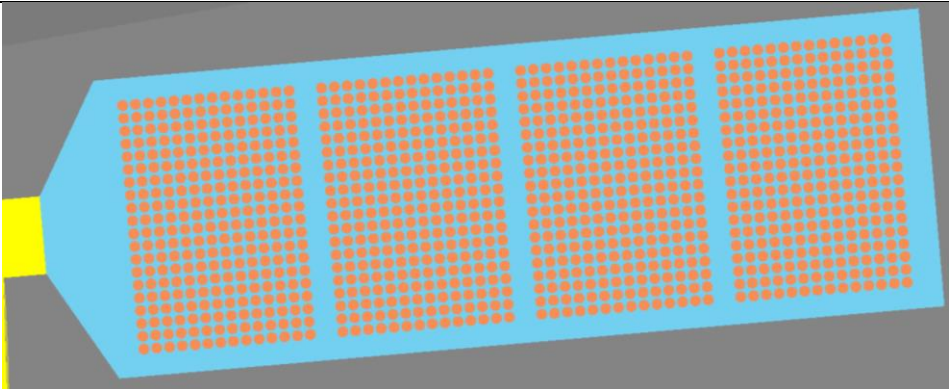
Stator dimensions	Rotor dimensions

Number of slots: 36	Number of poles: 6
Stator outer diameter: 246mm	Magnet thickness: 22mm
Stator inner bore diameter: 150mm	Rotor sleeve thickness: 1mm
Axial length: 112mm	Shaft diameter: 50.6mm
Slot depth: 32.3mm	
Slot width: 10.3mm	
Airgap length: 2mm	
General information	Winding specification
Stator material: Hiperco50	Winding pattern: distributed winding
Rotor material: NO20	Strand diameter: 0.4mm
Permanent magnet material: Recoma32	Number of strands per bundle: 261
Copper conductivity: 58004640 S/m	

To fully capture the skin and proximity effect, each strand is discretised finely which results in large number of mesh elements. The mesh plot is provided in the Table 4.14 below:

Table 4.14 The mesh plot of machine level Litz wire model

Mesh plot of one slot
Zoomed in view of mesh plot of single strand
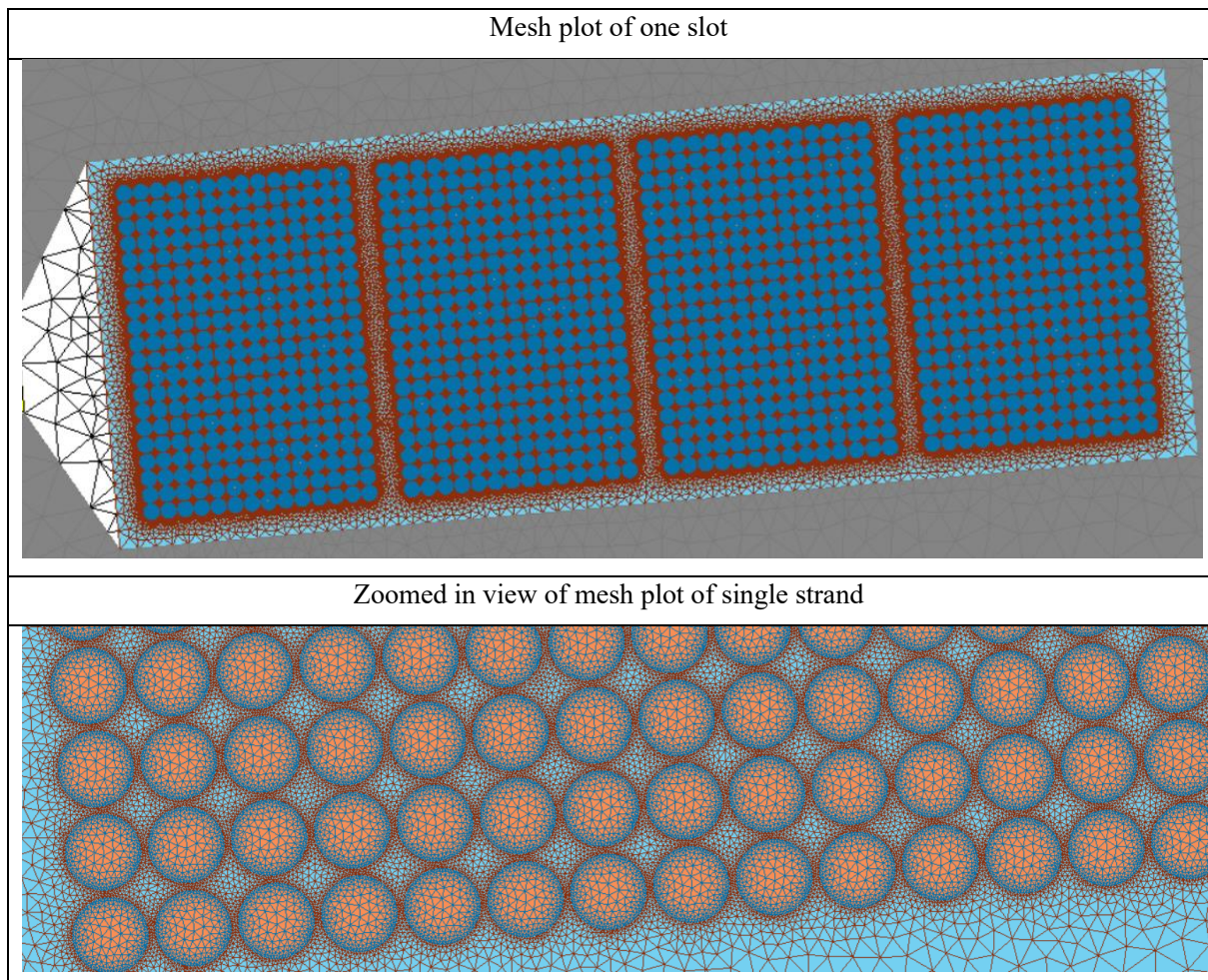
Note that the magnitude of current injected to individual strand is determined under the principle of same Ampere turns per slot as that of baseline model equipped with bar conductor. The coupled electrical circuit consists of 840 parallel branches with 8 solid conductors connected in series for each branch, making a total of 6720 (8*840) finite element coupled circuit component elements in addition to the current sources. The number of parallel branches is 840 because each phase of Litz wire winding has 280 parallel connected strands and this machine adopts a conventional 3 phase winding hence the number 840 (280*3). The construction of the electrical circuit is achieved with a Python script. The model is solved over 1 electrical cycle with 30 time steps at rated torque and 6000RPM. Although this is fewer time steps than would normally be desirable, the solution time even with this reduced number of steps is ~58 hours due to the very fine mesh. The total loss predicted by this model is 3738W compared to the quasi-static loss of 3684W, i.e., an increase of only 54W due to eddy currents.

As noted previously, the very fine mesh required to model all the strands in each phase resulted in a very long and arguably prohibitive solution time. An alternative model was developed in an attempt to shorten the solution time, in which only one phase (which occupies 2 slots in the 1/6th model) was modelled on a strand-by-strand basis with the remaining two phases modelled as conventional non-conducting current carrying regions with a uniformly distributed current density. Figure 4.34 shows the geometry of this revised model.
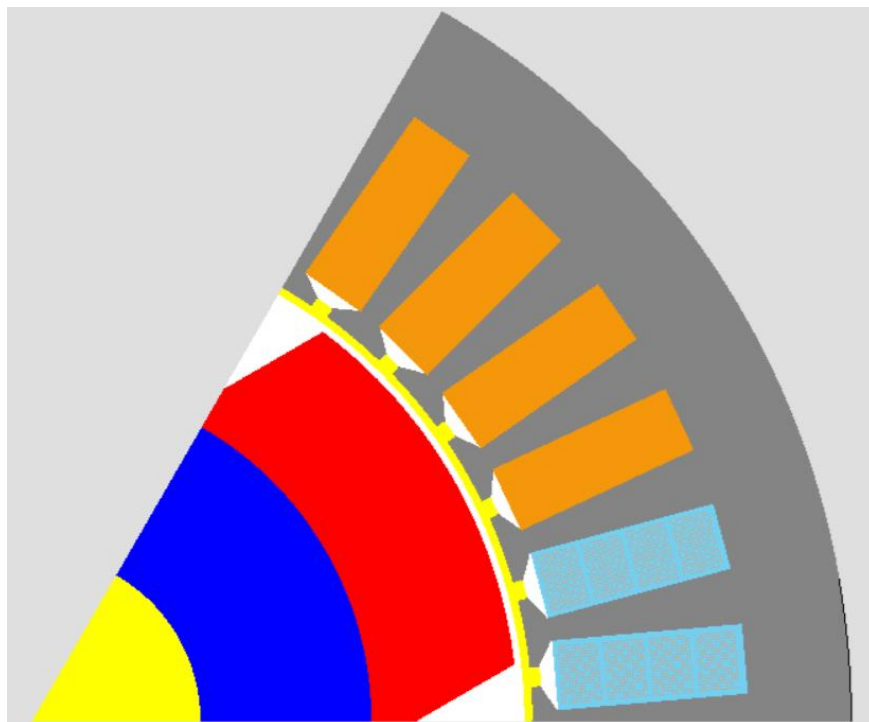
Figure 4.34 Geometry view of simplified machine level Litz wire model

A zoomed-in version of the electrical circuit illustrating the connection between different phases is shown in Figure 4.35.
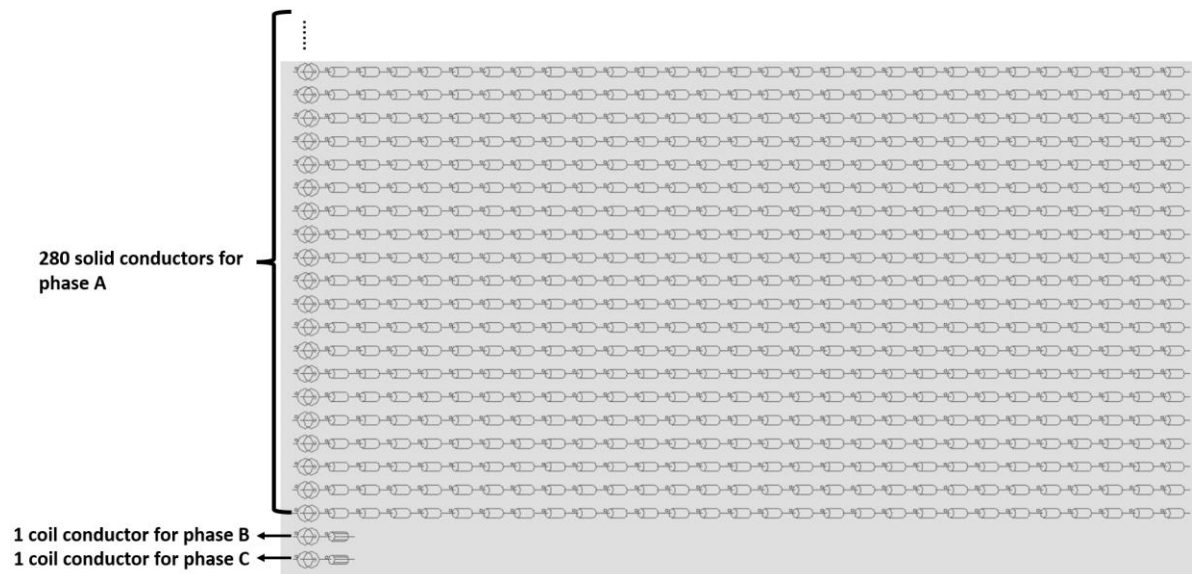
Figure 4.35 Zoomed-in version of electrical circuit for models equipped with one phase Litz wire

The mesh settings are same as that of full machine level model and the model was solved for the same operating conditions. The losses predicted by three phase detailed strand and one phase detailed strand model together with their solution time are shown in Table 4.15. The total machine loss for the one phase detailed model was calculated as 3 times the loss in the stranded phase. As would be expected, the coupling between phases in terms of eddy current field redistribution will be minimal with Litz wire and hence there is no discernible difference between the all stranded and one-phase stranded models.

Table 4.15 Comparison between machine level Litz wire models

	DC loss (W)	Total loss (W)	Modelling set up time	Solving time
Three-phase stranded	3684	3738	1 day	58 hours
One-phase stranded	3684	3736	4 h	6h 20min

In principle, the homogenised model should be applicable to a transient time-stepped model within the FLUX2D environment. This would have allowed the logical next step of testing the homogenised model for the more complex excitation variations in an electrical machine compared to static and steady-state AC current only excitation. Although it is claimed to be

possible in the FLUX2D documentation, the author and support engineers from FLUX could not confirm that this functionality could in fact be deployed. Hence, only the results associated with detailed strand-by-strand model in transient magnetic solver could be produced.

4.7 A conclusion for Litz wire modelling techniques

In this section, three different techniques including detailed modelling, homogenization and semi-analytical method are proposed to calculate the losses associated with Litz wire bundles. At first, a simplified motorette model is built in 2D steady state AC context to evaluate the performance of those three methods. Simulation results indicate that the losses predicted by three techniques agree with each other for frequencies below base frequency. When the frequency exceeds base frequency, the semi-analytical method starts to overestimate the losses because this method ignores the eddy current reaction field. On the other hand, the losses predicted by homogenization method almost align with that of detailed strand model over the whole frequency ranges. This is because the homogenization method takes eddy current reaction field into consideration. Both homogenization and semi-analytical model can give accurate results below base frequency with significant reduction on modelling and computational time. In addition, those two techniques are relatively easy to use because they are embedded in two commercial FEA software.

Then the 3D motorette models are built in steady state context to evaluate the situation when end-winding region is included. The 3D evaluations are split into two parts: 1. comparison between 3D homogenization and 3D semi-analytical and 2. comparison between 3D simplified detailed strand model with 2mm active length and equivalent homogenization model. The losses predicted by 3D semi-analytical model and 3D homogenization model give similar trend as that of 2D models.

While for the comparison between 3D simplified strand model and corresponding homogenization model, the loss predicted by homogenization is generally higher than that of detailed strand model except for one special case, the one bundle model. This is because in simplified 3D one bundle model, the requirement of homogenisation is not satisfied (at least ten elementary strands in width and height direction). Another reason that causes this misalignment is that the 3D detailed strand model is not fully representative of commercial Litz wire (In commercial Litz wire, each strand should have similar averaged length due to the twisting effect, but this effect is not considered in 3D detailed model). In addition, the mesh quality is manually controlled to be reasonably good instead of 'perfect' to reduce

computational time. This will also lead to small variations on predicted winding losses. It is thus difficult to say which model gives more accurate results. The computational limit of working PC is also evaluated by progressively increasing the number of bundles in 3D detailed model. When number of bundles reaches to 6, the office PC with 12th i9-12900 processor and 64GB RAM struggles to solve the model and hence the 3D modelling stops at this point.

After the evaluation in steady state AC context, the Litz wire model is built in 2D transient magnetic context to simulate the realistic working conditions. The simulation results of 2D detailed model confirms the AC losses associated with Litz wire bundle is very small (only 1% of DC) and the assumption of no AC loss in Litz wire bundle can be regarded as valid. The building of 2D machine level strand model is complicated and time-consuming. To simplify the process, the model with one phase of detailed Litz wire representation and two phases simplified coil conductor region is proposed. This model is proved to be accurate with significant reduction on modelling and solving time and thus can be used when necessary. The 3D detailed model will inevitably lead to huge numbers of mesh elements and will be challenging and time-consuming to solve. Based on this, the 3D machine level modelling is not considered in this thesis.

To summarize, the detailed modelling of Litz wire is possible but the corresponding requirements on modelling skill and hardware are strict. When necessary, the computationally efficient method such as homogenization and semi-analytical model (implemented in Altair Flux and Ansys maxwell) should be used.

Chapter 5. Experimental testing

5.1 Introduction

The assessment of AC losses up to this point has been based on simulations, almost entirely using two- and three-dimensional finite element analysis. Some of these simulations were performed on a 350kW machine and others on motorettes which have been built based on representative slot and conductor geometries. Ultimately, machine level measurements would be required to provide validation of the conductor loss with all the sources of excitation and harmonics that are present in a machine. However, resource and time constraints did not allow a full prototype machine to be built for the validation of the simulations. Instead, the simplified motorette model (with same dimension as the motorette proposed in section 4.2) is used to perform some experimental validations on the proposed various types of winding configurations. The tests that are performed mainly includes the measurements of impedance and phase angle on motorettes equipped with Litz wire or equivalent bar conductor. The detailed AC loss measurement techniques and experimental apparatus will be introduced in the following sections.

5.2 AC loss measurement techniques

There are two sets of experiments that will be performed in this chapter and the detailed information is provided in the Table 5.1 below:

Table 5.1 Two sets of experiments that will be performed in this chapter

Case 1 Litz wire	Case 2 Bar conductor
Test 1: Impedance measurements of 10 turns of Litz wire in <u>air</u>	Test 1: Impedance measurements of 20 turns of bar conductor in <u>air</u>
Test 2: Impedance measurements of 10 turns of Litz wire in <u>core</u>	Test 2: Impedance measurements of 20 turns of bar conductor in <u>core</u>

Note that the motorette and Litz wire used in this chapter are same as the ones used in section 4.2. While for the bar conductors selected, each single turn has a dimension of 5.6mm × 1.9mm and hence 20 turns of bar conductor give equivalent cross-sectional area of 10 turns of Litz.

The Wayne Kerr 6500B precision impedance analyser is selected for the measurements of impedance and phase angle because this equipment provides precise (basic measurement

accuracy of $\pm0.05\%$ according to data sheet) and fast testing of components at frequencies up to 120Mhz. According to the specification, there are two AC drive operating modes for this equipment: voltage drive mode with 10mV to 1Vrms and current drive mode with $200\mu A$ to 20mArms both varies with frequency. The current drive mode with 20mArms excitation current is selected for all the following tests.

In coils not located within magnetic cores, the real component of impedance and the real power with increasing frequency corresponds to the conductor losses. However, when the coil is integrated into a magnetic core, the real component of the measured impedance includes a combination of the coil loss (including AC resistance effect) and iron loss. Figure 5.1 shows one proposed equivalent circuit for the impedance of a coil within a slot.
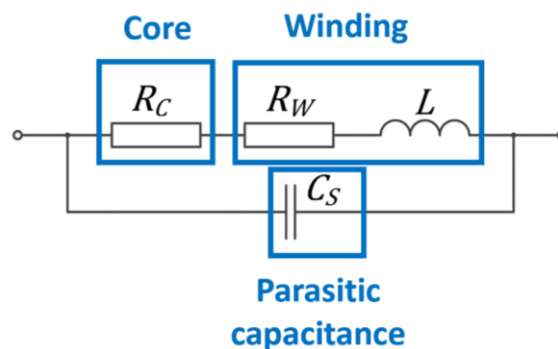
Figure 5.1 Equivalent circuit for impedance measurement

As will be apparent from Figure 5.1, the measurement of the magnitude and phase angle of the impedance cannot separate out the AC conductor loss from the iron loss even if the parasitic capacitance is neglected. Published studies on AC losses have attempted to separate out the AC conductor loss by subtracting a FEA calculated iron loss from the total measured input power. However, this makes the accuracy of AC losses measurements dependant on the accuracy to which the core loss is predicted. This is particularly problematic in cases with low AC conductor losses where the core loss equivalent resistor can be the dominant component and hence any uncertainties in the predicted core loss could have disproportionate effect on the uncertainty in the AC resistance.

However, in the case of testing processes in this chapter, there is no need to separate the conductor loss and iron loss because the maximum allowable 20mA operating current means that the maximum mmf per slot is only 282 m A.turns. This very small mmf means that the magnetic core is likely to operate on the reversible (i.e., non-hysteretic) region of the magnetisation characteristic in which the core loss is very small. Hence, all the measurements

were performed assuming no correction was required for iron loss when using the impedance analyser and the AC conductor loss can be directly calculated from the impedance and phase angle. As will be demonstrated later in this chapter, the assumption of no iron loss was borne out by the good correlation between measured and predicted AC resistance with no iron loss correction.

5.3 Experimental apparatus

5.3.1 Motorette

The experimental testing in this chapter was performed on a motorette which was based around a 300mm long core manufactured from M250-35A Silicon iron. A cross-section of the motorette core and the actual core are shown in Figure 5.2.

(a) Geometrical view of motorette

(b) Front view of motorette with focus on parallel slot
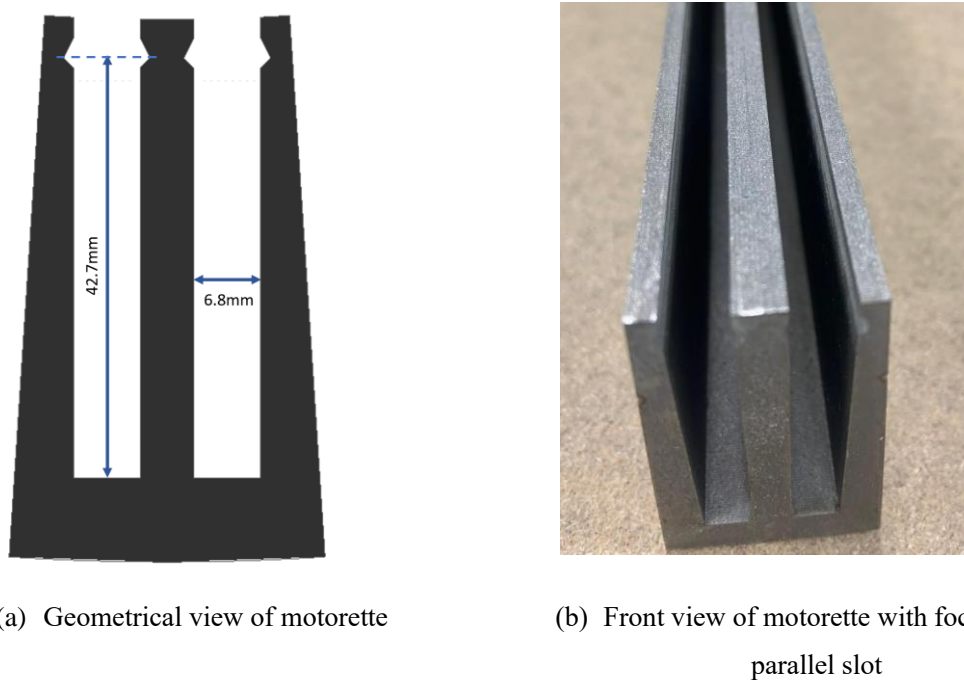
Figure 5.2 Geometrical view of motorette core

Two different windings were fitted to the motorette core for testing:

Solid strip conductor – A winding was formed from 20 series turns of a copper strip (5.6mm wide and 1.9mm thick) sourced from stock at the University of Sheffield. The end windings involve a tight bend radius and to achieve the repeatable bends required, the Rigon SBD1 precision wire bending machine shown in Figure 5.3 was used. This is a manual device which is designed to bend copper strip for insulation testing in accordance with IEC 60851-3.5.1.2.
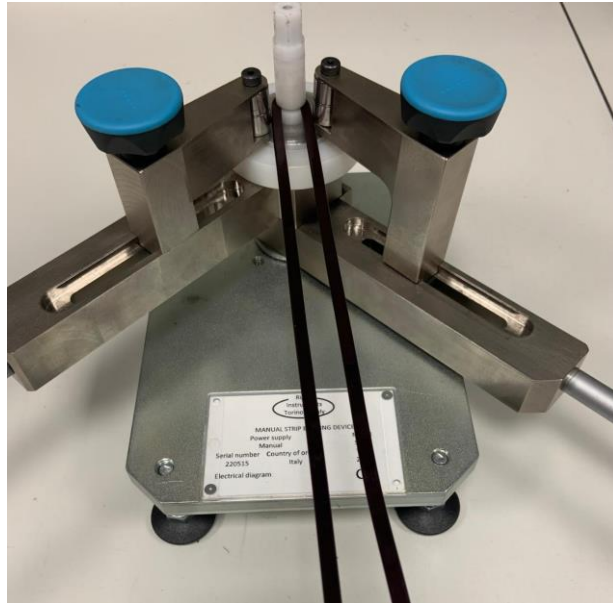
Figure 5.3 Rigon SBD1 precision wire bending machine

Litz winding – A winding with 10 series turns was formed using a rolled Litz conductor with an overall cross-section of 5.6mm × 3.8mm. This was also sourced from available stock from University of Sheffield and comprised 115 strands of 0.4mm diameter circular conductors. An important factor when comparing the measured and predicted performance of Litz wire is to recognise that the twisting of the wire along the Litz conductor length is usually not accounted for in either the finite element modelling or straightforward volume and length per turn calculations. The length of the conductor in FEA models and calculation methods is usually based on the mean path length of the bulk geometry of the overall conductor, which in turn tends to underestimate the length of the individual conductor strengths and hence their resistance. To account for the twisting factor, the DC resistance of the Litz wire set is measured before the testing with a precision ohmmeter available in the lab. Then the DC resistance of same Litz wire in a FEA model is calculated to obtain the twisting factor. The comparison between measured DC resistance and FEA calculated DC resistance is provided in the Table 5.2 below:

Table 5.2 Comparison between measured DC resistance and FEA calculated DC resistance

Measurement by precision ohmmeter	Calculation from FEA model	Twisting factor
$9.44 m\Omega$	$8.45 m\Omega$	1.12

As can be observed from Table 5.2, the twisting factor is 1.12, which means that any predicted resistance values from FEA model or simple geometric representations of the bulk conductor need to be scaled by this factor for comparison with measurements. Another thing to note is that the effective slot-fill factors (pure copper area / slot area) achieved within the 42.7mm × 6.8mm wide slot was 69% for the copper strip and 44% for the Litz wire. These packing factors do not represent the upper limit on the slot-fill factor for these two conductor types but reflect the existing stock available to support this research.

5.4 Test of Litz wire coil without the motorette core

The first testing was performed on the Litz winding as a free-standing winding before it was integrated into the motorette core. In order to ensure that the geometry of the winding was well defined, the testing was done in a custom-manufactured wooden coil holder. This was a simple rectangular block of the same dimension as the motorette core. The coil was located into this wooden holder and connected to the Wayne Kerr impedance analyser as shown in Figure 5.4.
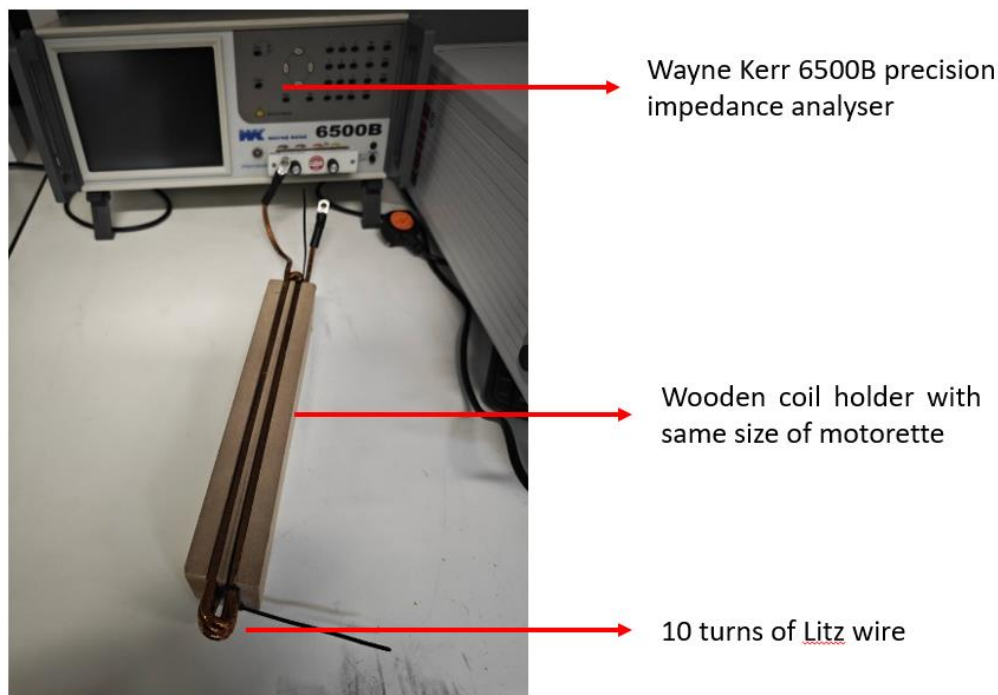
Figure 5.4 Litz winding in wooden coil holder connected to Wayne Kerr 6500B precision impedance analyser

Recall that from previous chapters that the strand-by-strand modelling of 10 turns Litz wire in the motorette is difficult to achieve, thus the homogenization technique which gives good accuracy over wide frequency range is used to make comparison with experimental results. The measured resistance of the coil as a function of frequency over the range 2730Hz to 80kHz (upper limit approximately equivalent to three times the base frequency of the 0.4mm strands

which make up the wire) is shown in Figure 5.5 alongside the values predicted from the finite element homogenised model. As will be apparent, there is reasonable agreement between the two characteristics. The same tendency of the homogenised model to overestimate the loss at higher frequencies that was observed in chapter 4 is also present in this set of results. This is a consequence of its resistance limited assumptions.
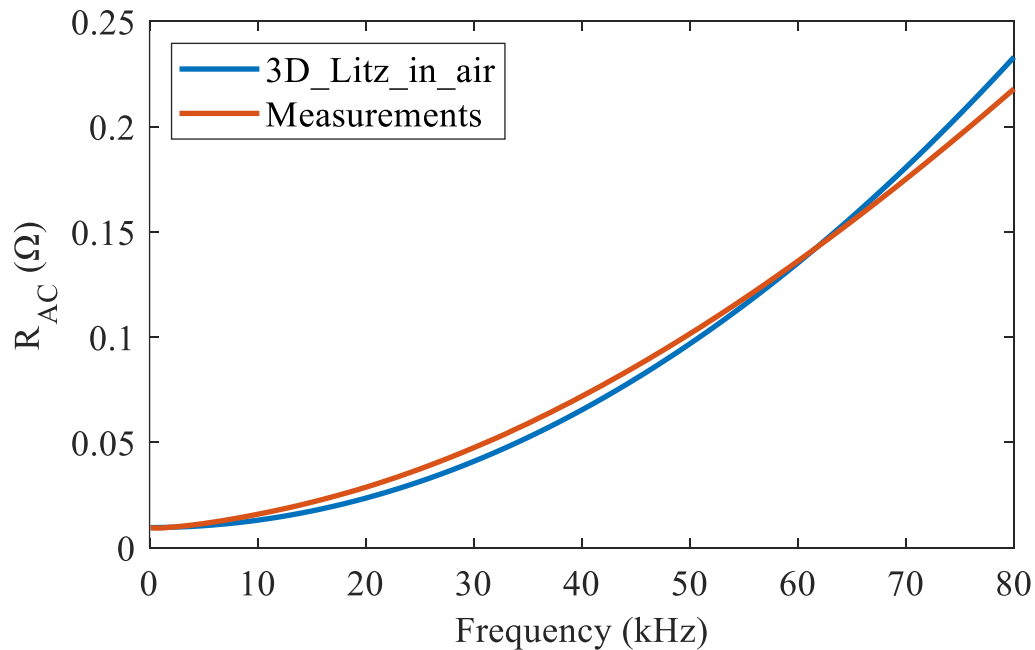
Figure 5.5 Comparison of predicted and measured resistance of Litz winding outside core

5.5 Test of long motorette with Litz wire in core

Having characterised the AC resistance of the Litz wire coil in a non-magnetic holder, the process was repeated with the Litz coil inserted into the 300mm core as shown in Figure 5.6.
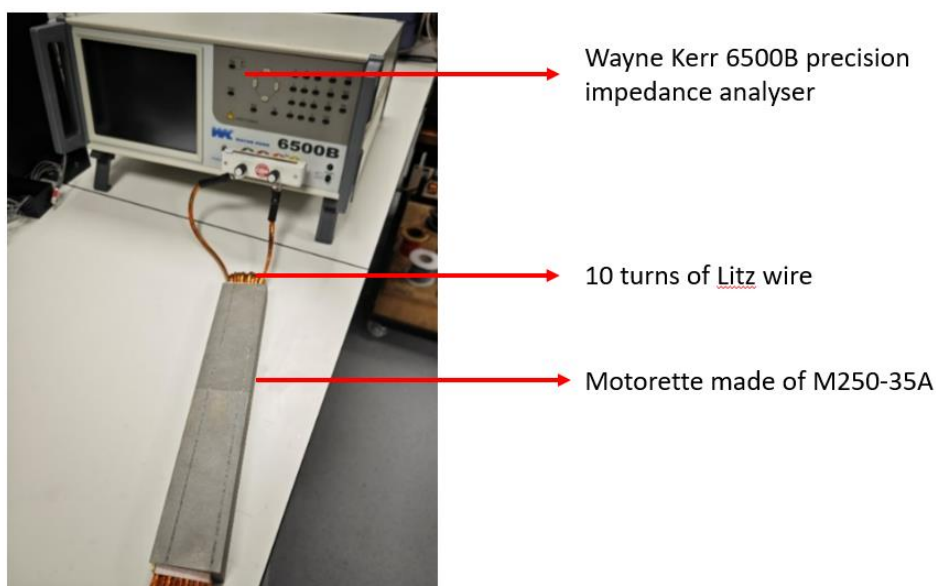
Figure 5.6 Litz winding in motorette core and connected to Wayne Kerr 6500B precision impedance analyser

183

The measured variation in the effective resistance of the coil as a function of frequency was measured up to 2kHz using the Wayne Kerr 6500B precision impedance analyser. A comparison between the measured and predicted AC resistance of the coil (with no correction for iron loss) is shown in Figure 5.7.
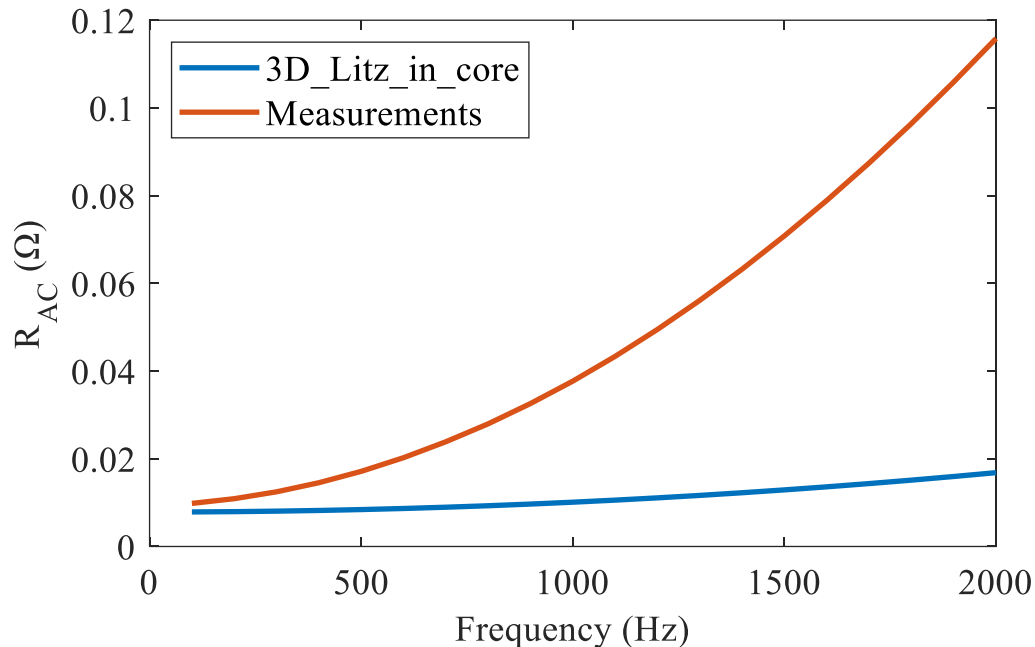
Figure 5.7 Litz winding in motorette core and connected to Wayne Kerr 6500B precision impedance analyser

As can be seen from Figure 5.7, the measurements do not agree with the FEA results. The main reason caused this misalignment is that the measured Litz wire AC resistance is obtained by a post-processing process, which is achieved by calculating the AC resistance based on measured impedance and phase angle. In a motorette model equipped with well-defined Litz wire, the AC loss is already very negligible, and the dominant loss component will be iron loss and hence any small variation in the measured phase angle is likely to have significant impact on the calculated AC resistance. Note that some attempts are made to include the FEA calculated iron loss in the comparison, but the inclusion of additional iron loss resistance component does not give better results and hence is not provided here.

5.6 Testing of the strip winding without the motorette core

The 20 turns of strip winding were placed in the wooden coil holder as shown in Figure 5.8.
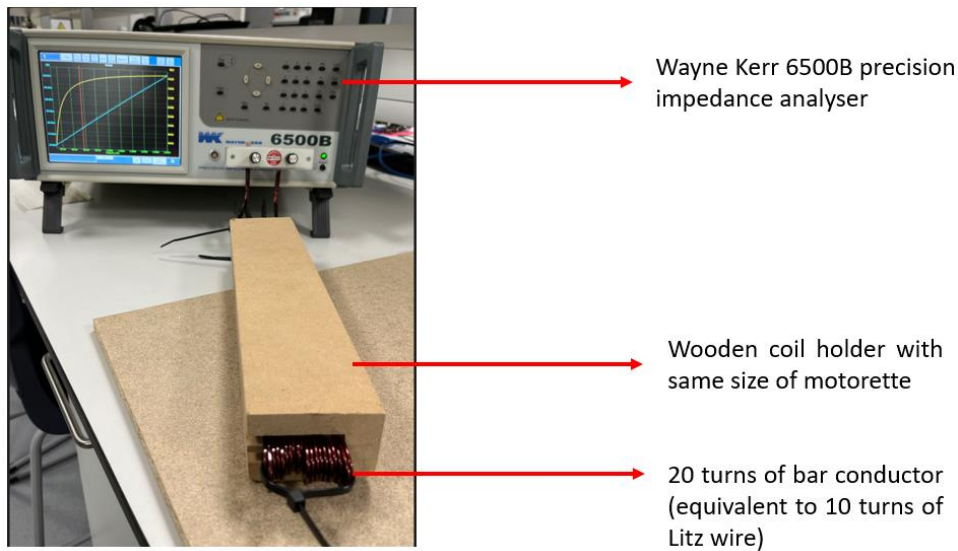
Figure 5.8 Strip wound coil in non-magnetic coil holder

The measured and simulated total effective resistance of the winding as function of frequency up to 2kHz are shown in Figure 5.9. Note that in the context of 3D FEA motorette model equipped with 20 turns of bar conductor, the detailed geometry of each single turn is built in the model and linked to solid conductors of external circuit to account for the skin and proximity effect. In addition, the meshes are manually adjusted to give the accurate results and reduce computational time just as the process introduced in section 4.5. As can be seen there is good agreement between the two characteristics.
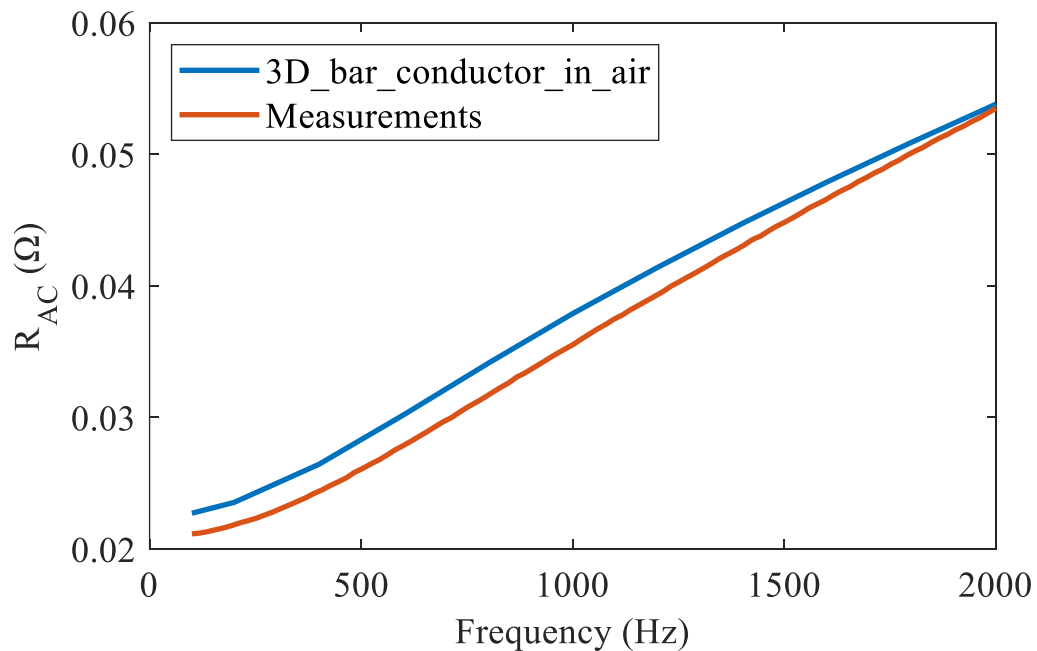
Figure 5.9 Variation in measured and simulated winding resistance as a function of frequency

5.7 Testing of the strip winding with the motorette core

The same procedure was applied to measure the effective resistance of the solid strip conductor over a 0 to 2kHz range when placed inside the motorette core. Figure 5.10 shows the motorette core with the 20-turn strip coil.
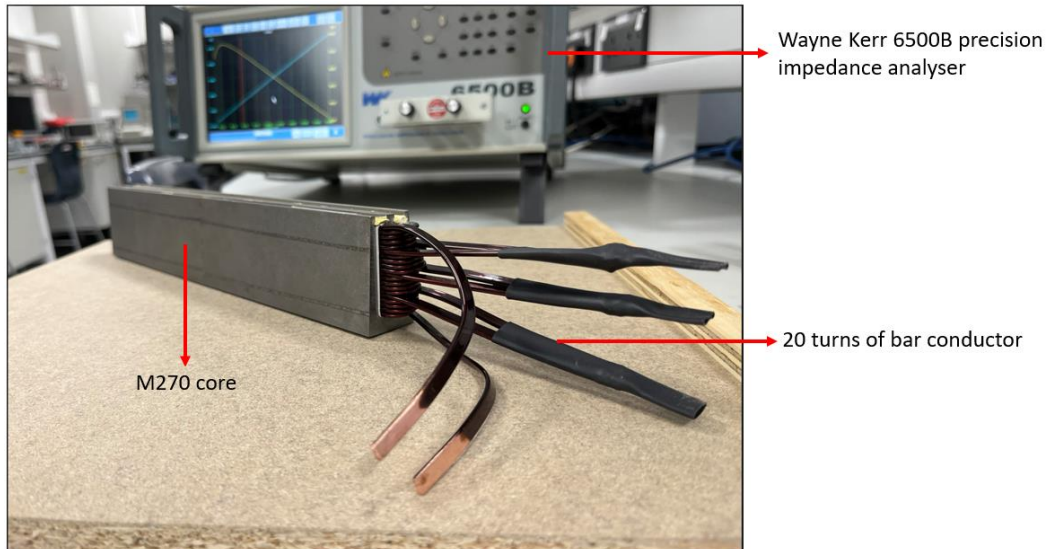
Figure 5.10 20 turns strip coil in motorette core

A comparison between the measured and predicted AC resistance of the coil (with no correction for iron loss) is shown in Figure 5.11 from which it can be seen that there is an excellent correlation because the magnitude of conductor loss within the bars is higher and thus makes the winding loss component dominant during the testing.
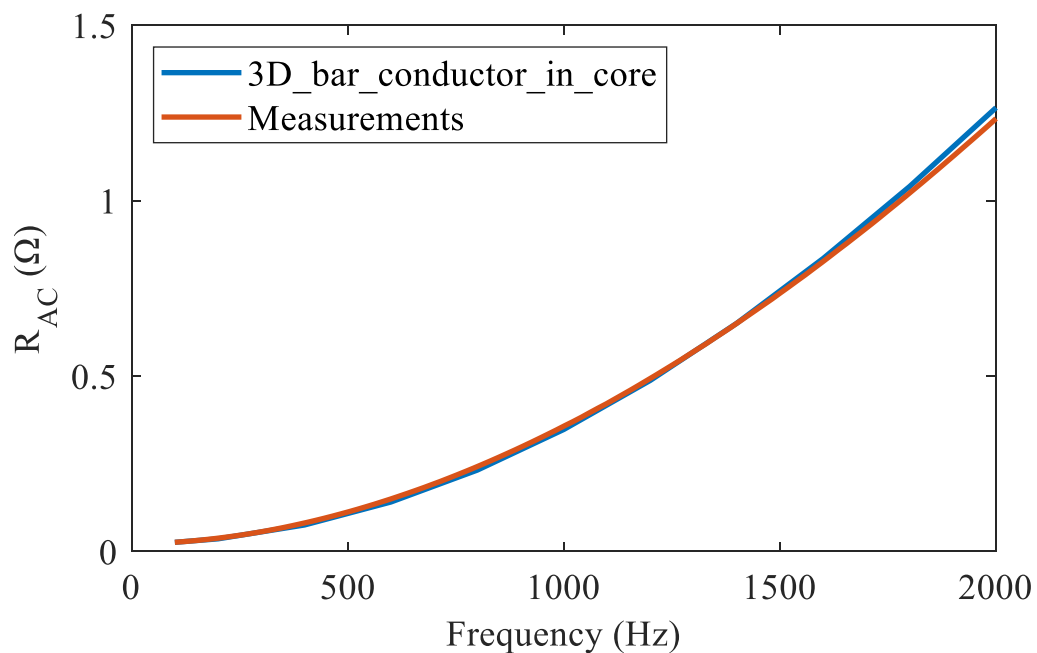
Figure 5.11 Variation in equivalent resistances with frequency for the strip conductor in motorette core

The flux density plot of the motorette equipped with 20 turns of bars with 20mArms injected current at 100Hz is provided in Figure 5.12 below. As can be seen, the flux density magnitude across core region is very small (with maximum value of 0.005T) and hence the assumption of no iron loss in the measurement is valid.
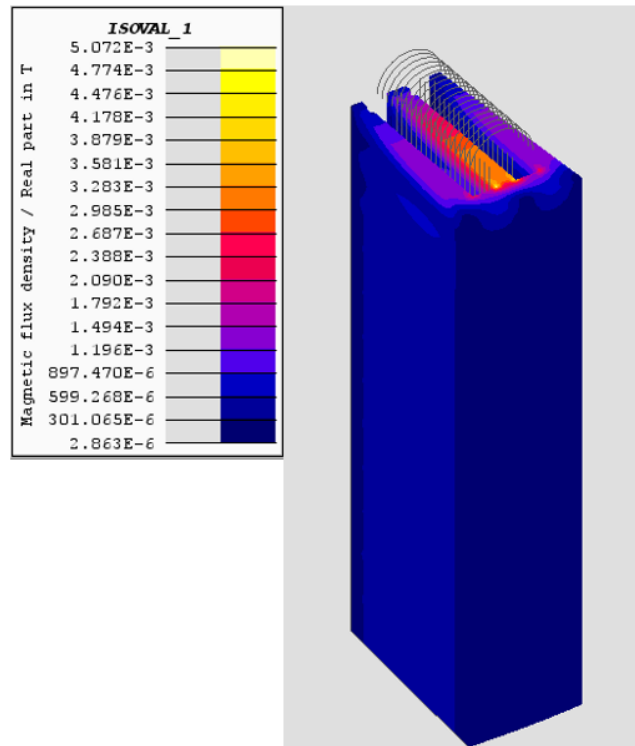
Figure 5.12 Flux density plot of core at 100Hz

5.8 Summary

This chapter has presented a series of measured results of AC resistance in various types of conductors for comparison with three-dimensional finite element models. It can be concluded that good agreements were generally obtained with the coils placed in air (both for Litz wire and bar conductor). When two sets of coils were inserted into the iron core, good alignment between FEA and test results is maintained for the bar conductor set but the accuracy for Litz wire winding set is compromised by the uncertainty associated with phase angle measurement which has significant impact on the AC conductor loss. Then the flux density amplitude across core region is plotted and the diagram confirms that the assumption of no iron loss is valid. Note that although most of experimental results in this chapter give reasonably good results, the testing process which neglects the effect of iron loss is rather ideal. To account for the iron loss and excite the core to reach its normal working condition, a new test rig including AC source, power amplifier, oscilloscope and power analyser is required, which is worth considering in the future.

Chapter 6. Conclusions and Future Work

6.1 Main conclusions

This thesis has reported on a series of investigations into conductor loss in high power density permanent magnet machines. It has been shown that electric loading is the key to increase torque density and that slot-fill factor plays an important role in determining conductor loss. Whereas employing rectangular conductors whose dimensions are closely matched to the geometry of the slot is common approach to improving slot-fill, it has been shown in this thesis that it is essential to take detailed consideration for induced eddy current losses in machine windings.

Chapter 2 reported on a detailed design study and optimisation process using static analysis in which significant improvements in power density were achieved by careful optimisation. This was based on quasi-static considerations only with the use of sizing equations and magneto-static finite element analysis. It was shown that even with a modest electrical frequency of 300Hz, the use of large section bar conductors resulted in almost an order of magnitude increase in loss to an entirely unsustainable level.

The fundamentals of eddy current effects in electrical machine windings were explored in chapter 3. It was shown in chapter 3 that guidance for selecting a conductor cross-section based on the classical skin depth of a single conductor greatly underestimates the problems that will be encountered by conductors when located in a slot with high levels of current density and a saturated core. By progressive implementation of various design features and dimensional optimisation, a reduction in conductor losses of a factor of 8 was achieved while maintaining the same rated torque within the same machine envelope. The most effective AC loss mitigation strategy which can be applied to other machines was the use of transposed parallel strips instead of a single large conductor. However, the adoption of transposed strips involved a modest reduction in slot-fill factor to accommodate the additional insulation layers within the slot. Another very effective modification, which was specific to this machine, was to increase the stator tooth width to reduce magnetic saturation which greatly reduced flux leakage across the slot. Although this involved reducing the conductor cross-section to accommodate a wider tooth and hence increasing the current density, up to a certain point this reduced the overall conductor loss. Other features such as incorporating magnetic slot wedges and moving the conductor towards slot bottom did not bring sufficient benefits compared to the other strategies. The impact of using of aluminium conductors and aluminium / copper hybrid windings was

investigated with a variety of uniform and asymmetric combinations. Although hybrid windings demonstrated some benefits in the proposed machine designs, once the various paralleling, transposition and tooth width modifications were incorporated, ultimately the lowest loss option was all-copper.

Chapter 4 investigated the potential benefits and drawbacks associated with type 8 Litz wire (with rectangular bundle shape) as an alternative type of conductor in high performance electrical machines. The modelling of Litz wire with many hundreds or thousands of parallel strands poses many challenges in finite element analysis. To reduce the modelling time and computational complexity, alternative Litz wire AC loss modelling techniques (semi-analytical and homogenization) were investigated systematically. The semi-analytical model is based on post-processing of the FEA model to extract field solutions of B and then use those B values to calculate the AC loss analytically. While for the homogenization technique, Litz wire bundle is considered as homogeneous region assigned with frequency dependent resistivity and complex permeability and then magnetic loss stored in coil region can be calculated based on those properties. The simulation results show that for the frequencies that are normally encountered in electrical machines (<2kHz), the homogenised model and semi-analytical model are adequate in both 2D and 3D context with significant reduction in modelling and computational time. For the Litz wire conductor selected for the machine, extensive modelling was performed to show the penalty in low-speed loss which is incurred due to the reduced packing factor.

Some measurements of conductor losses based on a long motorette equipped with two various sets of windings were introduced in chapter 5. The Wayne Kerr 6500B precision impedance analyser is used for measuring the impedance and phase angle and then the winding loss can be calculated. Note that this equipment only allows for 20mA current drive mode, resulting in a very small mmf in the slot and hence the core is very un-excited. Based on this, the core loss can be neglected and most of the testing results agree with that of simulation results.

A summary of some key features and performances of the best performing design with rectangular bar conductors and Litz wire are shown in Table 6.1 alongside the original design based on a single large bar conductor which was designed with consideration of quasi-static losses only. As can be seen from Table 6.1, the total winding loss has been reduced from 22,016W to 3,387W with a series of optimisation processes including paralleling, transposition and widening stator tooth. Although the current density of the optimal design has been

increased to a value higher than that normally seen in an electrical machine, this level of current density is entirely plausible with implementation of aggressive cooling method.

For the model equipped with Litz wire, the total winding loss is slightly higher than that of optimal model equipped with transposed bar conductors. This is caused by the penalty of reduced packing factor in the Litz wire bundle. Another thing to note is that to make the comparison between bars and Litz more consistent and equitable, the same level of NI per slot is maintained and this requirement of same torque leads to huge increase on the strand level current density ($27.4A/mm^2$) in a Litz wire bundle which is clearly prohibitive. However, this model can still be used as a reference to demonstrate that in a high power density machine operating at medium to low-speed range, the bar conductor tends to outperform Litz wire especially when thermal performances are also factored in. While in the context of high speed/ high frequency application, the Litz wire is likely to outperform bar conductor.

Table 6.1 A summary of key features and performances of the best design with rectangular bar conductors and Litz wire

	Static based design of chapter 2	Lowest loss solid bar design	Lowest loss Litz design
Mass (including end-winding)	49.5kg	47.3kg	43.2kg
Stator tooth width	10.3mm	7.8mm	10.3mm
Winding configuration	Thick bar conductor (4 turns)	6 parallel paths transposed with widened tooth	Type 8 Litz wire (0.4mm diameter) with bundle size same as baseline bar
Slot fill factor	0.79	0.67	0.47
Conductor losses at rated torque and 6000rpm	22,016W	3,387W	3,738W
Rms current density	$11.7A/mm^2$	$16.8A/mm^2$	$27.4A/mm^2$

6.2 Contributions to knowledge

The following are regarded as the main contributions to knowledge in the field

1. A systematic comparison of the advantages and disadvantages of different models for simulating eddy current loss in Litz wire.
2. A demonstration of the importance of dimensioning the stator core to reduce conductor loss even if this is at the expense of a reduced conductor cross-section.
3. A quantitative demonstration of the very significant improvements in AC loss which can be achieved by in-depth understanding and detailed modelling.

6.3 Future work

Several issues have been raised in this programme of research which would make interesting future research topics and would complement and extend the research reported in this thesis:

Build and testing of a full machine - In order to validate the various machine level conductor loss predictions made in this thesis, the build and testing of a full-scale machine would make a major contribution. This would need to include the facility to swap-in different coils. Although the build of full machine would allow some of the lossy coil designs to be tested, this would need to operate on a short-term transient basis to avoid overheating the coils since these could not necessarily be potted into the stator slots to allow removal.

Testing of hybrid aluminium / copper windings – The modelling in chapter 3 and reported in the recent ITEC paper suggest that hybrid windings could offer some advantages over all-copper winding. Difficulties in sourcing coated rectangular aluminium conductors prevented testing in this project but it would make an interesting addition to the analysis presented.

Effect of high frequency switching waveforms on loss – This thesis has focussed on a machine with an electrical frequency of 300Hz and even recognising the presence of significant flux harmonics, the frequencies do not approach the frequencies generated by converter switching. Developing models and design guidelines to account for switching events would provide a useful advance on the research in this thesis.

The thermal modelling and electromagnetic thermal coupled modelling – The focus of this thesis up to this stage is on winding loss optimisation in the context of electromagnetic modelling. It should be noted that the amplitude of losses in electrical machines is closely linked to thermal behaviour. For example, a higher loss will give higher operating temperature inside of machine and the temperature rise will influence the conductor material property, insulation integrity, the potentials of demagnetisation on magnets. It is thus necessary to carry some electromagnetic thermal coupled modelling and testing to fully assess the performances of proposed AC loss mitigation techniques.

References

[1] Advanced Propulsion Centre UK, "Electric machines roadmap," no. February 2021, p. 3, 2017, [Online]. Available: https://www.apcuk.co.uk/app/uploads/2018/02/EMC_Full_Pack.pdf

[2] M. Villani, M. Tursini, G. Fabri, and L. Castellini, "High reliability permanent magnet brushless motor drive for aircraft application," *IEEE Trans. Ind. Electron.*, vol. 59, no. 5, pp. 2073–2081, 2012, doi: 10.1109/TIE.2011.2160514.

[3] C. Friedrich and P. A. Robertson, "Hybrid-electric propulsion for automotive and aviation applications," *CEAS Aeronaut. J.*, vol. 6, no. 2, pp. 279–290, 2015, doi: 10.1007/s13272-014-0144-x.

[4] I. Eryilmaz, H. Li, V. Pachidis, P. Laskaridis, Z. Q. Zhu, and G. W. Jewell, "Performance and operability of an electrically driven propulsor," *Int. J. Engine Res.*, vol. 24, no. 3, pp. 843–855, 2023, doi: 10.1177/14680874211066396.

[5] O. Zaporozhets, V. Isaienko, and K. Synylo, "Trends on current and forecasted aircraft hybrid electric architectures and their impact on environment," *Energy*, vol. 211, p. 118814, 2020, doi: 10.1016/j.energy.2020.118814.

[6] 'Electrical Systems Technology Roadmap', Aerospace Technology Institute, Doc. FZO-PPN-MAP-0029, March 2022

[7] A. El-Refaie and M. Osama, "High Specific Power Electrical Machines: A System Perspective," *CES Trans. Electr. Mach. Syst.*, vol. 3, no. 1, pp. 88–93, 2019, doi: 10.30941/CESTEMS.2019.00012.

[8] N. Thapa, S. Ram, S. Kumar, and J. Mehta, "All electric aircraft: A reality on its way," *Mater. Today Proc.*, vol. 43, pp. 175–182, 2020, doi: 10.1016/j.matpr.2020.11.611.

[9] T. S. Tse and C. A. Hall, "Aerodynamics and Power Balance of a Distributed Aft-Fuselage Boundary Layer Ingesting Aircraft †," *Aerospace*, vol. 10, no. 2, 2023, doi: 10.3390/aerospace10020122.

[10] C. Goldberg, D. Nalianda, D. MacManus, P. Pilidis, and J. Felder, "Method for simulating the performance of a boundary layer ingesting propulsion system at design and off-design," *Aerosp. Sci. Technol.*, vol. 78, pp. 312–319, 2018, doi: 10.1016/j.ast.2018.04.026.

[11] C. L. Bowman, "Visions of the Future : Hybrid Electric Aircraft Propulsion," *AIAA Aircr. Electr. Power Propuls. Work.*, 2016.

[12] A. Al-Qarni, A. El-Refaie, and F. Wu, "Impact of Machine Parameters on the Design of High Specific Power Permanent Magnet Machines for Aerospace Applications," *2021 IEEE Int. Electr. Mach. Drives Conf. IEMDC 2021*, pp. 1–8, 2021, doi: 10.1109/IEMDC47953.2021.9449592.

[13] M. S. Donea and D. Gerling, "Design and calculation of a 300 kW high-speed PM motor for aircraft application," *2016 Int. Symp. Power Electron. Electr. Drives, Autom. Motion, SPEEDAM 2016*, no. 5, pp. 1–6, 2016, doi: 10.1109/SPEEDAM.2016.7525839.

[14] X. Zhang and K. S. Haran, "High-specific-power electric machines for electrified

transcription applications-technology options," *ECCE 2016 - IEEE Energy Convers. Congr. Expo. Proc.*, pp. 1–8, 2016, doi: 10.1109/ECCE.2016.7855164.

[15] J. A. Swanke, D. Bobba, T. M. Jahns, and B. Sarlioglu, "Design of high-speed permanent magnet machine for aerospace propulsion," *AIAA Propuls. Energy Forum Expo. 2019*, no. August, 2019, doi: 10.2514/6.2019-4483.

[16] J. Swanke, D. Bobba, T. M. Jahns, and B. Sarlioglu, "Comparison of Modular PM Propulsion Machines for High Power Density," *ITEC 2019 - 2019 IEEE Transp. Electrif. Conf. Expo*, 2019, doi: 10.1109/ITEC.2019.8790587.

[17] Z. Cheng, Z. Cao, J. T. Hwang, and C. Mi, "A Novel Single-Turn Permanent Magnet Synchronous Machine for Electric Aircraft," *Energies*, vol. 16, no. 3, pp. 1–15, 2023, doi: 10.3390/en16031041.

[18] J. A. Haylock, B. C. Mecrow, A. G. Jack, and D. J. Atkinson, "Operation of a fault tolerant PM drive for an aerospace fuel pump application," *IEE Proc. Electr. Power Appl.*, vol. 145, no. 5, pp. 441–448, 1998, doi: 10.1049/ip-epa:19982164.

[19] J. J. Cathey and J. A. Weimer, "Control of an Aircraft Electric Fuel Pump Drive," *IEEE Trans. Aerosp. Electron. Syst.*, vol. 24, no. 2, pp. 171–176, 1988, doi: 10.1109/7.1050.

[20] J. Li, Z. Yu, Y. Huang, and Z. Li, "A review of electromechanical actuation system for more electric aircraft," *AUS 2016 - 2016 IEEE/CSAA Int. Conf. Aircr. Util. Syst.*, pp. 490–497, 2016, doi: 10.1109/AUS.2016.7748100.

[21] P. Giangrande *et al.*, "Considerations on the Development of an Electric Drive for a Secondary Flight Control Electromechanical Actuator," *IEEE Trans. Ind. Appl.*, vol. 55, no. 4, pp. 3544–3554, 2019, doi: 10.1109/TIA.2019.2907231.

[22] A. M. El-Refaie, "Role of advanced materials in electrical machines," *2017 20th Int. Conf. Electr. Mach. Syst. ICEMS 2017*, vol. 3, no. 2, pp. 124–132, 2017, doi: 10.1109/ICEMS.2017.8055927.

[23] R. Wrobel and B. Mecrow, "A Comprehensive Review of Additive Manufacturing in Construction of Electrical Machines," *IEEE Trans. Energy Convers.*, vol. 35, no. 2, pp. 1054–1064, 2020, doi: 10.1109/TEC.2020.2964942.

[24] N. Simpson, D. J. North, S. M. Collins, and P. H. Mellor, "Additive Manufacturing of Shaped Profile Windings for Minimal AC Loss in Electrical Machines," *IEEE Trans. Ind. Appl.*, vol. 56, no. 3, pp. 2510–2519, 2020, doi: 10.1109/TIA.2020.2975763.

[25] M. Henke *et al.*, "Challenges and opportunities of very light high-performance electric drives for aviation," *Energies*, vol. 11, no. 2, 2018, doi: 10.3390/en11020344.

[26] A. Carriero, M. Locatelli, K. Ramakrishnan, G. Mastinu, and M. Gobbi, "A Review of the State of the Art of Electric Traction Motors Cooling Techniques," *SAE Tech. Pap.*, vol. 2018-April, pp. 1–13, 2018, doi: 10.4271/2018-01-0057.

[27] X. Zhang, C. L. Bowman, T. C. O'Connell, and K. S. Haran, "Large electric machines for aircraft electric propulsion," *IET Electr. Power Appl.*, vol. 12, no. 6, pp. 767–779, 2018, doi: 10.1049/iet-epa.2017.0639.

[28] A. Aggarwal, E. G. Strangas, and A. Karlis, "Review of segmented stator and rotor designs for AC electric machines," *Proc. - 2020 Int. Conf. Electr. Mach. ICEM 2020*,

pp. 2342–2348, 2020, doi: 10.1109/ICEM49940.2020.9270678.

[29] Wu, L., Xia, Z.P, "Stator tooth segmentation method for electric machines", European Patent Application, EP2757662A1, 2013.

[30] P. Mellor, R. Wrobel, and N. Simpson, "AC losses in high frequency electrical machine windings formed from large section conductors," *2014 IEEE Energy Convers. Congr. Expo. ECCE 2014*, no. 2, pp. 5563–5570, 2014, doi: 10.1109/ECCE.2014.6954163.

[31] J. W. Chin, K. S. Cha, M. R. Park, S. H. Park, E. C. Lee, and M. S. Lim, "High Efficiency PMSM with High Slot Fill Factor Coil for Heavy-Duty EV Traction Considering AC Resistance," *IEEE Trans. Energy Convers.*, vol. 36, no. 2, pp. 883–894, 2021, doi: 10.1109/TEC.2020.3035165.

[32] A. Yu and G. W. Jewell, "Systematic design study into the influence of rotational speed on the torque density of surface-mounted permanent magnet machines," *J. Eng.*, vol. 2019, no. 17, pp. 4595–4600, 2019, doi: 10.1049/joe.2018.8204.

[33] J. F. Gieras, "Multimegawatt synchronous generators for airborne applications: A review," *Proc. 2013 IEEE Int. Electr. Mach. Drives Conf. IEMDC 2013*, pp. 626–633, 2013, doi: 10.1109/IEMDC.2013.6556160.

[34] N. Jiao, Z. Li, S. Mao, C. Sun, and W. Liu, "Aircraft Brushless Wound-Rotor Synchronous Starter-Generator: A Technology Review," *IEEE Trans. Power Electron.*, vol. 38, no. 6, pp. 7558–7574, 2023, doi: 10.1109/TPEL.2023.3260091.

[35] G J Li, G. Jewell, Z Q Zhu, "Permanent magnet machines and actuators," *EEE6204 lecture notes*, The Univeristy of Sheffield, September 2018.

[36] J. K. Noland, M. Leandro, J. A. Suul, and M. Molinas, "High-Power Machines and Starter-Generator Topologies for More Electric Aircraft: A Technology Outlook," *IEEE Access*, vol. 8, pp. 130104–130123, 2020, doi: 10.1109/ACCESS.2020.3007791.

[37] P. E. Kakosimos, A. G. Sarigiannidis, M. E. Beniakar, A. G. Kladas, and C. Gerada, "Induction motors versus permanent-magnet actuators for aerospace applications," *IEEE Trans. Ind. Electron.*, vol. 61, no. 8, pp. 4315–4325, 2014, doi: 10.1109/TIE.2013.2274425.

[38] R. Krishnan, D. Blanding, A. Bhanot, A. M. Staley, and N. S. Lobo, "High Reliability SRM Drive System for Aerospace Applications," *IECON Proc. (Industrial Electron. Conf.*, vol. 2, pp. 1110–1115, 2003, doi: 10.1109/IECON.2003.1280202.

[39] H. Hofmann and S. R. Sanders, "High-speed synchronous reluctance machine with minimized rotor losses," *IEEE Trans. Ind. Appl.*, vol. 36, no. 2, pp. 531–539, 2000, doi: 10.1109/28.833771.

[40] J. Borg Bartolo, M. Degano, J. Espina, and C. Gerada, "Design and Initial Testing of a High-Speed 45-kW Switched Reluctance Drive for Aerospace Application," *IEEE Trans. Ind. Electron.*, vol. 64, no. 2, pp. 988–997, 2017, doi: 10.1109/TIE.2016.2618342.

[41] A. Schramm and D. Gerling, "Researches on the suitability of switched reluctance machines and permanent magnet machines for specific aerospace applications demanding fault tolerance," *Int. Symp. Power Electron. Electr. Drives, Autom. Motion, 2006. SPEEDAM 2006*, vol. 2006, pp. 56–60, 2006, doi:

10.1109/SPEEDAM.2006.1649744.

[42] J. M. D. Coey, "Perspective and Prospects for Rare Earth Permanent Magnets," *Engineering*, vol. 6, no. 2, pp. 119–131, 2020, doi: 10.1016/j.eng.2018.11.034.

[43] A. G. Sarigiannidis, M. E. Beniakar, P. E. Kakosimos, A. G. Kladas, L. Papini, and C. Gerada, "Fault tolerant design of fractional slot winding permanent magnet aerospace actuator," *IEEE Trans. Transp. Electrif.*, vol. 2, no. 3, pp. 380–390, 2016, doi: 10.1109/TTE.2016.2574947.

[44] A. Balachandran, M. Boden, Z. Sun, S. J. Forrest, J. D. Ede, and G. W. Jewell, "Design, construction, and testing of an aero-engine starter-generator for the more-electric aircraft," *J. Eng.*, vol. 2019, no. 17, pp. 3474–3478, 2019, doi: 10.1049/joe.2018.8235.

[45] B. Wang, Y. Liu, G. Vakil, T. Yang, and Z. Zhang, "Feasibility of permanent magnet fault tolerant machines for aircraft starter/generator systems," *Proc. - 2020 Int. Conf. Electr. Mach. ICEM 2020*, pp. 2104–2110, 2020, doi: 10.1109/ICEM49940.2020.9270965.

[46] J. A. Swanke, D. Bobba, T. M. Jahns, and B. Sarlioglu, "Design of high-speed permanent magnet machine for aerospace propulsion," *AIAA Propuls. Energy Forum Expo. 2019*, no. August 2019, pp. 1–12, 2019, doi: 10.2514/6.2019-4483.

[47] E. Ganev, "Selecting the best electric machines for electrical power-generation systems: High-performance solutions for aerospace More electric architectures," *IEEE Electrif. Mag.*, vol. 2, no. 4, pp. 13–22, 2014, doi: 10.1109/MELE.2014.2364731.

[48] D. J. Powell, "Modelling of high power density electrical machines for aerospace," PhD thesis, The Univeristy of Sheffield, May 2003.

[49] Y. Gai *et al.*, "Cooling of automotive traction motors: Schemes, examples, and computation methods," *IEEE Trans. Ind. Electron.*, vol. 66, no. 3, pp. 1681–1692, 2019, doi: 10.1109/TIE.2018.2835397.

[50] Y. Zhao, D. Li, T. Pei, and R. Qu, "Overview of the rectangular wire windings AC electrical machine," *CES Trans. Electr. Mach. Syst.*, vol. 3, no. 2, pp. 160–169, 2019, doi: 10.30941/cestems.2019.00022.

[51] T. Ishigami, Y. Tanaka, and H. Homma, "Motor Stator With Thick Rectangular Wire Lap Winding for HEVs," *IEEE Trans. Ind. Appl.*, vol. 51, no. 4, pp. 2917–2923, 2015, doi: 10.1109/TIA.2015.2391435.

[52] H. V. Khang, J. Saari, and A. Arkkio, "Form-wound stator winding for high-speed induction motors," *Proc. - 2014 Int. Conf. Electr. Mach. ICEM 2014*, vol. 1, pp. 169–175, 2014, doi: 10.1109/ICELMACH.2014.6960176.

[53] P. E. M. Ieee, N. Boubaker, and D. Matt, "Bar Winding for the Low-Voltage Motorization of an Electric Tractor .," pp. 1711–1717, 2020.

[54] G. Jewell, "Introduction Electrical Machines Short Course," Future Electrical Machines Manufacturing Hub, September, 2019.

[55] A. Yoon, X. Yi, J. Martin, Y. Chen, and K. Haran, "A high-speed, high-frequency, air-core PM machine for aircraft application," *2016 IEEE Power Energy Conf. Illinois, PECI 2016*, pp. 1–4, 2016, doi: 10.1109/PECI.2016.7459221.

[56] J. D. Widmer, C. M. Spargo, G. J. Atkinson, and B. C. Mecrow, "Solar plane propulsion motors with Precompressed aluminum stator windings," *IEEE Trans. Energy Convers.*, vol. 29, no. 3, pp. 681–688, 2014, doi: 10.1109/TEC.2014.2313642.

[57] K. Atallah , Z. Q. Zhu , J. K. Mitchell and D. Howe (1994) Curvature Effects in Radial-Field Permanet magnet machines, Electrical and Machines and Power Systems, 22:4, 511-520, DOI: 10.1080/07313569408955583.

[58] A. YU, "An Investigation of torque density and losses in high-speed permanent magnet machines," PhD thesis, The University of Sheffield, October 2018.

[59] J. Jacobus and H. Paulides, "High performance 1.5MW 20,000rpm permanent magnet generator with uncontrolled rectifier for 'more-electric' ship applications," PhD thesis, The Univeristy of Sheffield, March, 2005.

[60] H. L. Ornaghi, J. H. S. Almeida, F. M. Monticeli, and R. M. Neves, "Stress relaxation, creep, and recovery of carbon fiber non-crimp fabric composites," *Compos. Part C Open Access*, vol. 3, no. July, p. 100051, 2020, doi: 10.1016/j.jcomc.2020.100051.

[61] P. S. Ghahfarokhi, A. Podgornovs, A. J. Marques Cardoso, A. Kallaste, A. Belahcen, and T. Vaimann, "Hairpin Windings for Electric Vehicle Motors: Modeling and Investigation of AC Loss-Mitigating Approaches," *Machines*, vol. 10, no. 11, pp. 1–14, 2022, doi: 10.3390/machines10111029.

[62] D. Lin, C. Lu, N. Chen, and P. Zhou, "An Efficient Method for Litz-Wire AC Loss Computation in Transient Finite Element Analysis," *IEEE Trans. Magn.*, vol. 58, no. 5, 2022, doi: 10.1109/TMAG.2022.3153130.

[63] D. K. K. Padinharu, G. J. Li, Z. Q. Zhu, R. Clark, A. Thomas, and Z. Azar, "AC Losses in Form-Wound Coils of Surface Mounted Permanent Magnet Vernier Machines," *IEEE Trans. Magn.*, vol. 58, no. 6, 2022, doi: 10.1109/TMAG.2022.3170658.

[64] P. M. Lindh, J. J. Pyrhonen, P. Ponomarev, and D. Vinnikov, "Influence of wedge material on losses of a traction motor with tooth-coil windings," *IECON Proc. (Industrial Electron. Conf.*, pp. 2941–2946, 2013, doi: 10.1109/IECON.2013.6699598.

[65] L. Frosini and M. Pastura, "Analysis and design of innovative magnetic wedges for high efficiency permanent magnet synchronous machines," *Energies*, vol. 13, no. 1, 2020, doi: 10.3390/en13010255.

[66] S. Han *et al.*, "In-Service Monitoring of Stator-Slot Magnetic Wedge Condition for Induction Motors," *IEEE Trans. Ind. Appl.*, vol. 52, no. 4, pp. 2900–2910, 2016, doi: 10.1109/TIA.2016.2539128.

[67] T. R. Gaerke and D. C. Hernandez, "The temperature impact of magnetic wedges on TEFC induction motors," *IEEE Trans. Ind. Appl.*, vol. 49, no. 3, pp. 1228–1233, 2013, doi: 10.1109/TIA.2013.2252135.

[68] M. J. Islam, H. V. Khang, A. K. Repo, and A. Arkkio, "Eddy-current loss and temperature rise in the form-wound stator winding of an inverter-fed cage induction motor," *IEEE Trans. Magn.*, vol. 46, no. 8, pp. 3413–3416, 2010, doi: 10.1109/TMAG.2010.2044387.

[69] Y. Xiao, L. Zhou, J. Wang, and J. Liu, "Design and performance analysis of magnetic slot wedge application in double-fed asynchronous motor-generator by finiteelement

method," *IET Electr. Power Appl.*, vol. 12, no. 7, pp. 1040–1047, 2018, doi: 10.1049/iet-epa.2017.0730.

[70] G. De Donato, F. G. Capponi, and F. Caricchi, "No-load performance of axial flux permanent magnet machines mounting magnetic wedges," *IEEE Trans. Ind. Electron.*, vol. 59, no. 10, pp. 3768–3779, 2012, doi: 10.1109/TIE.2011.2169638.

[71] G. De Donato, F. G. Capponi, and F. Caricchi, "On the use of magnetic wedges in axial flux permanent magnet machines," *IEEE Trans. Ind. Electron.*, vol. 60, no. 11, pp. 4831–4840, 2013, doi: 10.1109/TIE.2012.2225392.

[72] J. Haldemann, "Transpositions in stator bars of large turbogenerators," *IEEE Trans. Energy Convers.*, vol. 19, no. 3, pp. 553–560, 2004, doi: 10.1109/TEC.2004.832067.

[73] J. Zou, B. Zhao, Y. Xu, J. Shang, and W. Liang, "A new end windings transposition to reduce windings eddy loss for 2 MW direct drive multi-unit pmsm," *IEEE Trans. Magn.*, vol. 48, no. 11, pp. 3323–3326, 2012, doi: 10.1109/TMAG.2012.2201701.

[74] J. Liu, Y. Liang, and P. Yang, "Research on Novel Flat Wire Transposed Winding of PMSM for Electric Vehicle," *IEEE Trans. Transp. Electrif.*, vol. 9, no. 1, pp. 771–781, 2023, doi: 10.1109/TTE.2022.3198950.

[75] Y. Liang, F. Zhao, K. Xu, W. Wang, J. Liu, and P. Yang, "Analysis of Copper Loss of Permanent Magnet Synchronous Motor with Formed Transposition Winding," *IEEE Access*, vol. 9, pp. 101105–101114, 2021, doi: 10.1109/ACCESS.2021.3094833.

[76] P. B. Reddy, T. M. Jahns, and T. P. Bohn, "Transposition effects on bundle proximity losses in high-speed PM machines," *2009 IEEE Energy Convers. Congr. Expo. ECCE 2009*, no. 1, pp. 1919–1926, 2009, doi: 10.1109/ECCE.2009.5316037.

[77] D. Wang, Y. Liang, L. Gao, X. Bian, and C. Wang, "A New Global Transposition Method of Stator Winding and Its Loss Calculation in AC Machines," *IEEE Trans. Energy Convers.*, vol. 35, no. 1, pp. 149–156, 2020, doi: 10.1109/TEC.2019.2947082.

[78] BSI Standard Publication, "Specifications for particular types of winding wires - Part 0-2: General requirements - Enamelled rectangular copper wire (IEC 60317-0-2:2020)",2020

[79] BSI Standard Publication, "Specifications for particular types of winding wires - Part 0-8: General requirements - Polyester glass-fibre wound unvarnished and fused, or resin or varnish impregnated, bare or enamelled rectangular copper wire (IEC 60317-0-8:2019)",2019

[80] R. Yoshida *et al.*, "Effect of Magnetic Properties of Magnetic Composite Tapes on Motor Losses," *Energies*, vol. 15, no. 21, p. 7991, 2022, doi: 10.3390/en15217991.

[81] P. W. Han, Y. Do Chun, J. H. Choi, M. J. Kim, D. H. Koo, and J. Lee, "The study to substitute aluminum for copper as a winding material in induction machine," *INTELEC, Int. Telecommun. Energy Conf.*, pp. 12–14, 2009, doi: 10.1109/INTLEC.2009.5352008.

[82] M. Peter, J. Fleischer, F. S. Le Blanc, and J. P. Jastrzembski, "New conceptual lightweight design approaches for integrated manufacturing processes: Influence of alternative materials on the process chain of electric motor manufacturing," *2013 3rd Int. Electr. Drives Prod. Conf. EDPC 2013 - Proc.*, 2013, doi: 10.1109/EDPC.2013.6689735.

[83] J. D. Widmer, R. Martin, and B. C. Mecrow, "Precompressed and Stranded Aluminum Motor Windings for Traction Motors," *IEEE Trans. Ind. Appl.*, vol. 52, no. 3, pp. 2215–2223, 2016, doi: 10.1109/TIA.2016.2528226.

[84] A. G. Jack *et al.*, "Permanent-magnet machines with powdered iron cores and prepressed windings," *IEEE Trans. Ind. Appl.*, vol. 36, no. 4, pp. 1077–1084, 2000, doi: 10.1109/28.855963.

[85] V. Buchholz, R. Frank, and C. Morton, "Corrosion and current burst testing of copper and aluminum electrical power connectors," *Proc. IEEE Power Eng. Soc. Transm. Distrib. Conf.*, pp. 996–1001, 2006, doi: 10.1109/TDC.2006.1668638.

[86] R. Wrobel, D. Salt, N. Simpson, and P. H. Mellor, "Comparative study of copper and aluminium conductors - future cost effective PM machines," *7th IET Int. Conf. Power Electron. Mach. Drives, PEMD 2014*, pp. 1–6, 2014.

[87] C. R. Sullivan, "Aluminum windings and other strategies for high-frequency magnetics design in an era of high copper and energy costs," *IEEE Trans. Power Electron.*, vol. 23, no. 4, pp. 2044–2051, 2008, doi: 10.1109/TPEL.2008.925434.

[88] F. Wu, A. M. El-Refaie, and A. Al-Qarni, "Minimization of Winding AC Losses Using Inhomogeneous Electrical Conductivity Enabled by Additive Manufacturing," *IEEE Trans. Ind. Appl.*, vol. 58, no. 3, pp. 3447–3458, 2022, doi: 10.1109/TIA.2022.3152457.

[89] M. S. Islam, I. Husain, A. Ahmed, and A. Sathyan, "Asymmetric Bar Winding for High-Speed Traction Electric Machines," *IEEE Trans. Transp. Electrif.*, vol. 6, no. 1, pp. 3–15, 2020, doi: 10.1109/TTE.2019.2962329.

[90] P. L. Dowell, "Effects of eddy currents in transformer windings," *Proc. Inst. Electr. Eng.*, vol. 113, no. 8, p. 1387, 1966, doi: 10.1049/piee.1966.0236.

[91] J. A. Ferreira, "Improved Analytical Modeling of Conductive Losses in Magnetic Components," *IEEE Trans. Power Electron.*, vol. 9, no. 1, pp. 127–131, 1994, doi: 10.1109/63.285503.

[92] M. Albach, "Two-dimensional calculation of winding losses in transformers," *PESC Rec. - IEEE Annu. Power Electron. Spec. Conf.*, vol. 3, no. c, pp. 1639–1644, 2000, doi: 10.1109/PESC.2000.880550.

[93] C. R. Sullivan, "Computationally Efficient Winding Loss Calculation with Multiple Windings , Arbitrary Waveforms , Geometry," vol. 16, no. 1, pp. 142–150, 2001.

[94] F. Tourkhani and P. Viarouge, "Accurate analytical model of winding losses in round Litz wire windings," *IEEE Trans. Magn.*, vol. 37, no. 1, pp. 538–543, 2001, doi: 10.1109/20.914375.

[95] X. Nan and C. R. Sullivan, "An improved calculation of proximity-effect loss in high-frequency windings of round conductors," *PESC Rec. - IEEE Annu. Power Electron. Spec. Conf.*, vol. 2, pp. 853–860, 2003, doi: 10.1109/pesc.2003.1218168.

[96] H. Igarashi, "Semi-analytical approach for finite-element analysis of multi-turn coil considering skin and proximity effects," *IEEE Trans. Magn.*, vol. 53, no. 1, pp. 1–7, 2017, doi: 10.1109/TMAG.2016.2601066.

[97] A. Robkopf, C. Joffe, and E. Bar, "Calculation of ohmic losses in litz wires by

coupling analytical and numerical methods," *2014 4th Int. Electr. Drives Prod. Conf. EDPC 2014 - Proc.*, 2014, doi: 10.1109/EDPC.2014.6984423.

[98]   J. Gyselinck and P. Dular, "Frequency-domain homogenization of bundles of wires in 2-D magnetodynamic FE calculations," *IEEE Trans. Magn.*, vol. 41, no. 5, pp. 1416–1419, 2005, doi: 10.1109/TMAG.2005.844534.

[99]   A. D. Podoltsev, K. G. N. B. Abeywickrama, Y. V. Serdyuk, and S. M. Gubanski, "Multiscale computations of parameters of power transformer windings at high frequencies. Part II: Large-scale level," *IEEE Trans. Magn.*, vol. 43, no. 12, pp. 4076–4082, 2007, doi: 10.1109/TMAG.2007.908371.

[100]   J. R. Sibué, J. P. Ferrieux, G. Meunier, and R. Périot, "Modeling of losses and current density distribution in conductors of a large air-gap transformer using homogenization and 3-D FEM," *IEEE Trans. Magn.*, vol. 48, no. 2, pp. 763–766, 2012, doi: 10.1109/TMAG.2011.2174143.

[101]   R. V. Sabariego, P. Dular, and J. Gyselinck, "Time-domain homogenization of windings in 2-D finite element models," *IEEE Trans. Magn.*, vol. 44, no. 6, pp. 1302–1305, 2008, doi: 10.1109/TMAG.2007.915908.

[102]   R. V. Sabariego, P. Dular, and J. Gyselinck, "Time-domain homogenization of windings in 3-D finite element models," *IEEE Trans. Magn.*, vol. 44, no. 6, pp. 1302–1305, 2008, doi: 10.1109/TMAG.2007.915908.

[103]   J. J. A. C. and A. J. M. Z. Sun, J. D. Ede, J. Wang, G. W. Jewell, "Testing of a 250-Kilowatt Fault-Tolerant Permanent Magnet Power Generation System for Large Civil Aeroengines," p. 10.

[104]   W. Zhu, X. Chen, and G. W. Jewell, "Effects of the Randomness of Winding Distribution in Slot on the Bearing Voltage and the Electric Discharge Machining Bearing Current," *IET Conf. Proc.*, vol. 2022, no. 4, pp. 652–659, 2022, doi: 10.1049/icp.2022.1131.